



UNIVERSITY OF
BIRMINGHAM

HIGH POWER GALLIUM NITRIDE MICRO-ELECTRONICS: THERMAL MANAGEMENT USING MICROFLUIDICS

by

Gan Zhang

A thesis submitted to
The University of Birmingham
For the degree of
DOCTOR OF PHILOSOPHY

School of Chemical Engineering
University of Birmingham
July 2020

**UNIVERSITY OF
BIRMINGHAM**

University of Birmingham Research Archive

e-theses repository

This unpublished thesis/dissertation is copyright of the author and/or third parties. The intellectual property rights of the author or third parties in respect of this work are as defined by The Copyright Designs and Patents Act 1988 or as modified by any successor legislation.

Any use made of information contained in this thesis/dissertation must be in accordance with that legislation and must be properly acknowledged. Further distribution or reproduction in any format is prohibited without the permission of the copyright holder.

Abstract

Last four decades have seen unprecedented development in communication, defence, electronics, and computing technologies. The increased power density plus the miniaturisation of the device present challenges in managing the high heat flux in the microchip level. Besides, the highly heterogeneous heat flux in electronic devices presents more challenges to thermal management (TM). This calls for the development of more efficient cooling technologies for these high-power microelectronic devices. This PhD study aims to address this challenge by developing the high performance of heat transfer fluids (HTFs) and compact cooling devices. Gallium Nitride (GaN) based transistors which acted as inhomogeneous high heat flux output were targeted in this work.

The work involves formulating, characterisation and performance measurements of various heat transfer fluids (including base fluids and nanofluids), design, fabrication and assemble, and package and experiments of microfluidics including foam metal, micro-jet impingement. Both experimental work and modelling were performed and the following main conclusions were obtained.

- Heat transfer fluids study

Two types of nanofluids were formulated and investigated for the application in room temperature and the low temperature. The BN/DI water nanofluids used in the room temperature shows 5.2 % enhancement in the thermal conductivity compared to the base fluid for the 0.5 wt.%. The other material rGO/EG+DW nanofluids used for the temperature as low as -50 °C has 17 % thermal conductivity increase with the concentration of 2.0 wt.%. This suggests that the nanofluids can have a better thermal performance for the microfluidic channel than the base fluids.

- Performance of the microfluidics

With the experimental comparison of the copper-foam based microfluidic channel and the micro-jet channel, the micro-jet channel was chosen due to a higher heat transfer coefficient. Both base fluids and nanofluids were experimental tests and the numerical simulation was validated with the micro-jet channel. The test showed that the BN/DI water nanofluids with a concentration of

0.5 wt.% can increase the heat transfer coefficient 5 % compared to the DI water. Meanwhile, the 2.0 wt.% rGO/EG+DW nanofluids showed a similar trend with an 11% increase in the heat transfer coefficient compared to EG+DW base fluid.

The direct measurement of the temperature with Raman thermography was used to measure the temperature in the finger of the die. The experiment test suggests that with the target power density of 5 W/mm in the finger (1×10^7 W/mm² in the finger), the peak temperature in the devices was 120 °C far below 200 °C. The thermal resistance for the jetting channel was 19.76 °C/W. The device used in the experiment was GaN-on-SiC. For the GaN-on-Diamond, a higher power density can be obtained.

Thus, for the thermal management of the GaN devices, the nanofluids, material selection for the devices thermal package and micro-jet channel play important roles once the specific GaN transistors are selected.

Keywords: *thermal management, GaN transistors, microfluidic channel, micro-jet channel, copper-foam based channel, nanofluids, rGO, heat flux, heat transfer coefficient, thermal resistance, thermal conductivity, viscosity*

Contents

1.	Introduction.....	1
1.1	Background.....	1
1.2	Aim and objective and for this PhD project.....	2
1.3	Project description and methodology.....	3
1.4	Structure of the thesis.....	4
2.	Literature review	4
2.1.	Thermal management of Gallium Nitride microelectronics	4
2.2.	Nanofluids as heat transfer fluids.....	6
2.1.1.	Preparation of nanofluids	7
2.1.2.	Base fluids for low and ambient temperature applications	9
2.1.3.	Classification of the nanoparticles	10
2.1.4.	Properties of nanofluids with predictive models.....	13
2.1.5.	Boron Nitride nanofluids	16
2.1.6.	Graphene nanofluids	17
2.3.	Die attach selection	19
2.2.1.	Requirement for the die attach material	19
2.2.2.	Types of die-attach.....	20
2.4.	Liquid cooling methods for the microchip.....	25
2.3.1.	Microchannel	26
2.3.2.	Metal foam	27
2.3.3.	Micro-jet impingement	28
2.5.	Numerical simulations of microchips and micro-jet channels	34
2.5.1.	Numerical simulation of thermal management of microchips	34
2.5.2.	Numerical simulation of the micro-jet	40
2.6.	Summary	44
3.	Numerical simulation.....	47
3.1.	Simulation of the fluid domain	48
3.1.1.	Parameters of the micro-jet cooling channels	49
3.1.2.	Governing equation for micro-jet impingement channel	51
3.2.	Simulation of solid domain.....	54
3.2.1.	Govern equation of the die model.....	54
3.2.2.	Simplified and detail device model for the simulation	55
3.3.	Combination of fluid domain with solid domain	59
3.4.	Summary	61
4.	Experimental apparatuses and uncertainty.....	61
4.1.	Experimental apparatuses for thermal management of microchip.....	61

4.1.1.	Test-rigs for thermal management of microchip.....	61
4.1.2.	Pressure drop measurements for microfluidic channels.....	66
4.2.	Integration of microchip with microfluidic channels.....	67
4.2.1.	Thermal package - micro-jet channel.....	67
4.2.2.	Thermal package - copper-foam based channel.....	72
4.3.	Equipment used in experiments	73
4.3.1.	Thermal conductivity	74
4.3.2.	Viscosity	75
4.3.3.	Particle size distribution and ξ potential	77
4.3.4.	Infra-red camera.....	78
4.3.5.	Raman Thermography.....	79
4.3.6.	3D printer	80
4.4.	Uncertainty analysis.....	82
4.4.1.	Uncertainty in thermal Management of microchip	82
4.4.2.	Thermal conductivity uncertainty analysis	83
4.4.3.	Viscosity uncertainty analysis.....	84
4.5.	Summary	85
5.	Results and discussions.....	86
5.1.	Results and discussion 1 - Nanofluids	86
5.1.1.	Deionised water nanofluids - formulation and characterisation.....	86
5.1.2.	Ethylene glycol+distilled water based nanofluids - formulation and characterisation	103
5.2.	Results and discussion 2 - Microfluidic channels	112
5.2.1.	Performance of copper-foam based microfluidic channels.....	112
5.2.2.	Performance of micro-jet channel with deionised water based fluids.....	121
5.2.3.	Performance of micro-jet channel with ethylene glycol+distilled water-based fluids	136
5.3.	Results and discussion 3 - Material selection for the thermal package.....	150
5.3.1.	Assumption and geometry in simulation.....	150
5.3.2.	The temperature difference in different layers of the microchip	153
5.3.3.	Maximum temperature on the microchip.....	158
5.3.4.	Summary of material selection for the thermal package	159
5.4.	Results and discussion 4 - Performance of Gallium Nitride transistors.....	161
5.4.1.	Experiment and validation with simulation	161
5.4.2.	Temperature in Gallium Nitride transistors with deionised water	164
5.4.3.	Thermal performance of Gallium Nitride transistors	168
5.4.4.	Thermal resistance of Gallium Nitride transistors	174
5.4.5.	Summary of thermal performance of Gallium Nitride transistors	178
6.	Conclusions and recommendations for future work	181

6.1. Conclusions.....	181
6.2. Recommendations for future work	183
Appendix.....	185
Appendix A.....	185
Appendix B	187
Appendix C	189
Appendix D.....	190
Appendix E	195
Appendix F.....	199
Reference	203

List of Figures

Figure 2. 1 Thermal management of the GaN transistors	6
Figure 2. 2 Schematic preparation of nanofluids via a one-step method	7
Figure 2. 3 Schematic preparation of nanofluids via a two-step method.....	8
Figure 2. 4 Freezing- point of the EG and water mixture	9
Figure 2. 5 Schematic diagrams of a microchip with a cooling channel combined via the die-attach layer	19
Figure 2. 6 SEM images of sintered Si die on Ag plated Cu/Alumina/Cu substrate[103].....	21
Figure 2. 7 Schematic of test specimens for the sintered silver nanoparticle paste (not to scale)[102]	21
Figure 2. 8 Schematic representation of the Au–Sn system [102]	22
Figure 2. 9 Schematic illustrations of heat dissipation route of the DAAs (A) before and (B) after adding one-dimensional nano-fillers, or (C) after adding nanoparticles [108]	23
Figure 2. 10 Schematic view of fluids flow in the microchannel view [144]	26
Figure 2. 11 Microchannels for cooling the die attached on (1/4 model)	27
Figure 2. 12 Structure of the metal foam [157].....	28
Figure 2. 13 A figure of metal foam based cooling channel [154]	28
Figure 2. 14 the schematic of the jet impingement	29
Figure 2. 15 Schematic of micro-jet impingement with the die-on-diamond heat spreader	31
Figure 2. 16 Schematic of direct impinging jet cooling as well as dimensions and electrical connections[158].....	32
Figure 2. 17 Spray visualization of a 91-nozzle MES system with a packing density of 253 sources/cm ² [160].....	32
Figure 2. 18 Jet impingement flow chamber [161]	33
Figure 2. 19 Schematic 3-D images of the new hybrid jet-based cooling solution with MDMTs [162],[163], [164].....	33
Figure 2. 20 Temperature distribution of the device [167]	34
Figure 2. 21 Effect of the die and sub-mount adhesive material on-die junction temperature [168]....	35
Figure 2. 22 3D meshed models of different LED assemblies. (i) Module/assembly (A), (ii)module/assembly (B), and (iii) module/assembly (C) [172]	36
Figure 2. 23 Schematic diagrams of a mixed-mode approach for electro-thermal simulation [176]....	37
Figure 2. 24 Transient temperature response of the bonding wire array under different heat sources .	37
Figure 2. 25 Gate dimensions used in the simulation that mimics CREE-CGH-60120D (b) Conduction simulation result using 3-D COMSOL Multiphysics [180]	38
Figure 2. 26 Multiple layers from junction to heat transfer fluid in simulations [180].....	38
Figure 2. 27 Left picture shows the DirectFET Power MOSFET package mounted on a PCB. The right panel displays a schematic cross-section of the DirectFET package equipped with a standard plate cooler and TIM [158]	41
Figure 2. 28 Variation of temperature contour at different cross-sections for model A and model B [191].....	41
Figure 2. 29 Temperature prediction by k- ϵ and SST models and its comparison with the experimental data [194]	42
Figure 2. 30 heat transfer coefficient at the bottom surface of the DBA [194]	42
Figure 2. 31 Blow-up schematics showing the three layers of the microdevice [195]	43
 Figure 3. 1 Half image illustrating the modelling domain consisting of impingement jet channel and microchip	47
Figure 3. 2 Meshing of the fluid domain	48
Figure 3. 3 Size of the micro-jet orifices	49
Figure 3. 4 Detailed structure of microchips.....	56
Figure 3. 5 Structure of the die in the simplified model	57

Figure 3. 6 Detailed die model with its mesh in Ansys	58
Figure 3. 7 Flow chart of simulation models combination	60
Figure 4. 1 Schematic diagram of TM of the microchip with IR camera	62
Figure 4. 2 GaN electronics temperature measurement with Raman thermography	64
Figure 4. 3 Dimension of the CGHV60040D GaN-on-SiC transistor	64
Figure 4. 4 Test rig with Raman thermography and the location for the measured point in the centre of fingers	65
Figure 4. 5 Schematic diagram of TM of the microchip with copper-foam based microfluidic channel	66
Figure 4. 6 Schematic of the experimental apparatus for jet arrays used for pressure drop	67
Figure 4. 7 Flow chart of test rig fabrication	68
Figure 4. 8 Combination of the diamond heat spreader with GaN	69
Figure 4. 9 Curve for the sintering process	69
Figure 4. 10 (Top) design of the 3D print lid and (bottom) the 3D printed lid with PCB	70
Figure 4. 11 Lid combined with the device	70
Figure 4. 12 Wire bonding machine.....	71
Figure 4. 13 Die with gold wire bonding	71
Figure 4. 14 (Top) design of 3D print micro jet channel (bottom) the 3D printed channel	71
Figure 4. 15 Flow chart of the combination of the die with the copper lid for copper-foam based channel	72
Figure 4. 16 Copper lid with die inserted in	73
Figure 4. 17 Schematic diagrams of the heat –wire sensor, sample holder and temperature control system	74
Figure 4. 18 Schematic diagrams of rheometer, chiller, and temperature monitor.....	76
Figure 4. 19 Schematic diagrams of the IR camera	78
Figure 4. 20 Schematic diagrams of Raman thermography	80
Figure 4. 21 Schematic diagrams of the 3D printer with micro-jet channel printed.....	81
Figure 4. 22 Schematic of the thermal characteristic of the microfluidic channel.....	82
Figure 4. 23 Thermal conductivity of distilled water at different temperature	84
Figure 4. 24 Viscosity of distilled water at different temperature	85
Figure 5. 1 Flow chart of the BN/DI water nanofluids	87
Figure 5. 2 Average sizes of nanoparticles with sonication time.....	87
Figure 5. 3 PDS of 0.05 wt. % BN/DI water nanofluids with and without wet milling	88
Figure 5. 4 ESEM of BN dry powder	89
Figure 5. 5 ESEM of BN nanoparticles after the formation process in different magnification: (a) $\times 20,000$ and (b) $\times 80,000$	89
Figure 5. 6 ξ potential values of BN nanofluids as a function of pH value	90
Figure 5. 7 Average particle sizes with time (a) process 1 without surfactant, (b) process 1 with surfactants and (c) process 2 without surfactant	91
Figure 5. 8 Thermal conductivity of nanofluids via process 1 (a) Gum Arabic, (b) Tween 20 and (c) Tween 80.....	94
Figure 5. 9 Thermal conductivity versus temperature at various concentrations.....	95
Figure 5. 10 Thermal conductivity versus concentration at various temperature	95
Figure 5. 11 Thermal conductivity BN/DI water nanofluids at 25 and 75 °C for different particle volume fractions.....	96
Figure 5. 12 Viscosity versus the shear rate at 0.5 wt. % with 25 °C	97
Figure 5. 13 Viscosity versus the shear rate at 1wt. % and 2 wt. % with 25 °C	97
Figure 5. 14 Structure changes of nanofluids showing shear thinning behaviour: (a) at rest and (b) during shearing.....	99

Figure 5. 15 Viscosity versus concentration at various temperatures with the Einstein equation	99
Figure 5. 16 Viscosity versus temperature at various concentrations with Arrhenius equation	100
Figure 5. 17 Electrical conductivity as a function of concertation at room temperature	101
Figure 5. 18 Reaction scheme for the acid treatment of Graphene	103
Figure 5. 19 ESEM of (a) graphene and (b) well-dispersed rGO nanoparticles	104
Figure 5. 20 Apparent particle size with ultrasonication	105
Figure 5. 21 Particle size distribution of rGO in EG+DW media after 20 min sonication	105
Figure 5. 22 ξ potential as a function of pH for rGO nanoparticles in EG+DW media.....	106
Figure 5. 23 Apparent shear viscosity (a) base fluids(b) 0.5 wt.%,(c) 2.0 wt% and (d) 5.0 wt% - influence of temperature.....	108
Figure 5. 24 Temperature dependence of dynamic viscosity	108
Figure 5. 25 Thermal conductivity versus concentration at various temperature	109
Figure 5. 26 Thermal conductivity versus temperature at various concentrations.....	109
Figure 5. 27 Thermal conductivity of rGO/EG+DW nanofluids and its enhancement.....	110
Figure 5. 28 3 types of the copper-foam based microfluidic channel	113
Figure 5. 29 Schematic diagram of the test rig with thermocouples inserted in	114
Figure 5. 30 Schematic diagrams of the heat transfer coefficient and thermal resistance distribution	115
Figure 5. 31 Temperature measured in the experiment for GEO 1, GEO 2 and GEO 3.....	118
Figure 5. 32 (a) Heat transfer coefficient and (b) the thermal resistance of the copper-foam channel with the flow rate	119
Figure 5. 33 Size of the jetting array.....	121
Figure 5. 34 The surface of micro-jet impingement under a microscope	121
Figure 5. 35 IR image of microchip and diamond surface at a flow rate of 0.2L/min (left) without power applied; (right)with the power of 6.118 W.....	122
Figure 5. 36 Temperature on diamond surface 0.2L/min.....	123
Figure 5. 37 Temperature difference between inlet and outlet	124
Figure 5. 38 Temperature distribution and location for the point in simulation with a flow rate of 0.2 L/min.....	126
Figure 5. 39 Temperature difference with simulation and experiment	126
Figure 5. 40 Temperature at 2.000 V 1.012A with 0.53 m/s in experiment and simulation for BN/DI water nanofluids.....	128
Figure 5. 41 Distribution of the heat transfer coefficient with the different flow rates	129
Figure 5. 42 Average htc heat transfer coefficient with inlet velocity.....	129
Figure 5. 43 Distribution of the htc with inlet temperature at a heat flux of 5W/mm ²	130
Figure 5. 44 Average and maximum heat transfer coefficient with inlet temperature at a heat flux of 5W/mm ²	131
Figure 5. 45 Temperature on the diamond with heat flux.....	132
Figure 5. 46 Distribution of the htc with heat flux.....	132
Figure 5. 47 Heat transfer coefficient distribution on the surface of the diamond heat spreader	133
Figure 5. 48 Average heat transfer coefficient of DI water and 0.5 wt.% BN/DI water nanofluids with velocity.....	133
Figure 5. 50 IR images for EG+DW fluid with 2.500 V 1.270 A (a) without power and (b) with power	138
Figure 5. 51 IR images for 2.0 wt.% rGO nanofluids at 2.000 V 1.000 A (a) without power and (b) with power	139
Figure 5. 52 Experiment and simulation of temperature on the diamond surface with $V_{in} = 0.246$ m/s for EG+DW base fluid	139
Figure 5. 53 Experiment and simulation of temperature on the diamond surface with $V_{in} = 0.246$ m/s for 2.0 wt.% rGO nanofluid	140

Figure 5. 54 Average htc of the base fluid and nanofluid with different inlet temperature at v=0.53 m/s	141
Figure 5. 55 ΔP of the base fluid and nanofluid with different inlet temperature at v=0.53 m/s.....	142
Figure 5. 56 ΔP of nanofluid with different inlet velocity at the temperature of -5 °C	142
Figure 5. 57 Average htc of nanofluid with different inlet velocity at the temperature of -5 °C.....	143
Figure 5. 58 Average htc of nanofluid with different inlet velocity and temperature.....	144
Figure 5. 59 the Tmax on the diamond surface with different inlet velocity and temperature	145
Figure 5. 60 Temperature distribution on diamond heat spreader and microchip	145
Figure 5. 61 ΔP of nanofluid with different inlet velocity and temperature	146
Figure 5. 62 Htc and temperature distribution on diamond heat spreader at an inlet velocity of 0.1 m/s	146
Figure 5. 63 Temperature on the diamond surface with heat flux	147
Figure 5. 64 ΔP of nanofluid with different heat flux	148
Figure 5. 66 Geometry of the die simulation	150
Figure 5. 67 ΔT in the die layer with different die-attach.....	153
Figure 5. 68 ΔT in the die-attach layer with different die-attach.....	154
Figure 5. 69 ΔT in the heat spreader with different die-attach	155
Figure 5. 70 Thermal resistance schematic of the devices with heat spreader.....	157
Figure 5. 71 Heat flux distribution at the back of SiC die with copper heat spreader	157
Figure 5. 72 Heat flux distribution at the back of the die-attach surface with copper heat spreader ..	157
Figure 5. 73 Heat flux distribution at the back of copper heat spreader with SiC die	158
Figure 5. 74 Maximum temperature on die with different die-attach	159
Figure 5. 75 Temperature with the power density	161
Figure 5. 76 (a) Experimental location of the die;(b) simulation with die non-centre (c) simulation with die in the centre.....	163
Figure 5. 77 Thermal conductivity of different materials with temperature in simulation	163
Figure 5. 78 Temperature distribution (a) in fingers (0 μm); (b) bottom of the AlGaN layer (1.5 μm); (c) bottom of the SiC layer (101.5 μm), (d) bottom of the silver sintered die-attach layer and (e) cross-sectional temperature profile for the different layers with the inlet velocity of 0.53 m/s and inlet temperature of 20.0 °C	167
Figure 5. 79 Temperature contour plot of the finger layer with (a) 0.53 m/s; (b) 1 m/s ;(c) 2 m/s and (d) 3m/s).....	169
Figure 5. 80 Maximum temperature in the die with die in different locations	170
Figure 5. 81 Heat flux of device with $V_{in} = 0.53$ m/s (a) bottom surface of die non-centre (b) bottom surface of die centre (c) bottom surface of diamond heat spreader non-centre (d) bottom surface of diamond heat spreader centre; with $V_{in} = 3.00$ m/s (e) bottom surface of die non-centre(f) bottom surface of die centre (g) bottom surface of diamond heat spreader non-centre (h) bottom surface of diamond heat spreader centre.....	171
Figure 5. 82 Temperature of the packaged die with different velocity	173
Figure 5. 83 Schematic diagram of the thermal resistance for the thermal packaging	175
Figure 5. 84 Thermal resistance with the inlet velocity	175
Figure 5. 85 (a) Thermal resistance with different velocity and location;0.53 m/s (b) non-centre (c) in-centre;3.00 m/s (d)non-centre,(e) in-centre for deionised water	176
Figure 5. 84 Thermal resistitance of the micro-jet with inlet velocity of (a) 0.20 m/s (d) 0.53m/s for rGO nanofluids.....	178
Figure 1 Blackbody Radiation Spectrum from Planck's law and Wien's displacement law	189
Figure 2 Schematic diagram of light interacting with matter	191
Figure 3 Schematic diagram for Rayleigh scattering, Raman Stokes scattering and Raman anti-stokes scattering.....	191
Figure 4 Raman spectrum of GaN on the SiC die.....	192

Figure 5 Schematic diagram of the DLS measurement	196
Figure 6 Phase addition of scattered light falling on the detector. (A), the opposite phase of two beams cancels each other out resulting in a decreased intensity. (B), the same phase two beams enhance each other resulting in an increased intensity.....	196
Figure 7 Schematic diagram of the measurement position with moving of the focus lens for (a) small, weakly scattering samples and for (b) concentrated, opaque samples.....	198
Figure 8 Schematic illustration of the ξ potential	199
Figure 9 Schematic of the Huckel approximation and the Smoluchowski approximation.....	201
Figure 10 Optical configuration of the Zetasizer Nano series for zeta potential measurements.....	201

List of tables

Table 2. 1 Typical base fluids for synthesising nanofluids	8
Table 2. 2 Physical properties parameters of the water and EG	10
Table 2. 3 Thermophysical properties of nanoparticles	11
Table 2. 4 Thermophysical properties of nanofluids with different nanoparticles	12
Table 2. 5 A summary of thermal conductivity model	13
Table 2. 6 A summary of viscosity model	14
Table 2. 7 Thermal conductivity and viscosity increase of BN nanofluids in literature	16
Table 2. 8 The thermal conductivity enhancements and viscosity increase in literature	17
Table 2. 9 Thermal conductivity and thickness of the die attach	23
Table 2. 10 Parameters for the numerical simulation of the micro-jet channel	43
Table 4. 1 Technical data of the LAMBDA-system	75
Table 4. 2 Technical data of the MCR502 Anton Paar	76
Table 4. 3 Technical data of the nano Zetasizer Nano ZS	77
Table 4. 4 Technical data of VarioCAM HR head 600.....	79
Table 4. 5 Technical data of Formlab form 2	81
Table 5. 1 Flow rates and power applied on the die in the experiment	115
Table 5. 2 Thermophysical properties of water with temperature	123
Table 5. 3 Power generated by power supplier and dissipated by water	125
Table 5. 4 Thermophysical properties of 0.5 wt.% BN/DI water nanofluids with temperature	127
Table 5. 5 Temperature on the diamond with inlet temperature at a heat flux of 5W/mm ²	131
Table 5. 6 Properties of EG+DW and 2.0 wt.% rGO nanofluid	136
Table 5. 7 Comparison of the base fluid and nanofluid	143
Table 5. 8 Dimension of the die device	152
Table 5. 9 Material used in Ansys.....	152
Table 5. 10 Thermal conductivity of different materials in the simulation.....	163
Table 5. 11 Experimental temperature and simulation temperature	163

Nomenclature

	Latin letter		t	Time	s
A	Current	A	U	Voltage	V
Cp	Specific heat capacity	J/kg	v	Velocity	m/s
d	Diameter	m	U_E	Electrophoretic mobility	$\mu\text{m}\cdot\text{cm}/\text{V}\cdot\text{s}$
F	Force	N	F(ka)	Henry's function	/
g	Gravity	m/s^2	D	Translational diffusion coefficient	m^2/s
H	Height	m	d(H)	Hydrodynamic diameter	m
h	Heat transfer coefficient	$\text{W}/(\text{m}^2\cdot\text{K})$	NA	Numerical aperture	/
k	Thermal conductivity	$\text{W}/(\text{m}\cdot\text{K})$	$r_{lateral}$	Lateral resolution	μm
L	length	m			
Nu	Nusselt number	/		Greek letter	
P	Pressure	Pa	μ	Dynamic viscosity	Pa.s
PPI	Pore per inch	/	kB	Boltzmann constant	J/K
Pr	Prandtl number	/	α	Thermal diffusivity	m^2/s
q	heat flux	W/m^2	ΔP	Pressure drop	Pa
Q	Power	W	ΔT	Temperature difference	$^\circ\text{C}$
R	Gas constant	$\text{J}/(\text{mol}\cdot\text{K})$	ϵ	Dielectric constant	/
Re	Reynolds number	/	ρ	Density	Kg/m^3
Rth	Thermal resistance	$^\circ\text{C}/\text{W}$	φ	Volume concentration	/
T	Temperature	$^\circ\text{C}$	ξ	Zeta potential	mV

Acknowledgements

First of all, I would like to express my sincere thanks and special appreciations to my supervisor Professor Yulong Ding for all your valuable guidance. You have offered me constant supervision, priceless pieces of advice, precious supports and genuine instructions throughout my entire PhD project in the last four years.

I would also like to show my deepest gratitude to my co-supervisor Dr Yongliang Li for all the advice and guidance he gave me. It had a significant influence on my research in my whole work.

My sincere thanks also give to Dr Hui Cao and Dr Helena Navarro for their great supports in my entire PhD journey.

My deepest thanks all go to the Birmingham Centre for Energy Storage. It offered me a marvellous chance to successfully finish all my research at the University of Birmingham.

Many thanks to all my friends in Birmingham for a friendly environment they created. It helps me a lot to finish my PhD.

Very special thanks to my beloved family. My mother, my father, my sister, my brother-in-law and my energetic niece. They are the endless sources of supporting They offer so much comfort to me when I need it most. My niece's words always excite my heart to follow my dreams.

A sincere and deep thank to Confucius. His philosophy has encouraged me when I was at my lowest mood. At this turning point of my life journey, it reminds me that Confucius once said '*The experience and knowledge can only be obtained by practice not empty talk signifying nothing*'. I had managed to practice it my past four years journey. Hope it will guide my next journey.

Gan Zhang

Birmingham April 2020

1. Introduction

1.1 Background

Last four decades have seen an unprecedented increase in communication, defence, and computing technology. This leads to the high demand for electronic devices such as microchips with better performance. Thus, obtaining higher power density [1] and meanwhile, a smaller size [2] is one of the most important aims of high-performance GaN semiconductors and mini- and micro-scale electronic devices. A larger and larger heat flux on smaller and smaller microchips needs to be efficiently dissipated to maintain the performance of an electronic device. According to the literature, 0GaN based microelectronic devices can achieve a power density well over 4 W/mm [3]. So an effective cooling is a vital step to increase the lifespan of the device [1], as the heat flux at the backside can still be larger than 1.96 kW/cm² [4].

One of the main bottlenecks for the power dissipating is the highly heterogeneous heat flux in the electronic devices. If heat cannot be efficiently removed from the electronic devices, the temperature on the device keeps increasing which can significantly decrease the device's reliability and might lead to its failure. According to the literature [1], with the increase of operating temperature, the possibility of the device's failure increases almost exponentially. Thus, thermal management (TM) is crucial for electronic devices and heat transfer intensification (HTI) is one of the key technologies to enable TM.

HTI can be realized using an efficient heat transfer fluid (HTF) [5]–[9], an extended heat transfer surface and/or extending the flow path of the HTF [10]–[13]. The traditional technology with air-cooling for the electronic device is simply not sufficient for the increase of the high heat flux. The forced convection with liquid is one of the solutions for heat removal. The traditional HTFs used for cooling channel such as water, EG, and/or their mixture etc. have disadvantages in thermophysical properties. To enhance those properties, nanofluids with nanoparticles in the base HTF seems to be a promising vision for the novel HTF. The other possibility for the efficient dissipation of heat flux is combining the electronic devices directly with the micro-jet impingement array. Compare with other different cooling channels

such as microchannel and metal foam based channel, the micro-jet impingement has the highest heat transfer coefficient with an acceptable pressure drop in the cooling channel for devices.

1.2 Aim and objective and for this PhD project

This PhD project aims to investigate the potential of maintaining a low temperature at the back of GaN-on-Diamond microchip. The main challenge for the objective is the high power density on the GaN layer of the devices. To achieve the required aim, the objective has divided into 3 tasks: TM with novel HTFs, microfluidic channels and thermal packaging of the devices with the microfluidic channels.

- (1) The first task is to find candidates for novel HTFs. As the microelectronic devices are used in the out space and/or other location with ambient temperature as low as -50 °C, nanofluid with reduced graphene oxide (rGO)/ethylene glycol (EG)+water mixture (6:4) was used for temperature below 0°C. Meanwhile, Boron Nitride (BN)/DI water nanofluids were used for temperature above 0°C.
- (2) The second task is to find a suitable design of microfluidic channels. For the microfluidic channels, geometry optimization was done with simulation to obtain a high heat transfer coefficient (htc). After the geometry optimization, 3D printing technology was used to fabricate the optimized microfluidic channel. Then, a test rig was used to experimentally acquire the htc with formulated nanofluids and base fluids for the comparison.
- (3) The third task is the reliable thermal packaging of the device with the microfluidic channel. This task includes the die-attach material selection, the thermal packaging method and the experimental test of the packaged system. For die attach material's selection, numerical simulation was the main vehicle to compare the thermal performance of different types of the die attach materials that can be purchased in the market. The thermal resistance in the different parts of the device was analysed. Due to the size difference between the microchip and the microfluidic channel, it is also important to have a simple method to estimate the ability of the given cooling channel with different microchips of different heat flux via the data obtained in

the experiment. In this investigation, different methods including experiment and simulation were applied to investigate the thermal performance of the cooling channel.

1.3 Project description and methodology

In this project, experiment and simulation for the thermal performance of GaN electronics with microfluidic channel were investigated. Meanwhile, the goal for the characterisation of nanofluids such as morphology, stability, thermal conductivity, and rheology behaviour was experimentally tested and measured.

The package of the microchip with the microfluidic channel inevitably requires appropriate die-attach materials. Thus, the extra thermal resistances were introduced in the whole system. The heat spreader and the die attach material were selected via the simulation.

In the simulation, the geometry of the die with detailed structure was made by the University of Bristol for the simulation of the temperature in microchip and validation with temperature measured by Raman thermography. The simulation of the GaN electronics with software Ansys Steady-State Thermal was built to validate and predict the thermal behaviour of GaN-based microchips.

For the experiment with micro-jet impingement channel, the test rig was assembled with 3D print cooling channel fabricated in the University of Birmingham, the U.K. and the microchips mounted on the diamond heat spreader characterised by the University of Bristol, the U.K. To prevent potential leaking during the experiment, a test rig for pressure drop were made prior to the thermal performance test. After the experiment, the simulation of the micro-jet channel with software Ansys Workbench was done to validate and predict the thermal behaviour of the cooling channel.

The method for combination of the detailed die model in Ansys Steady-State Thermal and the micro jetting model in Ansys Fluent was given to reduce the time in the simulation and decrease the consumption of the resource for the numerical computation.

As for the nanofluids, a two-step method was used for the formulation of rGO/EG+DW and BN/DI water nanofluid. The SEM was applied for the morphology of the nanoparticles. The stability, particle

size distribution, thermal conductivity, and viscosity were measured with corresponding instruments. All those measurements were done in the Birmingham Centre for Energy Storage. These measured parameters were used in the simulation referred.

1.4 Structure of the thesis

The following thesis is divided into five chapters including the literature review, the methodologies, results and simulations and the future work.

- Chapter two literature review

This chapter is the literature review part of the potential material and method used for the thermal management of the microelectronics.

- Chapter three methodology of the numerical simulation

This chapter is the methodology of the numerical simulation which was used to simulate the performance of the die and the micro-jet impingement channel.

- Chapter four methodology of the experiment

This chapter is the methodology of the experiment which includes the experimental setup, the thermal packaging for the microchips and the uncertainty and the equipment used in the experiment.

- Chapter five results and discussion

This chapter is the results and discussions which includes experiment results and simulation results.

- Chapter six conclusions and future work

This chapter is about the conclusion and future work of the thermal management of the GaN-based microchip.

2. Literature review

GaN-on-SiC high-electron-mobility-transistors (HEMTs) are now the incumbent commercialised technology for high-power high-frequency radio frequency (RF) amplifiers, benefitting from high current density, high-frequency operation and high breakdown field. This results in high operating power densities, with over 30 W/mm being reported in laboratory tests [14]. However, with typical power-added efficiencies of 50-60%, an equivalent amount of power is dissipated as Joule heating inside the transistor channel. As a result, the heat flux can exceed 1 MW/cm² in each gate finger. Considering the Arrhenius relationship between the operating temperature and mean time to failure (MTTF), [15] GaN-on-SiC HEMTs are typically derated to an RF operating power density of ≤ 5 W/mm to limit the channel temperature rise, usually to below 200 °C [16], to ensure long term reliability [15]. Improved thermal management (TM) is therefore needed to unlock the full potential of GaN RF HEMTs while maintaining MTTF [1]. The requirement for improved package-level cooling is even more demanding for GaN-on-diamond, which has a 3-fold increase in areal power density [17]–[21]. GaN-on-diamond addresses the die-level thermal management, so the particular challenge is to efficiently dissipate heat at the die backside, which has an area of only a few mm², leading to heat fluxes of the order of tens of W/mm².

2.1. Thermal management of Gallium Nitride microelectronics

In the past few decades, the power density of microelectronic power devices has shown an unprecedented increase with the size of the devices gradually shrinking. The ever increasing local heat flux generated by the devices has to be efficiently dissipated to maintain the stability and reliability of the devices. This makes Thermal Management (TM) a vital technology for the sector. This chapter provides an overview of the research on TM. Figure 2. 1 shows schematically the main technologies for thermal management enhancement, which fall into two categories and they explained in the following:

- ***Microfluidic channels for far end cooling of the devices*** consisting of two aspects -
 - Heat transfer fluid plays an important role in the cooling as well as carrying the heat away. This can be sub-divided into traditional heat transfer fluids such as water and glycols and new and emerging heat transfer fluids such as nanofluids e.g. BN and reduced graphene oxide (rGO) nanofluids.
 - Microfluidic channel itself plays a crucial role, which affects heat transfer coefficient and pressure drop. There are many types of microfluidic channels including micro-jet channel, micro-channel, metal-foam based channel.
- ***Materials for GaN devices to efficiently spread and dissipate heat*** consisting of the following three aspects -
 - Substrates for the GaN transistors is vital for the TM of the GaN microelectronics due to high heat flux at the GaN layer. There are many different types of GaN transistors including GaN-on-SiC and GaN-on-Diamond.
 - Die-attach is equally important for the heat flux dissipation from the GaN devices. There are numerous types of materials for the die-attach. Examples include silver paste, epoxy, metal alloy, etc.
 - Heat spreader for the integration of the device and the microfluidic channel is also important for the TM as heat is transferred to the heat transfer fluid through this layer. There are different heat spreaders including copper alloy and diamond etc.

A sound thermal management strategy for GaN electronics requires the consideration of all of those aspects and the balance of conflict requirements to achieve the optimised performance of GaN devices.

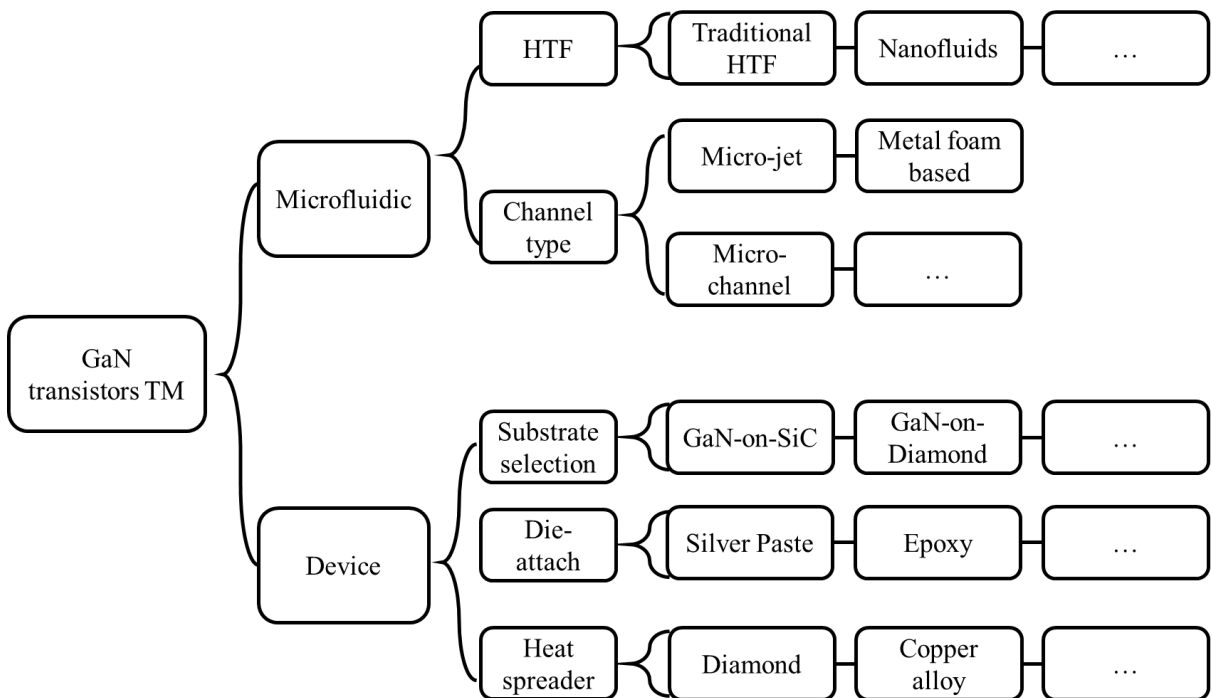


Figure 2. 1 Thermal management of the GaN transistors

As a result, this literature review focuses on the following aspects, which, as explained above, are all important to make optimised thermal management solution to GaN electronics.

- Recent research on nanofluids as HTFs in Section 2.2;
- Die-attach for microelectronics in Section 2.3;
- Microelectronic cooling technologies in Section 2.4; and
- Numerical simulation of the thermal performance of microelectronic devices in Section 2.5.

2.2. Nanofluids as heat transfer fluids

Nanofluids are dilute suspensions of highly thermally conductive nanometre-sized particles (smaller than ~ 100 nm). The base fluids of nanofluids include water, ethylene glycol, oil etc. as is shown in Table 2. 1. The work on nanofluids for cooling started around 1995 when Steve Choi [22] proposed the concept of nanofluids and there are numerous publications on the topic [15] – [23]. However, no significant industrial applications of such fluids have occurred so far after more than two decades of

research and development. An efficient heat transfer fluid should lead to the energy saving, the reduction in the processing time, the increase of the lifespan of microelectronic devices and the improvement of the performance of the system. However, nanofluids with all the expected advantages over traditional heat transfer fluids are yet to be formulated. As a result, a considerable amount of global effort is still made in the area.

2.1.1. Preparation of nanofluids

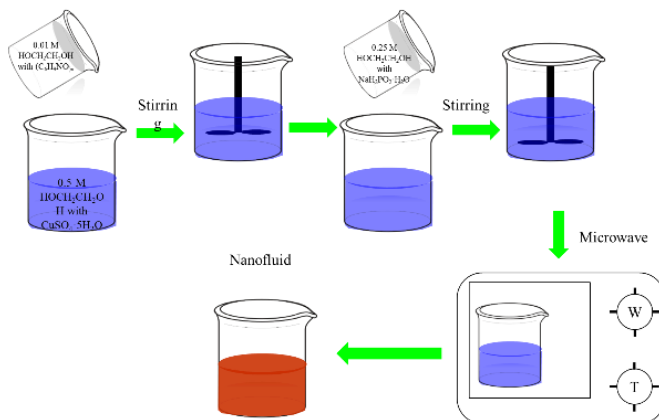


Figure 2. 2 Schematic preparation of nanofluids via a one-step method

There are two main methods for the preparation of nanofluids there are discussed in the following. The first is the so-called one-step method nanofluid which consists of synthesising and dispersing the nanoparticles at the same time in the base fluid. The most obvious advantage for this kind of the nanofluids preparation is that the stability of the nanofluids can increase as it decreases the possibility of the agglomeration of nanoparticles in the drying, the storage, the transportation etc. As is illustrated in Figure 2. 2, Zhu et al [32] have obtained the non-agglomerated and stable suspended Cu nanofluids via the one-step chemical method. The nanofluid was fabricated by reducing the copper sulphate pentahydrate ($\text{CuSO}_4 \cdot 5\text{H}_2\text{O}$) with the sodium hypophosphite ($\text{NaH}_2\text{PO}_2 \cdot \text{H}_2\text{O}$) in the ethylene glycol solution under with microwave irradiation. However, there are several disadvantages to the one-step method. Compared with the two-step method, the cost of the one-step method is quite high. It is also difficult to synthesis the nanofluids in a large scale [33]. In some cases, due to the incomplete reaction, there are residual reactants in the nanofluids that need to be eliminated to evaluate the nanoparticles' effect.

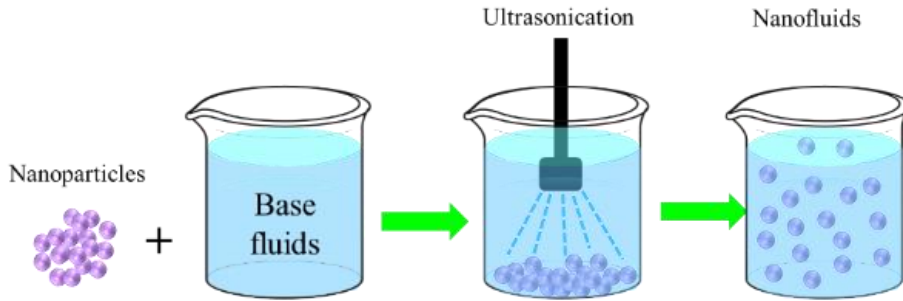


Figure 2. 3 Schematic preparation of nanofluids via a two-step method

The most commonly used method in the synthesis of the nanofluid is the two-step method that is illustrated in Figure 2. 3 are produced by the physical and/or chemical method. It has been stored and transported before it dispersed into the base fluids. The nanoparticles dispersed into the based fluids are homogenized by ultrasonication, high shear mixing and/or magnetic force agitation etc. The advantages of the two-step method are: (1) compared to the one-step method, it is an economical method for the mass production; (2) the purity of the nanoparticle can be granted. However, the most obvious disadvantage is the tendency of the agglomeration of the nanoparticle due to the high surface area and surface activity. Meanwhile, the stability of the nanofluids in the high temperature needs to be concerned during the fabrication.

Table 2. 1 Typical base fluids for synthesising nanofluids

Base Fluid	k* Enhancement	Volume Fraction	References
Mineral oil	8.7 %-76 %	0.01-0.1 wt.%	[34]
Water	1.1–78 %	0.001-15 %	[35],[36]
EG	2 %-30.3 %	0.025-5.5 %	[37]
	26 %-168 %	0.05-0.2 %	[38]
EG-water (50:50)	5 %-22 %	0.03-3 %	[39]

EG-water (10:90)	5 %	0.1-0.5 wt.%	[40]
------------------	-----	--------------	------

* k is the thermal conductivity.

2.1.2. Base fluids for low and ambient temperature applications

The ambient temperature for the GaN-based microchips is around room temperature to as low as -50 °C [41]. Thus, it is important to find the base fluids used in that temperature range. Water, glycols, and their mixtures have been mostly used as low temperature and room temperature heat transfer fluids. Water has many advantages such as low price, high abundance and high specific heat capacity; therefore, it has been widely used and studied. However, because the freezing point of the water is 0 °C, it is not suitable for the application of the temperature below that point. Ethylene glycol (EG) and water mixtures decrease the freezing point of the formulation as is Figure 2. 4. Thus, it can work at a lower temperature range. Water and EG, as is shown in Table 2. 2 present a low thermal conductivity that has a significant effect on the thermal performance of the system where it is used. Hence, nanofluids can be one solution to solve these drawbacks.

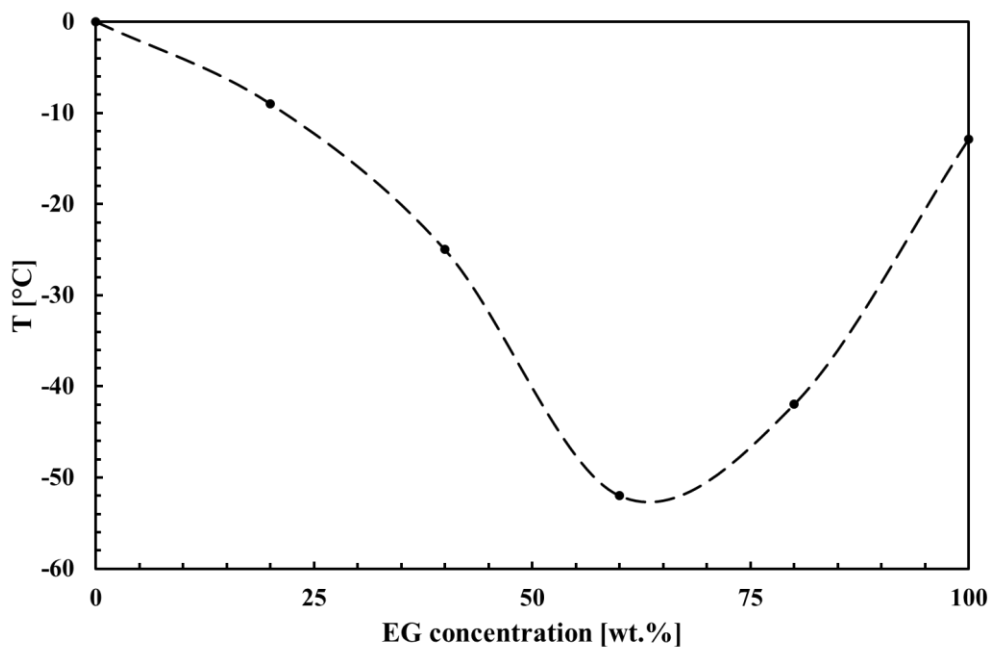


Figure 2. 4 Freezing- point of the EG and water mixture

Table 2. 2 Physical properties parameters of the water and EG

Base fluid	k W/(m K)	μ^* mPa·s	ρ^* g/cm ³	Cp* kJ/(kg·K)	Ref
EG	0.252	15.7	1.114	2.415	[31]
Water	0.5990	1.1404	1.0000	4.1900	[7]

* μ , ρ and Cp are viscosity, density and specific heat capacity, respectively.

2.1.3. Classification of the nanoparticles

Nanofluids have been shown by many studies to be able to give a higher heat transfer performance than the base fluids [42]–[44]. In some reports, the addition of a small concentration of nanoparticles was shown to dramatically enhance the thermophysical properties of the base fluids [45]. Any solid nanostructure with appropriate properties (such as thermal conductivity, chemical compatibility with the base fluid etc.) can be used as an additive to the base fluids. The selection of nanoparticle depends on its thermal properties, morphology, chemical compatibility with the base fluid, the chemical stability in the working temperature range and other factors such as the toxicity and the cost. Table 2. 3 summarized the main thermal properties of the nanoparticles mentioned above with the formulation of water and EG based nanofluids.

- Metal oxides, such as the Aluminium oxide (Al_2O_3) [9], the Copper oxide (CuO) [46] and the Titanium oxide (TiO_2) [46], as they present a high oxidation resistance; hence are chemically stable and lower density than their respective metals so the nanofluid particles are more difficult to settle down [47]. Those can increase the stability of the nanofluid.
- Carbides and nitrides (Silicon Carbide (SiC) [8] and Boron Nitride (BN) [48]) as they present a high thermal conductivity e.g. SiC has the 220 W/(m·K) [27] and low-density e.g. BN has a density of 2.27 g/cm³ [49].
- Metals (Silver (Ag) [50]and Copper (Cu) [51] as they present a high thermal conductivity. Ag and Cu have a thermal conductivity of 430 [26] and 401 W/(m·K) [52], respectively. Those properties make it suitable for nanoparticles.

- Carbon-based materials (graphene [53] and multiwall carbon nanotubes (MWCNT)[54]) has the merits of high thermal conductivity which is 3000 W/(m·K) in parallel and (2) chemical stability and reasonable price.

Table 2. 3 Thermophysical properties of nanoparticles

nanoparticle	k [W/(m K)]	ρ g/cm ³	Cp kJ/(kg·K)	Ref
Al ₂ O ₃	40	3.970	765	[31]
CuO	20	6.500	535.6	[31]
ZnO	13	5.6	495.2	[31]
TiO ₂	8.9538	4.250	656.2	[52]
SiC	220	–	–	[27]
Ag	430	10.49	235	[26]
Cu	401	8.933	385	[52]
Parallel to surface 3000				
Graphene		2.0-2.25	–	[55]
Perpendicular to surface 6				

For the same nanoparticle, the morphology can significantly affect the properties of nanofluids. There are researches [56]–[59] about the effect of nanoparticle's size on the thermal conductivity and viscosity of the nanofluids, as is illustrated in Table 2. 4 In those researches, Anoop et al. [57] have investigated the effect of particle size on the thermal conductivity and viscosity of alumina nanofluid. The nanoparticles with sizes of 45 nm and 150 nm were used in experiments. It is observed that as particle size reduced, the thermal conductivity of the nanofluid was increased.

The researches [60]–[66] showed that an increase in temperature enhances the thermal conductivity ratio of nanofluid. And the velocity of nanoparticles leads to enhance heat conduction in micro-convection might be a reason for the enhancement [67]. Esfahani et al. [60] have investigated the thermal conductivity of silica/water-ethylene glycol (40%–60%) nanofluid at different temperatures.

Temperatures in experiments were between 25 °C and 50 °C. Results showed that with raising the temperature from 25 °C to 50 °C, in the volume fraction of 5 %, thermal conductivity increased from 38.4 % to 45.5 %.

Table 2. 4 Thermophysical properties of nanofluids with different nanoparticles

Base fluids	Nanoparticle	Size	k enhancement	Ref
	reduced GO	–	1.5 %	[68]
	Cu	40nm	–	[54]
	Al ₂ O ₃	235nm	4.22 %	[9]
	γ-Al ₂ O ₃	50nm	1.8 %	[10]
	TiO ₂	120nm	–	[69]
	α-SiC	115±35nm	20 %	[8]
	Ag	10nm	–	[70]
	Ag	165nm	9.0 %	[50]
	Cu	63~100nm		
	Al	40nm		
	Al ₂ O ₃	20nm		
	Fe ₂ O ₃	40nm	–	[51]
water	Graphite	40nm		
	MWCNT	10nm		
	Al ₂ O ₃	20-30 nm	7.8 %	
	CuO	40 nm	10.2 %	[46]
	TiO ₂	10 nm	3.1 %	
	SiO ₂	2-10 nm	43 %	[71]
	graphene	thickness 1-5nm	7 %	[53]
	graphene	–	27.6 %	[72]
	GO	thickness 3-7nm	28 %	[73]
	h-BN	60-80nm	13 %	[48]
	h-BN	80 nm	16.08 %	[49]
EG	Al ₂ O ₃		-	

CuO	20-80nm	[31]
SiO ₂		
ZnO		

2.1.4. Properties of nanofluids with predictive models

Adding nanoparticles into the base fluids significantly affects the thermophysical properties of the base fluids such as thermal conductivity, viscosity, density, specific heat capacity etc. A summary of the calculation of those parameters is given in this section.

Thermal conductivity

Table 2. 5 A summary of thermal conductivity model

Author	Model	Ref.
Maxwell	$k_{\text{eff}} = \frac{k_p + k_f + 2\varphi_p(k_p - k_f)}{k_p + 2k_f - \varphi_p(k_p - k_f)} k_f \quad (2-1)$	[74]
Nan	$k_{\text{eff}} = \frac{3 + \varphi_p [2\beta_{11}(1 - L_{11}) + \beta_{33}(1 - L_{33})]}{3 - \varphi_p (\beta_{11}L_{11} + \beta_{33}L_{33})} k_f \quad (2-2)$	[75]
Hamilton	$k_{\text{eff}} = \frac{k_p + (n-1)k_f + (n-1)\varphi_p(k_p - k_f)}{k_p + 2k_f - \varphi_p(k_p - k_f)} k_f \quad (2-3)$	[76]
	$k_{\text{eff}} = k_{\text{static}} + k_{\text{Brownian}} \quad (2-4)$	
Koo & Kleinstreuer	$k_{\text{static}} = \frac{k_p + k_f + 2\varphi_p(k_p - k_f)}{k_p + 2k_f - \varphi_p(k_p - k_f)} k_f \quad (2-5)$	[77]
	$k_{\text{Brownian}} = 5 \times 10^4 \beta \varphi_p \rho_p C_p \sqrt{\frac{k_B T}{\rho_p D}} (T, \varphi_p) \quad (2-6)$	
Yu & Choi	$k_{\text{eff}} = \frac{k_{pe} + k_f + 2\varphi_p(k_{pe} - k_f)(1 + \beta)^3}{k_{pe} + 2k_f - \varphi_p(k_{pe} - k_f)(1 + \beta)^3} k_f \quad (2-7)$	[78]

$$k_{pe} = \frac{2(1-\gamma)+(1+\beta)^3(1+2\gamma)\gamma}{-(1-\gamma)+(1+\beta)^3(1+2\gamma)} k_p \quad (2-8)$$

Prasher $k_{eff} = (1 + ARe^m Pr^{0.333} \varphi_p) \left[\frac{k_p + k_f + 2\varphi_p(k_p - k_f)}{k_p + 2k_f - \varphi_p(k_p - k_f)} \right] k_f \quad (2-9)$ [79]

The widely studied model for the thermal conductivity of the nanofluids is the effective medium theory model. Maxwell's model is based on the assumption of spherical particles and random suspensions as is given in Table 2. 5. For the differential effective medium with a high concentration of nanoparticles, Hamilton's model can be used for spherical particles. In reality, particles, such as carbon nanotube, graphene etc., are not spherical. Taking into account of the effects due to the different shapes of nanoparticles, Yu's model and Nan's model models can be used. For graphene-based nanofluids, Nan's model seems to agree well with experiment results[23], [40], [80]–[86]. Another factor may not be neglected for the nanoparticles are the Brownian motion. Both Prasher's model and Koo's model have been proposed to include the Brownian motion in Maxwell's model.

Viscosity

Table 2. 6 A summary of viscosity model

Author	Model	Ref.
Einstein	$\mu_{eff} = (1 + 2.5\varphi_p)\mu_f \quad (2-10)$	[87]
Adedain	$\mu_{eff} = \mu_f / (1 - 2.5\varphi_p) \quad (2-11)$	[88]
Brinkman	$\mu_{eff} = \mu_f / (1 + 2.5\varphi_p)^{2.5} = (1 + 2.5\varphi_p + \dots)\mu_f \quad (2-12)$	[89]

Chen

$$\mu_{eff} = \mu_f(1 + \varphi_p + (10.6\varphi_p)^2) \quad (2-13)$$

[89]

Xuan & Roetzel

$$\mu_{eff} = \mu_f/(1 - \varphi_p)^{2.5} \quad (2-14)$$

[90]

With nanoparticles dispersed into the base fluids, the dynamic viscosity of the base fluid increases. There might be also a dramatic change for the rheological behaviour with concentration increases. The trend for the viscosity of nanofluid with the concentration is similar to the thermal conductivity. This means the pumping power in the system with nanofluids as heat transfer fluid might be higher than base fluids in the same condition. Some models for the prediction the effective viscosity are given Table 2.

6. In 1906, Einstein proposed a model to calculate the viscosity of the mixture. This model assumes the infinitely diluted suspensions of spherical shape nanoparticles with no interaction between particles. However, Non-applicable for high concentration (>2%) is its main shortage. Thus, several other models have been given to extend the use of Einstein's model. Adedain's model is an extension of Einstein's model with a concentration of up to 20%. Brinkman's model considered the effect of the addition of one solute molecule to an existing solution. As the rheological behaviour might change with the shear-rate, Chen's model can be used for that condition.

Density

Another important thermophysical property is the density of the dispersion. According to the literature, there is a very simple correlation for the density of the dispersion with base fluids and nanoparticles in low concentration. It is expressed;

$$\rho_{eff} = (1 - \varphi_p)\rho_f + \varphi_p\rho_p \quad (2-15)$$

Specific heat capacity

The specific heat capacity has a very similar correlation as the density in low concentration as which is derived from the mixture rule principle. The equation is;

$$C_{p,eff} = \frac{(1-\varphi_p)\rho_f C_{p,f} + \varphi_p \rho_p C_{p,p}}{\rho_{eff}} \quad (2-16)$$

2.1.5. Boron Nitride nanofluids

Water-based Boron Nitride (BN) nanofluids due to its favourable thermal properties, chemical, physical stabilities and high electrical resistance [34], [38], [39], [48], [49], [91]–[93], makes the BN nanofluids suitable for the cooling of electronic devices with little electromagnetic interference. Zyła et al. [38] have investigated the thermal conductivity enhancement of BN/EG nanofluids. The results showed that the highest enhancement is about 260 % at a volume concentration of 12 %. Ilhan et al. [48] have investigated the hBN/water nanofluids with a volume concentration range of 0.1 %-1.0 %. The thermal conductivity enhancement and viscosity increase in their studies was about 13 % and 8 %, respectively, at 1.0 vol. %. More works about BN nanofluids can be seen in Table 2. 7.

Table 2. 7 Thermal conductivity and viscosity increase of BN nanofluids in literature

based fluid	concentration	k enhancement	μ increase	Ref.
EG	5%-20 wt.%	260 % in 20 %	-	[38]
Mineral oil	0.01 %-0.1 wt.%	76 % in 0.1 %	-	[34]
Water	0.6 %-6 vol. %	260 % in 6 % BNNTs 160 % in 6 % BNNSS	About 1200% in 6 % About 200% in 6 % BNNSS	BNNTs [92]
DI water	0.001 %-0.1 vol.%	16 % in 0.1 %	16 % in 0.1 %	[49]
Water	0.1%-1 vol.%	12 % in 1 %	8 % in 1 %	[48]

As is referred before, the smaller size seems to have a better thermal conductivity enhancement with the same concentration. In this PhD study, the wet milling has been applied to decrease the particle size of BN. The main highlight of the experiment is the fabrication and characterization of the morphology, the stability, the thermal properties, the rheology behaviour, and the electrical conductivity of the BN/DI water nanofluids. Great attention has been given to explain the properties of the stable wet milling nanofluids. Besides, there is little research about the influence of different temperature on thermal conductivity and the rheological behaviour of wet milling BN/DI water nanofluids. Therefore, the temperature dependence of thermal conductivity and rheology behaviour has been investigated. Moreover, the stability of the BN-nanofluids is studied with its zeta potential and storage time.

2.1.6. Graphene nanofluids

As is shown in Table 2. 8, Nano-platelet graphene due to its favourable properties has been widely used to enhance thermophysical properties of the base fluids. Gao et al. [94] have investigated the thermal conductivity of graphene nanofluid with water and ethylene glycol as base fluid. The results showed that compared to the pure EG, GNP/EG+DW (1:1) nanofluid has higher thermal conductivity enhancement with a more obvious difference at sub-zero temperature than that at a higher temperature. Kole et al.[80] have measured the stability, thermal conductivity and viscosity of the surfactant-free graphene/EG+DW nanofluid. The results show that the Hummers' method prepared functionalised graphene shows long stability over 5 months. For the thermal conductivity enhancement, the results suggested Nan's model could be used for the explanation. This same enhancement trend was also found in the work of Yu et al [95] and Cabaleiro et al[81]. More works related to the viscosity and thermal conductivity from literature is given in Table 2. 9.

Table 2. 8 The thermal conductivity enhancements and viscosity increase in literature

base fluids	k enhancement	μ increase	Ref.
EG	4.6 %		[94]
DW	6.8 %		

EG+DW (1:1)	18 %		
EG+DW (7:3)	~15 %	~100 %	[80]
EG	61 %		[95]
EG+DW (1:9)	4.0 %	12.6 %	[81]
Propylene-glycol(PG) - water (3:7)		222 %	[28]
Water	14.2 %	~87 %	[96]
Water	45.1 %		[97]
Water	~20 %	21.4 %	[98]
EG+DW(1:9)	5 %	12.6 %	[40]
Water	22.22 %	30 %	[29]
EG	12.7 %		[99]
Water	37.2 %		[100]
Water	10.3 %		[101]
Water	12 %	24 %	[102]
EG	30 %	127 %	[82]
Water	47.5 %		[103]
Water	27.64 %	44 %	[83]
Water	15 %	100 %	[84]
Water	30.2 %		[104]
PG	62.3 %		
Liquid paraffin	76.8 %		
Water	~75 %		[105]
EG	~8 %		
Water	17 %		[106]

Water	32.19 %	~200 %	[107]
Water	6.24 %	15.65 %	[108]
EG	86 %		[85]

2.3. Die attach selection

As the die-level heat fluxes can be $\geq 1 \text{ kW/cm}^2$ [109] for the GaN-on-Diamond /GaN-on-SiC device.

To make the heat sufficiently dissipated to the microfluidic channel, it is important to choose the die-attach material.

2.2.1. Requirement for the die attach material

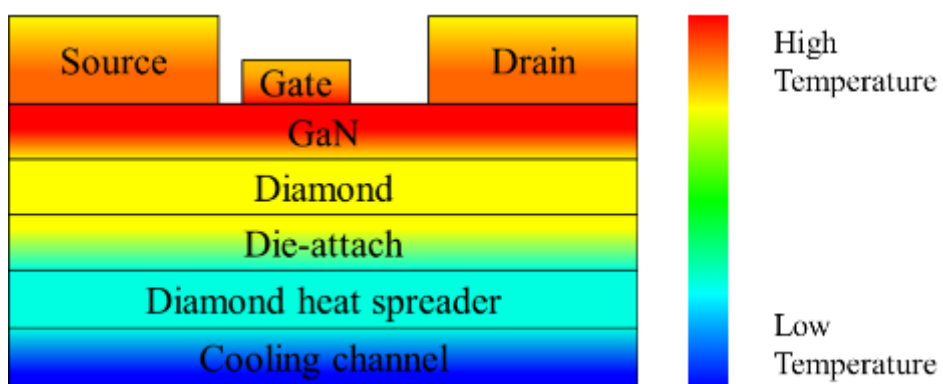


Figure 2. 5 Schematic diagrams of a microchip with a cooling channel combined via the die-attach layer

Heat flux at the bottom of the die is still high. Thus, thermal management in this part is also vital. High thermal resistance will prevent the heat transferred from this the die to the microfluidic channel as is shown in Figure 2. 5 The heat transfer at this layer follows Fourier's law,

$$\Delta T = \frac{qL}{k} \quad (2-17)$$

$$R_{th} = L/k \quad (2-18)$$

Where ΔT is the temperature gradient in the die-attach layer,

R_{th} is the thermal resistance of the die attach layer,

q is the heat flux,

k is the thermal conductivity of the die attach material,

L is the thickness of die attach.

In order to decrease the temperature drop in the die-attach layer, it is important to decrease the thermal resistance. Thus the aim is to find a die attach material with high thermal conductivity meanwhile the thickness at this layer cannot be large.

2.2.2. Types of die-attach

(1) Sintered metal

The most common sintered metal used for die attach is silver due to its high thermal conductivity (428 W/(m·K)). However, during the sintering process, the thermal conductivity decreased. Some investigations gave the value of 200 ± 20 W/(m·K) for the silver [110]. The reason for the decrease of thermal conductivity might be the porous structure formulated during the sintering as is Figure 2. 6 The thickness of the sintered silver die attach varies a lot with the different investigations. Some search achieved a thickness of 20 μm [111], while others claimed the thickness of several hundred micrometres in the research [112]. As for the reliability test, some research has experimented with the test rig shown in Figure 2. 7 [113]. Another sintered metal can be used for the die attach is made of copper which has a thermal conductivity of 401 W/(m·K). After the sintering, the die-attach has a thermal conductivity of 94 W/(m·K) [110].

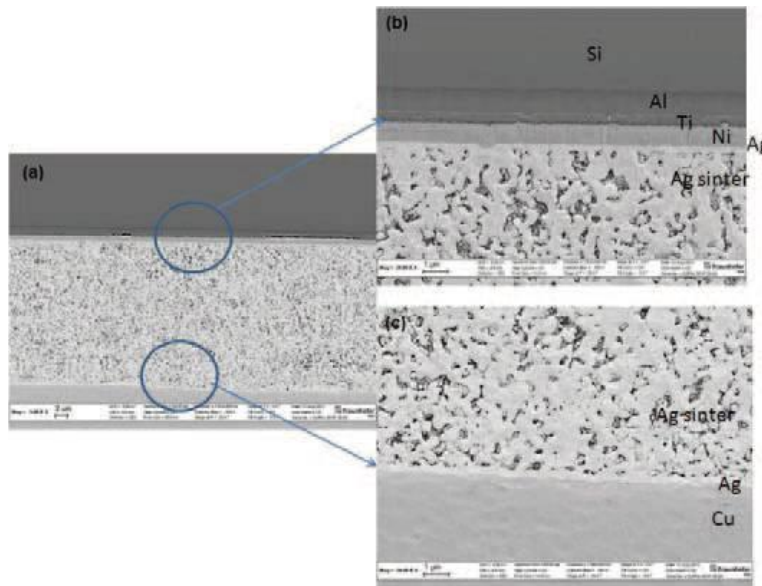


Figure 2.6 SEM images of sintered Si die on Ag plated Cu/Alumina/Cu substrate[114]

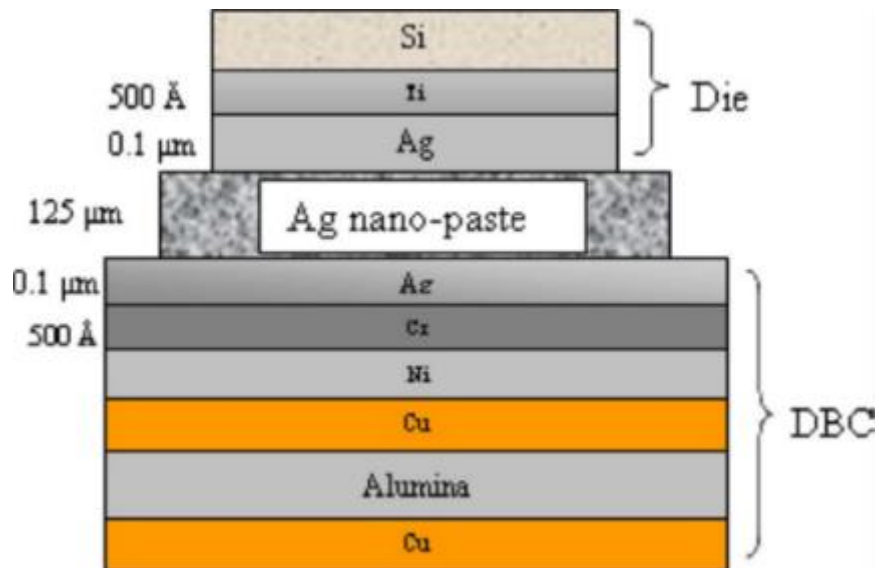


Figure 2.7 Schematic of test specimens for the sintered silver nanoparticle paste (not to scale)[113]

(2) Gold-based alloy

Gold-tin (Au-Sn) system are one of the most used gold-based alloys [115],[116]. This type of die-attach relies on the theory of the solid-liquid inter-diffusion. The thermal conductivity of this type of die-attach is around 50 W/(m·K). As is shown in Figure 2.8, the thickness of the die attach can be less than 10 μm. However, compared to the pure gold, the die attach is stiffer and brittle. Meanwhile, the alloy is

harder than tin. The reason for this is the inherent properties of die attach material with the inter-diffusion process.

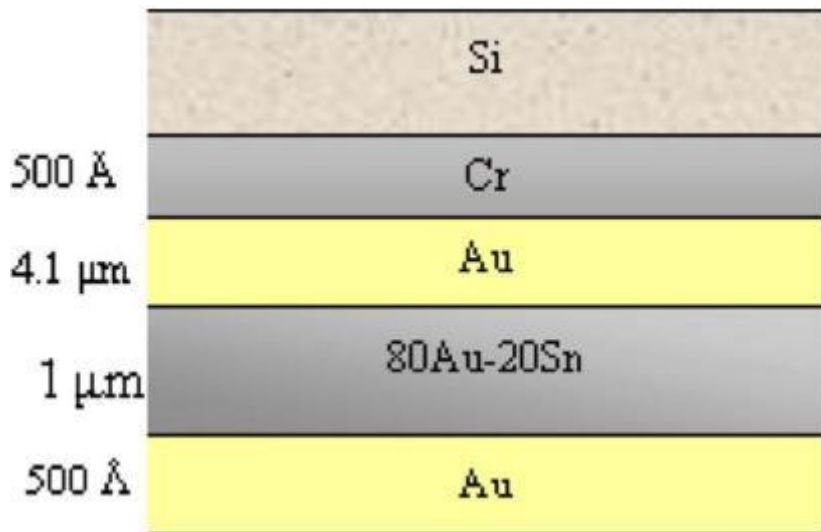


Figure 2. 8 Schematic representation of the Au–Sn system [113]

(3) Lead-based alloy

Another type of the most widely used metallic alloy for die-attach is lead (Pb) based material, especially Pb-Sn alloy. The research showed that the thermal conductivity for the Pb-Sn system is around 40W/(m·K) [117]. The main disadvantage of the lead alloy is the threat of lead to human and environment.

(4) Epoxy adhesives

The traditional adhesive is made of epoxy that has quite low thermal conductivity. Some research showed this value of around 0.38 W/(m·K) [118]. To increase the thermal conductivity in the adhesive die attach layer, silver has been added into the adhesive material. The thermal conductivity for those silver-filled adhesives various from 5-25 W/(m·K). The reason for the enhancement of thermal conductivity is illustrated in Figure 2. 9 Due to the nanoparticles formed shortcuts for the micro size particle that increases the multichannel heat dissipation pathway and the increase of contact area in the adhesive material, the thermal conductivity, thus, enhanced. The thickness for the adhesive is roughly around 25 μm.

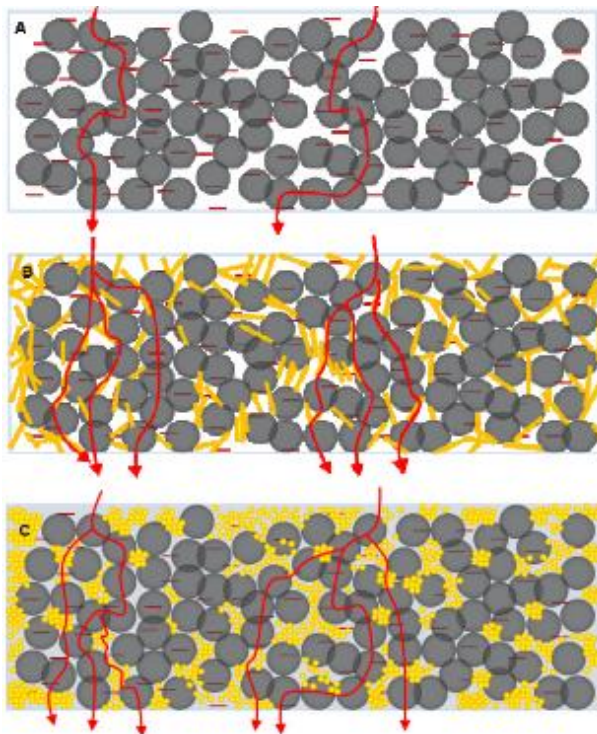


Figure 2.9 Schematic illustrations of heat dissipation route of the DAAs (A) before and (B) after adding one-dimensional nano-filters, or (C) after adding nanoparticles [119]

(5) Other die-attach types

There are some other types of the die attach material such as Ag-Al alloy, SAC solder, transient liquid phase bonding, Sn-Ag-Cu etc. The thermal conductivity and thickness which affect the heat-dissipating of the die are listed in Table 2. 9.

Table 2. 9 Thermal conductivity and thickness of the die attach

	Material	Thickness	k	Ref.
			μm	
Ag-based die attach	Sinter sliver	40	80	[117]
	Sinter silver	25-50	100-170	[120]
	Sinter silver	100		[121]
	Sinter silver	25-55		[114]
	Sinter silver		100-170	[118]
	Sinter silver	60		[122]
	Sinter silver	40		[123]
	Sinter silver		200±20	[110]
	Sinter silver	30		[124]
	Sinter silver	20		[111]

	Sinterable nanosilver	25-50	[125]
	Sinter silver normal	320	[112]
	Sinter silver annealed	320	[112]
	Sinter silver Non-pressurized	1460	[112]
	Sinter silver+SiC	200	~50 [126]
	Sinter silver + hBN	200	~50 [126]
	Sinter porous Ag	50	[127]
	mAgic sinter silver	25	>100 [128]
	Nanosilver	130	[129]
	Nanosilver	18	[130]
	Ag nano-paste	125	[113]
	Silver paste	50	[131]
	Silver paste	75	[132]
	Silver paste		2-25 [133]
	Sliver paste	25	250 [134]
	Silver paste	25-50	60 [120]
	Silver paste	10	0.616 [135]
	Novel silver paste		98 [136]
	Nanosilver paste	180	[137]
	Nanosilver paste		200 [138]
	Nanosilver paste	125	[139]
	Nanosilver paste		100 [140]
	Silver bonded LTJT no pressure		29 [136]
	Silver bonded LTJT 40 MPa		220 [136]
	Sn-Ag solder	100	30-50 [128]
	Sn-Ag solder	120	[141]
	Sn-Ag solder	94	[116]
	Sn-3Ag-0.5Cu		65±1 [142]
	Sn _{95.5} Ag _{3.9} Cu _{0.6}	200	[132]
	Ag-In solder	5	[143]
	Ag rich alloy	10	[143]
	Ag ₈₀ -Al ₂₀	25.4	[144]
	Ag ₈₀ -Al ₂₀	54	[145]
	Ag stress-migration bonding	4	[146]
	80Au-20Sn	5	[139]
	Au-Sn30		58 [147]
	Au-20Sn		59.1 [148]
Au based alloy	Au-Sn solder	<5	[113]
	Au-Sn Solder	26-27	[115]
	Au-Ge solder	48	[129]
	Au/Sn eutectic bonding	5	28 [135]
	AuGe12 solder	75	44 [138]

	AuIn19 solder	50	28	[138]
Pb based alloy	Sn-Pb37		51	[147]
	Sn-Pb solder		43	[117]
	Pb-5Sn		35.6	[148]
epoxy adhesive	epoxy		0.38	[118]
	Silver filled epoxy		29	[118]
	Epoxy		0.2-0.3	[133]
	DDA		10.38	[119]
	DDA+10% commercial flake		13.12	[119]
	DDA+5% NSPs		13.52	[119]
	DDA+10%NSPs		21.94	[119]
	DDA+5% silver nanorod		13.72	[119]
	DDA+10% silver nanorod		15.78	[119]
	DDA+5% Ni nano chains		10.68	[119]
Other types	DDA+10% Ni nano chains		13.88	[119]
	Ag-epoxy adhesive		5.1±0.2	[142]
	Silver filled epoxy	25.4		[149]
	Paste	150	143±7	[142]
	Sinter copper		94	[110]
	SAC 305 solder		57.8	[140]
	SAC305	50		[133]
	SN100C solder		64.0	[140]
	Zn-Al-Mg-Ga -Solder	30		[150]
	Cu-Sn transient liquid phase	15		[151]
	Ni-Sn transient liquid phase	15		[151]
	Zn-Sn solder	200	100-106	[148]
	Lead-free solder	50		[152]
	Solder	10	4.2	[135]
	Solder	100	32.2	[153]
	Solder	20	48	[154]
	Solder	10	4.2	[135]
	Solder		~60	[133]

2.4. Liquid cooling methods for the microchip

Several designs of microfluidic channels have been studied for efficient heat dissipation. The following section will review some of the most commonly used technologies for the microfluidic channels.

2.3.1. Microchannel

Beni et al. [155] studied microelectronic cooling with different shapes of microchannels, as shown in Figure 2. 10 Their studies suggested different microchannel shapes would have significant effects on thermal performance and pressure drop. The sinusoidal structure can increase the lifespan of the electronic devices by 44% with pressure drop increase by 18%. Reddy et al.[156] have investigated the performance of micro pin-fin arrays for cooling electronic with a hot spot. In their studies, the pressure drop between inlet and outlet was over 0.25 MPa to keep the highest temperature below 75 °C. Al-Waaly et al.[157] have studied the thermal performance of the microchannel with sub-channels for the cooling of a microchip. The results showed that a 20 % decrease for the thermal resistance was found for the microchannel with sub-channels. Meanwhile, the pumping power showed an 11 % increase in pumping. There are researches [5], [158], [159] combining nanofluids with microchannel to enhance the performance of the cooling channel. According to the literature [16], [160]–[162], to maintain the temperature in the die to be less than 200 °C, the velocity in the microchannel was relatively large (in some cases, larger than 10 m/s), as is shown in Figure 2. 11. The high inlet velocity can cause a large pressure drop (over 1 bar) in the channel. Many other problems such as the sealing of the channel without liquid leaking may occur due to the high pressure in the channel.

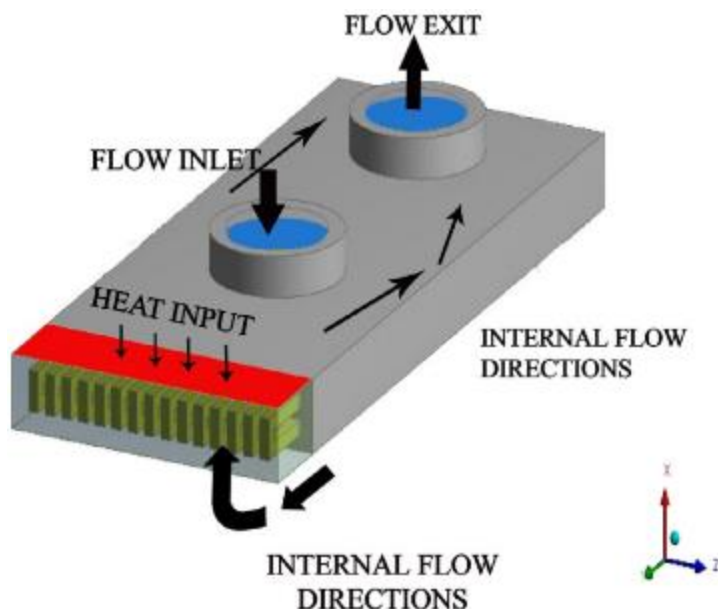


Figure 2. 10 Schematic view of fluids flow in the microchannel view [155]

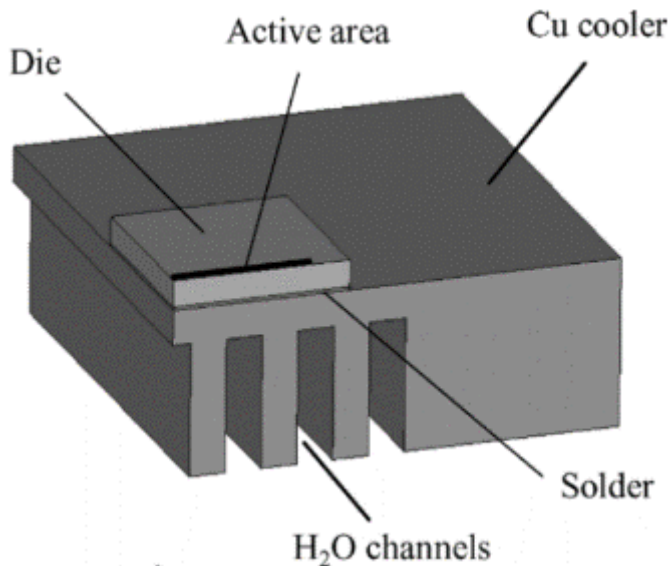


Figure 2. 11 Microchannels for cooling the die attached on (1/4 model)

2.3.2. Metal foam

Metal foams have been studied as a possible solution to enhance heat transfer in microfluidic devices. The large surface area to volume ratio (about 1000-3000 m²/m³) [163] and the porous metal tortuosity provide an extended heat transfer area, as is shown in Figure 2. 12. The metal foam characteristics, such as porosity, pore per inch (PPI), pore size, and permeability, directly affects the properties of the flow, and hence the heat transfer performance. Boyomy et al. [164] studied the heat transfer development and characteristics of an aluminium foam heat sink for an Intel Core i7 processor, as is shown in Figure 2. 13. They observed that the Reynolds number increased with the thermal entry length increase. Wang et al. [165] investigated the pressure drop and heat transfer in a metal foam filled with tubes. The results showed compared with constant heat flux, a lower Nusselt number under convective boundary conditions was obtained. Nazari et al. [166] found that the heat transfer rate increases when a nanofluid flows through a pipe filled with a metal foam, comparing to an empty tube. According to the literature, the heat transfer coefficient of the copper-foam is roughly around 1.5-10.9 W/(cm²·K) with an acceptable pressure drop. However, the given heat transfer coefficient is not high enough to dissipate the high local heat flux on the die without large temperature increases.

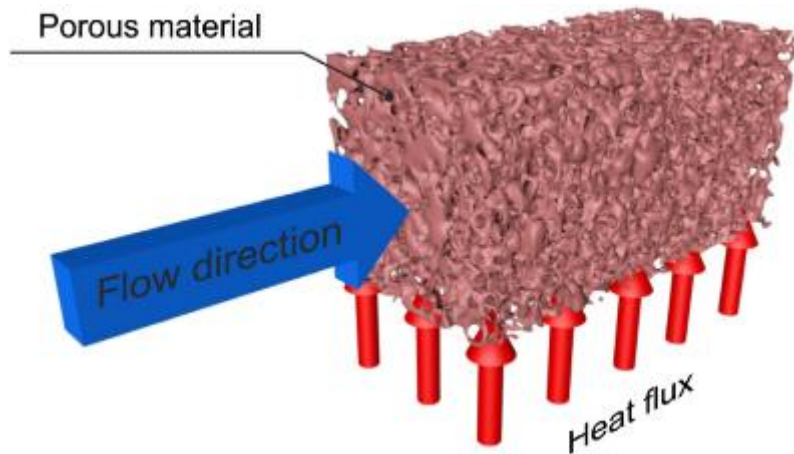


Figure 2. 12 Structure of the metal foam [167]

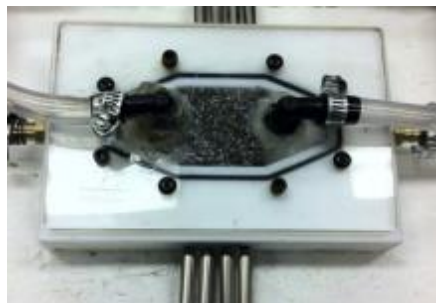


Figure 2. 13 A figure of metal foam based cooling channel [164]

2.3.3. Micro-jet impingement

Compared to the microchannel and metal foam based cooling channel, the micro-jet impingement is one of promising technology as it has the largest heat transfer coefficient for single-phase flow with acceptable pressure drop [167].

Jet, as is defined by its name, is made of a jet flow from nozzles, orifices, and/or slots and mixed with its surrounding fluid. The jet has been used in many fields such as pump, steam pump, chemical engineering equipment etc. The jet can be classified by different criteria. (1) flow state as laminar jet and turbulence jet; (2) temperature between the jetting area and environment area as isothermal jet and temperature difference jet; (3) concentration between the jetting area and the environment area as equal concentration jet and difference concentration jet; (4) the space of the jetting as free jet and confined jet. As for the free jet, the jet flow is not confined by the solid wall otherwise the confined jet.

- **Background of the jet impingement**

Figure 2. 14 shows the flow of the submerged jet impingement of a round orifice through several regions.

It should be noticed that in the real application, not all of the regions are existed due to the distance between the orifice of the jet to jet impinging plate H might not be long enough. The important geometrical parameters are the jet-to-jet impinging plate H and the diameter of the orifice D as is illustrated in Figure 2. 14. The H is relatively long enough to have all regions in a schematic illustration.

After the liquid exiting the orifice, the flow behaviour of the liquids can be regarded as a free jet as the far distance of the impingement wall. In this region, the peripheral velocity gradient causes the entrainment of mass, momentum, and energy from the quiescent ambient fluids due to the shear-driven interaction the peripheral velocity gradient causes.

However, in the impinging forepart, the flow interior is not influenced by the heat transfer and momentum transfer in the shear-driven layer, although this shear driven layer progressively widen. This area is called the potential core region, which is made of the quasi-conical unperturbed area. In the potential core region, the original velocity, temperature, and total pressure are the same as the initial value in the orifice.

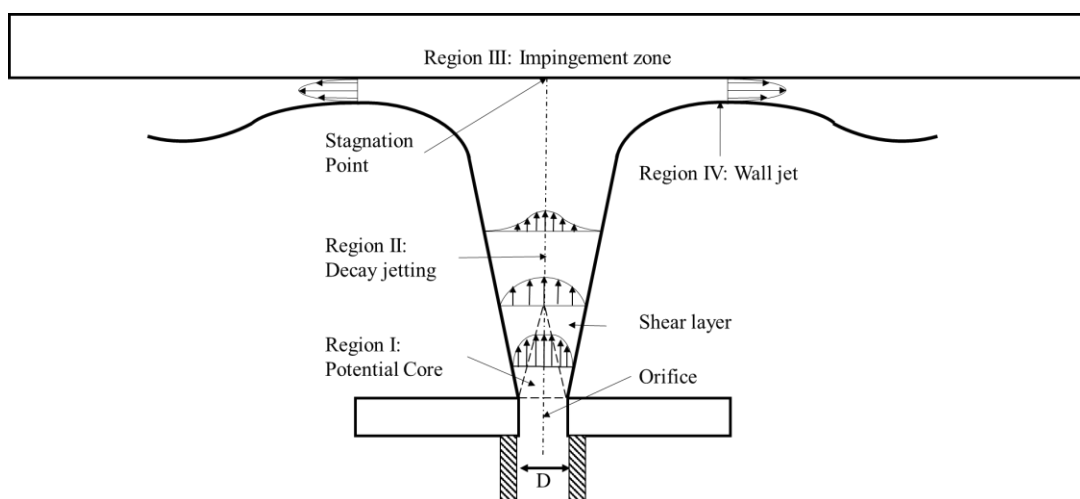


Figure 2. 14 the schematic of the jet impingement

The decay jetting region follows the potential core region as the axial velocity component in this region continuously shrinks. This region can also be called flow developing-region or jet fully developing-region.

The stagnation region refers to the area where the axial velocity of the jet flow sharply decreased to zero due to the jet hit the impingement wall. In addition, the axial velocity component decreases and transfers its direction in parallel to the impinging wall. Thus, high static pressure has been build up in the stagnation area and then it decreases as the velocity accelerates along the impinged wall. This inhomogeneous transition of the flow affects all the local transport properties as the high normal and tangential stresses created in this region.

The wall jet region is in the downstream of the stagnation region where the flow spreads radially outwards and force to be parallel to the impinged plate. This eventually developed into a semi-confined flow. The thickness of the boundary layer gradually increases as the wall jet progress. In-wall jet, the laminar boundary layer exists due to the stabilizing effect of the acceleration. However, the transition from laminar to turbulence can occur after the flow reaches its maximum velocity.

In this study, the micro-jet array with die mounted on diamond heat spreader is illustrated as is shown in Figure 2. 15 A 3D printed channel with micro-jet fabricated on the jet plate. The whole channel is directly bonded with the diamond heat spreader with die mounted on top of it. This design eliminated any potential contact resistance between device and cooling channel. Between the jetting orifice and the device, a relatively large jetting chamber is used to circulate the heat transfer fluid pumped from reservoir impinges on the back of heated diamond heat spreader. The dissipated heat is carried by heat transfer fluids from the outlet to the reservoir. It should be mentioned that the heat transfer fluids during the micro-jet impingement do not change their phase to prevent the instability of the whole system due to the large pressure drop in the phase change.

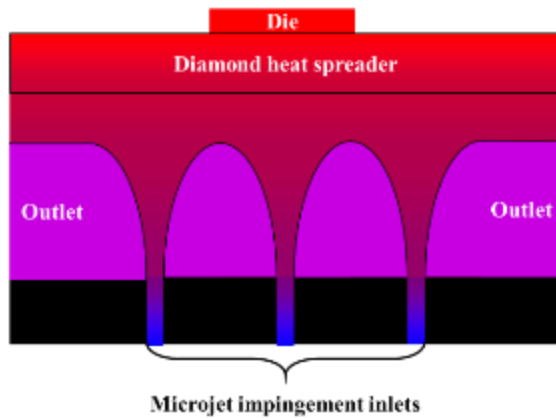


Figure 2. 15 Schematic of micro-jet impingement with the die-on-diamond heat spreader

- **Application of micro-jet impingement with microelectronics**

Jorg et al [168] investigated the thermal performance of micro-jet impingement for a microelectronic module. The core unit consisted of a 12 mm × 10 mm cooling chamber, which was 9 mm in height. The size of the micro-jet orifice was 900 μm as is shown in Figure 2. 16 The results showed that with an inlet temperature of 22.5 °C, the inlet flow rate of 30 mL/min and power of 51 W in the microelectronic device, the maximum temperature on the device was 163 °C. The heat transfer coefficient up to 6000 W/(m²·K) was achieved with the same flow rate using only 10.8 cm³ of assembly space for the cooling device. The assumption of pumping power was 3 mW. Jorg et al. [169] also performed the direct cooling of the microelectronic with a micro-jet array. The results showed that reducing the nozzle diameter from 1.6 mm to 0.6 mm lowered semiconductor peak temperature from 110 °C down to 90 °C. However, with the diameter decreasing to 0.6 mm, the power consumption increased over 30 times. Compared with pin fin heat sink, the 3 micro-jet orifices with a diameter of 0.6 mm can achieve similar thermal performance. Deng et al. [170] have carried out electrospray cooling for microelectronics. As is illustrated in Figure 2. 17 a cooling system with micro-fabricated multiplexed electrosprays in the cone-jet mode could remove a heat flux of 96 W/cm² with a cooling efficiency reaching 97 %.

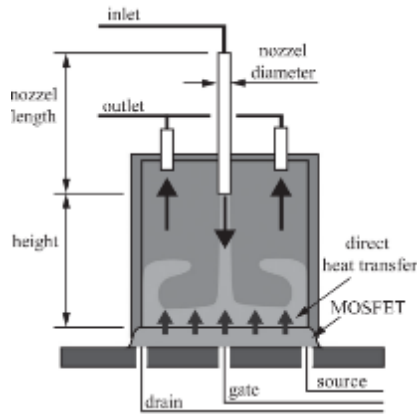


Figure 2. 16 Schematic of direct impinging jet cooling as well as dimensions and electrical connections[168]

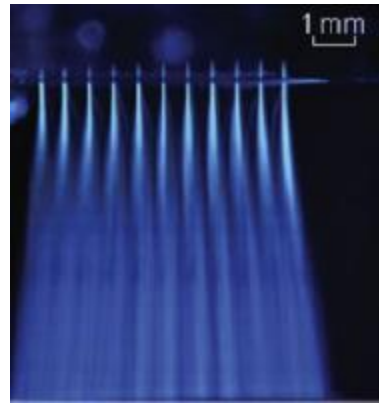


Figure 2. 17 Spray visualization of a 91-nozzle MES system with a packing density of 253 sources/cm²[170]

Maddox et al. [171] have investigated the cooling of power electronics with a confined array of impinging liquid jets, as is shown in Figure 2. 18. The effects of jet height, nozzle length, and Reynolds number on the heat transfer coefficient were investigated. The results showed that the maximum local heat transfer coefficient of 15,600 W/m²·K were measured for $H/D_n = 1$, $L/D_n = 2$, and $Re_{Dn}=14,000$; while the maximum surface average heat transfer coefficient of 13,700 W/m²K were achieved for $H/D_n = 3$, $L/D_n = 0$, and $Re_{Dn}=14,000$.

Han et al. [172] have studied the thermal management of microelectronics with the jet-based Si micro cooler as is illustrated in Figure 2. 19. The results showed that with 50 mW pumping power for the micro cooler, the microelectronic device's temperature can be maintained under 51 °C with the heat dissipation of 260 W/cm². The results also showed that the pressure drop for the micro-jet impingement channel was around 19 kPa with a flow rate of 0.3 L/min.

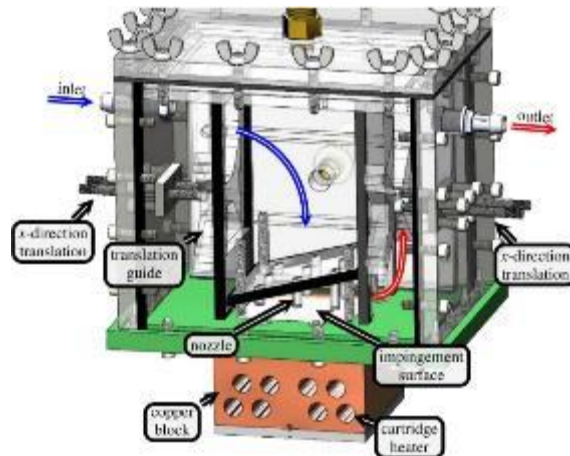


Figure 2. 18 Jet impingement flow chamber [171]

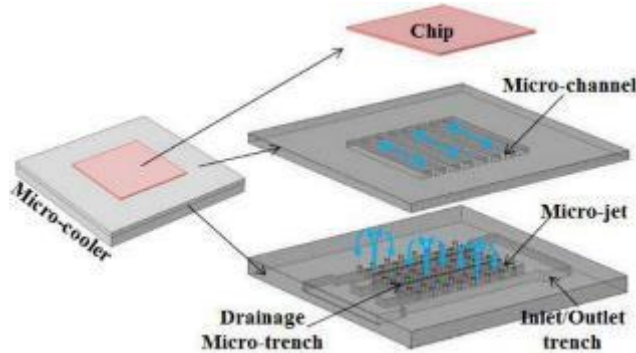


Figure 2. 19 Schematic 3-D images of the new hybrid jet-based cooling solution with MDMTs [172],[173], [174]

San et al [175] have studied the effects of jet height and jet-to-jet spacing on the thermal performance of an impinging jet array. The results showed that at a small jet-to-jet spacing to jet diameter ratio and jet height to jet diameter ratio, a maximum Nu, due to a strong flow impact on the impingement plate, was observed between the middle jet and every neighbouring jet. With an increase of the jet-to-jet spacing to jet diameter ratio and jet height to jet diameter ratio, the jet interaction decreased. The result also showed that the maximum Nu variation in the region under the jet array almost linearly increased with the jet-to-jet spacing to jet diameter ratio. Huang et al. [176] have investigated the heat transfer on a microfluidic channel with impinging jets and dimples. The result showed that convex dimples have the best cooling performance, followed by those without dimples, with mixed dimples, and with concave dimples. The pressure drop decreased with the application of convex dimples.

2.5. Numerical simulations of microchips and micro-jet channels

Due to the mismatch of the size of the detailed microchip and the cooling channel, the difference in fluid domains and solid domain for the microchip and the cooling channel, the methods for the numerical simulations might not be the same.

2.5.1. Numerical simulation of thermal management of microchips

Thermal performance of the electronic devices is widely studied via the numerical simulation. The analysis can be used to predict the thermal performance of new material, to analysis the thermal resistances in different layer etc. There is a lot of software used for numerical simulation such as ANSYS, COMSOL, GRADIENT, VHDL - AMS, FLOTHERM, Spectre, CircuitFire, HeatWave, Sentaurus device, and HSPICE.

Li et al. [177] have investigated the thermal, electrical, electromagnetic and mechanical performance of 140 mm × 190mm × 38 mm dimension single-switch high voltage insulated-gate bipolar transistor (IGBT) with commercial software in Ansys, as is shown in Figure 2. 20 To obtain better thermal and/or mechanical performance, the structure and assembly have been optimized. With 3D modelling and simulation, the parasitic inductance showed a 30 % decrease.

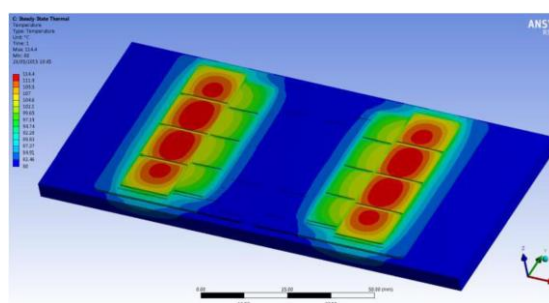


Figure 2. 20 Temperature distribution of the device [177]

Vipradas et al. [178] have studied the high power LED package with numerical simulation in steady-state thermal simulation with Ansys. A 3D structure LED system, consisting of LED chip, sub-mount, heat slug and silicone enclosure has been used for the numerical simulation to decrease the junction temperature. The size of the die, the thickness of the sub-mount, the thickness of the die attach and the

thermal conductivity of the die attach. However, as is shown in Figure 2. 21, the temperature drastically decreased with the increase in the thermal conductivity of die-attach material.

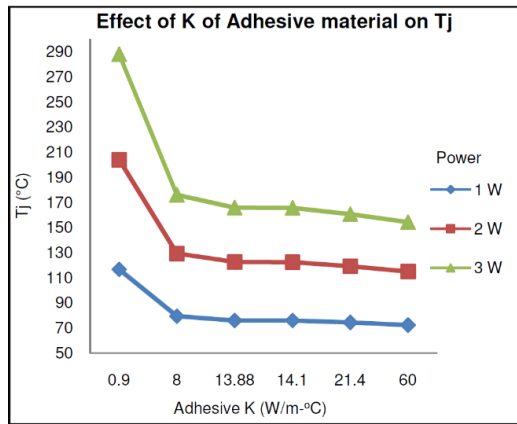


Figure 2. 21 Effect of the die and sub-mount adhesive material on die junction temperature [178]

Chvála et al [179] have investigated the InAlN/GaN high-electron-mobility transistor (HEMT) with 3-D Technology Computer-Aided Design (TCAD) for the thermal performance and with experiment for validation. Wong et al [180] have investigated the performance of Ga₂O₃ metal-oxide-semiconductor field-effect transistors via measurement and thermal modelling. The results showed a good agreement of the experiment with simulation with the ambient temperature varying from 25 °C to 175 °C

Kudsieh et al. [181] and [182] studied the thermal performance of the high-power solid-state lighting. In their study, GaN/AlGaN high power LEDs were investigated. Different kind of The LED array and different kind of the heat sink design The Chip-on-Plate packing technique was used as is shown in Figure 2. 22 3D modellings and simulation in Ansys were used for analysing the thermal performance of the LED chips. The results showed that conventional packages with circularly symmetric having non-uniform devices' distribution per unit area will have temperature differences ~7 °C among the chip-elements. The temperature difference was found to be < 1 °C for the uniform rectangular array module distribution, which ensured uniform output intensity for all devices. Vairavan et al. [183] have investigated the heat-dissipating of a single chip high power LED package with 3D numerical simulation on Ansys software. The result showed the maximum junction temperature of the LED chip was 121.71 °C. Tang et al. [184] have investigated the thermal performance of the high-power planar

Schottky diode-based multiplier microchips. A 3D numerical simulation with the steady-state and transient state in Ansys software was used to optimize the thermal characteristic of the microchip. The results simulation suggested that bonding agents with high thermal conductivity are required for fully exploiting the heat spreader. The results also suggested the GaN-on-SiC microchip has better thermal performance than the GaAs based counterpart. Cheng [185] investigated the thermal management of high-power white LED package. The numerical simulation was done in Ansys software. The package structure has been optimized based on thermal performance.

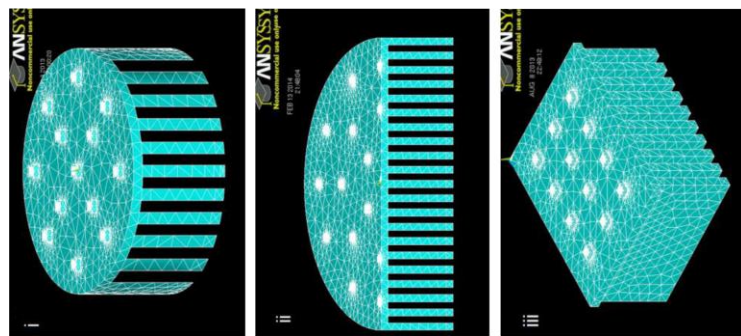


Figure 2. 22 3D meshed models of different LED assemblies. (i) Module/assembly (A), (ii)module/assembly (B), and (iii) module/assembly (C) [182]

Chvála et al. [186] have investigated the thermal analysis of multi-finger power HEMTs as is shown in Figure 2. 23 The simulation was developed for Synopsys TCAD Sentaurus environment using mixed-mode setup. The multi-finger HEMT structure metallization layout design had been analysis for its thermal performance. Rousseau et al. [187] have studied the efficient physical-thermal model for thermal effects in AlGaN/GaN high electron mobility transistors. The simulation was based on the 2D physical-thermal model. The results showed that to prevent the die from degrading, the maximum dissipated power must be no larger than 7 W/mm, 13 W/mm, and 38 W/mm for silicon, silicon carbide, and diamond substrates, respectively. Lu et al. [188] have investigated the high power RF/microwave circuits with simulation based on the finite element method. The results, as is shown in Figure 2. 24, suggested that it cost less than 20 ms for microchips to reach the steady-state. Pfost et al. [189] studied the thermal performance of the power double-diffusion metal–oxide–semiconductor (DMOS) transistors via the 3D numerical simulator. They have studied the behaviour of the temperature-

dependent DMOS transistor for high temperature the experiment has been experimentally verified with device temperatures exceeding 500 °C.

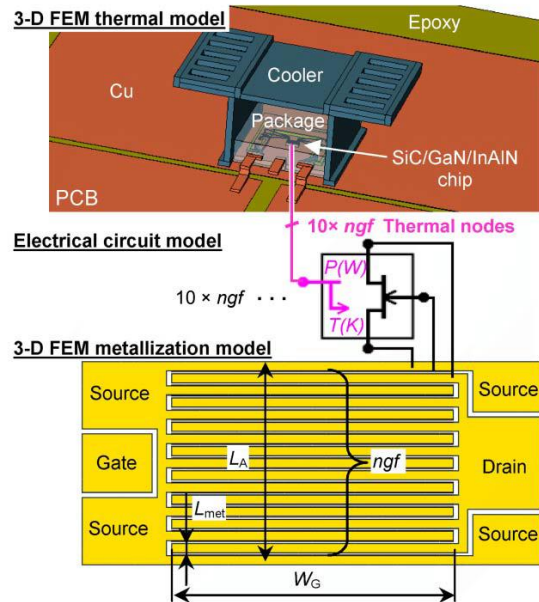


Figure 2. 23 Schematic diagrams of a mixed-mode approach for electro-thermal simulation [186]

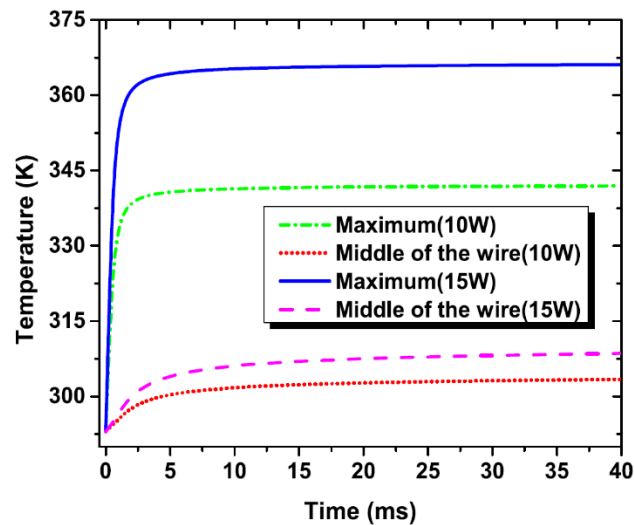


Figure 2. 24 Transient temperature response of the bonding wire array under different heat sources

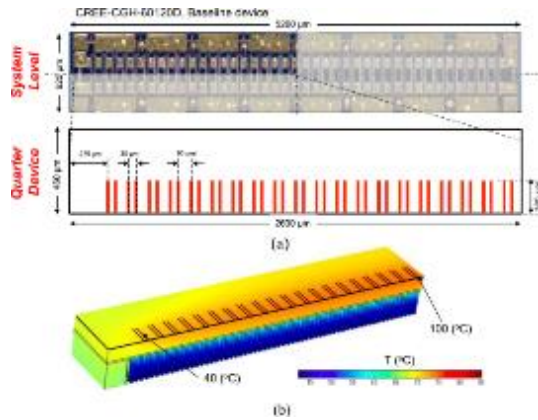


Figure 2. 25 Gate dimensions used in the simulation that mimics CREE-CGH-60120D (b) Conduction simulation result using 3-D COMSOL Multiphysics [190]

Won et al. [190] have studied the thermal performance of GaN high-electron-mobility transistor as is shown in Figure 2. 25 A 3D numerical simulation with the steady-state thermal model was applied on the commercial software COMSOL for the thermal performance of the test rig to determine the long-term heat flux feasibility. The thermal resistances with GaN layer, transition layer, device layer (SiC or diamond layer), thermal interface material layers, heat spreader layer and the heat sink as is shown in Figure 2. 26 have been analysed for temperature fields in the given layers.

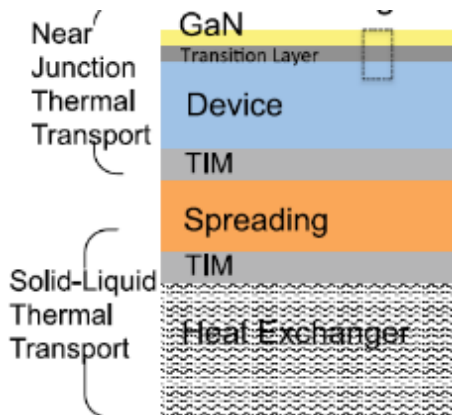


Figure 2. 26 Multiple layers from junction to heat transfer fluid in simulations [190]

Maize et al. [191] have investigated the steady-state and transient self-heating of the GaN high electron mobility power transistors with simulation and experiment. The simulation was set for the devices using the ISE Sentaurus Device with 3D geometry model. Lin et al. [192] have investigated the method for local thermal management using hexagonal boron nitride (h-BN) as a heat spreader and thick

counterpart as a heat sink for high electron mobility transistor (HEMT). A 2D numerical simulation has been used for its thermal performance. The results showed a temperature decrease of about 32 °C at the hotspot with the use of h-BN nano-sheet. Aaen et al.[193] have investigated the thermal performance of high-power RF and to laterally diffused metal-oxide-semiconductor (LDMOS) transistor microwave transistors in the commercial software Ansys. Li et al. [194] have investigated the High power Insulated Gate Bipolar Transistor (IGBT) modules. The standard 3.3 kV/1500 A single switch IGBT module with 190 mm × 140 mm footprint has been re-designed using latest metaphysics simulation packages with software Ansys for better performance. Ziabari et al. [195] have investigated the packaged integrated circuits and power devices with fast static and transient thermal analysis method. The software Ansys has been used for the numerical simulation to do a comparison with the numerical method of power blurring. Wang et al. [196] have studied the impact of diamond heat spreading layers on the performance of AlGaN/GaN high-electron-mobility-transistors (HEMTs). Numerical simulation with FEM was used to analyse the thermal performance of the microchips. The simulation results showed that the heat spreader shows a great influence on thermal performance. Prejs et al. [197] have investigated the thermal performance of GaN HEMT Amplifiers. The FEM has been used to simulate the thermal performance of the die with Ansys and do a validated with the IR camera measurement. The transient thermal resistance was calculated for a range of transistor structures and sizes as a function of power density, pulse length and duty factor and compared with measured channel temperatures and RF parameters. Baczkowski et al. [198] have investigated the thermal characterization of AlGaN/gallium nitride on silicon carbide high electron-mobility transistors in RF operating conditions. They have developed the thermal model and suitable temperature measurement to analyse the thermal performance of the channel in the operating condition. The temperature on the microchip was measured by the thermoreflectance microscopy and micro-Raman spectroscopy have been performed. A 3D numerical simulation with commercial software Ansys has been used to validate and analysis the temperature at the hot spot. Wu et al. [199] have analysed the thermal resistance for power device packaging by numerical method. With numerical simulation in ANSYS software under two different boundary conditions, the thermal resistance for power device in T03P package was obtained. The results showed

that the thermal resistance has positive correlation with heating power and more sensitive to the change of thermal conductivity of the die attach than that of epoxy mould compound.

2.5.2. Numerical simulation of the micro-jet

Robinson et al. [173], [174] have investigated the heat sink with a micro-jet array which was fabricated via high volume additive manufacturing. The design was used for the cooling of microelectronics with high heat flux applied on. Numerical simulation with Ansys Fluent has been used to analyse the performance of the microfluidic channel. The results showed that an overall heat transfer coefficient of $\sim 300 \text{ kW/m}^2 \cdot \text{K}$ with a pressure drop of 160 kPa can be achieved for a flow rate of 0.5 L/min. Han et al. [200] developed the micro-jet based Si micro-cooler for the microelectronic cooling, as is shown in Figure 2. 27 Numerical simulations with software COMSOL has been used to analyse the influence of nozzle length and nozzle shape on the thermal performance and pressure drop of the micro cooler. The results showed that with a flow rate of 300 mL/min, the Microfluidic channel could maintain the chip temperature of 50.7 °C with the heat flux of 260 W/m² on the chip.

Jorg et al [168] have studied the thermal management of a typical MOSFET transistor with direct single impingement jet, as is illustrated in Figure 2. 28 The single micro-jet was used for cooling the bottom surface of the MOSFET semiconductor package. Two different die-attach configurations have been used to investigate the die attach effect on the die temperature. The results showed that with a flow rate of 30 mL/min the die temperature was close to 163 °C with the power of 51 W and an inlet temperature of 22.5 °C. The results also showed that the die attach material with a thickness of 200 μm is the largest thermal resistance in the whole package. Naphon et al. [201] have numerically investigated the liquid jet impingement thermal performance with different outlet port position. As is illustrated in Figure 2. 29, the outlet port positions greatly influenced temperature distribution in the channel.

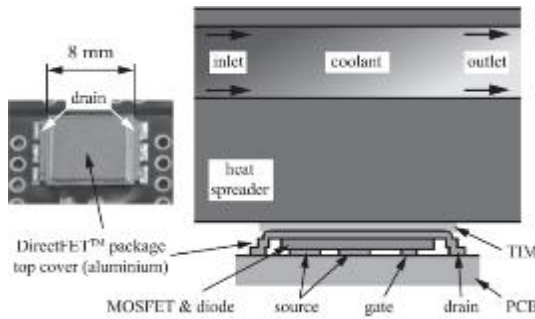


Figure 2. 27 Left picture shows the DirectFET Power MOSFET package mounted on a PCB. The right panel displays a schematic cross-section of the DirectFET package equipped with a standard plate cooler and TIM [168]

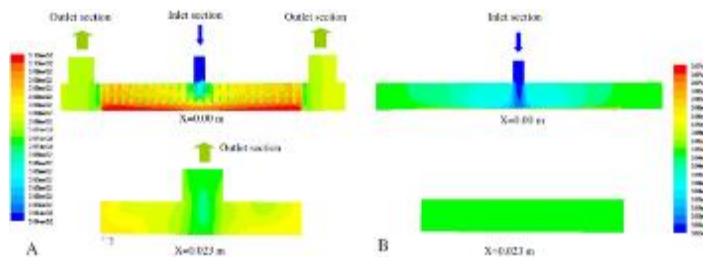


Figure 2. 28 Variation of temperature contour at different cross-sections for model A and model B [201]

Gorodetsky et al. [202] have investigated the micro-jet impingement combined with the micro gap. The parameters of jet array location, the pitch, micro jet slot hydraulic diameter and initial flow distribution has been analysed. The numerical and experimental results suggested that the jet increase the heat transfer of 60 % as compared to a plain gap with great improvement of the temperature uniformity. Han et al. [203] have investigated the microfluidic heat sink with micro jet slots for the high power data centre. The result showed that the microfluidic channel can have a high cooling capacity with low pumping energy. The results showed that with a flow rate of 0.5 L/min can have a thermal resistance of $0.13 \text{ }^{\circ}\text{C} \cdot \text{cm}^2/\text{W}$ with a pressure drop of 0.8 kPa. Parida et al. [204] have investigated the performance of the impingement based thermal management of automotive power converters. Both ANSYS-CFX and ANSYS-Fluent were used to study the flow and heat transfer performance in the designed micro-jet channel. Similar results could be obtained with both commercial software. For the flow model, the $k-\epsilon$ model, as well as the $k-\omega$ SST model, has been analysed and validated with the experiment, as is shown in Table 2. 10. The heat transfer coefficient as is shown in Figure 2. 30 A maximum of 24043 $\text{W}/(\text{m}^2 \cdot \text{K})$ heat transfer coefficient can be obtained.

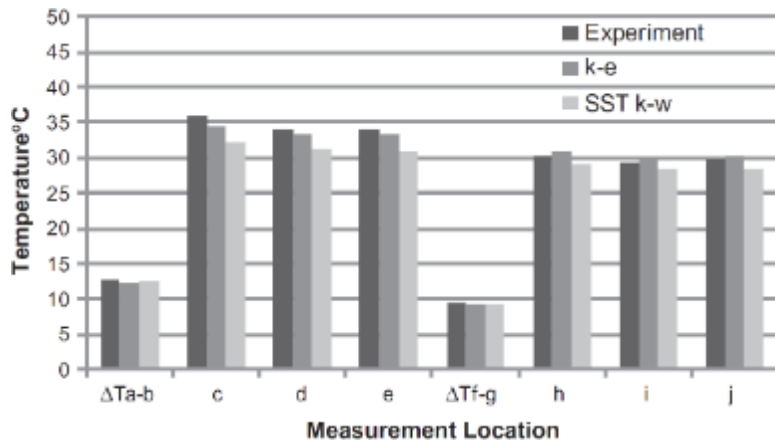


Figure 2. 29 Temperature prediction by $k-\epsilon$ and SST models and its comparison with the experimental data [204]

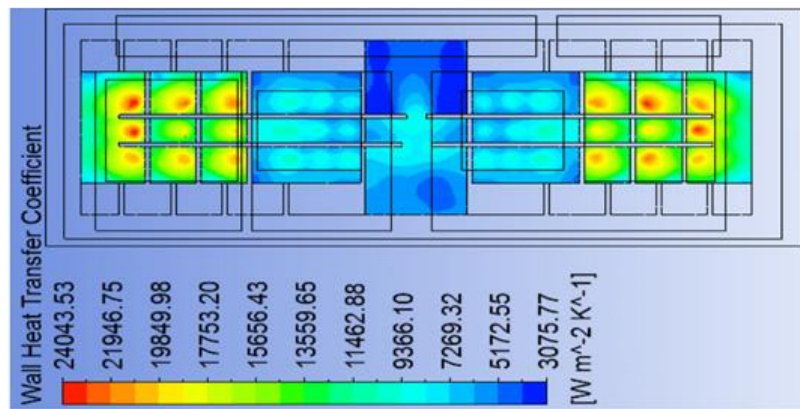


Figure 2. 30 heat transfer coefficient at the bottom surface of the DBA [204]

Gould et al [205] have investigated the thermal management of the 600-V/50-A Silicon Carbide power conversion module with liquid jet impingement. The water and the ethylene glycol coolant have been used for the coolant. The micro-jet channel has been optimized with numerical simulation via Ansys Fluent. Shin et al. [206] have experimentally and numerically investigated the thermal performance of the micro-jet impingement via HFE-700 cooling fluid as is shown in Figure 2. 31. The Reynolds number varied from 162 to 4057. The nominal heat flux was between 10 W/cm² and 80 W/cm². Penumadu et al. [207] have investigated the thermal performance and pressure drop of the multiple jet impingement in low Reynolds number regime. The results showed that the large-eddy simulations had a better understanding of the flow physic in multiple jet impingement array. The simulation results also suggested that the contraction effect at the nozzle entrance and viscous losses are the major factors for

the pressure drop. The results also suggested that the thermal performance was sensitive to minor changes in Z/D. However, it is insensitive to the jet diameter.

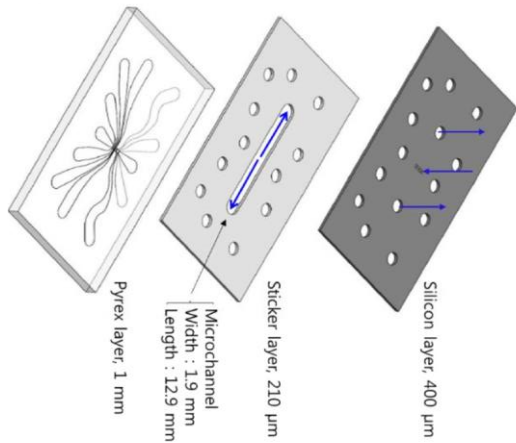


Figure 2. 31 Blow-up schematics showing the three layers of the microdevice [205]

Barrau et al [208] have investigated the thermal performance of the jet impingement with Ansys Fluent for high heat flux thermal management of electronic and high power devices. The numerical model has been developed based on the $\kappa-\omega$ SST turbulent model. The results showed the $\kappa-\omega$ SST model was effective for predicting the thermal performance of the jet channel. The results also showed that compared to the increase of heat transfer coefficient, the pressure drop increased faster with the Reynolds number. Han et al. [209] have investigated the thermal performance of the micro-jet fluidic channel for microelectronic devices, as is illustrated in. The results showed that the average heat transfer coefficient of 18.9×10^4 W/m²·K can be obtained with the pumping power of 0.17 W. The power density of 3.9 W/mm applied on the die can be dissipated with the maximum temperature no larger than 200 °C.

Table 2. 10 Parameters for the numerical simulation of the micro-jet channel

shape	Arrange type	Software	Dimensions	Flow model	Correlation	Ref.
round	array	Fluent	3D	-	-	[174]
round	single	Fluent	3D	-	$Nu=aRe^{0.5}+b$	[168]
slot	single	Fluent	2D	$k-\omega$ + near wall effect	-	[210]
round	single	Fluent	3D	$k-\epsilon$	-	[201]

slot	array	Fluent	3D	k-ε	Nu=0.48Re ^{0.53}	[202]
round	single	Fluent	3D	-	Nu=cRe ^{0.5} +d	[169]
round	array	CFX+Fluent	3D	k-ε+ k-ω SST	-	[204]
round	array	Fluent	3D	-	-	[205]
round	array	Fluent	3D	k-ε	Nu=0.225Re ^{0.693}	[206]
round	single	-	2D	k-ε	-	[211]
round	single	Fluent	3D	k-ω SST	-	[207]
round	single	-	3D	k-ε	-	[212]
round	single	-	2D	-	-	[213]
round	single	Fluent	3D	-	-	[214]
round	single	Fluent	2D	k-ε+ k-ω SST	-	[215]
round	single	Fluent	3D	k-ω SST	-	[208]
slot	single	Fluent	3D	-	Nu=0.25 Re ^{0.77} (μ/μ _w) ^{0.2} Nu=1.05 Re ^{0.5} (μ/μ _w) ^{0.2}	[216]
round	array	Fluent	3D	k-ε	-	[217]
round	array	COMSOL	3D	-	-	[218]
round	array	COMSOL	3D	-	-	[219]
round	array	COMSOL	3D	-	-	[220]
round	array	COMSOL	3D	-	-	[200]
slot	array	COMSOL	3D	-	-	[203]
round	array	COMSOL	3D	-	-	[209]
round	single	COMSOL	2D	-	-	[221]
round	array	CFX	3D	-	-	[222]

2.6. Summary

From this literature review, the following conclusions can be obtained:

- Thermal packages of the GaN transistors with high heat flux is still one bottleneck for the application of the transistors as the temperature can easily exceed over 200 °C. This PhD project has considered many factors for improving the thermal management of the device. Those technologies include the microfluidic channel for the far end cooling of the devices, the novel nanofluids used for the wide working temperature (from -50 °C~room temperature), the thermal interface material etc.

- The heat transfer fluid is one of the important parts in the cooling channel as the heat is eventually dissipated into it. This can be further divided into tradition heat transfer fluids such as water, glycols etc. and novel heat transfers fluid such as BN nanofluids, reduced graphene oxide (rGO) nanofluids etc.
- The microfluidic channel is an important part as it affects the heat transfer coefficient of the cooling channel. There are many types of the microfluidic channel can be used such as the micro-jet channel, micro-channel, metal-foam based channel etc.
- Good thermal management of the GaN electronics needs to consider all those factors of the given technologies and balance the importance of different technologies to obtain optimised performance for the GaN devices.

3. Numerical simulation

Numerical simulation was used as a major tool to understand the thermal behaviour of the device and the micro-jet impingement channel. It can provide some key parameters such as the maximum temperature in the fingers, the temperature distribution in the die, and the heat transfer coefficient of the working fluids, which are difficult to obtain directly through experimental measurements. Simulation, once validated, can also be used to predict and optimise the device and the channel.

In this work, modelling was done on the micro-jet impingement channel and the GaN transistors separately and their combination. Figure 3. 1 shows schematically the modelling domains, which can be divided into two parts: the solid domain and the fluid domain. The transistor sits on a SiC layer in the solid domain. Epoxy and/or sintered silver were used as die-attach material to combine the transistors with the diamond heat spreader. The fluid domain consists of mainly the micro-jet chamber. It also includes the inlet, two outlets and the jetting orifices.

The thickness of the die-attach was 25 μm and the diamond 250 μm . The dimension of the die and micro-jetting microfluidic channel was determined by the products fabricated and/or purchased. It should be mentioned that experiments with all different kind of HTFs were done in room temperature. However, in numerical simulation with HTF of EG+DW based fluids, the inlet temperature can be as low as -45 °C.

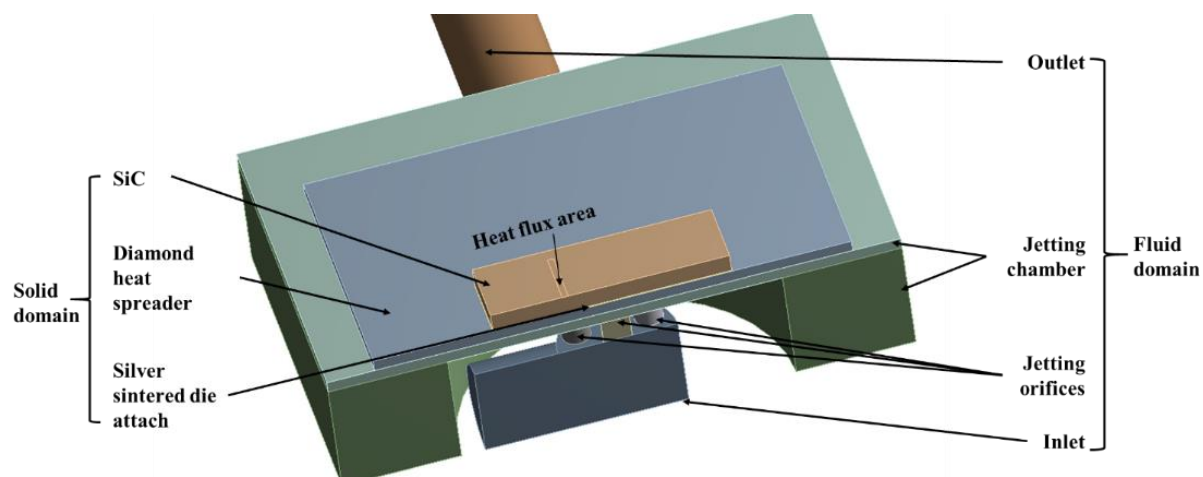


Figure 3. 1 Half image illustrating the modelling domain consisting of impingement jet channel and microchip

This chapter explains the models and how the modelling was done. The structure of this chapter is as follows:

- Section 3.1 describes the simulation of the fluid domain;
- Section 3.2 describes the simulation of the solid domain;
- Section 3.3 describes the combination of the fluid domain with the solid domain.

3.1. Simulation of the fluid domain

Numerical modelling has been used to study the cooling performance of the micro-jet impingement on microchips for decades. Such a method can be used to predict the heat transfer coefficient, temperature and pressure distributions in the micro-jet channel. Meanwhile, the numerical simulation can also be used to guide the design and optimisation of micro-jet impingement channels before the 3D printing of the required micro-jet channel.

The main difficulty in the numerical simulation for the micro-jet was the sharp gradient of velocity and resulted in complex flow due to the jetting. In this study, a CFD software, Ansys Fluent, was used to solve micro-jet flow and heat transfer in the microelectronics and the cooling channel. The geometry of the whole computational domain was drawn in Design Modeller with adjustable sizes for geometry optimization.

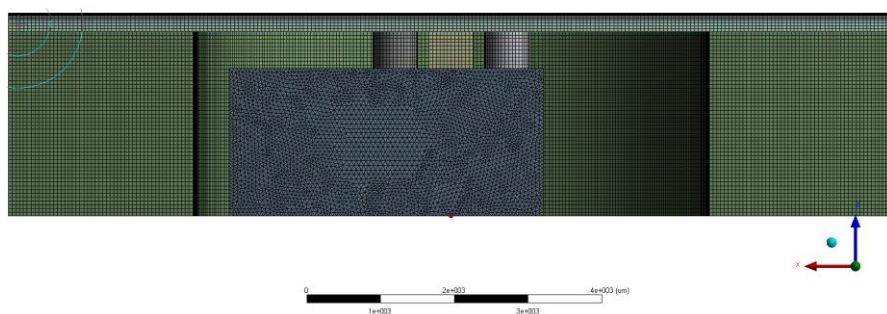


Figure 3. 2 Meshing of the fluid domain

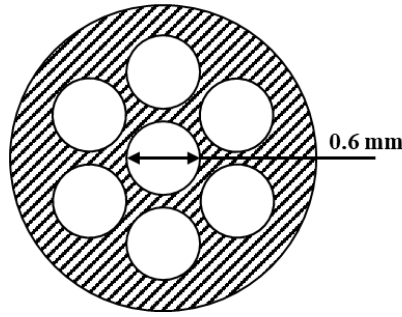


Figure 3. 3 Size of the micro-jet orifices

The meshing of the micro-jet impingement channel in the fluid domain as shown in Figure 3. 2. To increase the simulation efficiency and decrease the time consumption of the simulation, the so-called sweep method was used as the priory mesh method. Boundary layer theories were used for the impingement to capture the physical structure of the flow at the stagnation point and adjacent area.

The selected set of meshing has been validated by comparing with experimental results using de-ionised (DI) water, BN/DI water nanofluids, EG+DW and rGO/EG+DW nanofluids as heat transfers fluids. The simulation results were found to agree well with experiment results.

The micro-jet impingement channel with different jet orifices used in the experiment was illustrated in Figure 3. 3. The micro-jet orifice in an array with a diameter of 600 μm was designed and printed. The results showed that this can provide consistent thermal performance with an increased heat transfer area. The results also showed that fabrication via 3D printing had a limitation in terms of a minimum size of the diameter of the jet orifices, which can, in turn, affected the distribution and shape of the jet arrays.

3.1.1. Parameters of the micro-jet cooling channels

Several important dimensionless parameters were used in the analyses and processing the simulation and experimental results, including mainly the Reynolds number, the Prandtl number and the Nusselt number, as defined as follows:

Reynolds number The Reynolds number (Re) is defined as the ratio of inertial forces to the viscous forces:

$$Re = \frac{\rho v D}{\mu} \quad (3-1)$$

where:

- ρ is the fluid density;
- μ is fluid dynamic viscosity;
- v is the velocity at jetting;
- D is the jet diameter.

The state of the fluid flow, according to the different Re number, can be classified into:

- Dissipated laminar $Re < 300$
- Fully laminar $300 < Re < 1000$
- Transition $1000 < Re < 3000$
- Turbulence $Re > 3000$

Prandtl number Prandtl number (Pr) is defined as the ratio of momentum diffusivity to thermal diffusivity:

$$Pr = \frac{\mu C_p}{k} = \frac{v}{\alpha} \quad (3-2)$$

where:

- v is the fluid momentum diffusivity;
- α is the fluid thermal diffusivity;
- μ is the fluid dynamic viscosity;
- C_p is the fluid specific heat capacity;
- k is the fluid thermal conductivity.

Nusselt number Nusselt number (Nu) is defined as the ratio of convective to conductive heat transfer at the boundary layer:

$$Nu = \frac{hD}{k} \quad (3-3)$$

where:

- h is convective heat transfer coefficient;

When analysing the thermal performance of a designed micro-jet impingement microfluidic channel, Nu , Re number and Pr number can be correlated by:

$$Nu = C Re^m Pr^n \quad (3-4)$$

With the increase of the inlet velocity, better thermal performance with a higher heat transfer coefficient can be achieved. However, the pressure drop in the micro-jet impingement channel increases as well. Thus, it requires more pumping power and associated risk increase in the leakage. The trade-off between high thermal performance and high-pressure drop need to be balanced.

When it comes to the heat transfer fluids parts, the nanofluids, compared with the base fluids, have a higher viscosity and a higher thermal conductivity. Thus, with the same inlet velocity, the Re number decreases. However, the Pr number might increase or decrease depending on the nanofluids' properties. The selection for heat transfer fluids and/or their formulation should therefore be comprehensively considered, taking into account the thermal and viscous properties, as they have different contributions to the overall thermal performance of the microfluidic channels.

3.1.2. Governing equation for micro-jet impingement channel

There are mainly three govern equations for modelling micro-jet cooling channels. Those are mass conservation equation, momentum conservation equation and energy conservation equation. These equations, coupled with appropriate constitutive relationships, together with physical, geometrical, initial and boundary conditions, can be solved to obtain the flow and temperature fields. These data can then be used to obtain the convective heat transfer coefficient and pressure drop for engineering design applications.

- ***Mass conservation equation***

Mass conversation equation can be derived through mass balance over a volume element in a flow field and is given as:

$$\frac{\partial \rho}{\partial t} + \nabla \cdot (\rho \vec{v}) = S_m \quad (3-5) [223]$$

For steady-state problem without any mass sources, the mass balance equation:

$$\nabla \cdot (\rho \vec{v}) = 0 \quad (3-6)$$

Where ρ is the density of the fluid; t is the time; \vec{v} is the velocity of the fluid and S_m refers to the mass source.

- ***Momentum conservation equation***

Momentum conservation equation can be obtained by using Newton's second law of motion, again over a control volume, and is described as:

$$\frac{\partial}{\partial t}(\rho \vec{v}) + \nabla \cdot (\rho \vec{v} \vec{v}) = -\nabla p + \nabla \cdot (\bar{\tau}) + \rho \vec{g} + \vec{F} \quad (3-7) [223]$$

At a steady-state with no source, the equation reduces to:

$$\nabla \cdot (\rho \vec{v} \vec{v}) = -\nabla p + \nabla \cdot (\bar{\tau}) + \rho \vec{g} \quad (3-8)$$

$\bar{\tau}$ is the stress tensor which can be described as ;

$$\bar{\tau} = \mu[(\Delta \vec{v} + \nabla \vec{v}^T) - \frac{2}{3} \nabla \cdot \vec{v} I] \quad (3-9)$$

In the equation above, the second term on the right-hand side is the effect of volume dilation.

where p is the pressure; \vec{g} is the gravitational acceleration; and \vec{F} is the other types of force; μ is the molecular viscosity, I is the unit tensor.

- ***Energy conservation equation***

Consider energy balance over a volume element, one can derive the energy conservation, which takes the following form:

$$\frac{\partial}{\partial t}(\rho E) + \nabla \cdot (\vec{v}(\rho E + p)) = \nabla \cdot (k_{eff} \nabla T - \sum_j h_j \vec{j}_j + (\bar{\tau}_{eff} \cdot \vec{v})) + S_h \quad (3-10) [223]$$

In this equation, the terms on the right-hand side represent energy transfer due to conduction, species diffusion, viscous dissipation and heat source in the computation domain, respectively. In this study,

there is no species diffusion part and the effect of viscous dissipation in the simulation has not been considered during the simulation. The first term on the left of above energy equation disappears for steady-state operations; whereas the last term in the right-hand side should be zero as there is no heat source in fluid reign. Under the above conditions, the energy equation reduces to:

$$\nabla \cdot (\vec{v}(\rho E + p)) = \nabla \cdot (k_{eff} \nabla T) \quad (3-11)$$

In this equation, E is defined as:

$$E = h - \frac{p}{\rho} + \frac{v^2}{2} \quad (3-12)$$

and h, the sensible enthalpy for the incompressible flow is defined as

$$h = \int_{T_{ref}}^T C_{p,j} dT + \frac{p}{\rho} \quad (3-13)$$

In the simulation T_{ref} is set as 298.15 K.

where k_{eff} is the effective thermal conductivity, consisting of two parts, $k + k_t$, with k being thermal conductivity due to molecular scale diffusion and k_t for accounting due to turbulence-induced thermal conductivity defined according to the turbulence model being used; T is the temperature; S_h is the energy source.

- ***Turbulence model - The shear-stress transport (SST) κ - ω model***

For the flow with EG+DW based fluids, due to the high viscosity of the fluids, the experiment and simulation were in the laminar flow based on the Re number. However, the water-based fluids showed the transitional and/or turbulent flow with the same velocity. Thus, the turbulence model was used to simulate the given condition.

In the simulation, the SST κ - ω model of Menter [224] was used as the turbulence flow model to simulate the flow in the micro-jet channel. The SST κ - ω is suitable for the flows such as the micro-jet with a strong curvature. The advantages of the SST κ - ω model are low computational time, moderate ability

to predict the secondary peak. Due to those advantages, this type of turbulent model has been used in many pieces of research with numerical simulation [204], [208], [216].

According to the shear-stress transport model, the transport equations for the SST κ - ω model are displayed as:

$$\frac{\partial}{\partial \tau} (\rho k) + \nabla \cdot (\rho k \vec{v}) = \nabla \cdot (\Gamma_k \nabla k) + \widetilde{G}_k - Y_k + S_k \quad (3-14) [224]$$

$$\frac{\partial}{\partial \tau} (\rho \omega) + \nabla \cdot (\rho \omega \vec{v}) = \nabla \cdot (\Gamma_\omega \nabla \omega) + G_\omega - Y_\omega + D_\omega + S_\omega \quad (3-15) [224]$$

In these equations, \widetilde{G}_k represents the generation of turbulence kinetic energy due to mean velocity gradients. G_ω represents the generation of ω , Γ_k and Γ_ω represent the effective diffusivity of k and ω , respectively. Y_k and Y_ω represent the dissipation of k and ω due to turbulence. D_ω represents the cross-diffusion term, calculated as described below. S_k and S_ω are user-defined source terms. The detail of the model is attached in appendix A.

3.2. Simulation of solid domain

The modelling of the device includes the die with transistors, the die-attach material and the heat spreader layer. Since all those parts were made of solids materials, the governing equations differ from (and simpler than) the fluids part.

3.2.1. Govern equation of the die model

The energy conversation equation is the main govern equation;

$$E_{in} - E_{out} + E_{generation} = E_{stored} \quad (3-16)$$

Where $E_{in} - E_{out}$ represent the energy flow crossing the surfaces of the controlled system. $E_{generation}$ is defined as the energy generation rate. It represents the thermal energy conversion rate within the volume of the controlled system form any other type of energy such as chemical, electrical, electromagnetic, nuclear, etc. E_{stored} is defined as the thermal energy stored in the whole volume. The value can increase or decrease due to the transient process.

This equation can be written as:

$$\frac{\partial}{\partial x} k_x(T) \frac{\partial T}{\partial x} + \frac{\partial}{\partial y} k_y(T) \frac{\partial T}{\partial y} + \frac{\partial}{\partial z} k_z(T) \frac{\partial T}{\partial z} + E_{generation} = \rho C_p \frac{\partial T}{\partial \tau} \quad (3-17)$$

In the steady-state thermal software, the thermal conductivity can be anisotropic and dependent on the temperature. Thus, the thermal conductivity of the material is expressed as $k_x(T)$, $k_y(T)$ and $k_z(T)$.

There are three types of boundary condition for the numerical simulation. Those boundary conditions can be combined to obtain the thermal performance in the device.

- (1) Constant surface temperature

The boundary condition can be defined as the fixing temperature.

$$T_{wall} = T_c \quad (3-18)$$

- (2) Constant surface heat flux

The power applied in the transistors can be regarded as the heat flux condition. The area represents the fingers can be defined as the heat flux.

$$-kV\!T = -q \quad (3-19)$$

- (3) Convection surface condition

$$q = h_{tc}(T - T_{\infty}) \quad (3-20)$$

Where h_{tc} is the heat transfer coefficient at the boundary surface. T_{∞} is the temperature form the far end of fluid. In the simulation, the value of the heat transfer coefficient and T_{∞} for the given surface can be assigned with data required.

3.2.2. Simplified and detail device model for the simulation

The GaN-on-SiC and/or GaN-on-Diamond transistors combined with heat spreader via die attach/epoxy is shown in Figure 3. 4. The gate, drain and source part is mounted on the GaN layer. The GaN layer grows on the SiC or diamond to spread the high heat flux. The die-attach and heat spreader is used for the combination of the die with the microfluidic channels.

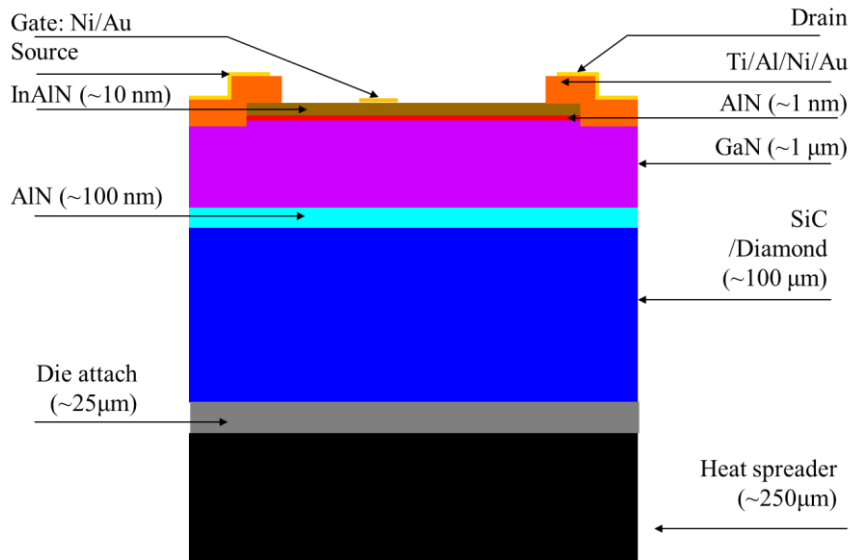


Figure 3. 4 Detailed structure of microchips

In many pieces of research, a quarter and/or half of the die model was used in the simulations due to the symmetric condition in the experiment and/or simulation. However, as the die might not be in the symmetric condition (such as the location of the die, the heat transfer coefficient etc. might not be symmetric in the real application situation) with the microfluidic channels as its cooling part, the whole model was also simulated in that case. Two types of die model, simplified die model and detailed die model were made for the die model. All those models were simulated in Ansys workbench with The Steady-state thermal software.

- ***Simplified die model***

As is illustrated in Figure 3. 5, the detailed stricture of transistors is not given in the simplified die model. Only the subtract layer such as the SiC layer and/or diamond layer with several hundred micrometres was constructed in the simulation model. Uniform heat flux within a confined area was the assumption of the heat flux distribution in the simplified model. There are serval advantages for this model. Firstly, it is easy to generate the geometry in the software for the simulation; secondly, it is also easy to generate the suitable mesh for the whole die because of the model with a size comparable to the micro-jet impingement channel; thirdly, the model can be directly combined with the microfluidic channel or simulated separately for the numerical simulation with short time consumption. However, there is one big disadvantage to this model. It cannot be used to simulate the temperature in the transistor

layer, as this layer is not given in the model. Thus, the maximum temperature in the die cannot be accurately obtained in the simplified model.

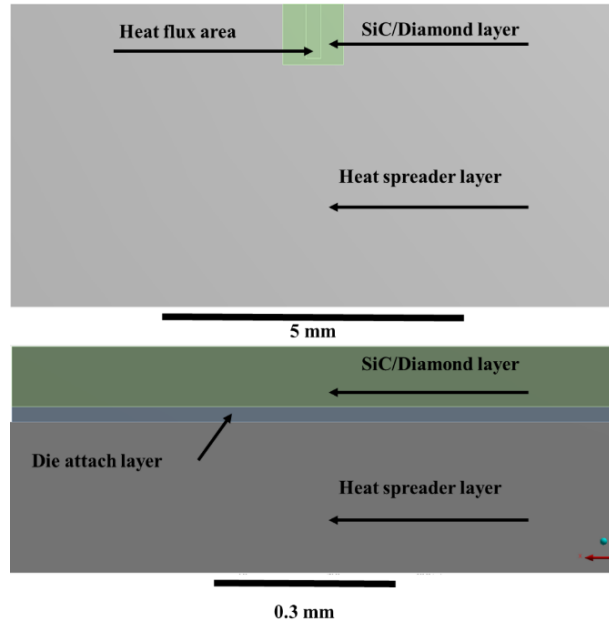


Figure 3.5 Structure of the die in the simplified model

There are several reasons for the application of this kind of model. Firstly, the study for the micro-jet mainly focused on the heat transfer in the impingement surface (the bottom surface of the diamond heat spreader); secondly, the heat flux at the bottom surface of the diamond heat spreader was widely spread due to the two heat spreaders in the devices; thirdly, it seemed to be difficult to use IR camera to measure the temperature on the top surface of the GaN layer, as the appearance of the GaN is transparent. fourthly, the IR camera used in the test rig had a resolution no smaller than 42 μm . It was difficult to directly obtain an accurate temperature in the finger area; lastly, the efficient of simulation increased without the mesh for the small structure in the GaN layer.

Due to the physical properties, half symmetry was used for computational efficiency. The heat flux area used in the simulation was 0.125×2.447 mm. the mesh size for heat flux was 6 μm . The input value of heat flux is defined as:

$$q = \frac{Q_{dis}}{A_{hf}} \quad (3-21)$$

Where Q_{dis} is the heat dissipated by HTF and A_{hf} is the area of heat flux.

The unstructured grid was applied on the SiC. The structured grid was used on the epoxy/die attach layer and diamond layer to increase the computational efficiency. The adiabatic condition was automatically applied on the entire surface undefined.

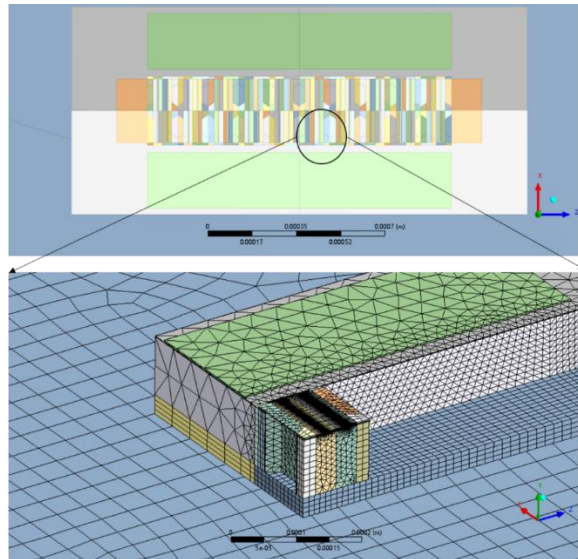


Figure 3.6 Detailed die model with its mesh in Ansys

- ***Die layer with detail structure***

As is illustrated in Figure 3.6, the structures such as the gates, sources, drains, AlN nuclear layer etc. were given in the detailed die model. For the mesh generated, there were 975268 nodes and 1146256 elements. Although compared to the simplified model, there are many disadvantages such as the long computational time; the complex structure for the model etc., the most important advantage for this model is that it can obtain the temperature distribution in the fingers. In some tests, such as the test-rig with the micro Raman thermography which has a high resolution (several hundred nanometres), the results can be used to validate this type of experiment.

- ***Epoxy/die attach layer***

To assemble the microchip with the micro-jet channel, the die was mounted on the heat spreader layer with epoxy or die-attach. To decrease the thermal resistance in this layer, high thermal conductivity material was used.

- ***Heat spreader layer***

The diamond layer was used for two purposes. (1) Due to the high thermal conductivity of diamond, this layer acted as a heat spreader. (2) The size of the diamond layer matched with the micro-jet channel for the thermal packaging.

3.3. Combination of fluid domain with solid domain

The design of the finger arrangement, the contact thermal resistance between the SiC/Diamond layer, the thickness of the GaN and SiC/diamond layer, the selection of the die attach material, the size of the microchip etc. suggest the simulation with detailed die model need to be flexible for the optimisation of parameters. In this project, different dies are involved (such as TriQuint TGF2022-06 and Cree Inc CGHV60040D). Some of those dies can be purchased from the market, while others are in the developing stage. It is time-consuming and waste of resources to directly combine the micro-jet channel with all those purposed dies especially for the detailed die model.

The simplified die combined with the jetting channel can be used for the validation the thermal performance of the micro-jet channel and the diamond heat spreader with IR camera. However, when it comes to the maximum temperature on the transistors, this type of model can not be used as it evens the heat flux and does not consider the thermal resistance between the GaN layer and SiC/diamond layer. Those can strongly underestimate the maximum temperature in the GaN transistor. To measure the maximum temperature in the die, the Raman thermography was used with the resolution of about $0.5 \mu\text{m}$. This means the mesh used for the die model should be on the same scale to capture the temperature in the simulation. Thus, the detailed die model needs to be combined with the micro-jet channel.

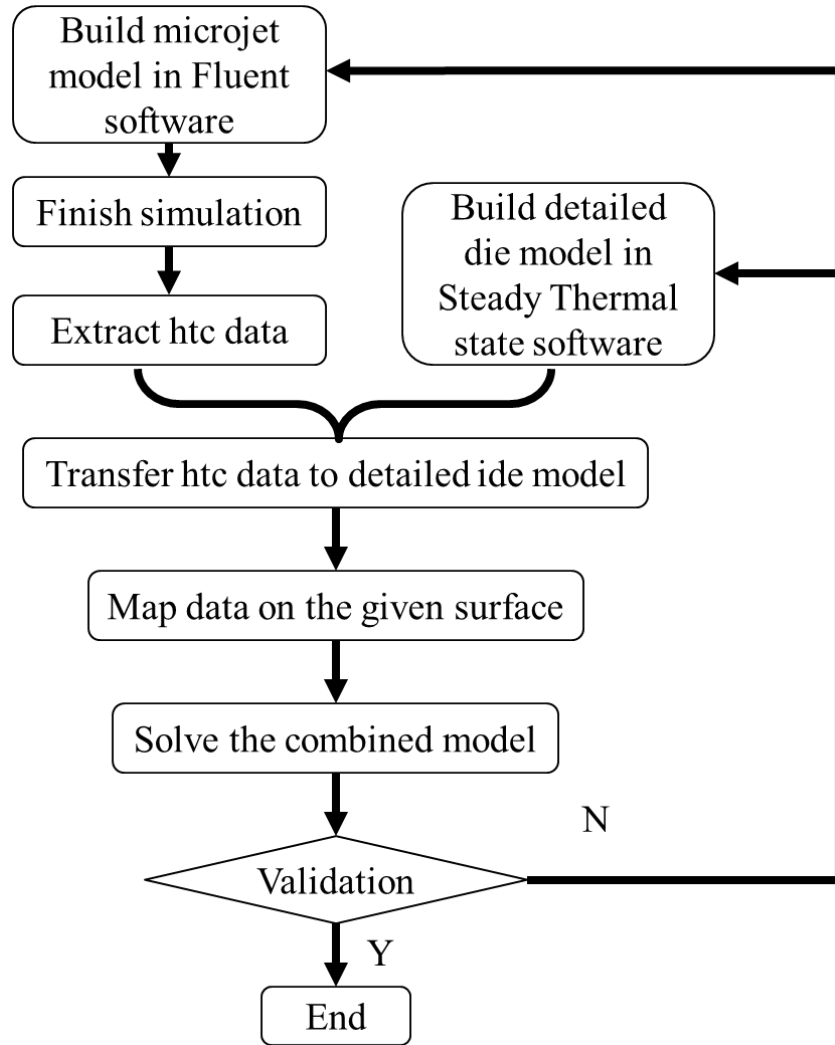


Figure 3. 7 Flow chart of simulation models combination

A solution for the combination of the micro-jet cooling channel and the detailed die model was purposed.

The flow chart for the method is illustrated in Figure 3. 7. The micro-jet model and detailed die model all share with the same heat spreader layer with a size of $10 \times 10 \times 0.25$ mm.

Firstly, the micro-jet model and detailed die model were built. Then, the micro-jet model was simulated with Ansys Fluent with htc data extracted after finishing the simulation. Then, the htc data was transferred to the detailed die and it is mapped to the bottom surface of the heat spreader. Then, this simulation was solved in the Ansys steady-state thermal. The solved results were compared with the experiment results for the validation. If the results agreed well with the simulation, the simulation can be used to predict the performance of the die. If it did not agree with the simulation results, it went back to the model parts for the change.

3.4. Summary

This chapter explains the mathematical models used for the numerical simulation of both the micro-jet impingement channels (the fluid part) and the device (the solid part). Governing equations are given for both parts, together with constitutional relationships, and geometrical, physical, initial and boundary conditions. The meshing of the domains is described.

- For the fluid domain, The Ansys Fluent was used to solve these equations to obtain the pressure distribution, temperature distribution and the distribution of heat transfer coefficient in the fluid domain.
- For the solid domain, The Ansys thermal-steady state was used to simulate the performance of the microchip for validation and prediction. The detailed and simplified die model has been generated and used for solving the temperature distribution in the device part.
- An indirect combination of the solid part with fluid part has been purposed and used to increase the simulation efficiency and the flexibility of the model.

4. Experimental apparatuses and uncertainty

This chapter introduces and explains experimental set-up, the thermal packages for the microchips, the uncertainty analysis and the pieces of equipment used in the experiment. It is structured in the following manner:

- Section 4.1 discusses the experimental test rigs for thermal management (TM) of GaN-based microchips;
- Section 4.2 discusses the combination of the microchip with the microfluidic channels
- Section 4.3 discusses the uncertainty of the experiments
- Section 4.4 discusses the equipment used in experiments

4.1. Experimental apparatuses for thermal management of microchip

The experimental testing rigs for the TM of microchips depend on several factors including microfluidic channels (e.g. micro-jet impingement channels and copper foam-based microfluidic channels etc.); fabrication methods of microfluidic channels (e.g. 3D printed, traditional cutting methods etc.); temperature measurement methods (e.g. thermal couples, infrared camera, and micro-Raman thermography etc.); measured parameters (e.g. pressure, temperature, flow rate etc.). These require different arrangements and combination of the equipment.

4.1.1. Test-rigs for thermal management of microchip

- **Temperature measurement with Infrared camera**

This kind of system is shown in Figure 4. 1, which is made of a temperature measuring unit (with IR camera and thermocouples), a heat transfer fluid (HTF) circulating unit (with flowmeter, reservoir, chiller and pump), a heating unit (providing by microchips with adjustable power input), and a data acquisition unit (with data logger and software installed in computer). This configuration allowed the measurements and monitoring all major parameters needed to assess the thermal performance of the microfluidic channels.

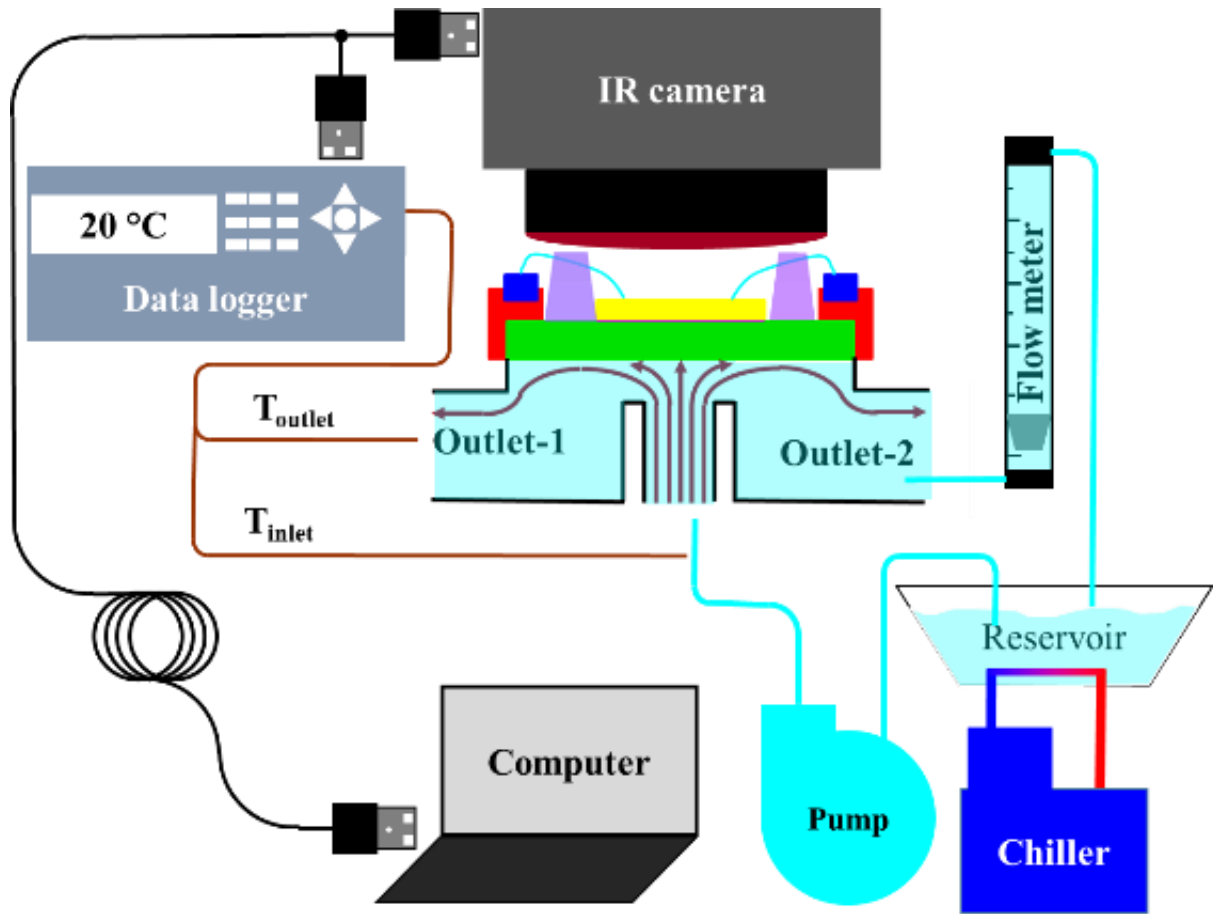


Figure 4. 1 Schematic diagram of TM of the microchip with IR camera

For the temperature measuring unit, both inlet and outlet of the HTF circulating unit were inserted with a thermocouple to record the temperature at pre-set positions. To keep the integral microchip during the test, contactless temperature measurement with IR camera was applied to record the temperature distribution on the die and diamond surface.

For the heat transfer fluids circulating unit, a gear pump provided the driving force for the flow of a heat transfer fluid from and return to the reservoir. After the heat transfer fluid impinged on the diamond heat spreader, the heat was transferred to heat transfer fluid, leading to temperature increase. Then, the fluid flowed through the flowmeter where the flowrate was measured before it finally returned to the reservoir integrated with a chiller to exchange the heat absorbed by the heat transfer fluid. To decrease the heat loss in the transportation, all the 2 mm inner diameter tube used for the connection was made of silicon with low thermal conductivity. The whole channel was fabricated by 3D printing method with photopolymer, which also acted as an insulation layer preventing heat loss.

For the heating unit, adjustable power output was applied to the microchips, which was provided by a DC power supplier. The die was mounted on a thin (250 µm thickness) diamond heat spreader by a highly thermally conductive material such as epoxy and/or silver-sintered die-attach.

For the data acquisition unit, an Agilent 34970A unit interfaced to the thermocouples was used for temperature data logging; an IRBIS 3 plus software was used to record and process the temperature data from the surface of the diamond heat spreader measured by the IR camera. The measurement data have enabled the validation of the simulation results with the simplified device model.

- **Temperature measurement with Micro-Raman thermography**

To obtain an accurate set of temperature data from the GaN electronics, Micro-Raman thermography was used to measure the temperature in the finger with a spot size of 0.5 µm as is shown in Figure 4. 2. The whole test rig is similar to the IR thermography. In this measurement, the pump, the data logger, the micro jetting channel, and the flow meter were all the same as for the IR thermography measurements (Section 4.1.1). The main difference was that the Micro-Raman thermography replaced the IR camera due to its much higher spatial resolution. This set-up can measure the peak temperature on the top of the GaN layer. The measurement was used to validate the simulation with a detailed device model. It should be pointed out that thermocouples were also attached on the surface of the diamond heat spreader to measure its surface temperature for cross-validation.

For the Raman thermography measurement, the transistor CGHV60040D was used, which was purchased from Cree Inc (USA). The dimension of the measured GaN-on-SiC device is illustrated in Figure 4. 3. The device consisted of 1.5 µm thickness GaN layer, 100 µm thickness SiC substrate and a thin AlN layer to accommodate the lattice mismatch during the GaN-on-SiC growth. The transistor was attached to the 250 µm diamond heat spreader with 25 µm silver sintered die-attach material with high thermal conductivity of 140 W/(m·K). The AlGaN/GaN HFET devices with 20×250 µm fingers were investigated. The total die size was around 820×1800 µm. The GaN-on-SiC device was not in the centre of the diamond heat spreader due to a spare die was attached on the same surface.

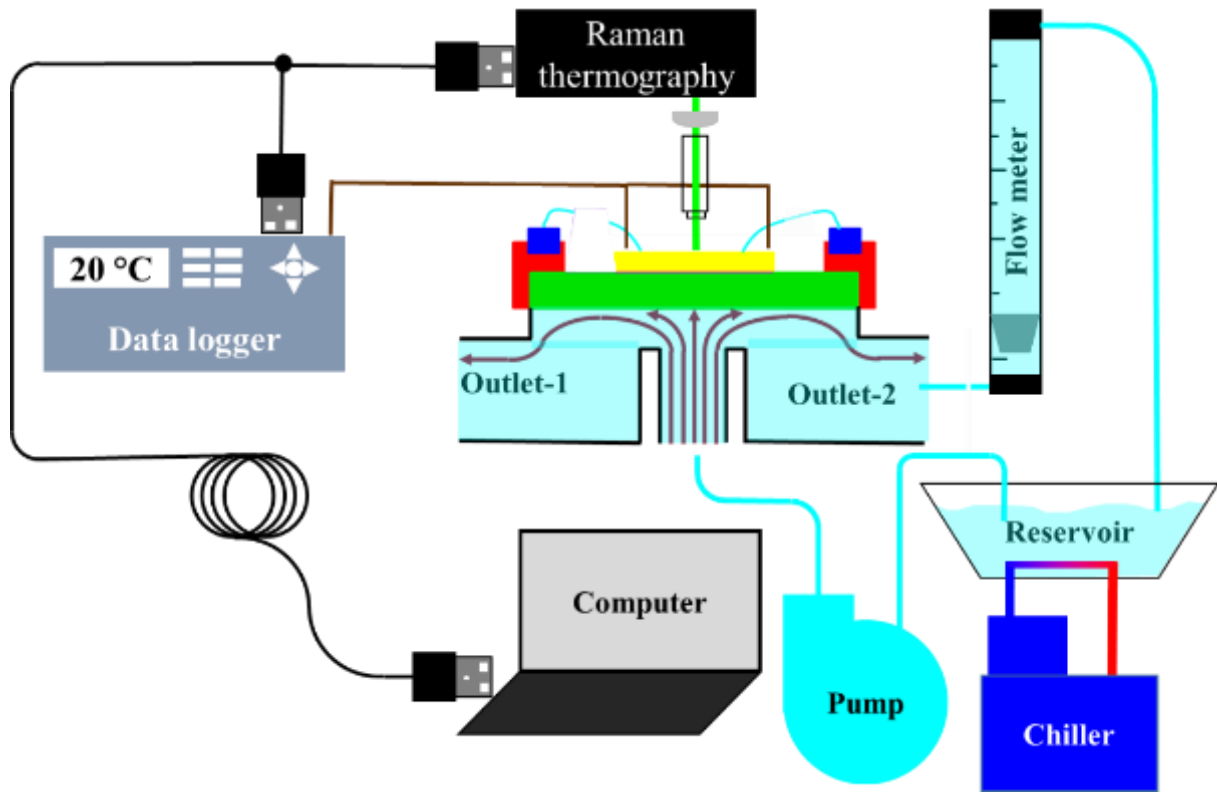


Figure 4. 2 GaN electronics temperature measurement with Raman thermography

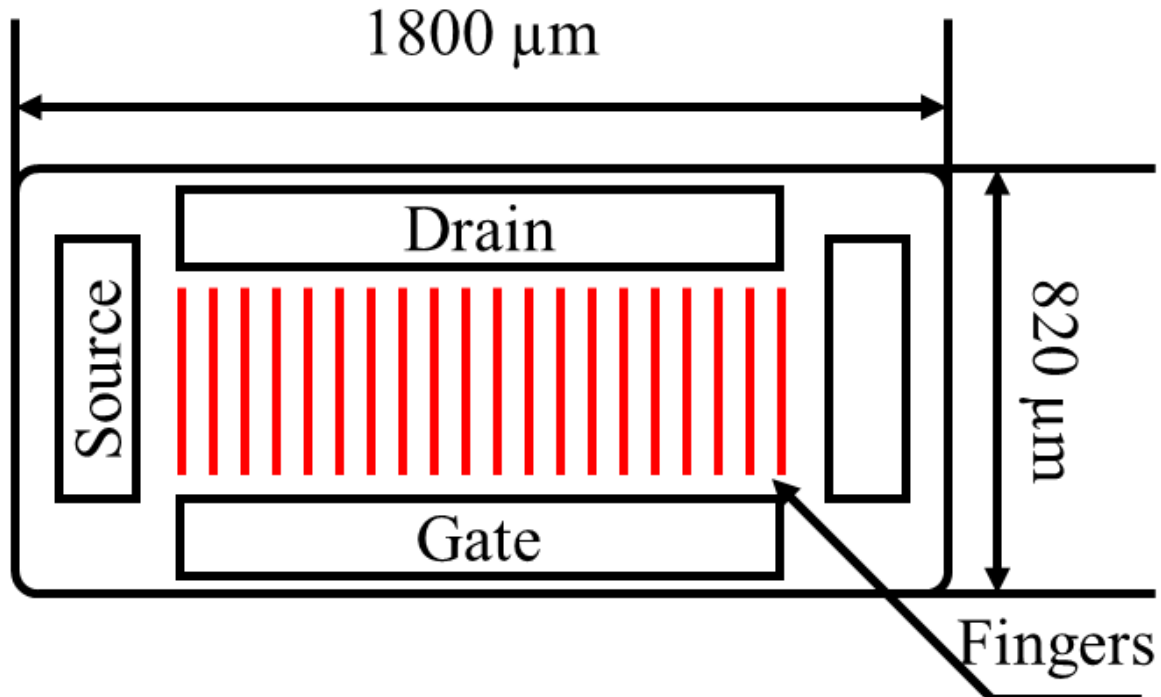


Figure 4. 3 Dimension of the CGHV60040D GaN-on-SiC transistor

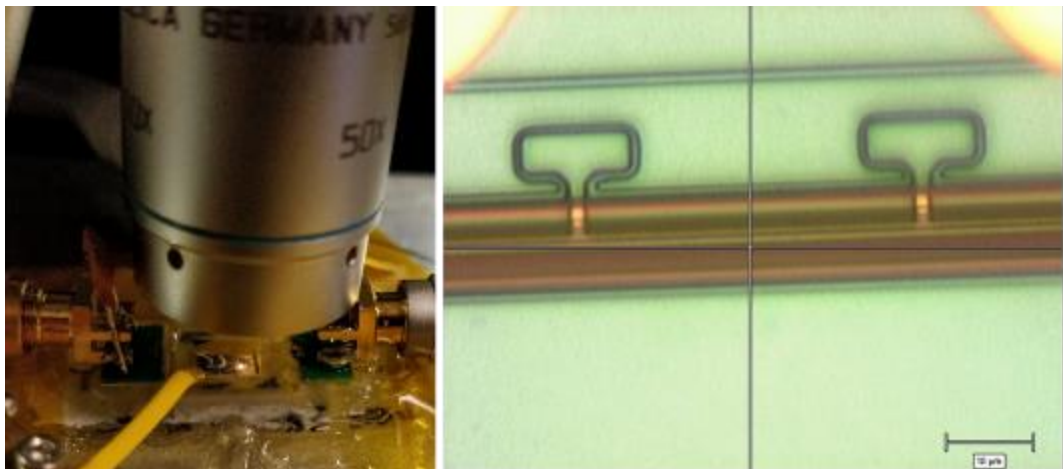


Figure 4. 4 Test rig with Raman thermography and the location for the measured point in the centre of fingers

A Renishaw inVia spectrometer with 488 nm A⁺ laser and 50×0.6 numerical aperture objective lens was used for the Raman thermography measurements. The lateral spatial resolution for the measurement was 0.5 μm. To obtain the highest temperature accuracy, the temperatures in the GaN layer were detected using A₁(LO) phonon peak shift due to its relative insensitiveness to the stress. It should be pointed out that the measured temperature in the GaN layer was a volumetric average value through the 1.5 μm GaN layer. As depicted in Figure 4. 17, the device was mounted on the micro jetting channel that was combined with a vacuum chuck. The device and chuck position was controlled by a motorized XYZ translation stage with a resolution of 0.1 μm step size. For the micro jetting channel, a micropump was used to supply a flow rate of 0.1 L/min. The heat transfer fluid during the measurement was distilled water. A chiller was used to maintain the water in the reservoir at 20 °C.

- **Temperature measurement with copper-foam based microfluidic channels**

Figure 4. 5 shows a schematic diagram of the testing rig for TM of the microchip with copper-foam based microfluidic channels. The test rig consisted of a temperature measuring unit (with 3 thermocouples at the inlet, outlet and the bottom surface of the diamond heat spreader), a heat transfer fluid circulating unit, a heating unit, and a data acquisition unit, for investigating and characterising the thermal performance of copper-foam based microfluidic channels.

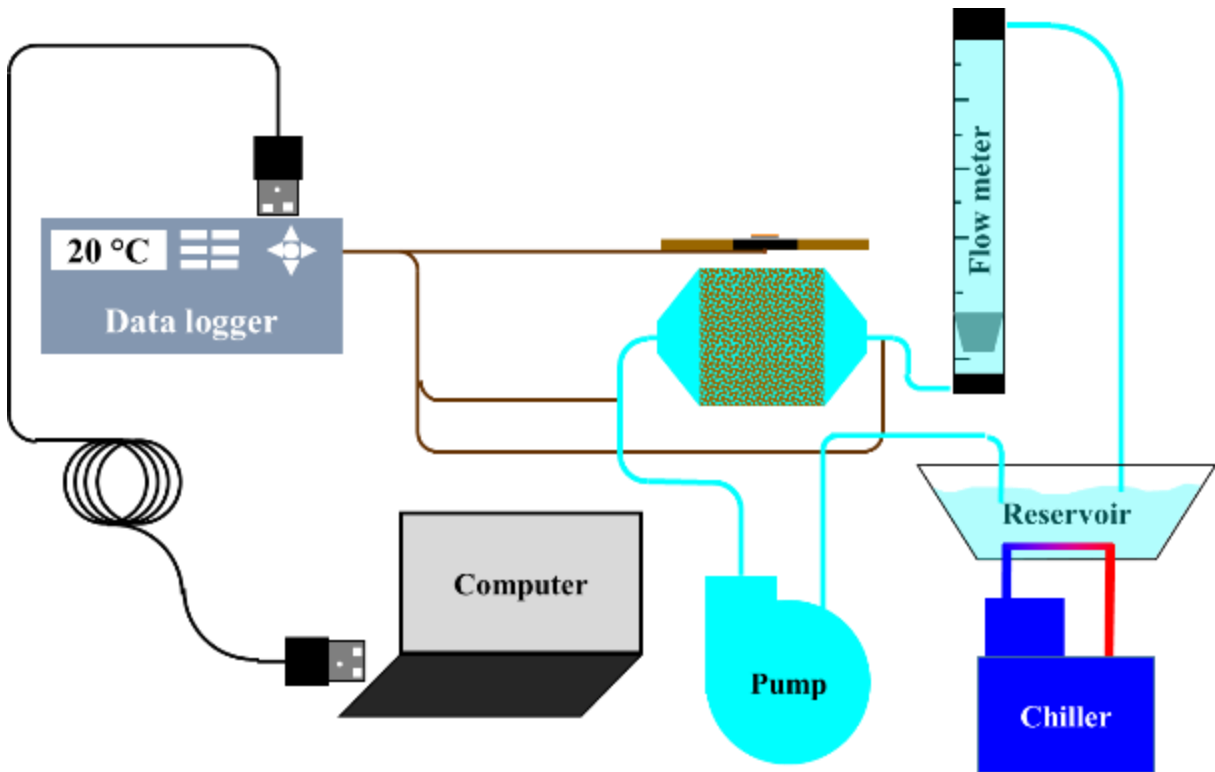


Figure 4. 5 Schematic diagram of TM of the microchip with copper-foam based microfluidic channel

For the temperature measuring unit, there were thermocouples at both inlet and outlet of the HTF circulating unit. In order to collect the temperature data on the bottom surface of the cooper-foam based microfluidic channel, a thermocouple was attached in the centre of the surface.

The heat transfer fluid circulating unit and the heating unit were similar to the testing rig for micro-jet impingement channels.

4.1.2. Pressure drop measurements for microfluidic channels

To prevent the possibility of damaging the microchip during pressure measurements, a testing rig for pressure drop measurement was built with no microchip on the lid, as shown in Figure 4. 6. The whole test rig consisted of 3 main units: a pressure drop measuring unit (with pressure transducer), a heat transfer fluid circulating unit (with flowmeter, reservoir, chiller and pump), and a data acquisition unit. The test rig was employed to investigate and characterise the performance of the microfluidic channel.

For the pressure drop measuring unit, an open hole (0.15 mm diameter) was drilled at both inlet and outlet of the channel. Those open holes were connected with a differential pressure manometer for the

pressure drop measurement. In this study, all the other pressure drop losses were neglected and assumed little influence on the pressure drop measurements.

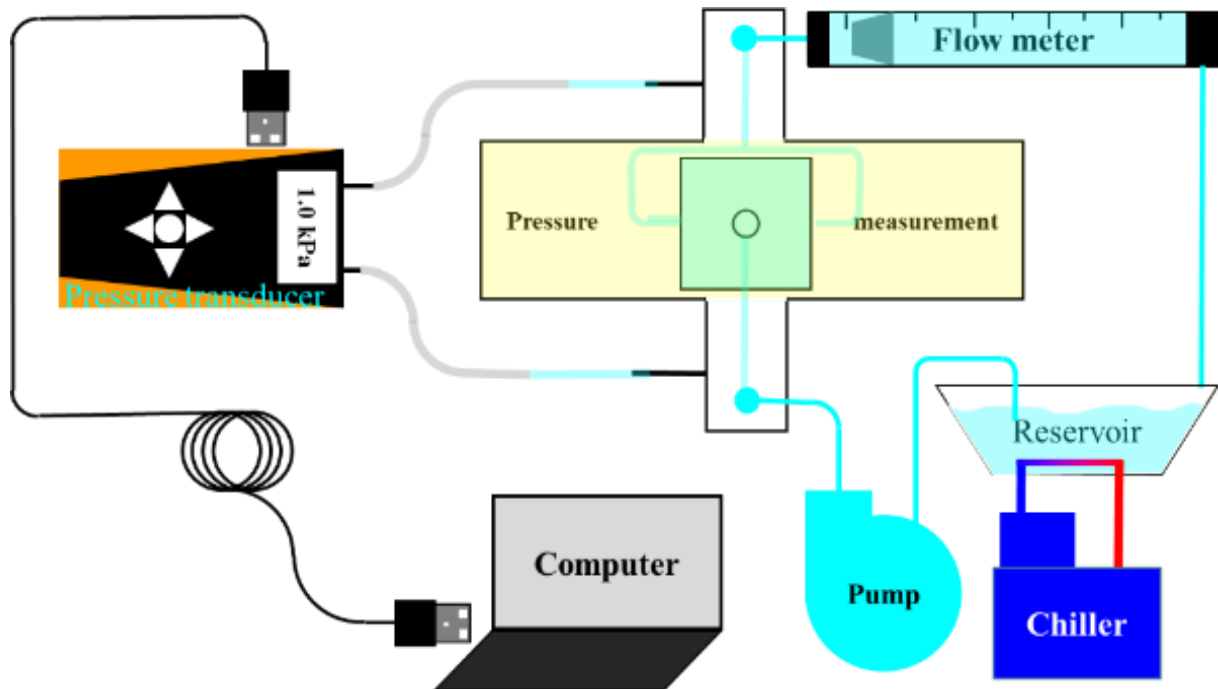


Figure 4. 6 Schematic of the experimental apparatus for jet arrays used for pressure drop

4.2. Integration of microchip with microfluidic channels

Two types of the microfluidic channels were successfully packaged with the microchips: the packaging of the microchip with the micro-jet channel; and the packaging of the microchip with copper-foam based channel.

4.2.1. Thermal package - micro-jet channel

The integration of the microchip with the micro-jet channel was the most important part of the whole project. Firstly, the application of the micro-jet channel depended on the successful combination of the microfluidic channel with the microchip. Secondly, the method for the combination affected the thermal performance of the die. For example, using different die-attach materials such as the epoxy, solder, silver sintered etc. had different thermal resistances in the die-attach layer. Thirdly, the performance of the micro-jet channel and die was measured experimentally via the integration system. Finally, yet

importantly, the combined system was used as the original geometry of the numerical simulation before the validation step.

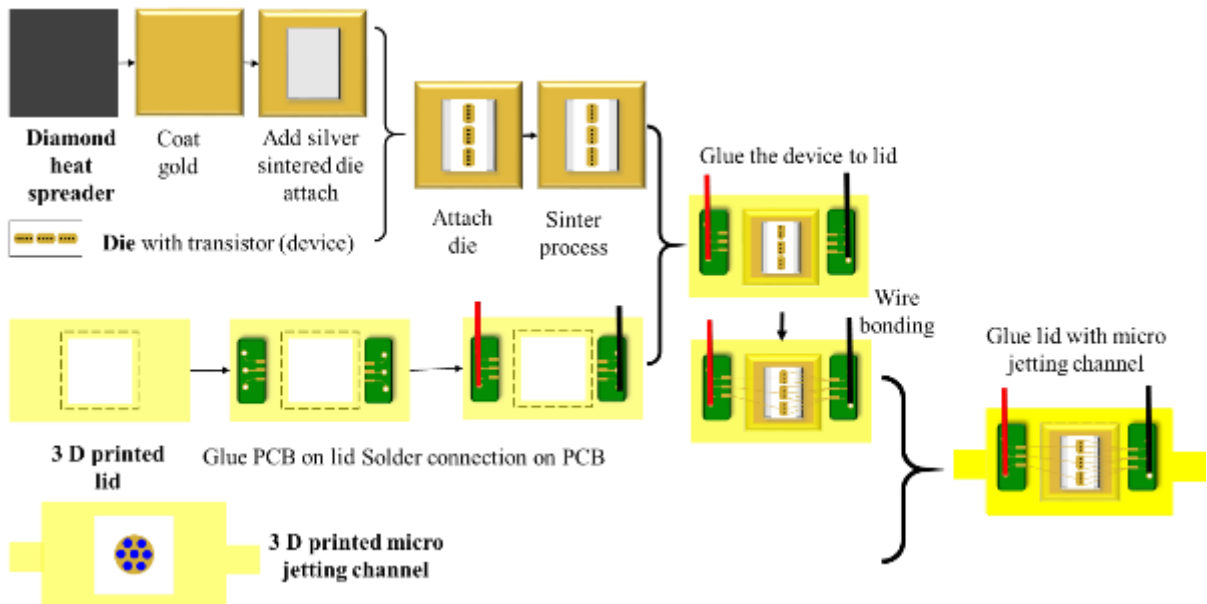


Figure 4. 7 Flow chart of test rig fabrication

The flow chart of the test rig fabrication, as is shown in Figure 4. 7, illustrates the main processes for the combination of the die with the microfluidic channel. Firstly, the die was combined with the gold-coated die with the die-attach material meanwhile the 3D printed lid was fabricated and with PCB inserted and cable soldered. Then, the device was combined with the lid as the top part of the micro-jet impingement channel. After the wire bonding for the microchips with the PCBs, the final step for the combination of the lid and the 3D printed micro-jet channel need to be properly processed to prevent the leaking. It can be used as a guild line of the liquid cooling for the microchips. The 3D printing technology was used to design the microfluidic channel and the lid, due to its advantages such as easy fabricating and the integration of the product. The package of the die with low thermal resistance was achieved to increase the thermal performance of the die.

- ***The combination of the diamond heat spreader and die***

Some of the designs [190] had more than one layer before it combined with the cooling channel. In this study, to decrease the thermal resistance, the heat spreader made of diamond, copper or other material with high thermal conductivity was directly cooling with the micro-jet channel.



Figure 4. 8 Combination of the diamond heat spreader with GaN

As is illustrated in Figure 4. 8, the top surface of the diamond heat spreader and the bottom surface of the die were coated with Au. The main material used for the combination of the die with the diamond heat spreader was the die-attach material. In this project, as the die need to dissipate the heat flux of 5 W/mm in the fingers, the silver sintered paste was chosen as interface thermal material. The sintering process is shown in Figure 4. 9. The combined material of the silver paste and the device was put into the chamber with a temperature increase from 30 °C to 160 °C in the first 60 min. Then the temperature was stable at 160 °C for 45 min before the 40 °C increase in the following 15 min. After the temperature reached 200 °C, the temperature was not changed for the next 60 min and then decreased to 30 °C in half an hour.

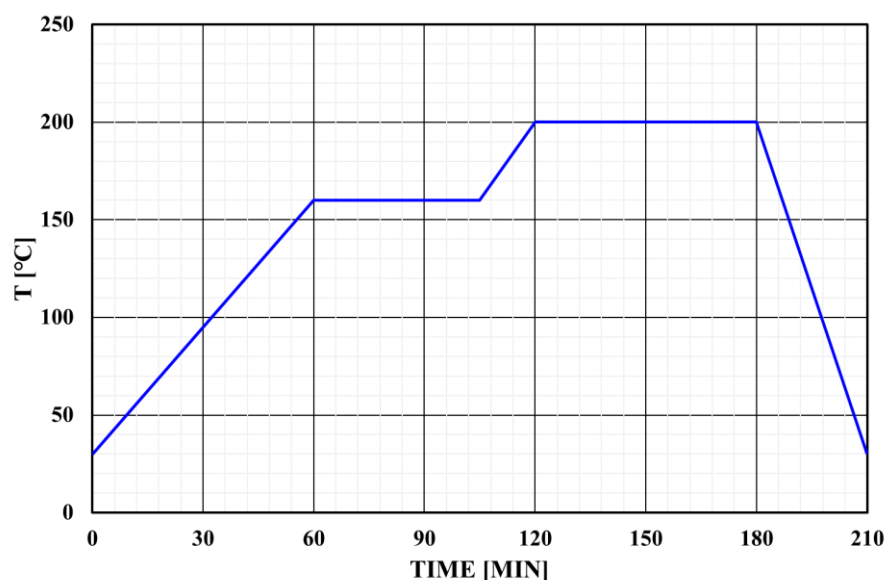


Figure 4. 9 Curve for the sintering process

- ***The combination of the lid with the die***

The main of the micro-jet channel was made of 3D print material. To combine the channel with the lid, the lid was also fabricated via the 3D print process as is shown in Figure 4. 10. The designed hole in the centre was for the diamond heat spreader. The other two areas with recession were used for the PCB. After the PCBs inserted in, the cables were soldered on the PCBs. With PCB inserted in and cabled soldered, the die with diamond heat spreader was glue on the lid, as is shown in Figure 4. 11.

In order to apply power on the die, it should be connected to the PCBs. The wire bonding process was for that aim. As is illustrated in Figure 4. 12, the wire-bonding machine can bond the Au wire or Ag wire to the microchips. In this project, the gold wire with a diameter of 25 μm was used in order to have the maximum current of 0.5 A on each wire. Part of the devices with a gold wire during the bonding was shown in Figure 4. 13.

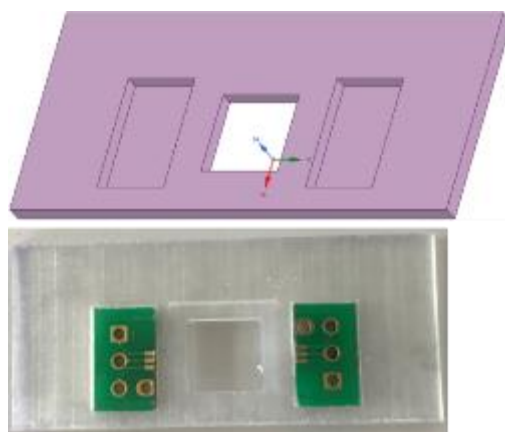


Figure 4. 10 (Top) design of the 3D print lid and (bottom) the 3D printed lid with PCB



Figure 4. 11 Lid combined with the device



Figure 4. 12 Wire bonding machine

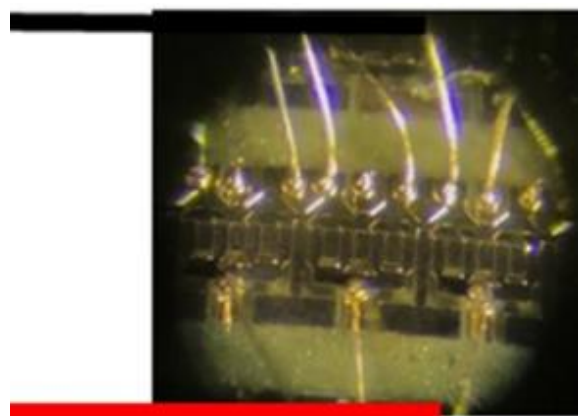


Figure 4. 13 Die with gold wire bonding

- ***The combination of the micro-jet channel with the lid***

The 3D print channel is shown in Figure 4. 14. For the combination with the lid, both lid and microchannel were made of the same photo-polymeric material which can stand for the temperature around 250°C. Those two part can be glued together with the same resin for 3D print to prevent the leakage due to the combination with the different material.

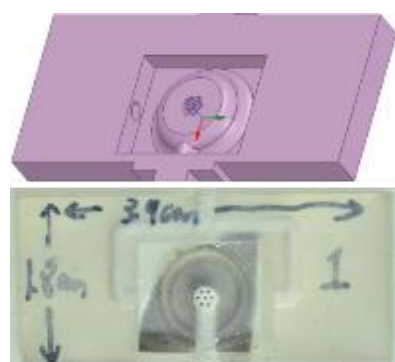


Figure 4. 14 (Top) design of 3D print micro jet channel and (bottom) the 3D printed channel

4.2.2. Thermal package - copper-foam based channel

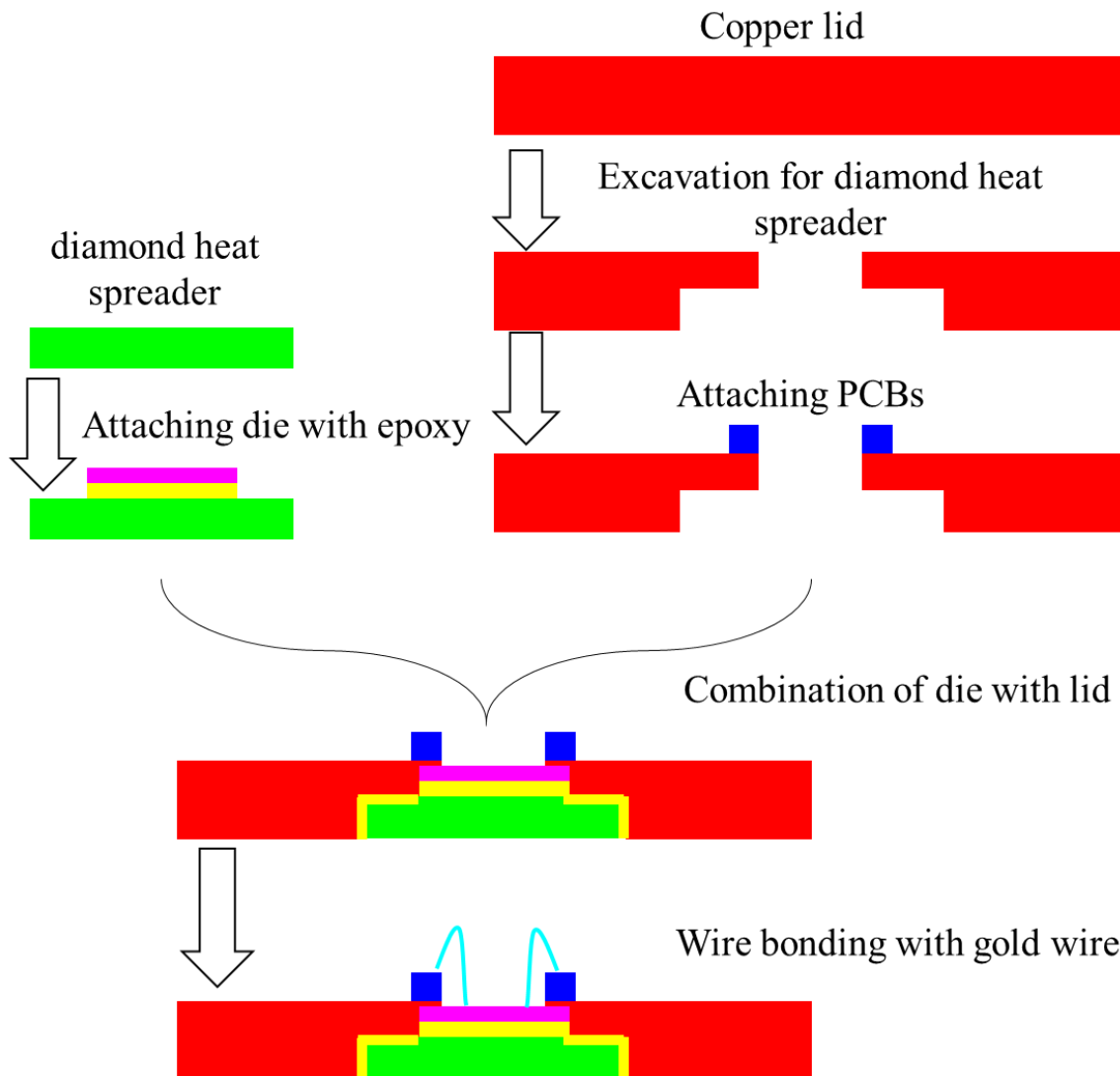


Figure 4. 15 Flow chart of the combination of the die with the copper lid for copper-foam based channel

The flow chart for the combination of the copper lid with the die as illustrated in Figure 4. 15. The process first began with a lid excavating a square hole with a size of $7 \times 7 \times 0.25$ mm. Then, the printed circuit boards (PCBs) which were used as electrodes were glued to the lid with epoxy. The epoxy has a low thermal conductivity around $1.4 \text{ W}/(\text{m}\cdot\text{K})$. Meanwhile, the diamond heat spreader with a dimension of $10 \times 10 \times 0.25$ mm was attached to the die with the epoxy as the die-attach material. After this process, the combined item was then placed on the hot plate with a temperature of 110°C with 30 min for the curing of the epoxy. Then, the die with the diamond heat spreader was attached to the excavated hole using the same epoxy. The same method of 30 min curing was applied. After the curing, the wire-

bonding process with gold wire was applied to make the electrical connection for die and PCBs. The diameter of the gold wire is 25 μm with a limitation of 0.5 A current. Five separate gold wires were bonded to the die. So, the device cannot be applied with the current larger than 2.5 A. Finally, the lid with die and the copper-foam based microfluidic channel was combined. The die (TriQuint TGF2022-06) was used in the experiment for the characterisation of the copper-foam based microfluidic channel. The die was attached on the copper lid, as is shown in Figure 4. 16.

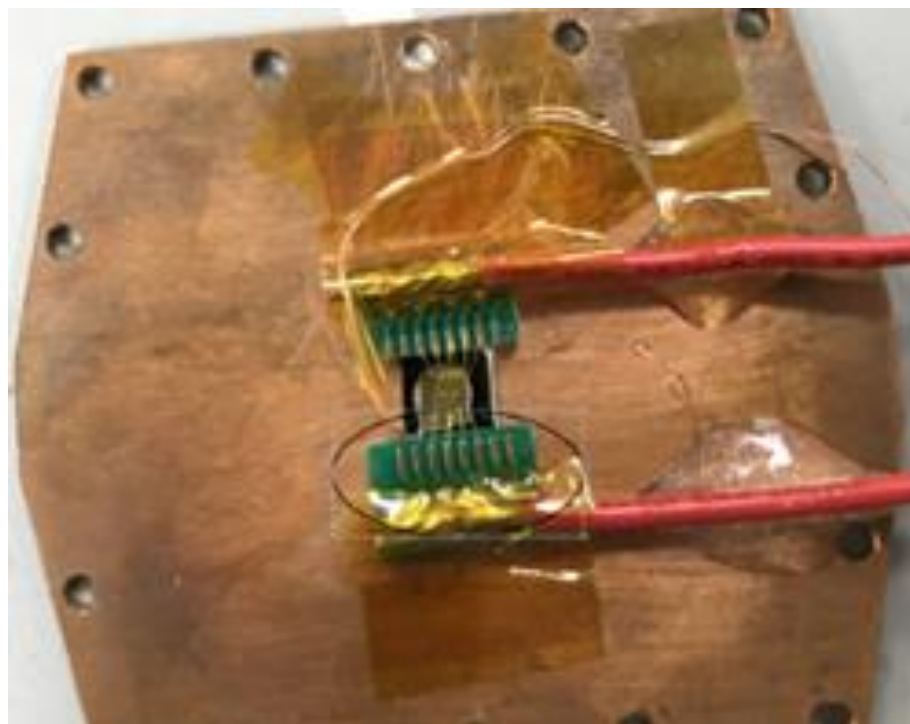


Figure 4. 16 Copper lid with die inserted in

4.3. Equipment used in experiments

The characterisation of the materials is investigated with different techniques to obtain the different properties of the material. This includes the thermal conductivity, the viscosity, and the stability in fluid media. The temperature measurement equipment with IR camera and the Raman thermography and the 3D printer is also investigated.

4.3.1. Thermal conductivity

The thermal conductivity of the base fluids and nanofluids were measured by the stationary heat-wire method (LAMBDA-system PSL Systemtechnik GmbH, German). The Fourier law of the heat conduction is the fundamental principle for this measurement. The theory for the system is attached in appendix B.

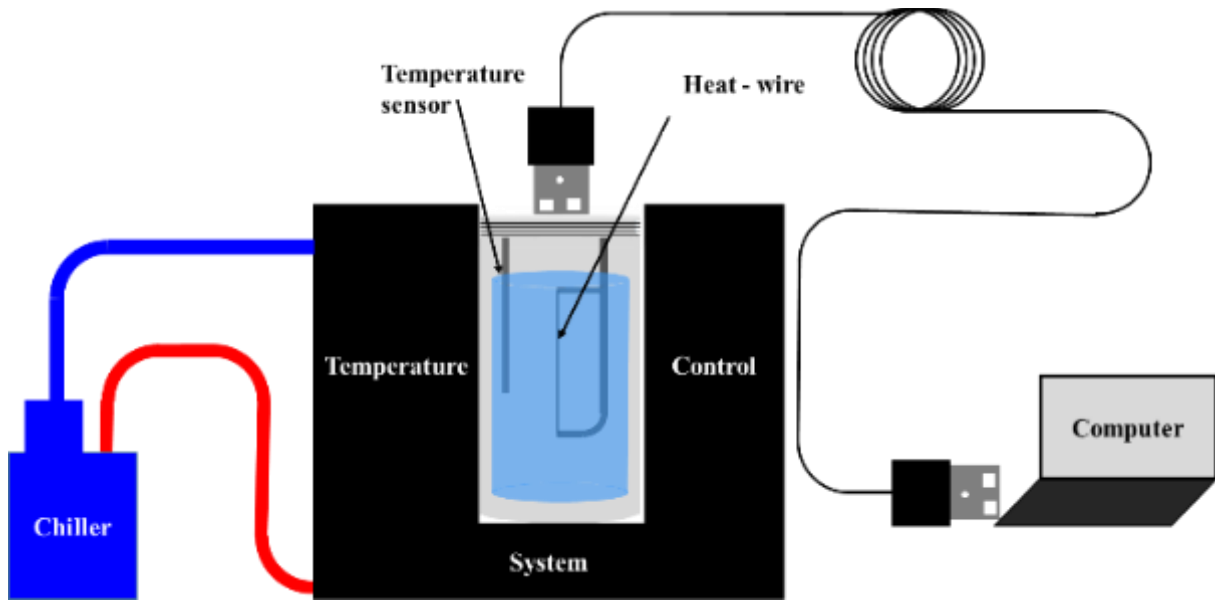


Figure 4. 17 Schematic diagram of the heat –wire sensor, sample holder and temperature control system

As is illustrated in Figure 4. 17, the probe of the heat-wire works as the temperature sensor and heat source. The tip of the probe has thin platinum with a diameter of 0.1 mm. The probe is submerged into the fluid with a volume of 35 mL at a stable temperature. A temperature control system (Lab Temp 30190, PSL Systemtechnik, German) is applied to maintain the temperature of the fluids with an accuracy of ± 0.1 °C. Using this technology, it can also obtain the thermal diffusivity and thermal capacity besides the thermal conductivity in each measurement. The main advantage of the stationary heat-wire method is eliminating the problem of convection caused by the ignition of the electric energy input to the heat-wire sorted, as an optimized electronic device guarantees relative short measuring times. There are many other advantages such as fast measurement, wide temperature range, and large thermal conductivity range as is illustrated in Table 4. 1. Due to the referred merits, this technique was used in many studies [225], [226].

CHAPTER 4 EXPERIMENTAL APPARATUSES AND UNCERTAINTY

Table 4. 1 Technical data of the LAMBDA-system

Technical term	Data
Measuring media	Fluids. gels powders
Sample quantity	Approx.. 35mL
Measuring range	10-1000 mW(m·K)
Repeatability	99%
Temperature range	-30°C -190°C
Temperature accuracy	± 0.1°C
Measuring time	Approx.60 s
Accuracy	1%

4.3.2. Viscosity

The viscosity of the base fluids and nanofluids were measured by a rotational rheometer (MCR502 Anton Paar, Austria). The parallel plate geometry is used for the high viscosity liquid and concentrated cylinder geometry for low viscosity, as is illustrated in Figure 4. 18. The equipment can measure both Newtonian behaviour and non-Newtonian fluids. To obtain the viscosity of the fluids, the torque of the rotating spindle is measured and converted into the viscosity of fluids. To maintain the temperature of fluids during the test, a chiller combined with the temperature control system containing a K type thermocouple with an accuracy of ± 1.5 °C is applied. For the measuring temperature larger than 0°C, the air cooling is used. However, for the temperature lower than 0°C, the liquid nitrogen is used to cool down the fluid to the target temperature. The technical data of the MCR502 Anton Paar rheometer is illustrated in Table 4. 2. According to the literature, accurate results can be obtained via this equipment [227], [228].

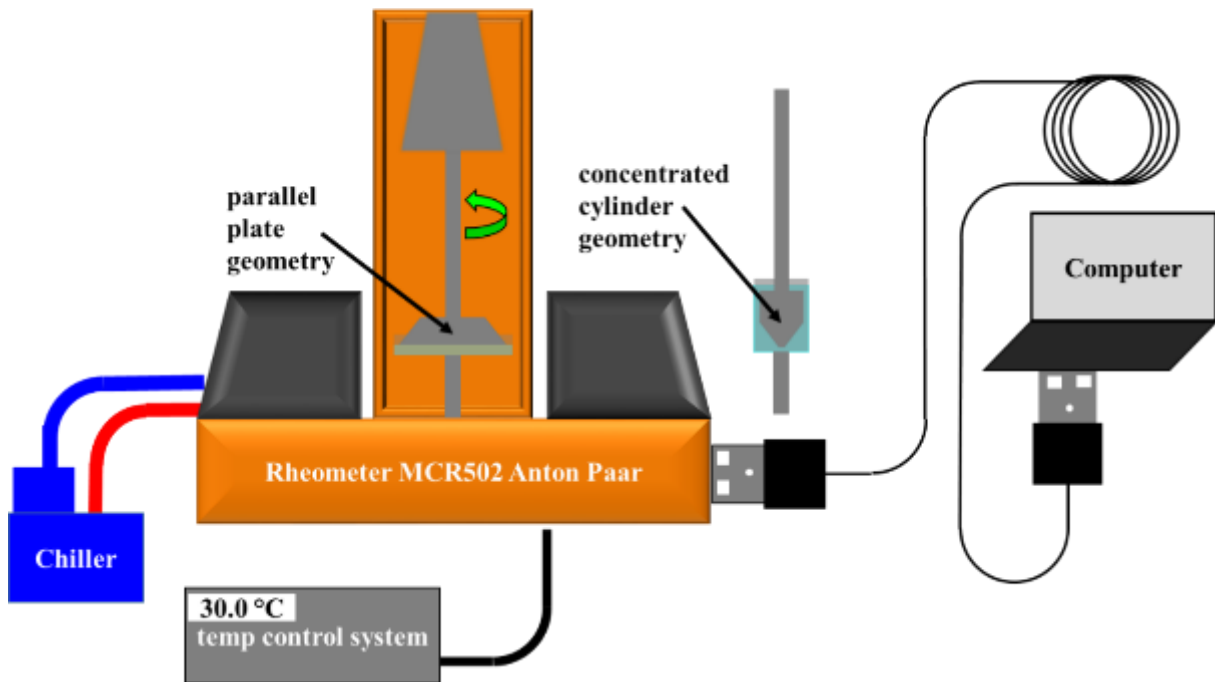


Figure 4. 18 Schematic diagrams of rheometer, chiller, and temperature monitor

Table 4. 2 Technical data of the MCR502 Anton Paar

Technical Term	Data
Maximum torque	300 mN·m
Min. torque, rotation	100 nN·m
Min. angular velocity	10-9 rad/s
Max. angular velocity	220 rad/s
Max. speed	2100 1/min
Min. angular frequency	10-7 rad/s
Max. angular frequency	628 rad/s
Normal force range	0.01 N - 70 N
Normal force resolution	1 mN
Max. temperature range	-160°C - +1000°C

4.3.3. Particle size distribution and ξ potential

The particle size distribution (PDS) of the nanofluids was measured by the dynamic light scattering (DLS) and the ξ potential by the electrophoretic light scattering (ELS) (Zetasizer Nano ZS Malvern, the U.K.). The theories for the measurements are attached in the appendix E and appendix F.

To measure the hydrodynamic diameter of the solid part in the base fluid, the indirect measurement with the DLS technique was applied. The size range of the instrument is between 0.3 nm and 10,000 nm, with an accuracy of $\pm 2\%$. The advantage of this technique is (1) indirect measurement without contaminating the sample, (2) very few and recyclable liquid is used during the measurement, (3) the backscatter in this technique reduces the multiple scattering that refers to the light from one particle is itself scattered by other particles. The technique data is illustrated in Table 4. 3. Due to the referred merits, this technique was used in many studies [229], [230].

The electrokinetic effect was used in the equipment to obtain the ξ potential of the nanofluid. It can be used to quantify the stability of the nanofluid. Some researches suggest that with its value larger than 30 mV, the nanofluid is stable. This technique was used in many studies [231], [232].

Table 4. 3 Technical data of the nano Zetasizer Nano ZS

Type	Technical term	Data
Particle size distribution	Size range	0.3 nm -10,000 nm
	Measurement theory	Dynamic Light scattering
	Minimum sample volume	1 mL
	Accuracy	$\pm 2\%$
	Temperature range	25 °C – 90 °C
ξ potential	Sensitivity	0.1 mg/mL
	Size range	3.8 nm to 100,000 nm
	Measurement theory	Electrophoretic Light Scattering
	Minimum sample volume	0.15 mL
	Accuracy	$\pm 5\%$
	Temperature range	25 °C – 90 °C

4.3.4. Infrared camera

To obtain the temperature on the surface of diamond surface without damaging the microchips and the diamond heat spreader, IR camera (VarioCAM hr head 600, German) is one of the optimized choices for the required measurement. The principles for IR radiation are Planck's law, Stefan-Boltzmann law, Kirchhoff's law of thermal radiation, and Wien's displacement law. This part was attached in Appendix C. As is shown in Figure 4. 19, the measuring surface emits infrared radiation whose intensity is a function of temperature it possesses. The detector of the IR camera records the signature intensity that is converted to the temperature by the IBIS 3 plus software. It is noticed that the standard lens does not have high resolution for the temperature measurement of the microchip. A $0.5\times$ close up lens which costs much cheaper than microscopic was used with a resolution of $42\text{ }\mu\text{m}$ as is given in Table 4. 4. According to the literature, the IR camera was successfully used to measure the temperature of the microchips [233], [234].

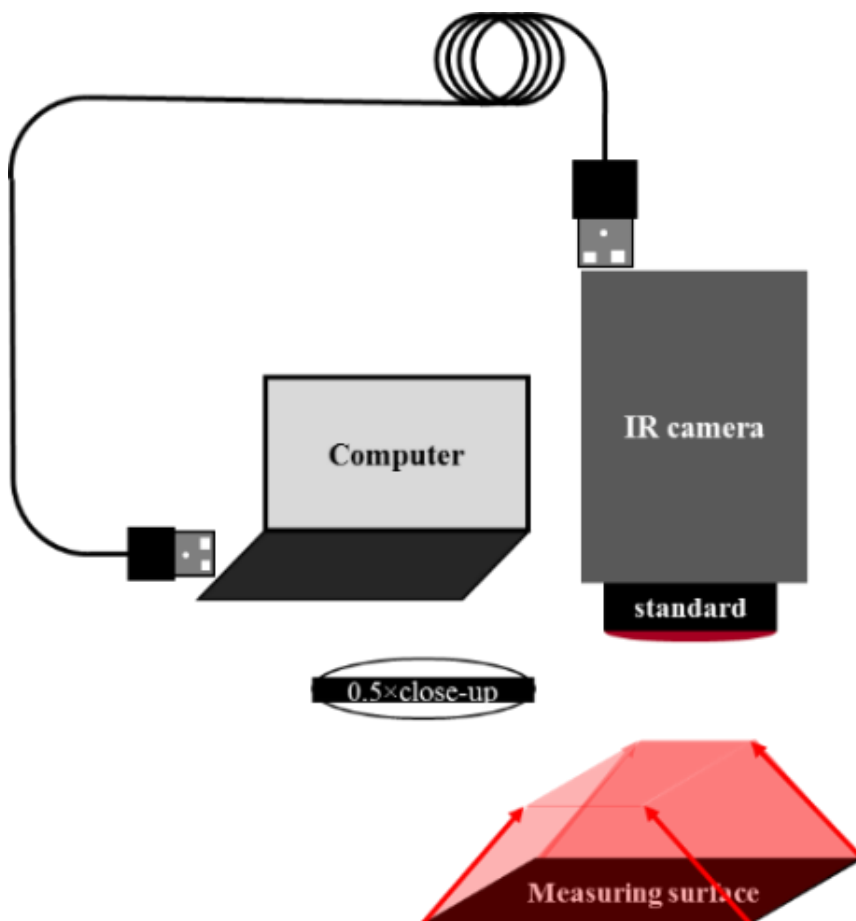


Figure 4. 19 Schematic diagrams of the IR camera

CHAPTER 4 EXPERIMENTAL APPARATUSES AND UNCERTAINTY

Table 4. 4 Technical data of VarioCAM HR head 600

Technical Term	Data
Spectral range	7.5-14 μm
Temperature measuring range	-40°C - 1200°C
Temperature resolution at 30°C	<0.05°C, $\geq 0.03^\circ\text{C}$
Measuring accuracy	$\pm 1.5^\circ\text{C}$ (0-100°C)
Emissivity	Adjustable from 0.1 to 1.0.
pixels	640×480
Standard lens	Focal length 30mm FOV 30°×23° Focus 50 mm
0.5×close-up lens	FOV 27 mm×20 mm Resolution 42 μm

4.3.5. Raman Thermography

The temperature in the finger of the die needs to be measured for the comparison with the simulation results and quantifying the quality of the microfluidics channel. Therefore, it is important to have an accurate temperature on the GaN layer. To measure the temperature in that layer, Raman thermography was used to collect the temperature in the fingers of the devices. During the test, Renishaw inVia spectrometer with 50×0.6 numerical aperture objective lens is one of the optimized choices for the required measurement. The principles for Raman thermography is the Raman shift. This part is attached in Appendix D. As is shown in Figure 4. 23, the light path shows that the laser with 488 nm wavelength generated from DPSS hits the GaN layer and then GaN layer scatters the light. This wavelength and intensity of the scattered light are recorded by the spectrometer and its function with the Raman shift can be calculated. According to the peak position of the Raman shift, the temperature in the GaN layer can be calculated. During the test, the diameter of the laser is around 500 nm. The accuracy of this measurement can be around $\pm 5^\circ\text{C}$. According to the literature, the Raman thermography was successfully used to measure the temperature of the microchips [220], [221].

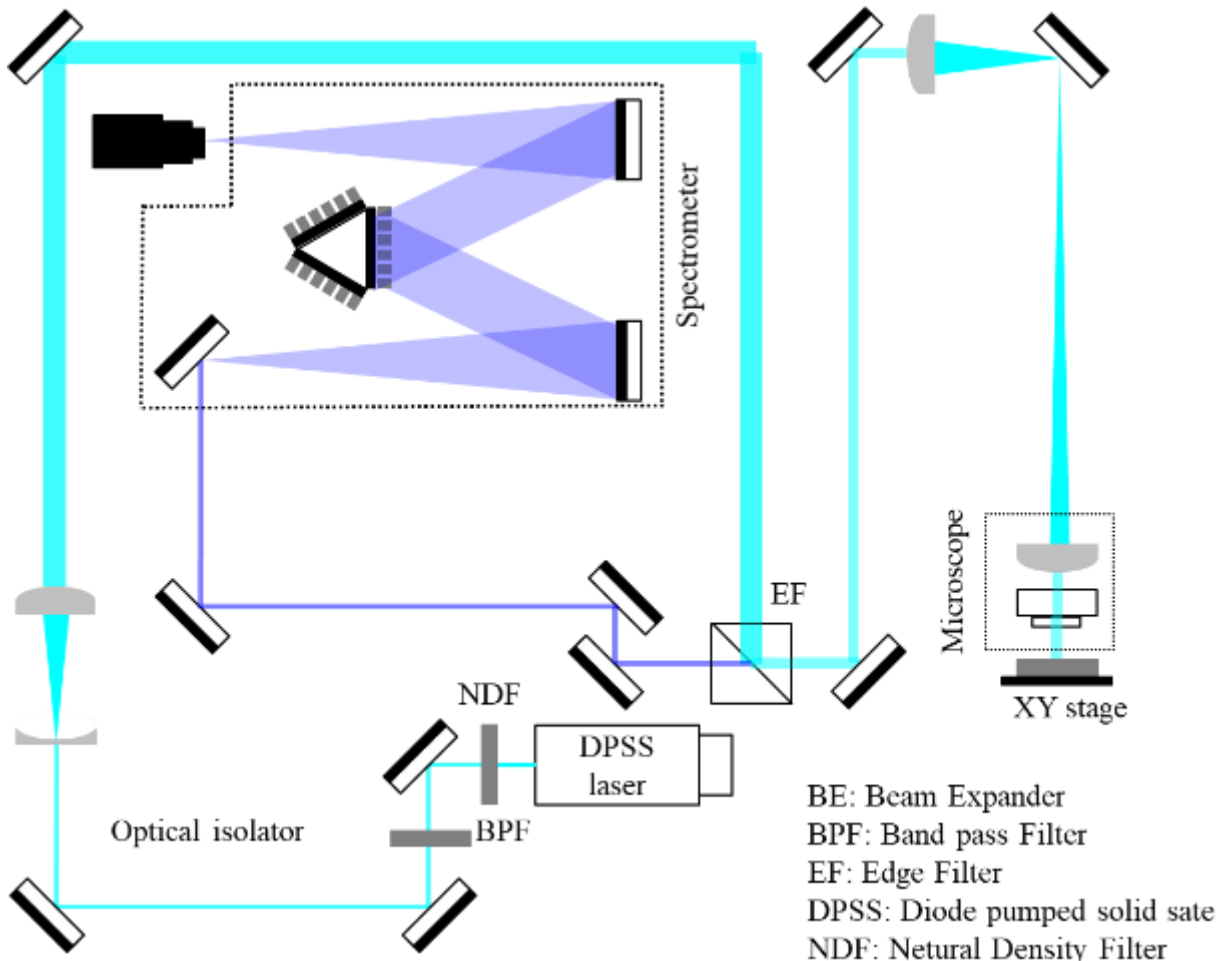


Figure 4. 20 Schematic diagrams of Raman thermography

4.3.6. 3D printer

The 3D printer (Formlab Form 2, the U.K.) was employed for the fabrication of the micro-jet impingement channel and the lid for the combination, as is illustrated in Figure 4. 21. In order to have high accuracy for the 3D printed microfluidic channel, the stereolithography for the 3D printing with a laser beam was used. The basic procedure of the 3D print is more or less the same. Firstly, the design of the micro jetting is generated via a 3D modelling software and then transferred to the 3D printer. After that, the resin used for the printing is chosen based on the working condition. In this study, as the lid might be exposed to the temperature around 175°C, a high-temperature resin was selected while the jetting channel uses the same resin. Then, the selection of the resolution was prioritized to the final step of the printing. The data the resolution is given in Table 4. 5. After the printing, the micro-jet channel was cleaned and put into the curing chamber for curing with UV light. Compared to the other microfluidic

fabrication method, the advantages of the 3D printer are the ability for any shape fabricating, cheap and mass production. However, it should be pointed out that, due to the laser spot size in the printing is around 140 μm , the morphology of the orifice was inevitably distorted compared to laser cutting or other types of the channel fabrication.

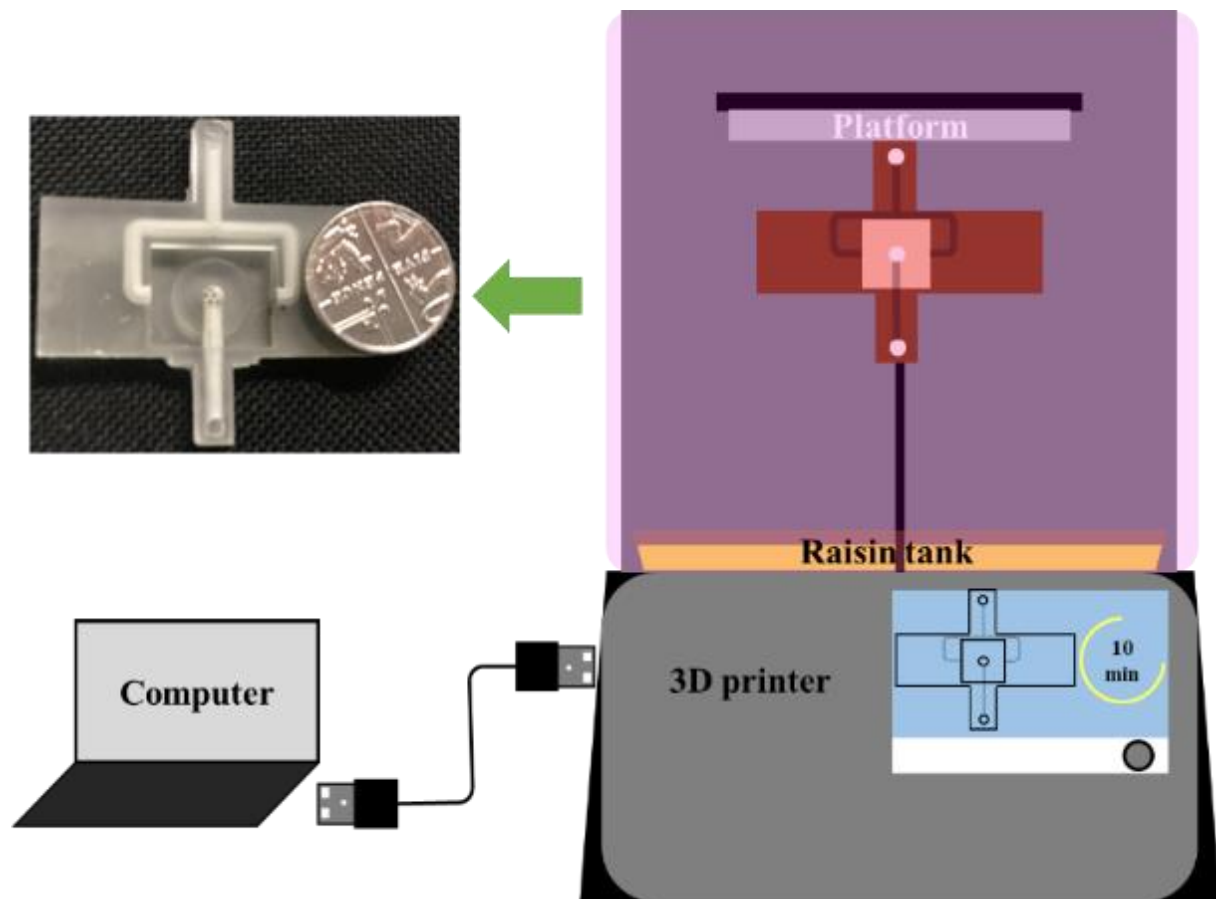


Figure 4. 21 Schematic diagrams of the 3D printer with micro-jet channel printed

Table 4. 5 Technical data of Formlab form 2

Technical term	data
Laser resolution	0.1 mm-0.025 mm
Laser spot size	140 μm
Laser power	250 mW
Layer thickness	25-300 μm
Technology	Stereolithography

4.4. Uncertainty analysis

Uncertainty analysis is important for the analysing and obtaining other parameters form the test rig. In many measurements for the TM of the microchip, the measured temperature does not show much difference. Thus, the error bar was required to show the accuracy of the measurement.

4.4.1. Uncertainty in thermal Management of microchip

The uncertainties of the parameters investigated need to be calculated to obtain reliable results. The accuracy of instruments and sensors is used for the referred calculation. As is illustrated in Figure 4. 22, the power generated by power supplier P, the heat dissipated by HTF Q, the heat flux q, heat transfer coefficient, h and their uncertainty are calculated by

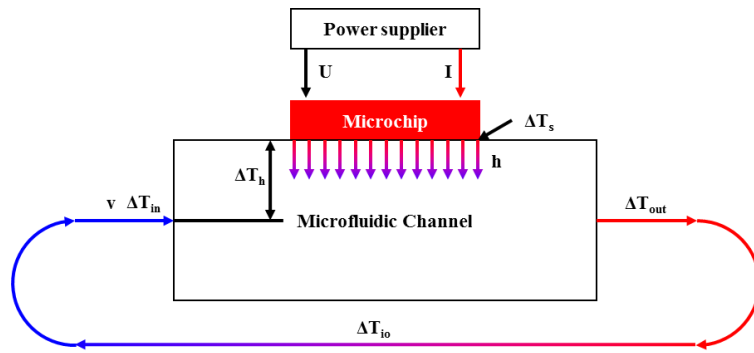


Figure 4. 22 Schematic of the thermal characteristic of the microfluidic channel

$$P = UI \quad (4-1)$$

$$\Delta P/P = \sqrt{(\Delta U/U)^2 + (\Delta I/I)^2} \leq \nabla U/U + \nabla I/I \quad (4-2)$$

$$Q = \rho C_p v \nabla T_{io} \quad (4-3)$$

$$\begin{aligned} \Delta Q/Q &= \sqrt{(\Delta \rho/\rho)^2 + (\Delta C_p/C_p)^2 + (\Delta v/v)^2 + (\Delta(\nabla T_{io})/\nabla T_{io})^2} \leq \nabla \rho/\rho + \nabla C_p/C_p + \nabla v/v + \\ &\quad \nabla(\nabla T_{io})/\nabla T_{io} \end{aligned} \quad (4-4)$$

$$T_{io} = T_{out} - T_{in} \quad (4-5)$$

$$\nabla T_{io} = \sqrt{\nabla T_{out}^2 + \nabla T_{in}^2} \quad (4-6)$$

$$q = Q/A \quad (4-7)$$

$$\Delta q/q = \sqrt{(\Delta Q/Q)^2 + (\Delta A/A)^2} \leq \nabla Q/Q + \nabla A/A \quad (4-8)$$

$$h = q/\nabla T_h \quad (4-9)$$

$$\Delta h/h = \sqrt{(\Delta q/q)^2 + (\nabla(\nabla T_h)/\nabla T_h)^2} \leq \nabla q/q + \nabla(\nabla T_h)/\nabla T_h \quad (4-10)$$

$$T_h = T_s - T_{in} \quad (4-11)$$

$$\nabla T_h = \sqrt{\nabla T_s^2 + \nabla T_{in}^2} \quad (4-12)$$

In the measurement, the K thermocouples, the power supplier, the flow meter have an accuracy of $\pm 0.5^\circ\text{C}$, 0.1% for both voltage and current and 1% by the manufacturer respectively.

4.4.2. Thermal conductivity uncertainty analysis

Experimental results of thermal conductivity for water were compared with the referenced values from the International Association for the properties of Water and Steam (IAPWS) to validate and repeat the thermal conductivity measurement. The result of the thermal conductivity of distilled water at a different temperature is shown in Figure 4. 23. According to the data, it is found that most data are within error of 3 % compared with the value from IAPWS for the thermal conductivity of distilled water. However, as is illustrated in the figure, the measured data are all slightly higher than the reference value. This is likely due to the systematic error of the equipment (LAMBDA-system PSL Systemtechnik GmbH, German). The reason for the systematic error might be the non-negligible natural convection that enlarges the thermal conductivity measured by the equipment during the measurement

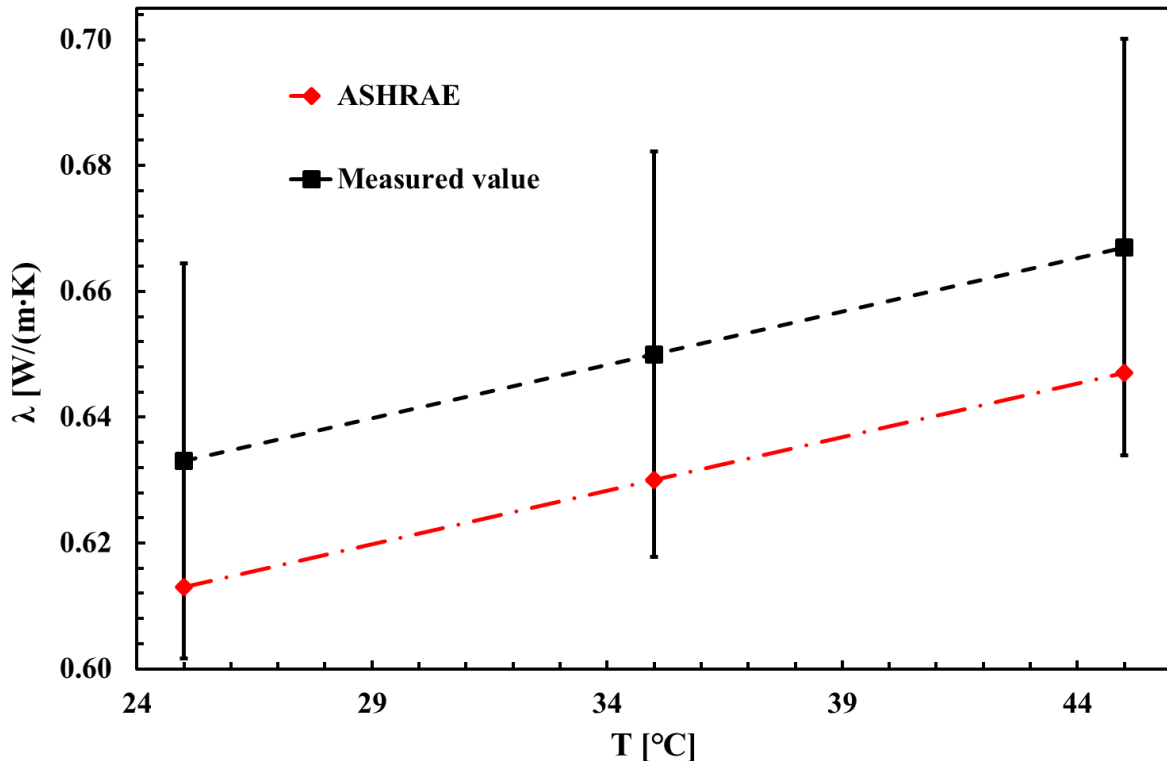


Figure 4. 23 Thermal conductivity of distilled water at different temperature

4.4.3. Viscosity uncertainty analysis

Experimental results of viscosity for water were compared with the referenced values from the IAPWS to validate and repeat the viscosity measurement. The result for the viscosity of distilled water at a different temperature is shown in Figure 4. 24. According to the figure, it is found that most data are within error of 5 % compared with the value from IAPWS for the viscosity of distilled water. This suggests that good repeatability of the measurement with measured viscosity close to the reference value can be obtained. So the rheometer (MCR502 Anton Paar, Austria) with the geometry of concentric cylinder can be used to measure the low viscosity such as water and the aqueous-based nanofluids.

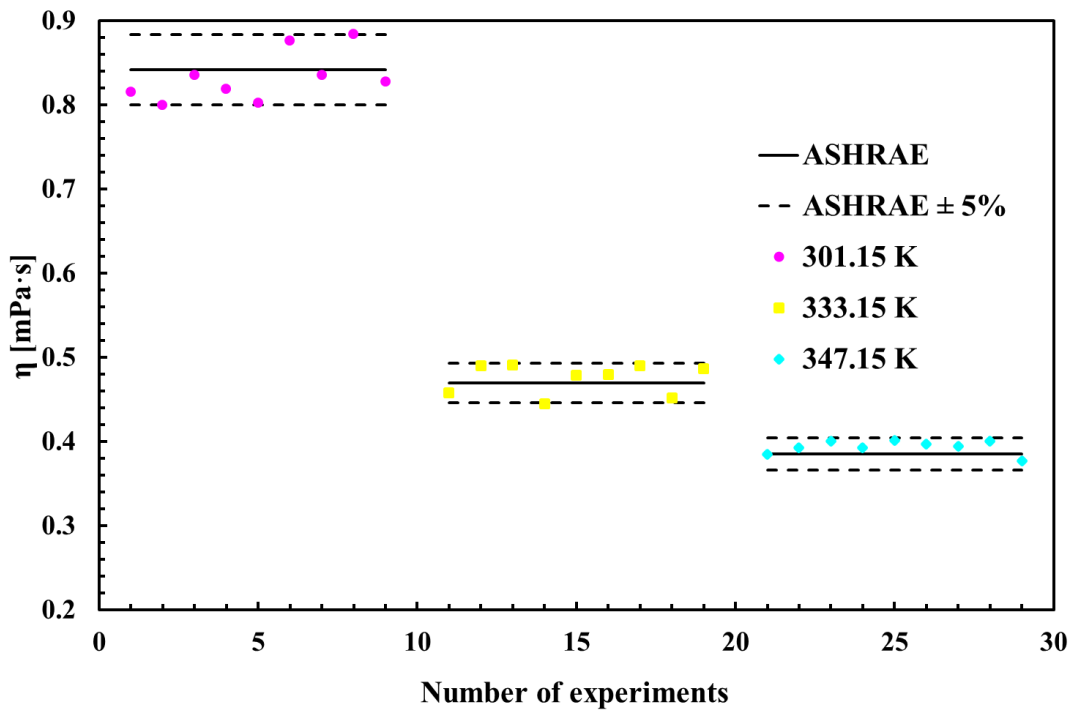


Figure 4. 24 Viscosity of distilled water at different temperature

4.5. Summary

This chapter investigated the experimental set-ups, the thermal packages for the microchips, the uncertainty analysis and the equipment used in the experiments.

- Four different types of set-up for the TM of the microchips with microfluidic channel were fabricated and investigated to obtain the thermal performance and pressure drop of the purposed channels with different heat transfers fluids
- Two types of thermal package of microchips with the microfluidic channels were successfully fabricated for the experiment test. In the experiment different types and technology was used for the thermal performance of the integrated system such as the thermocouples, the IR camera and the Raman thermography.
- The uncertainly for the measurement of the TM of microchips and the characterisation of the nanofluids was also studied.
- The equipment used for the characterisation of the nanofluids, the temperature measurement of the test rigs and the 3D printer for fabricating of the microfluidic channel was also investigated.

5. Results and discussions

This chapter consists of four major sections. Section 5.1 discusses the formulation and characterisation of nanofluids. Experimental results of the thermal performance of microfluidic channels are presented in Section 5.2. Section 5.3 presents the modelling results of materials for the package of the microelectronic devices. Finally, the experimental results of the thermal performance of GaN transistors are discussed in Section 5.4.

5.1. Results and discussion 1 - Nanofluids

In this section, two types of nanofluids were formulated according to their specific application condition. BN/DI water was used for the temperature above 0 °C and rGO/EG+DW for the temperature as low as - 50 °C as EG+DW was used as the coolant in these working conditions. After the formulation, the main properties of the nanofluids were characterised, such as the particle size distribution, stability, morphology, thermal conductivity, viscosity etc. Those properties have an important influence on the application of heat transfer fluids.

5.1.1. Boron Nitride nanofluids - formulation and characterisation

Due to the good thermophysical properties of BN such as high thermal conductivity and electrical resistance, its nanoparticle was added into the deionised (DI) water for formulating BN/DI water nanofluids.

- ***Formulation processes***

As is illustrated in Figure 5. 1, there are two types of method for the formulation of the BN/DI water nanofluids. The method 1 is a typical two-type method. After mixing dry BN powder with DI water, Gum Arabic, Tween 20 and Tween 80 acting as surfactants during the synthesis were added into the dispersants. As a comparison, the dispersion without surfactants was also formulated. The magnetic agitation was applied before sonication with the matched time which was determined by the particle size distribution during the experiment to have stable nanofluids which were tested by the long stability

test by the ζ potential and particle size during the time. The procedure of method 2 with wet milling was similar to Method 1. However, after adding the surfactant or not into the mixture, nano grinding was applied to decrease the particle size of the nanoparticles which had a good influence in the thermal conductivity enhancement according to the literature review in Chapter 2. The nanofluids with high concentration were diluted into the desired concentration for its further characterisation.

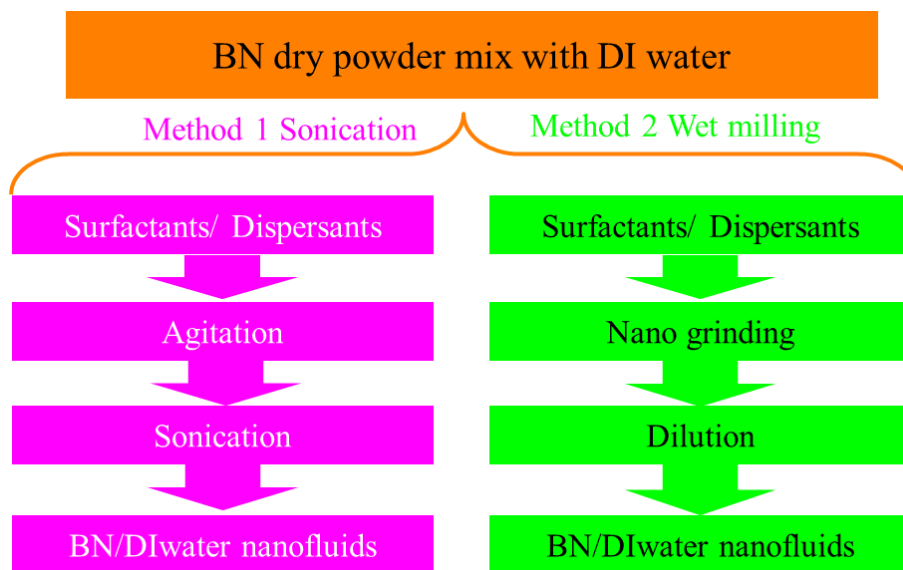


Figure 5. 1 Flow chart of the BN/DI water nanofluids

- *Particle sizes*

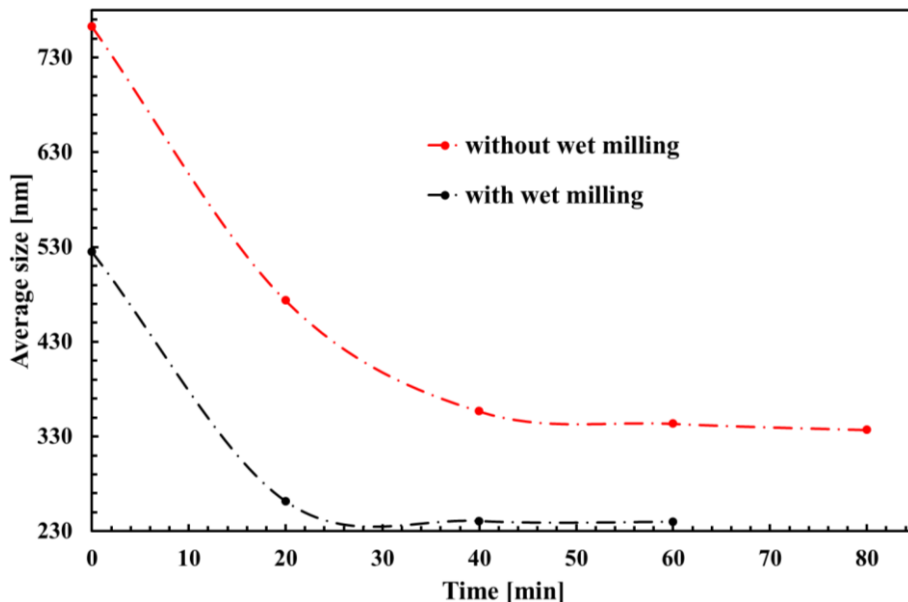


Figure 5. 2 Average sizes of nanoparticles with sonication time

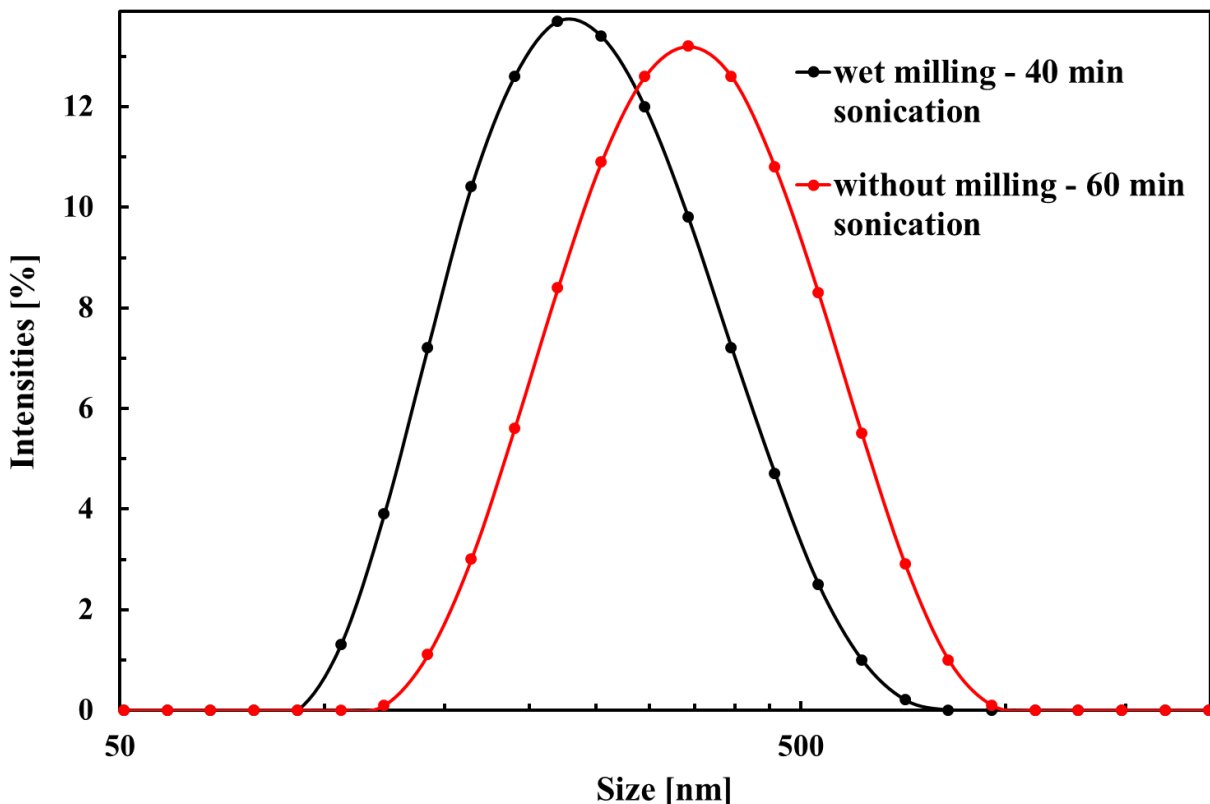


Figure 5. 3 PDS of 0.05 wt. % BN/DI water nanofluids with and without wet milling

Dynamic light scattering (DLS) was used to determinate the hydrodynamic diameter of the BN nanoparticles. Due to the limitation of the concentration of the nanofluids for the equipment, 0.05 wt. % of nanofluids were tested. As were shown in Figure 5. 2, For Method 2 with wet milling, 40 min sonication time was required to decrease the particle size to the plateau. The average hydrodynamic particle size of BN was about 230 nm with the assumption of the primary particles as spherical shape. However, for Method 1 without the wet milling, the BN nanofluid required 60 min to decrease particle size to the plateau. The average particle size of BN was about 350 nm which was 120 nm larger than its counterpart. From the curve of the hydrodynamic particle size distribution in Figure 5. 3, it can also be observed that for Method 2, the range of size was between 90 nm and 900 nm with its peak at 230 nm while its counterpart, Method 1, the range of the size was between 125 nm and 1000 nm with its peak at 350 nm. The difference in the PSD showed the wet milling can decrease the size of the particle in the whole size range which shifted the peak size. A comparison of the measured size with the nominal size of BN nanoparticles from the manufacturer (~150 nm) suggested that both the wet milling and ultrasonication cannot completely disaggregate the agglomerates.

- **Morphology**

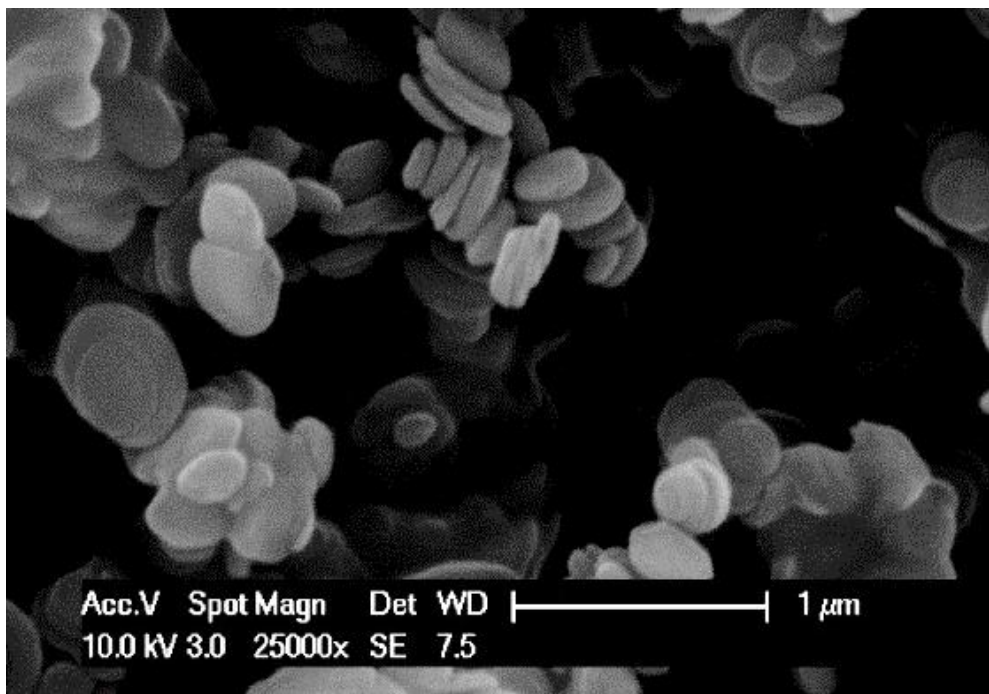


Figure 5. 4 ESEM of BN dry powder

Before the preparation of the BN nanofluid, the morphology of dry nanoparticle was characterized by ESEM. The size of the nanoparticle between the data provided by the manufacturer and the measurement by ESEM was compared. As can be seen in Figure 5. 4, h-BN's particles have a platelet shape with a mean diameter of 300 nm-500 nm. This size is 2-4 times larger than the manufacturer's specifications. Thus, there was agglomeration in dry powders. The agglomeration may be formed in transportation and storage conditions. Therefore, to reduce and break the agglomeration and obtain a well-dispersed nanofluid solution, processes such as wet milling and ultrasonication must be employed in the two-step method.

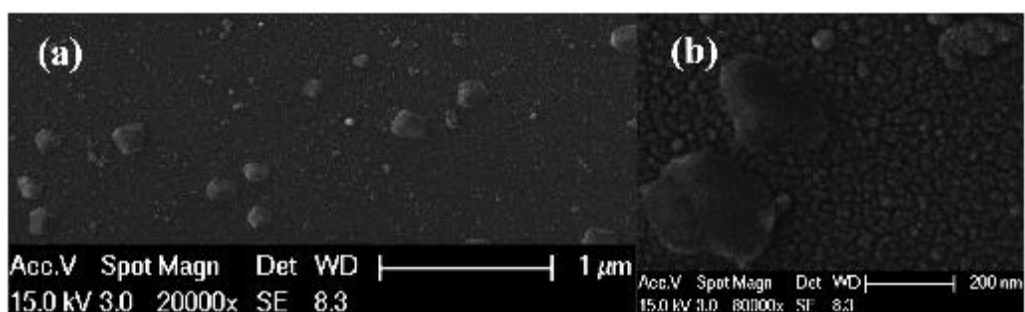


Figure 5. 5 ESEM of BN nanoparticles after the formation process in different magnification: (a) $\times 20,000$ and (b) $\times 80,000$

The ESEM analysis of the nanoparticles' size and morphology after the wet milling were shown in Figure 5. Compared with the dry particles, most of the large clusters were broken down during the wet milling and ultrasonication processes. The results also suggested the particles size from ESEM showed good agreement with the DLS measurement.

- ***Stability***

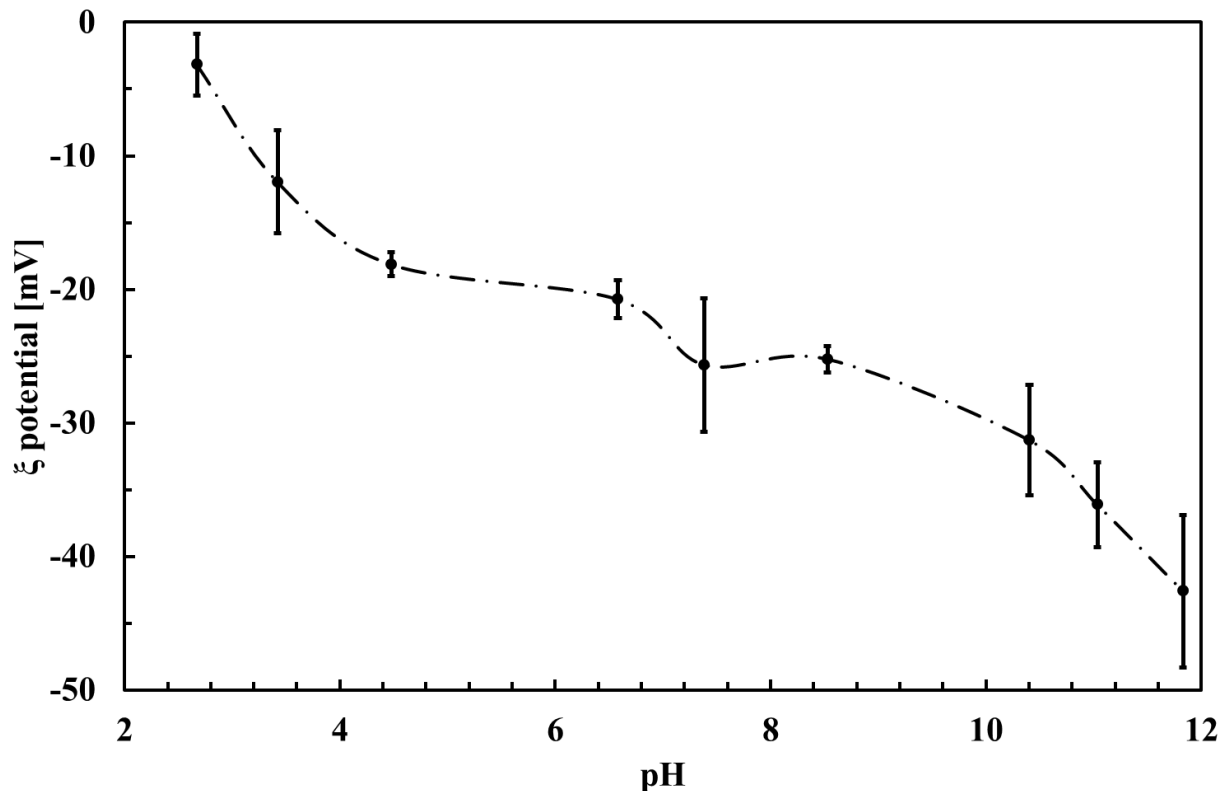


Figure 5. 6 ξ potential values of BN nanofluids as a function of pH value

The electrophoretic behaviour affects the dispersion of the nanoparticle in the base fluid. To obtain its value, the ξ potential of nanofluid was measured. Figure 5. 6 showed the change of ξ potential of BN/DI water nanofluid as a function of pH. It can be seen that isoelectric point (IEP) of BN nanoparticle in deionized water was pH = 2.4. The suspension was negatively charged after pH > 2.4. Some researches show that nanofluids have good stability with measured zeta potential above +25 mV or below -25 mV [235]. After the wet milling, the measured pH of the BN/DI water nanofluid was larger than 9. This implies that the electrostatic repulsion force between BN nanoparticles was high enough to overcome the attraction force between particles.

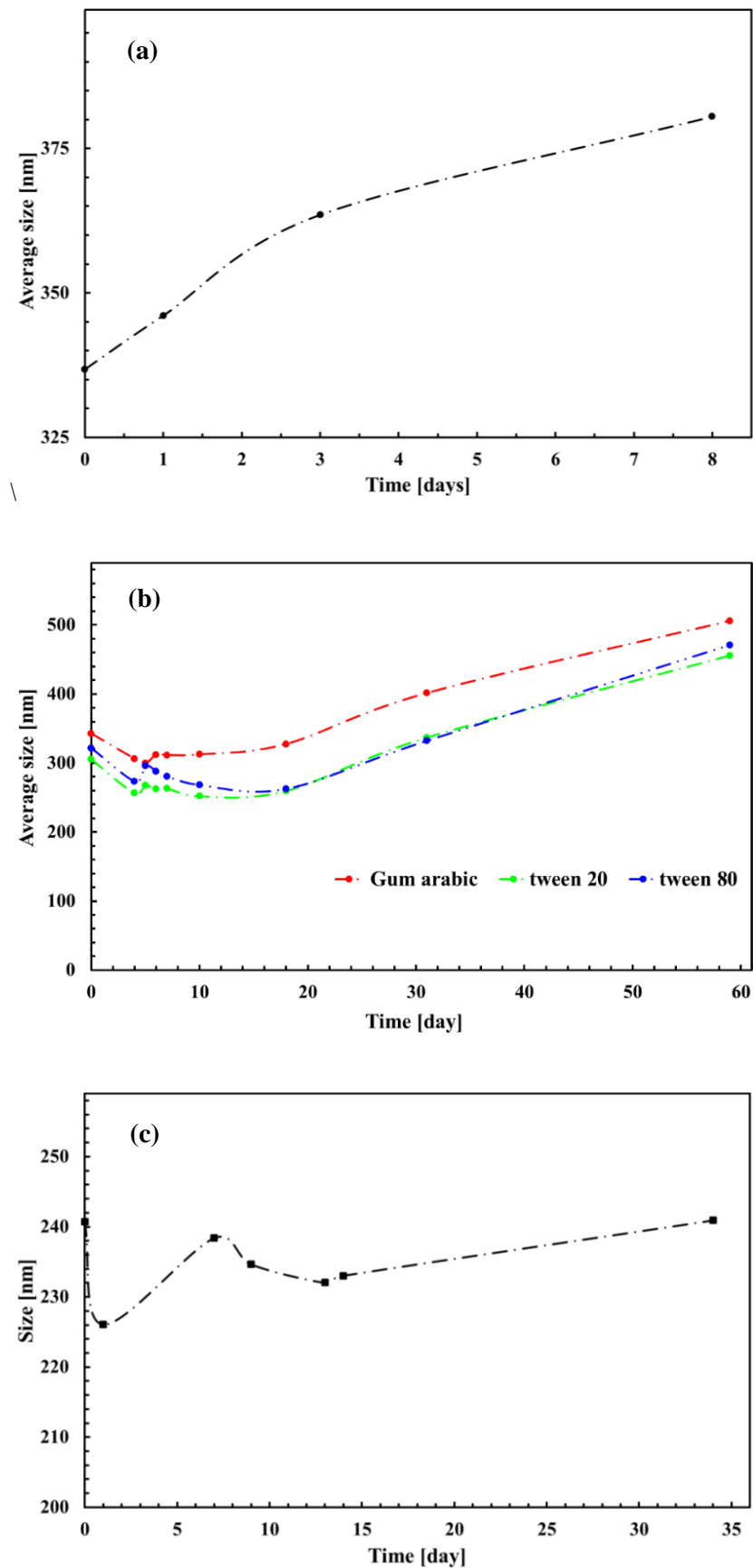


Figure 5.7 Average particle sizes with time (a) process 1 without surfactant, (b) process 1 with surfactants and (c) process 2

without surfactant

According to Figure 5. 7 (a), the average particle size of the nanofluid without surfactant increased day by day. At the beginning of the test, the size was about 340 nm and 8 days later, the size increased to 380 nm. Sedimentation can be observed at the bottom of the vials. Therefore, nanofluid was unstable without surfactants. In the following characterization, this type of nanofluid was not included. As is shown in Figure 5. 7 (b), with surfactants adding, the suspensions can be stable up to 20 days. One month later the sizes of particle eventual increased to 401 nm, 336 nm and 332 nm for Gum Arabic, Tween 20 and Tween 80 respectively. The increasing trend for the next month was still observed. As is depicted in Figure 5. 7 (c), the nanofluids with milling can be stable in the first 4 weeks after formulation. The reason for this might be the milling process. The pH of the nanofluids steadily increased during the wet milling. After 5.5 h milling, a pH of 9.45 was measured.

- ***Thermal conductivity***

One of the main advantages of nanofluid is the potential for high enhancement of efficient thermal conductivity which is one of the techniques to increase the heat transfer enhancement. The transient heat wire method was used to measure the thermal conductivity of the base fluid (DI water) and nanofluids.

Figure 5. 8 depicts the thermal conductivity of nanofluids via method 1 with 3 surfactants. Figure 5. 9 shows the thermal conductivity of nanofluids via method 2 versus temperature at various concentrations. Compared Figure 5. 8 with Figure 5. 9, results showed that nanofluids fabricated with wet milling had a higher thermal conductivity enhancement than the sonication in the temperature range. Therefore, in the following characterisation, only wet milling process was measured and analysed.

According to Figure 5. 9, it can be seen that the higher thermal conductivity belonged to BN nanofluids with higher temperature. According to Figure 5. 10, it can be obtained that the higher thermal conductivity belonged to the BN nanofluids with higher concentrations. Here, two thermal conductivity models for composites, the Maxwell model and the Prasher model were used to predict the thermal conductivity of nanofluids.

CHAPTER 5 RESULTS AND DISCUSSIONS

Maxwell model is based on the effective medium theory, and it is developed for a dilute suspension of non-interacting spherical particles. The expression of the effective thermal conductivity is;

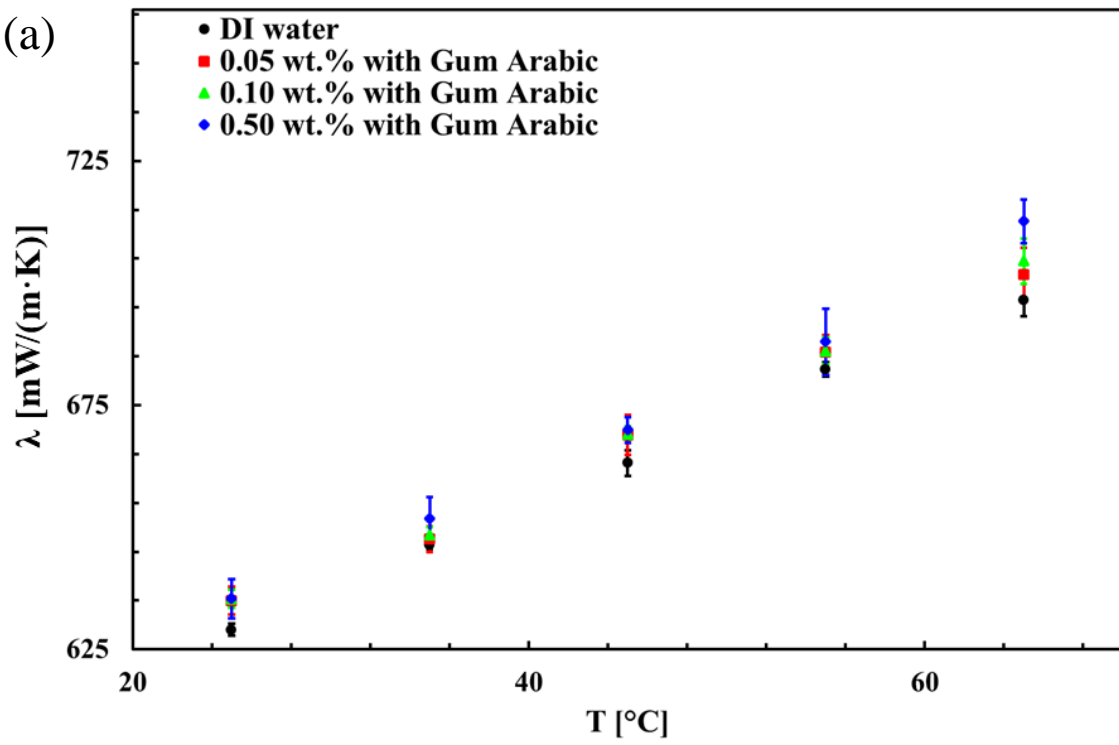
$$\frac{k_{nf}}{k_f} = \frac{k_s + 2k_f - 2\varphi(k_f - k_s)}{k_s + 2k_f + \varphi(k_f - k_s)} \quad (5-1)$$

Where k_{nf} , k_s , k_f , and φ are the thermal conductivity of nanofluids, the thermal conductivity of nanoparticles, the thermal conductivity of the base fluid, and the volume fraction of nanoparticles, respectively.

Local convection due to the Brownian movement of the nanoparticles was considered in this model. A modified Maxwell equation was used by including the Brownian-motion-induced convection from multiple nanoparticles. This semi-empirical model can be expressed as

$$\frac{k_{nf}}{k_f} = 1 + A Re^m Pr^{0.333} \frac{k_s + 2k_f - 2\varphi(k_f - k_s)}{k_s + 2k_f + \varphi(k_f - k_s)} \quad (5-2)$$

Where, The coefficient $A = 4 \times 10^4$; $m = 2$; Re is the Reynolds which is defined as $Re = \frac{1}{\nu} \sqrt{\frac{18k_b T}{\pi \rho_d d_p}}$ and Pr is Prandtl number [79]. In Reynolds number, k_b is the Boltzmann constant, T the temperature, ρ_d the density, and d_p the diameter of the nanoparticle.



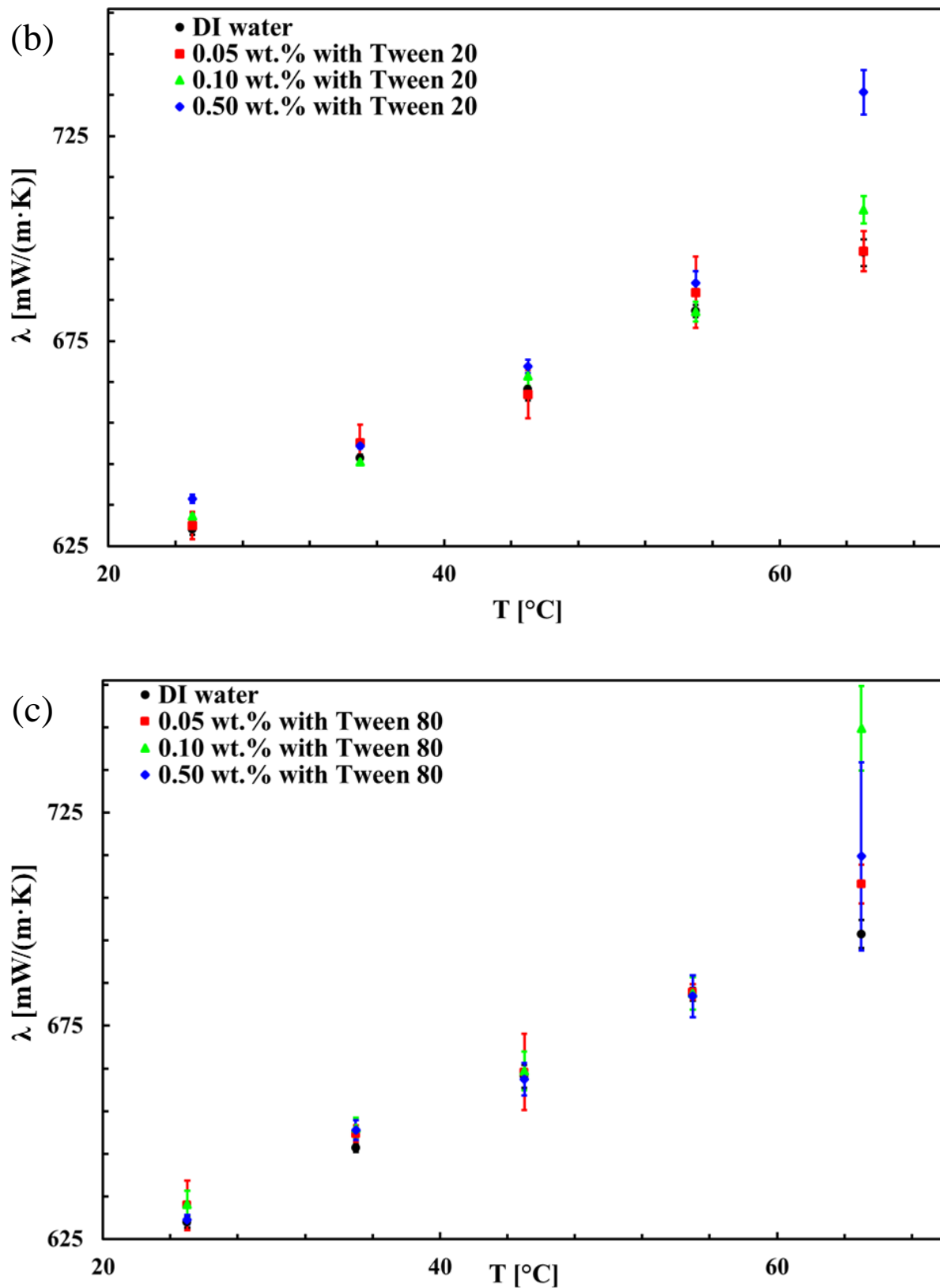


Figure 5. 8 Thermal conductivity of nanofluids via process 1 (a) Gum Arabic, (b) Tween 20 and (c) Tween 80

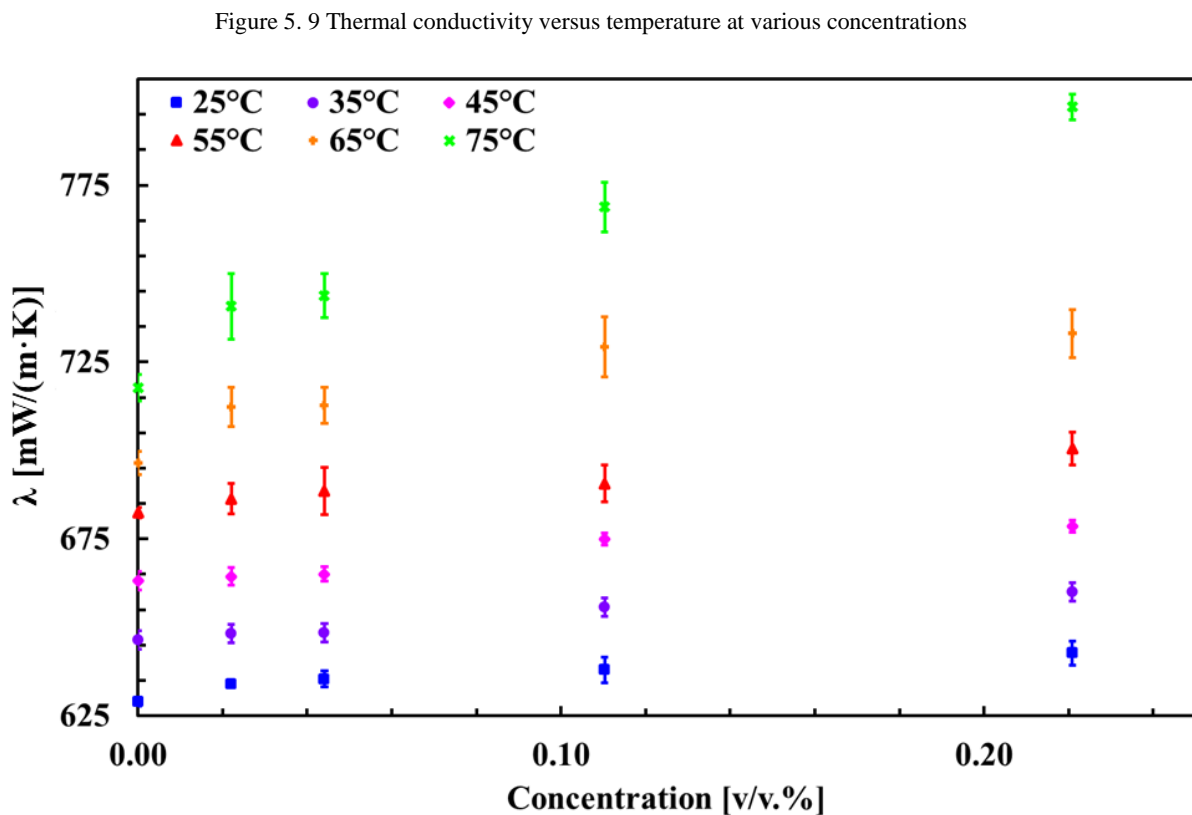
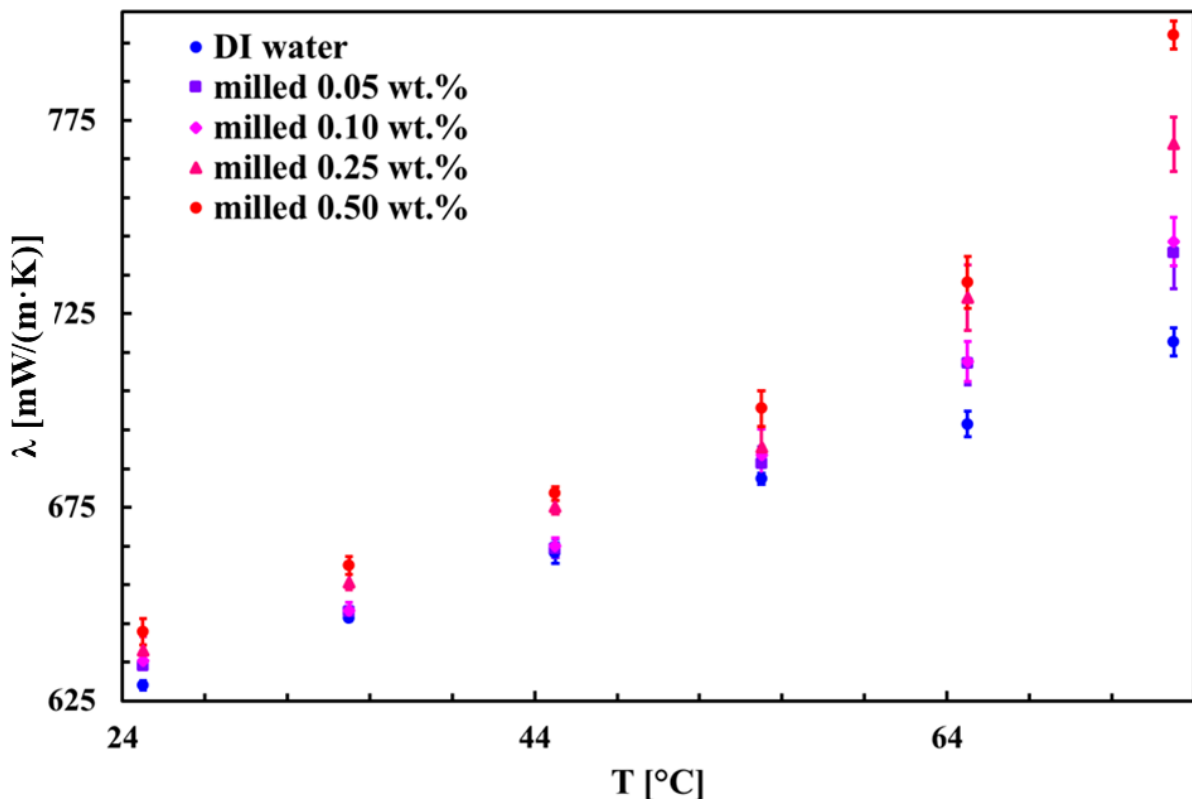


Figure 5. 11 depicted the measured and predicted the thermal conductivity of BN/DI water nanofluids to that of the base fluid for nanoparticle volume concentrations up to 0.5 wt. % (0.22 vol. %) at 25 and 75°C. According to the Maxwell equation, the effective medium theory only worked well at low concentration and low temperature. For high concentration and high temperature, there was a large deviation of measured data from the Maxwell model prediction. The measured data showed large enhancement with temperature increase due to the effect associated with the proposed mechanisms of thermal energy transfer in nanofluids.

Thus, the Brownian motion should be considered as one of the main mechanisms for the anomalous increase of thermal conductivity for nanofluids. In the same context, Prasher et al. model show more accurate prediction than the Maxwell model in both high and low temperature. By increasing the temperature, thermal movement of molecules with Brownian motion intensifies and intermolecular interactions become weakened, thus the viscosity decreases which is shown in the following section and thermal conductivity increases. Thus, BN/DI water nanofluids in high temperature can obtain higher thermal conductivity enhancement with lower viscosity compared to the room temperature.

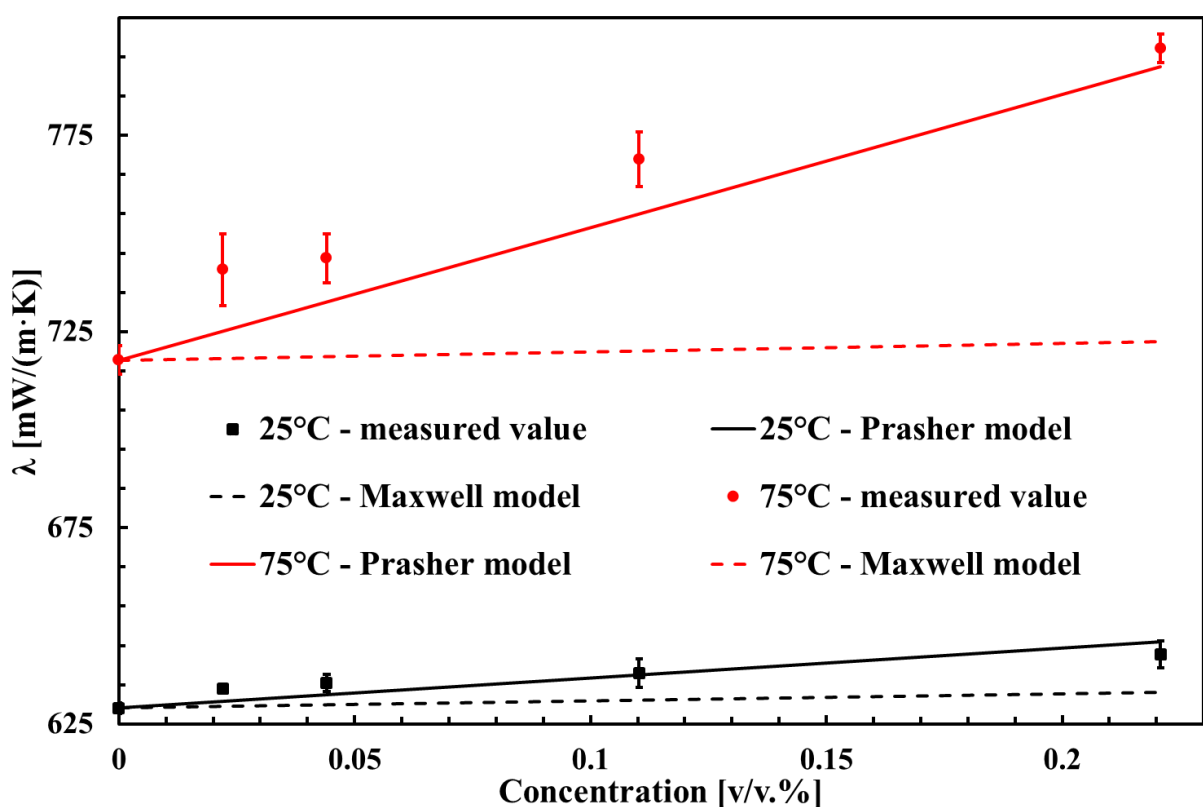


Figure 5. 11 Thermal conductivity BN/DI water nanofluids at 25 and 75 °C for different particle volume fractions

- *Viscosity*

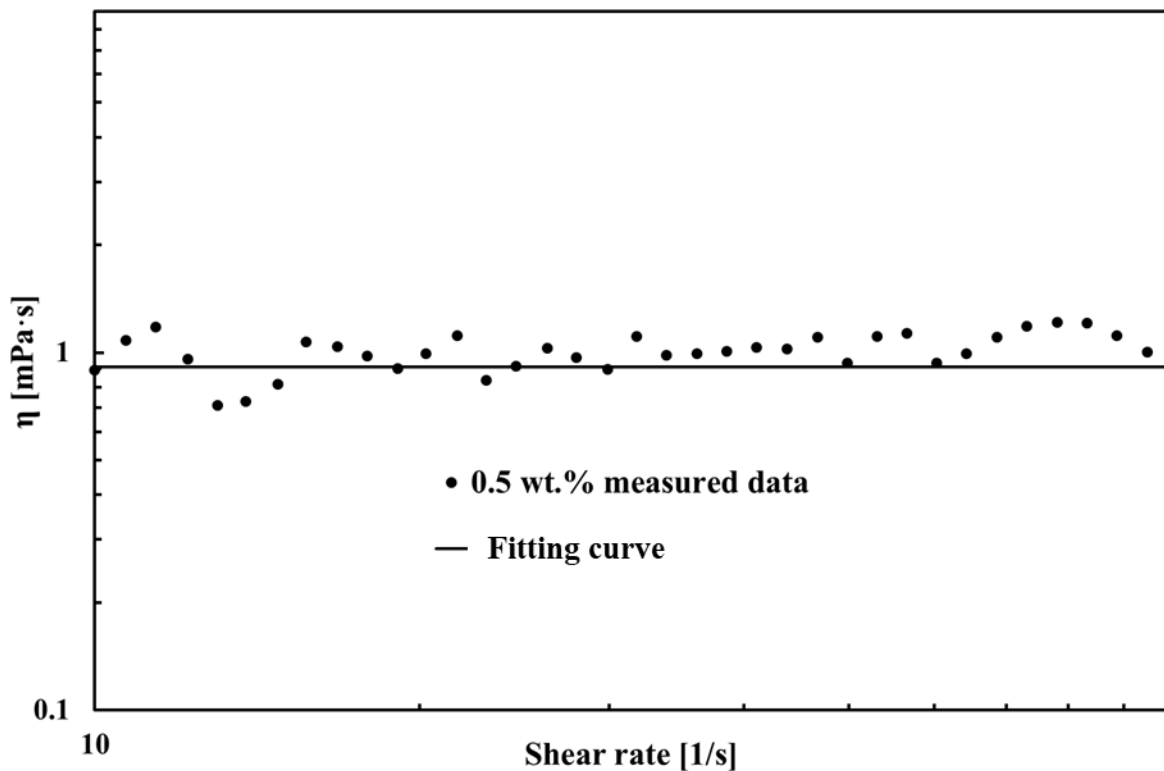


Figure 5.12 Viscosity versus the shear rate at 0.5 wt. % with 25 °C

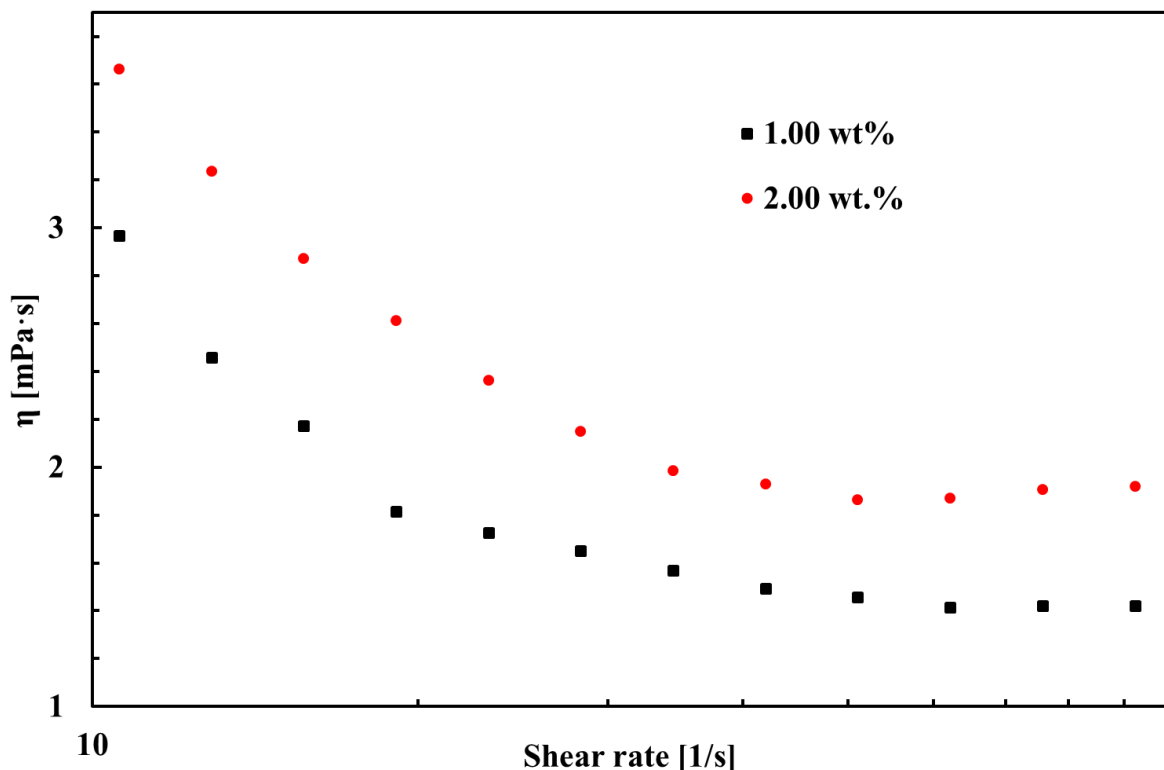


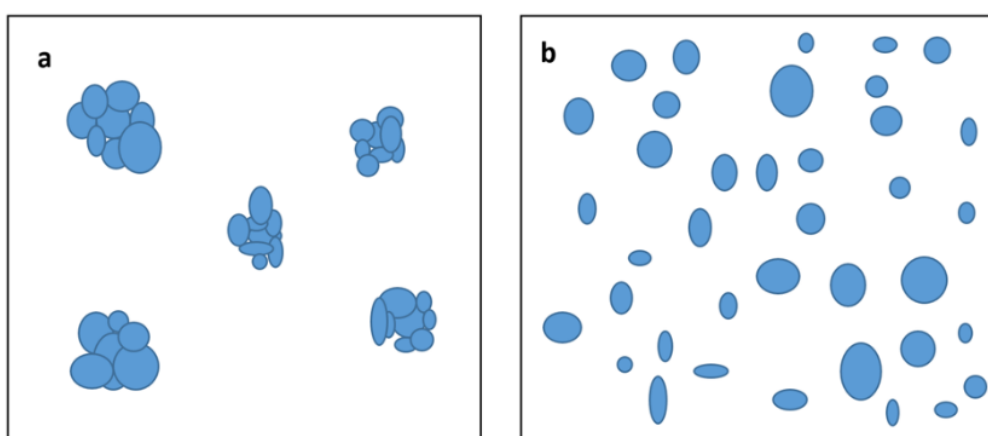
Figure 5.13 Viscosity versus the shear rate at 1wt. % and 2 wt. % with 25 °C

The viscosity of nanofluids is one of the most vital parameters, as it strongly affects the performance of heat transfer fluids. DI water, as is expected, shows a Newtonian behaviour in the rate ranges varied from 10 /s to 100 /s. To determine the rheological behaviours of BN nanofluids, the viscosity of BN/DI water nanofluids versus shear rate was measured and the results are shown in Figure 5. 12 and Figure 5. 13.

Figure 5. 12 reports the viscosity of 0.5 wt. % BN/DI water nanofluid versus the shear rate at 25 °C.

The suspension in this concentration still showed Newtonian behaviour. Applying the Newtonian regression, the value of viscosity was 0.9108 mPa·s which was close to the DI water's value of 0.9028 mPa·s. However, with the concentration of nanofluid increase, the rheology behaviour changed. As is shown in Figure 5. 13, the viscosity of BN suspensions with a concentration of 1.0 wt. % and 2.0 wt. % decreased exponentially as a function of shear rate. Thus, the nanofluids showed shear-thinning (pseudo-plastic) behaviour.

The cause of this shear-thinning behaviour can be generally explained as follows. As is shown in Figure 5. 14 when nanofluids are at rest, small primary particles form into agglomeration. Meanwhile, they surround a part of the dispersion and immobilize it. When the shearing force is applied to the nanofluid, the shearing disintegrates agglomerations into primary particles. Usually, the effectivity of interactive forces between the particles is gradually reduced. Thus, the flow resistance decreases. The observed shear-thinning behaviour indicates the nanofluids is unstable in the given concentrations, thus, in the following measurement, only 0.05 wt. % -0 .5 wt. % was considered and measured.



CHAPTER 5 RESULTS AND DISCUSSIONS

Figure 5. 14 Structure changes of nanofluids showing shear thinning behaviour: (a) at rest and (b) during shearing

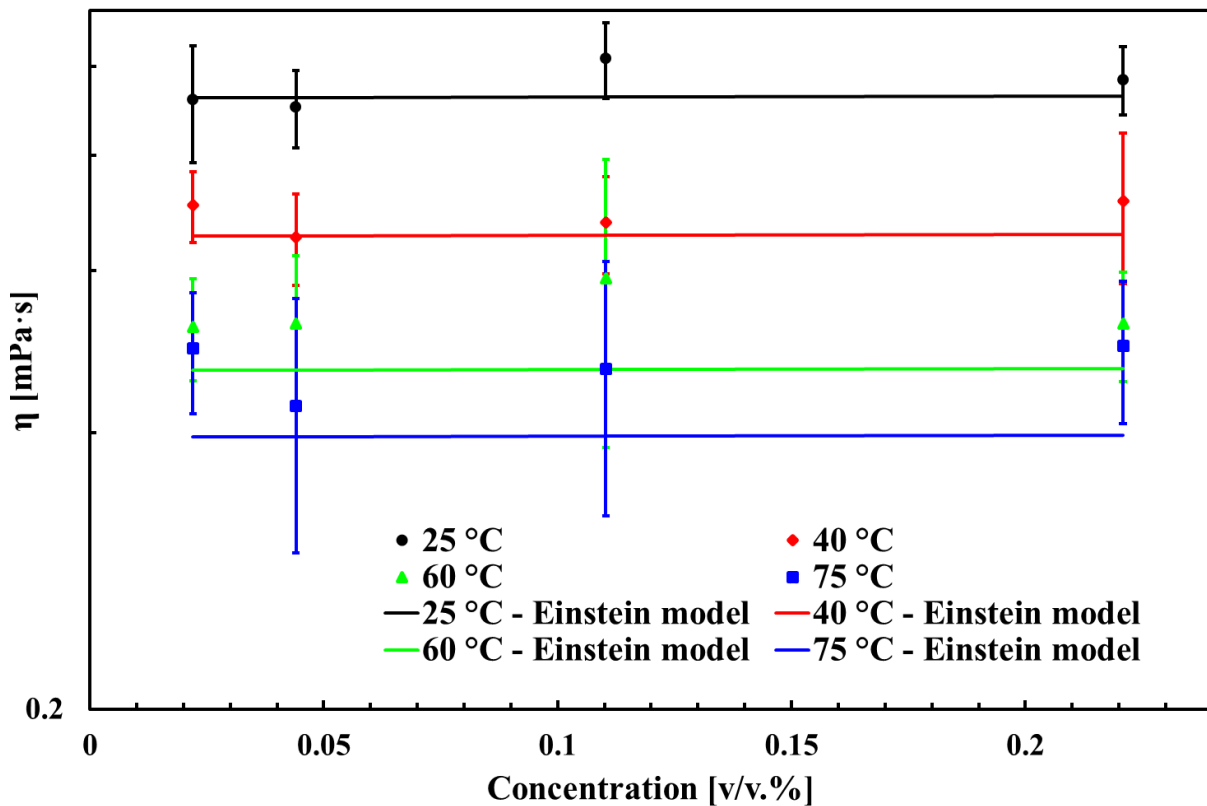
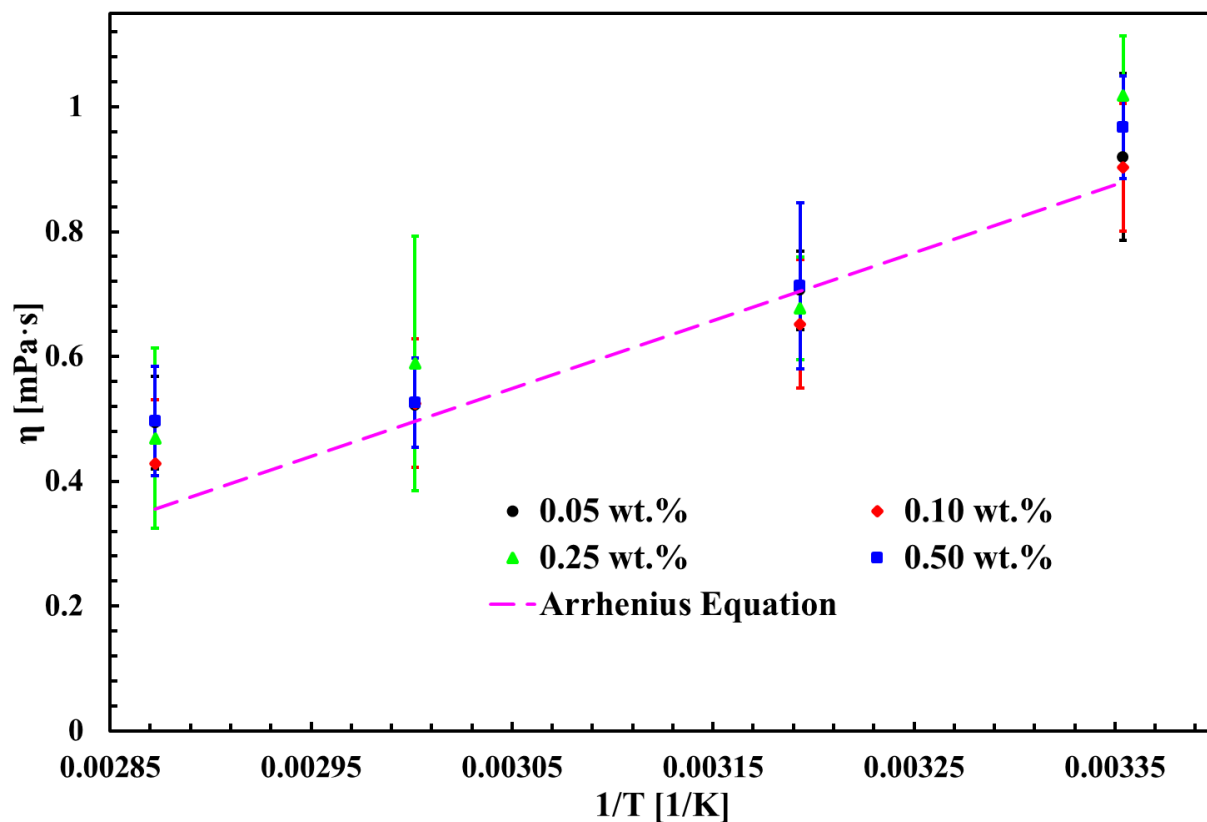


Figure 5. 15 Viscosity versus concentration at various temperatures with the Einstein equation



CHAPTER 5 RESULTS AND DISCUSSIONS

Figure 5. 16 Viscosity versus temperature at various concentrations with Arrhenius equation

Two important factors, concentration and temperature, were investigated for the BN/DI water nanofluids. Figure 5. 15 reports viscosity versus concentration at various temperatures with the Einstein equation. The increase of the viscosity of the suspension with hard solid spheres was first predicted by Einstein in 1906. He presented the following relation describing this enhancement:

$$\frac{\eta_{nf}}{\eta_{bf}} = 1 + 2.5\varphi \quad (5-3)$$

Where η_{nf} and η_{bf} is the viscosity of nanofluids and base fluids.

According to Figure 5. 15, because of the low concentration of nanofluids Einstein model suited well with the measured data. It can be seen that nanofluids show no obvious increase in viscosity in the given concentration range. Those values are similar to the water at that temperature.

Similar to simple fluids, the temperature is one of the main effective parameters on the viscosity of nanofluids. According to Figure 5. 16, nanofluids are strongly dependent on temperature, the viscosity decreased for higher temperatures. As the viscosity was close to DI water, the Arrhenius equation was used to predict the viscosity versus temperature.

$$\eta = Ae^{\frac{Q}{RT}} \quad (5-4)$$

Where A is a coefficient, Q is the activation energy and R is the universal gas constant.

According to Figure 5. 16, the Arrhenius equation can well suit the measured data. This meant that the viscosity exponentially dropped with the increase in temperature. The reason for the decrease is due to the weakening of the inter-particle and intermolecular adhesion forces.

- ***Electrical conductivity***

The electrical conductivity of nanofluids is important for the electronic device, as it required the minimum electromagnetic interference with the nanofluids. Here, the electrical conductivity at room temperature was measured. As is shown in Figure 5. 17, the electrical conductivity of nanofluids increased linearly with the concentration of BN. The electrical conductivity at 0.05 wt. % was around

120 $\mu\text{S}/\text{cm}$ and at 0.5 wt. %, it increased to about 600 $\mu\text{S}/\text{cm}$. The reason for the linear increase was that the pH of nanofluids gradually increased in the wet milling process. The change in pH meant electrical conductivity of nanofluids also increased. Then the high concentration of nanofluids diluted into desired concentration with DI water, thus the electrical conductivity showed a linear increase.

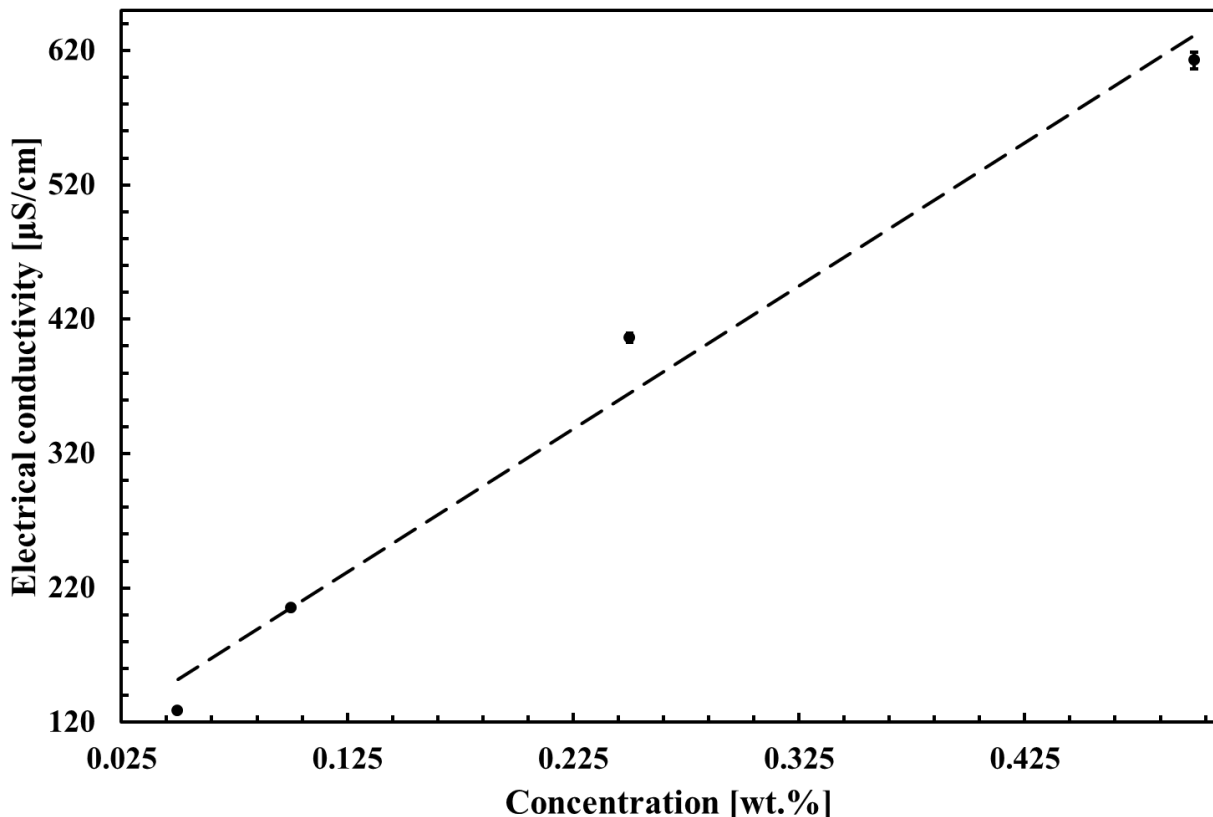


Figure 5. 17 Electrical conductivity as a function of concertation at room temperature

- ***Summary of results for the Boron Nitride nanofluids***

The following are main observations of the formulation and characterisations of BN/DI nanofluids:

- The average particle size of wet milling process BN/DI water nanofluids was 247 nm which was 100 nm small than the one without the wet milling process.
- Method of sonication without surfactants showed the worst stability. 2 weeks good stability can be achieved via the method of sonication with surfactant and method of wet milling.
- The wet milling BN/DI water nanofluids had a ζ potential large than -25 mV. The BN nanofluid showed good stability with its concentration no larger than 0.5wt. %.

CHAPTER 5 RESULTS AND DISCUSSIONS

- The thermal conductivity at 65 °C with 0.5 wt. % showed about 5.2 % enhancement compared with DI water. In addition, the Prasher et al. model can suit the thermal conductivity change with temperature and concentration well.
- The rheology showed that 1 wt. % and 2 wt. % of nanofluids had shear-thinning behaviour. This meant nanofluids are unstable. With concentration no larger than 0.5 wt. %, Newtonian behaviour had been observed. Besides, the viscosity change with concentration followed the Einstein equation. Moreover, the viscosity change with temperature followed the Arrhenius equation.
- The electrical conductivity was about 600 $\mu\text{S}/\text{cm}$ at 0.5wt. %. The electrical conductivity linearly decreases with the concentration decrease.
- The concentration of 0.5 wt. % BN/DI water nanofluids with wet milling was applied for the microfluidic channel.

5.1.2. Ethylene glycol+distilled water based nanofluids - formulation and characterisation

In order to work in the temperature as low as -50 °C, Ethylene Glycol (EG) with distilled water (DW) (6:4) was chosen for the heat transfer fluid. The graphene due to its high thermal conductivity and other properties was chosen as the nanoparticles.

- ***Nanofluids formulation***

Graphene (> 99.5 % purity, purchased from Nanografi, Turkey) with a nominal diameter of ~150 nm was used to formulate nanofluids with concentrations of 0.5 wt. % ~ 5.0 wt. %. EG, HNO₃ and H₂SO₄ were all purchased from Sigma-Aldrich and used without further purification. H₂SO₄ and HNO₃ were used as oxidizing agents for the acid treatment of graphene [236].

As is shown in Figure 5. 18, 4 g of graphene was added in 80 mL of a 1:3 mixture of HNO₃ (64-65 wt. %) / H₂SO₄ (>95 wt. %). The suspension was sonicated in a water bath at 75 °C for 6 h. The resultant suspension was filtered with a 200 nm pore membrane filter. After cleaning with distilled water, the filter cake was put into the vacuum oven for 45 °C overnight to collect the dry rGO. Then the two-step method was applied for synthesising the concentration needed.

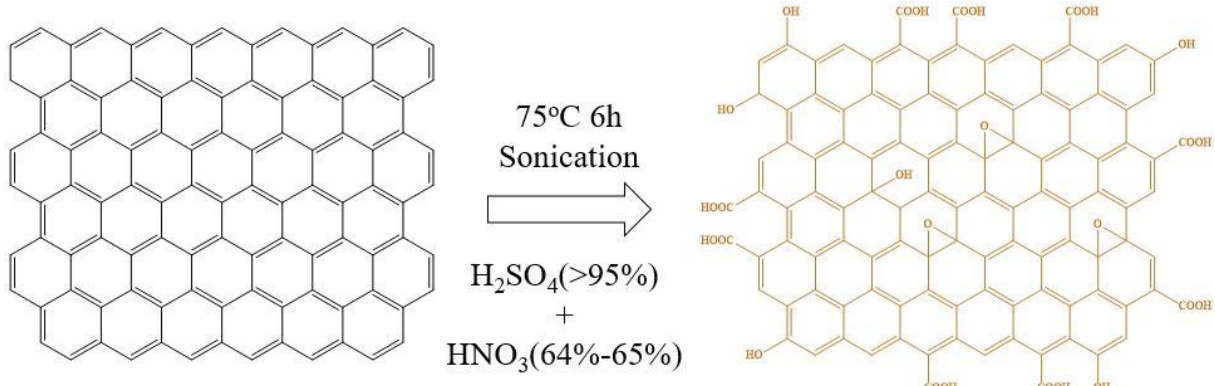


Figure 5. 18 Reaction scheme for the acid treatment of Graphene

- ***Morphology***

The morphology of the dry graphene powder and rGO nanoparticles were studied through ESEM analyses working at an accelerator voltage of 15 kV. As is shown in Figure 5. 19, graphene dry nano-

powders and rGO nanoparticles had flake-like morphology. The dry nanopowder had an estimated average size of 2 μm that was close to the manufacturer's given value. The ESEM image clearly showed the agglomeration of the dry powder. After the chemical reaction and ultrasonication, the rGO nanoparticle's size decreases to ~ 800 nm.

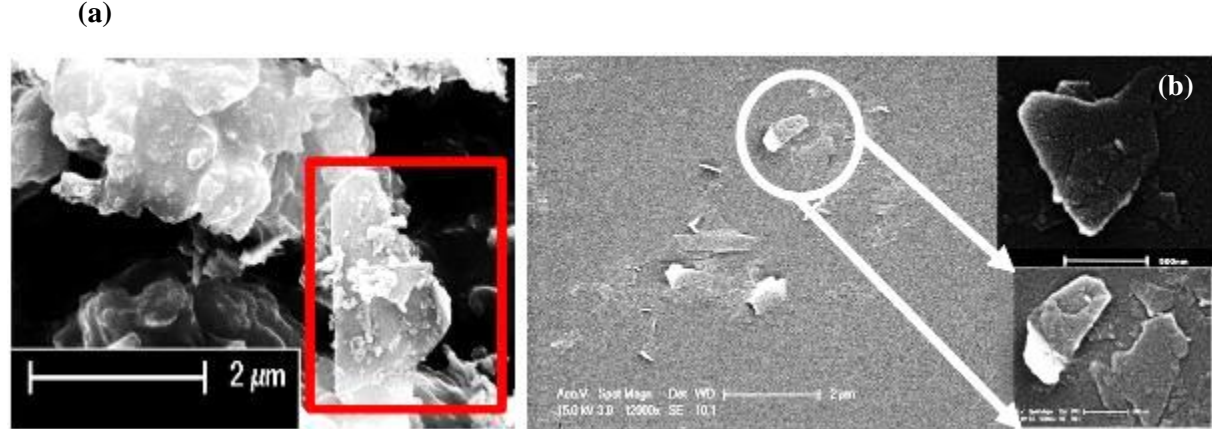
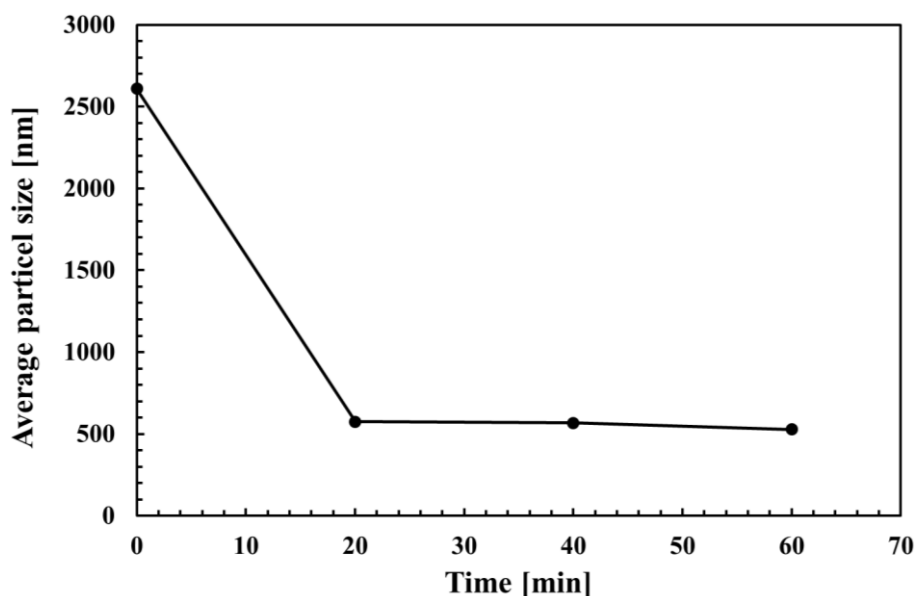


Figure 5. 19 ESEM of (a) graphene and (b) well-dispersed rGO nanoparticles

- ***Hydrodynamic size distribution***

The size distribution of the nanoparticle in the dispersions was studied at 20 °C by analysing the random changes in the intensity of scattered light collected with an angle of 173 °. In order to obtain the ultrasonication time, the apparent size with the ultrasonication time was investigated as is illustrated in Figure 5. 20. It should be mentioned that the DLS measurement has an assumption that that particles measured are spherical. However, the studied rGO nanoparticles are flake-like.



CHAPTER 5 RESULTS AND DISCUSSIONS

Figure 5. 20 Apparent particle size with ultrasonication

The average apparent size without any ultrasonication was over 2500 nm. With 20 min ultrasonication, it reached a plateau of 500 nm and barely showed any significant change for the following 40 min. Thus, 20 min was used in the following fabrication. Figure 5. 21 presented the particle size distribution of rGO in EG+DW media with 20 min ultrasonication. A bimodal distribution with apparent size from 100 nm to around 1000 nm was observed. It can be seen from Figure 5. 21 that the location of the second peak was around 800 nm which agreed with the ESEM image.

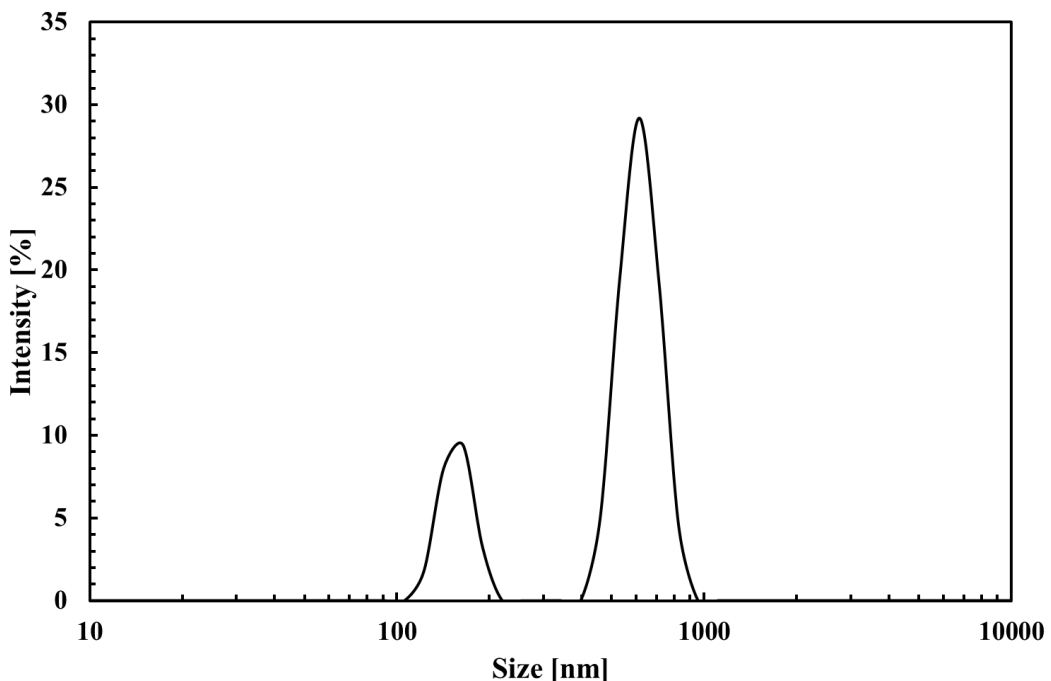


Figure 5. 21 Particle size distribution of rGO in EG+DW media after 20 min sonication

- **Stability**

Zeta potential was studied as a function of pH. Due to the acidic groups introduced in the graphene, pH of the rGO/EG+DW without any adding of HCl and/or NaOH was 3.84 for the concentration of 0.1 wt.%. HCl and NaOH were added into the dispersion to adjust pH from 2 to 12. As is indicated in Figure 5. 22, ξ potential seemed to be a constant around -50 mV for pH from 2 to 4 and then it decreased with the increase of pH. The ξ potential reached -120 mV at a pH value of 12. Since in all measured range, the absolute value of ξ potential was larger than 25 mV, the pH of rGO/EG+DW nanofluids did not change during the rest characterisation.

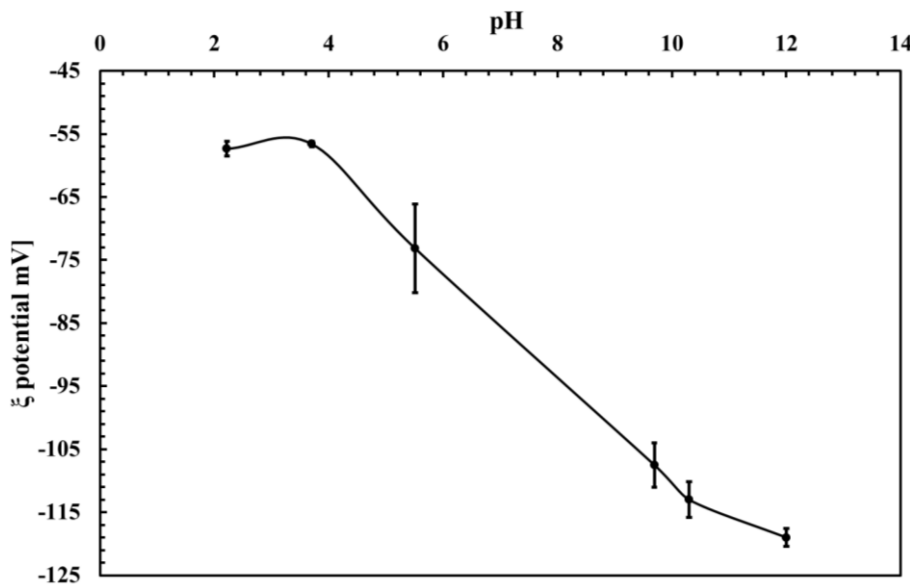
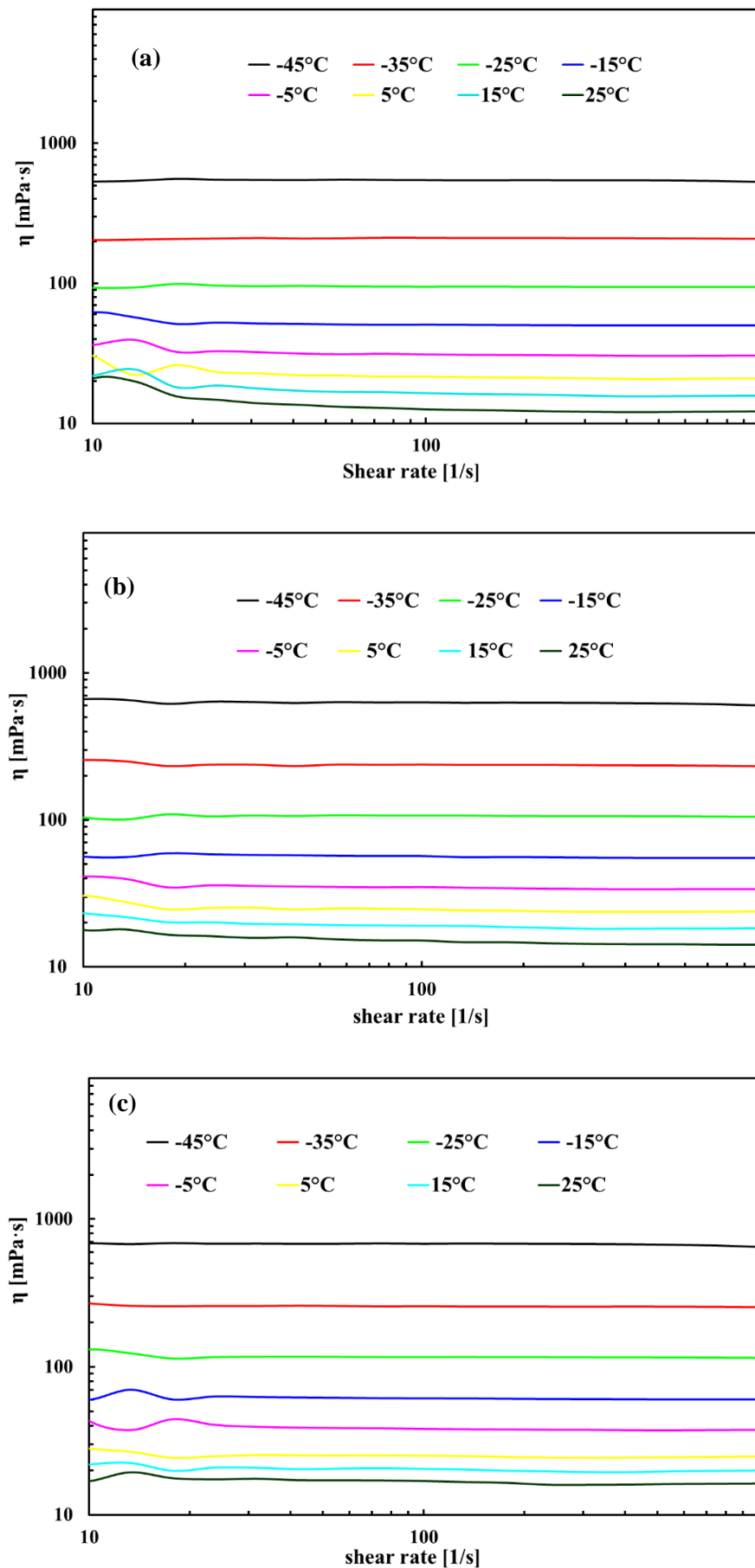


Figure 5. 22 ξ potential as a function of pH for rGO nanoparticles in EG+DW media

- **Viscosity**

The viscosity was measured with the rheometer (MCR502 Anton Paar, Austria) in the temperature range from - 45 °C to 25 °C. As is shown in Figure 5. 23, the viscosity of the base fluid showed Newtonian behaviour. With the increase of shear rate, the viscosity did not show significant change. For nanofluid, with a concentration of nanoparticle up to 2.0 wt. %, the viscosity still showed Newtonian behaviour. It can be observed that the viscosity of 0.5 wt. % nanofluid was higher than the base fluid. 2.0 wt. % nanofluid showed higher viscosity than 0.5 wt. % nanofluids in all temperature range. However, an obvious shear-thinning behaviour was detected in the measured shear rate range of 10 /s to 1000 /s for all the measured temperature from - 45 °C to 25 °C with the concentration increase to 5.0 wt. %. The shear-thinning behaviour indicated the nanofluids were unstable at this concentration.

As is seen in Figure 5. 24, the viscosity of both 2.0 wt. % rGO/EG+DW nanofluid and base fluid increased with the decrease of temperature. Both base fluid and 2.0 wt. % nanofluid followed the Arrhenius model. The viscosity difference between nanofluid and base liquid (133 mPa·s at - 45 °C) decreased with temperature increase, which became very small at room temperature (4 mPa·s at 25 °C).



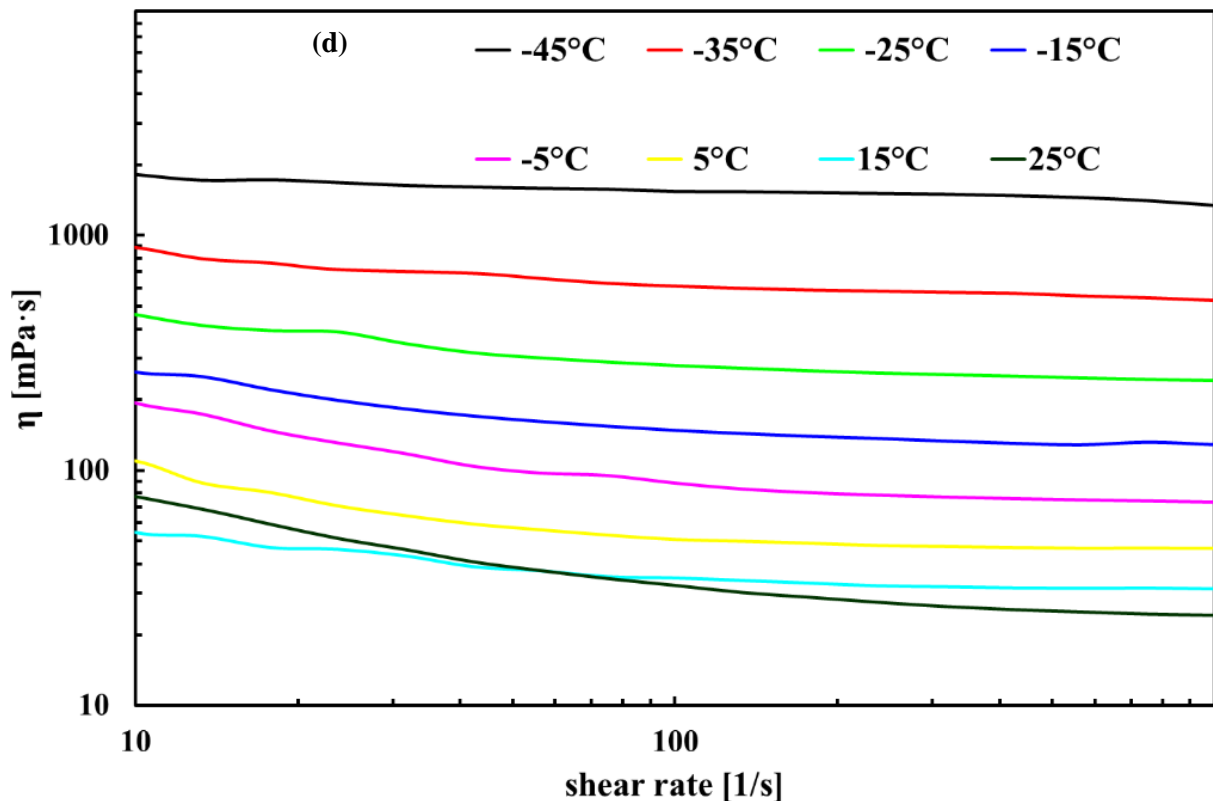


Figure 5. 23 Apparent shear viscosity (a) base fluids(b) 0.5 wt.%,(c) 2.0 wt% and (d) 5.0 wt% - influence of temperature.

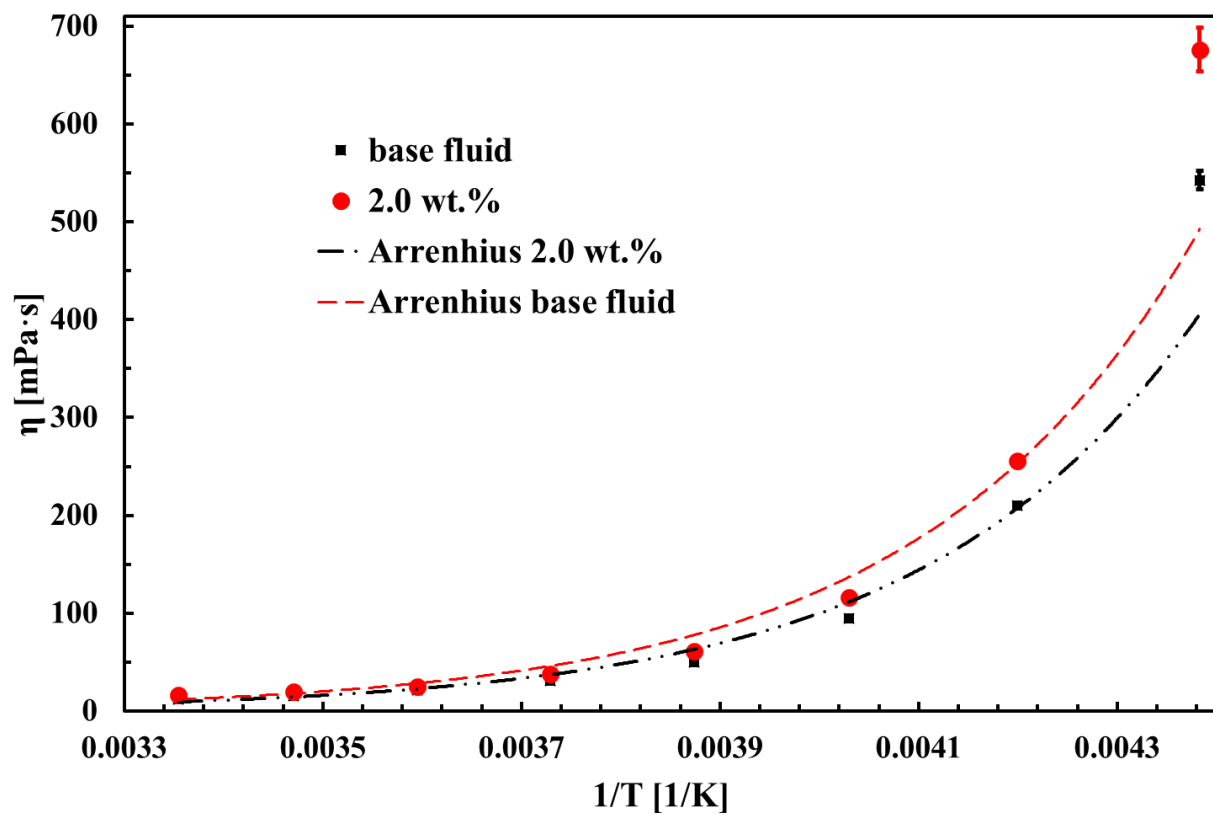


Figure 5. 24 Temperature dependence of dynamic viscosity

- *Thermal conductivity*

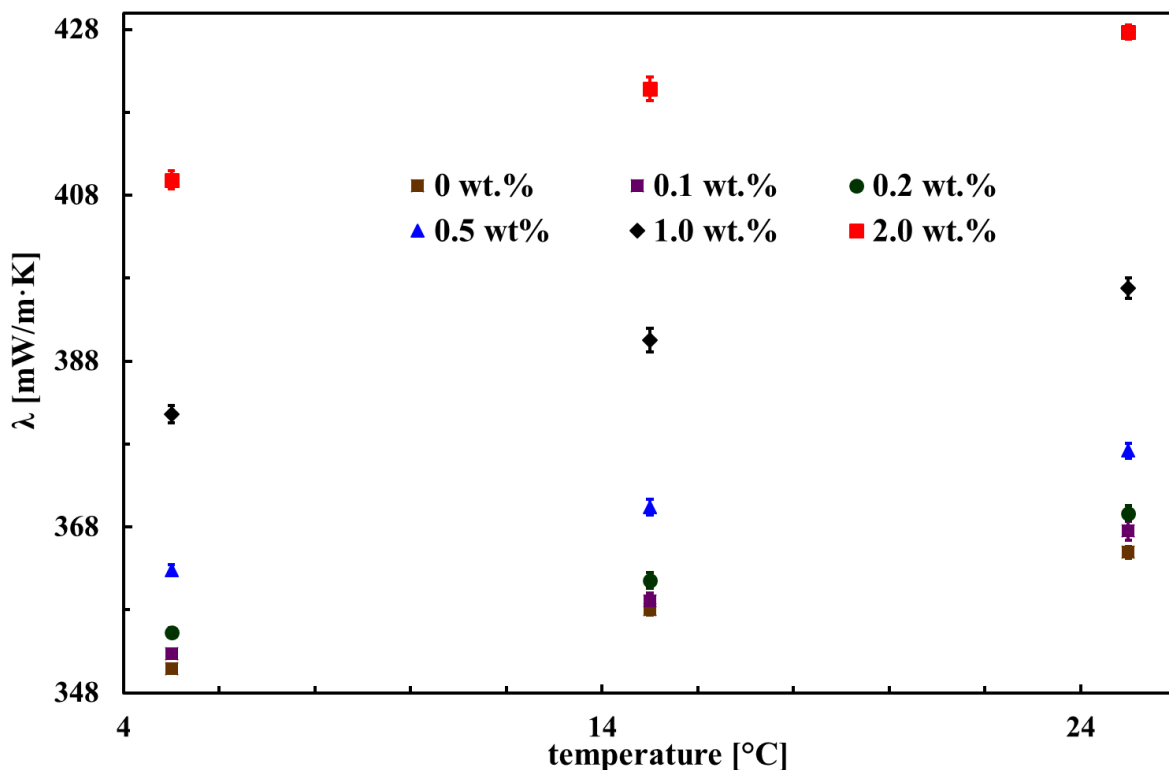


Figure 5.25 Thermal conductivity versus concentration at various temperature

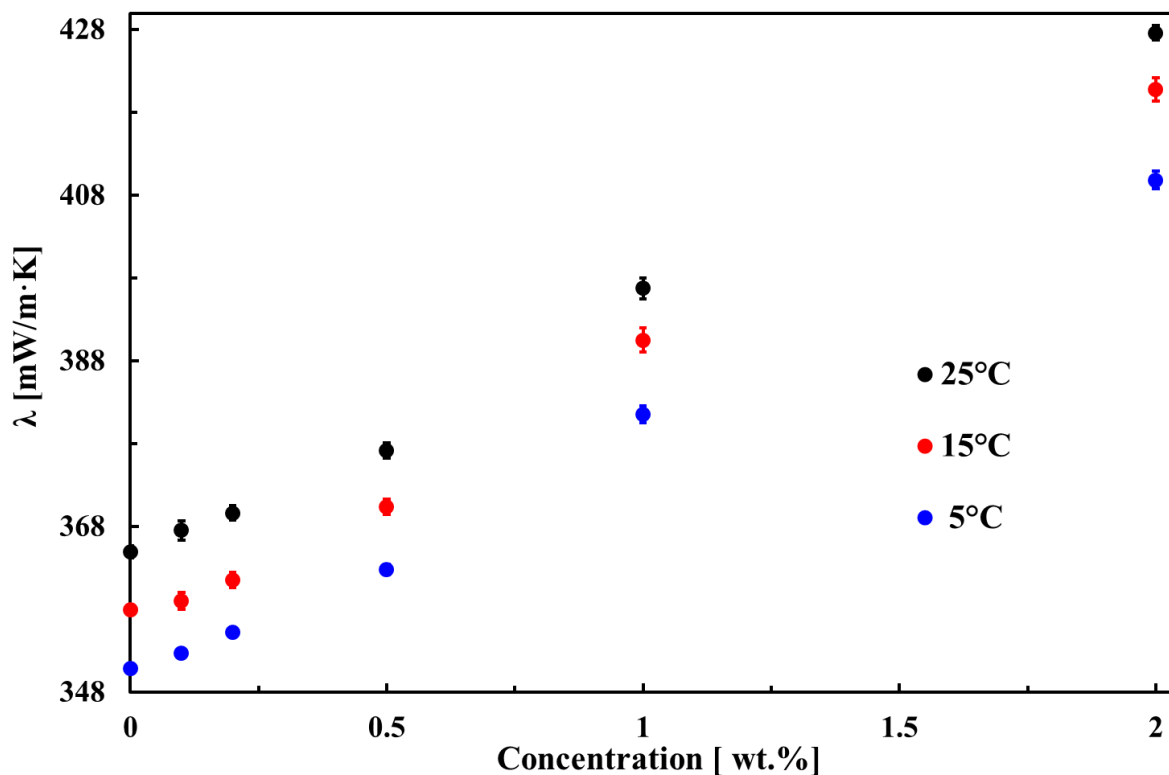


Figure 5.26 Thermal conductivity versus temperature at various concentrations

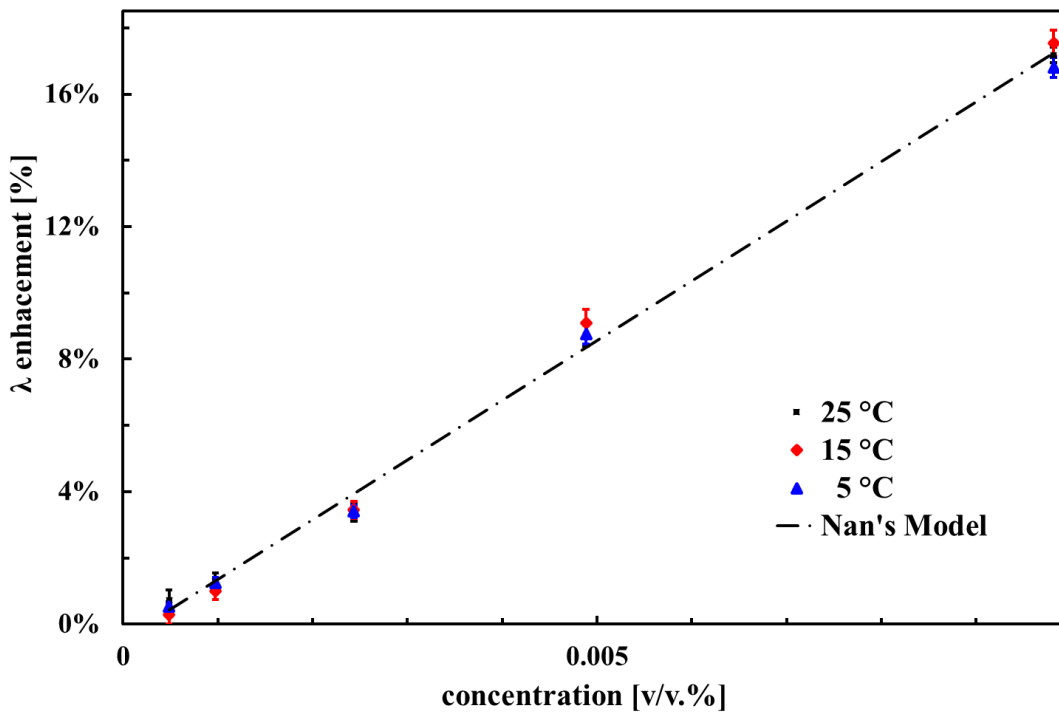


Figure 5. 27 Thermal conductivity of rGO/EG+DW nanofluids and its enhancement

The thermal conductivity was measured using a lambda measuring system (PSL Systemtechnik GmbH, Germany) in the temperature range from 5 °C to 25 °C. As is shown in Figure 5. 25, the thermal conductivity of the base fluid and nanofluids both enhanced with the increase of temperature. As is shown in Figure 5. 26, with concentration increasing from 0 wt. % to 2.0 wt. %, a linear increase in thermal conductivity was observed in all the measured temperature range. In order to investigate the increase of thermal conductivity with concentration, the thermal conductivity enhancement was used and compared with possible theory as is shown in Figure 5. 27. It can be seen that the thermal conductivity enhancement in line with the effective medium theory prediction Nan's model [237]. The reason is likely to be due to good dispersion of nanoparticle. The temperature showed little effect on thermal conductivity enhancement. An enhancement of 17 % achieved with 2.0 wt. % nanoparticles.

$$k/k_f = \frac{3+\emptyset[2\beta_{11}(1-L_{11})+\beta_{33}(1-L_{33})]}{3-\emptyset(\beta_{11}L_{11}+\beta_{11}L_{11})} \quad (5-5)$$

$$\beta_{ii} = \frac{k_p - k_f}{k_f + L_{ii}(k_p - k_f)} \quad (5-6)$$

Where $L_{11}=0$ and $L_{33}=1$, as the aspect ratio of rGO is very high.

- *Summary of results for reduced graphene oxide nanofluid*

The main conclusions for the rGO/EG+DW nanofluids are:

- After 20 min sonication and surface modification, the size of the agglomeration of flake-like nanoparticles decreased from $\sim 2 \mu\text{m}$ to $\sim 800 \text{ nm}$
- The absolute value of ξ potential of nanofluids with pH showed an increase with the increase of pH. Its value of -50 mV at pH is 2 suggested good stability in all the measured pH range.
- The base fluid and nanofluids up to a concentration of 2.0 wt. % showed Newtonian behaviour. However, for the concentration of 5.0 wt. % showed an obvious shear-thinning behaviour which suggests the poor stability in this concentration.
- The enhancement thermal conductivity of nanofluids with concentration agreed well with effective medium theory, with a 17 % increase at concentration of 2.0 wt. %
- The concentration of 2.0 wt. % rGO/EG+DW nanofluids were applied for the microfluidic channel.

5.2. Results and discussion 2 - Microfluidic channels

This section presents the results of two microfluidic channels of the cooper-foam based microfluidic channels and the micro-jet based microfluidic channels; including both experimental and modelling results.

5.2.1. Performance of copper-foam based microfluidic channels

The copper-foam based channel was tested due to its potential of a high heat transfer coefficient due to the large surface area to volume ratio (about 1000-3000 m²/m³) [163] and the porous metal tortuosity providing an extended heat transfer area. The copper-foam used in the experiment had the pore per inch (PPI) of 50 and the porosity of the copper-foam was 95 %.

- *Geometry optimisation*

Three different types of copper-foam based microfluidic channels were investigated in the experiments. They are illustrated in Figure 5. 28, marked as GEO1, GEO2 and GEO3 and representing three generations of development, respectively. In the GEO 1, the size of the copper-foam size was 52 × 52 × 10 mm. The copper-foam was inserted in the channel made with copper. The cross-section area of the channel for the copper-foam was 520 mm². It was made with pure copper material. To enhance and optimise the channel performance, GEO 2 and GEO 3 were designed and fabricated with aims to reduce the size and enhance heat transfer.

The size of the GEO2 copper-foam channel was 10 × 10 × 5 mm. To use the same copper casing and the lid, 3D printed insertion was made to fit the channel. The insertion was made of polymeric material with low thermal conductivity. The design allowed the creation of a converging flow into the microfluidic channels, realised by the use of a changing cross-sectional area from 10 × 10 mm at the inlet to 10 × 5 mm at the copper foam channel inlet. The size is 10.4 times smaller compared with the GEO 1. To fix the 10×10×5 mm copper foam in the channel, the size of the fluids chamber shown in Figure 5. 28 was designed as 12 × 10 × 5 mm. The outlet diverging flow pipe design was symmetrical.

CHAPTER 5 RESULTS AND DISCUSSIONS

GEO 3 is a further optimised version with a cross-section area further reduced compared with GEO2. Although the volume of copper-foam of the GEO 3 was also set to be $10 \times 10 \times 5$ mm, the converging inlet pipe cross-section area was reduced from 10×10 mm to 2×1 mm. Then, the heat transfer fluid flowed through the copper-foam chamber with a volume of 500 mm^3 for the copper foam. A diverging pipe flow with an area increases 2×1 mm to 10×10 mm was followed. Compared with the GEO 1, the cross-sectional area of the GEO3 was 260 times smaller (2mm^2 for GEO3, 52mm^2 for GEO1) The dimension of the copper-foam for the GEO3 was the same as the printed hole in the middle of the channel which was $10 \times 10 \times 5$ mm.

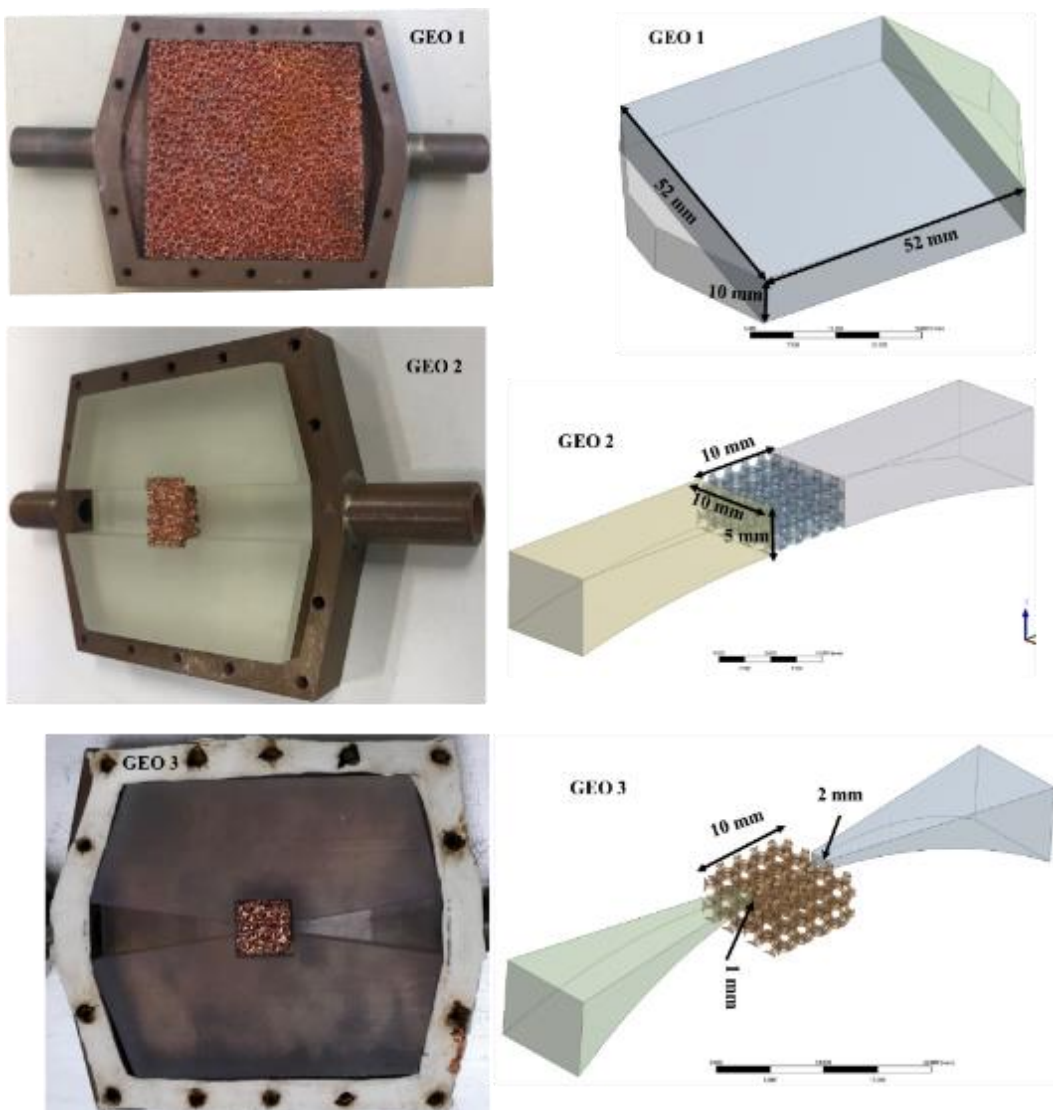


Figure 5.28 3 types of the copper-foam based microfluidic channel

- *Experimental test - rig*

Three K type thermocouples with an accuracy of ± 1.5 °C were inserted to the test rig as illustrated in Figure 5. 29. Two of the thermocouples were positioned at the inlet ($T_1=T_{in}$) and outlet ($T_3=T_{out}$). The third thermocouple (T_2) was positioned at the bottom surface of the diamond heat spreader. The diameter of the T_2 thermocouple was 75 μm and was attached to the centre of the diamond heat spreader. The measured temperatures were used to calculate the heat transfer coefficient and thermal resistance.

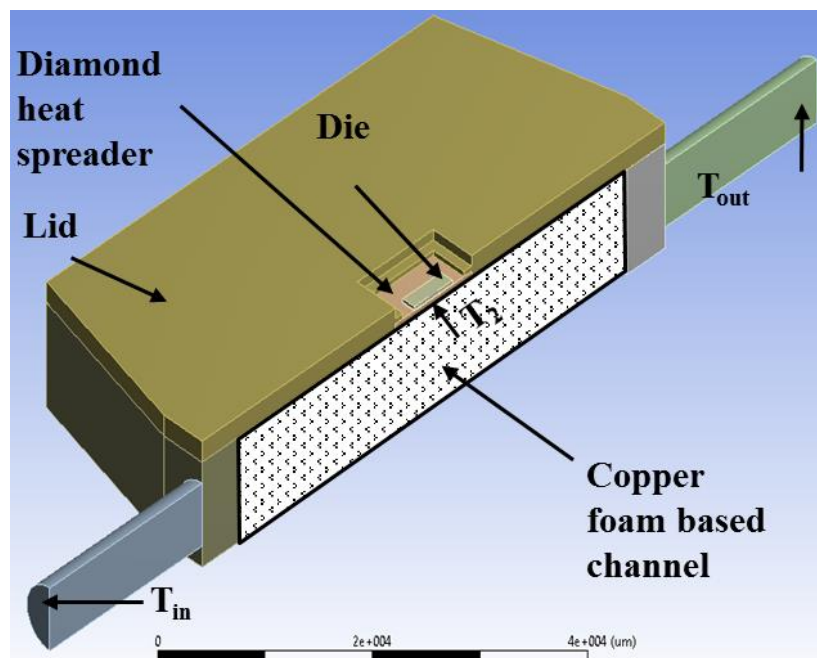


Figure 5. 29 Schematic diagram of the test rig with thermocouples inserted in

Two important parameters for the evaluation of the performance of the copper-foam based microfluidic channels are the heat transfer coefficient and the thermal resistance of the channel. A schematic diagram of the heat transfer coefficient and thermal resistance distribution is shown in Figure 5. 30. For the calculation the heat transfer coefficient, the following assumptions were made: firstly, the heat flux was homogeneously distributed at the bottom of the die surface; and secondly, the heat transfer coefficient was uniformly distributed in the microfluidic channel. The equations for the calculation of the heat transfer coefficient and the thermal resistance are as followed:

$$htc = \frac{q}{\Delta T} \quad (5-7)$$

$$q = \frac{Q}{A} \quad (5-8)$$

$$\Delta T = T_{diamond} - T_{in} \quad (5-9)$$

$$R_{th} = \frac{Q}{\Delta T} \quad (5-10)$$

where q is the heat flux at the bottom surface of the die; ΔT is the temperature difference between the centre of the diamond surface and inlet; Q is the power applied to the die; R_{th} is the thermal resistance of the channel; and A is the area of the die which is 1.86×4.82 mm.

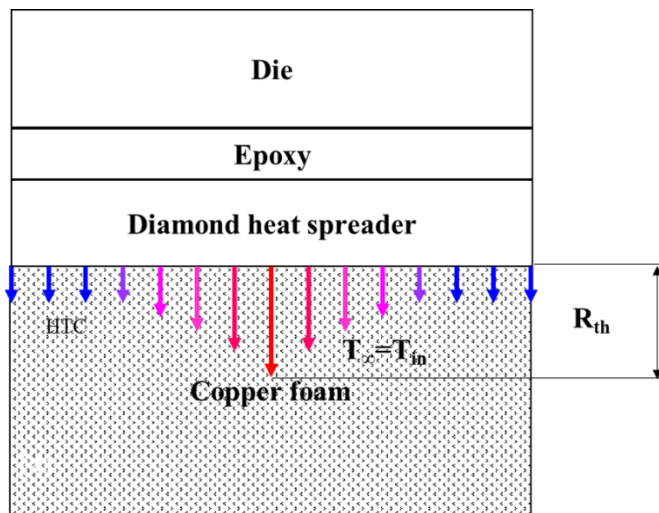


Figure 5. 30 Schematic diagrams of the heat transfer coefficient and thermal resistance distribution

Table 5. 1 Flow rates and power applied on the die in the experiment

Types	0.4 L/min		1.2L/min	
	voltage/current (V/A)	power (W)	voltage/current (V/A)	power (W)
GEO 1	3.000V/2.037A	6.111	/	/
GEO 2	3.000V/2.062A	6.186	3.000V/2.061A	6.183
GEO 3	5.000V/1.200A	6.000	20.000V/1.444A	28.880

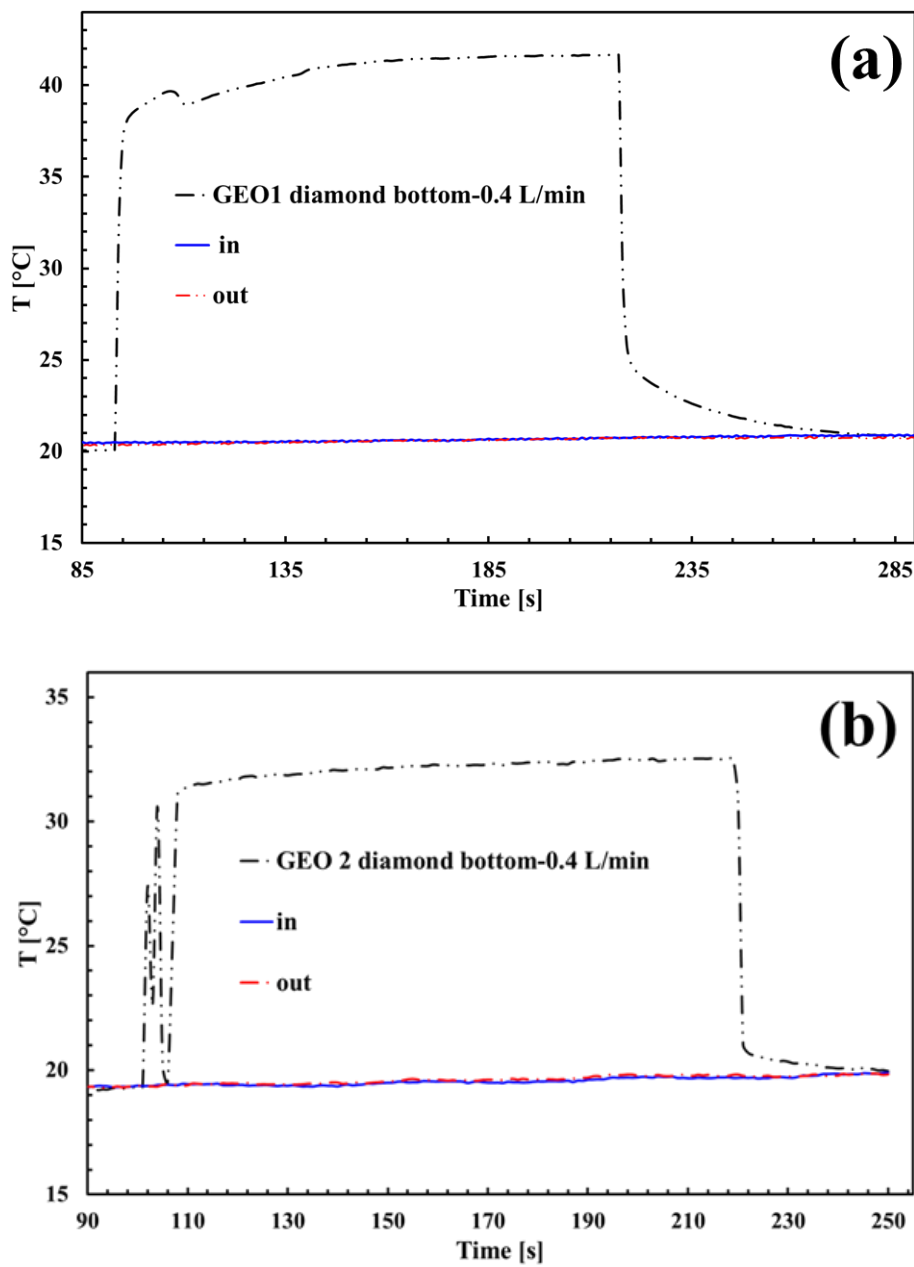
Table 5.1 gives the power level applied to the microchips and flow rate used in the experiments. (1) In the GEO 1, the flow rate of 0.4 L/min was used. In GEO 2, the flow rates were 0.4 L/min and 1.2 L/min. The power applied on the die during experiments with GEO 1 and GEO 2 was 3.000 V and the output power was around ~6W. (2) For the GEO 3 with the flow rate in 0.4 L/min, the voltage applied on the die was 5.000V and the current was 1.200A. Thus, the power applied on the die was 6.000 W. With the flow rate increase to 1.2 L/min, to decrease the uncertainty of heat transfer coefficient and thermal resistance, the voltage applied on the die was set to be 20.000V and the current was 1.444 A. and the power was set on the 28.880 W.

- ***Temperature distribution in the channel***

The temperature distribution in the channel as a function of time is illustrated in Figure 5. 31, showing the thermal performance of the copper-foam-based microfluidic channel. In all of the experiments, there were three stages: no-power stage; on-power stage; and off-power stage. In the no-power stage, there was no power applied to the device. The inlet temperature, outlet stage and the temperature on the surface of diamond heat spreader were almost the same. In the on-power stage, with the power applied to the transistors, the temperature on the surface of the diamond heat spreader immediately soared while the inlet and outlet temperature showed little change. The reason for this temperature behaviour in the channel suggested that (a) the heat flux can be immediately transferred to the cooling channel and (b) there was the large temperature gradient in the thin thermal boundary layer.

According to the Figure 5. 31 (a), with about 6 W power applied on the die and a flow rate of 0.4 L/min, the maximum temperature in the diamond heat spreader for the GEO 1 was about 41.52 °C. Thus, the temperature difference ΔT was 20.84 °C. According to the Figure 5. 31 (b) and Figure 5. 31 (c), for the GEO 2 with a flow rate of 0.4 L/min, the maximum temperature on the surface of the diamond heat spreader was 32.35 °C and the temperature difference ΔT was 12.73 °C. It showed that the optimized channel had better performance than the original design. With the flow rate increased 3 times, the maximum temperature slightly decreased to 31.46 °C. Thus, the temperature in the diamond heat spreader showed 1.16 °C decrease.

According to the Figure 5. 31 (d), in the GEO 3 with a flow rate of 0.4 L/min and power of 6 W applied on the device, the maximum temperature on the surface of diamond heat spreader was 29.75 °C and the temperature difference was 10.09 °C. This suggested the GEO 3 had better performance than the GEO 2. In the GEO 3 with a flow rate of 1.2 L/min and the output power of 28.88 W applied on the device, according to Figure 5. 31 (d), the maximum temperature on the surface of diamond heat spreader fluctuations in the on-power stage with the average temperature 60.04 °C and the temperature difference about 41.37 °C can be calculated during the test. The reason for the fluctuations of the temperature might due to the unstable performance of the transistors due to the high temperature.



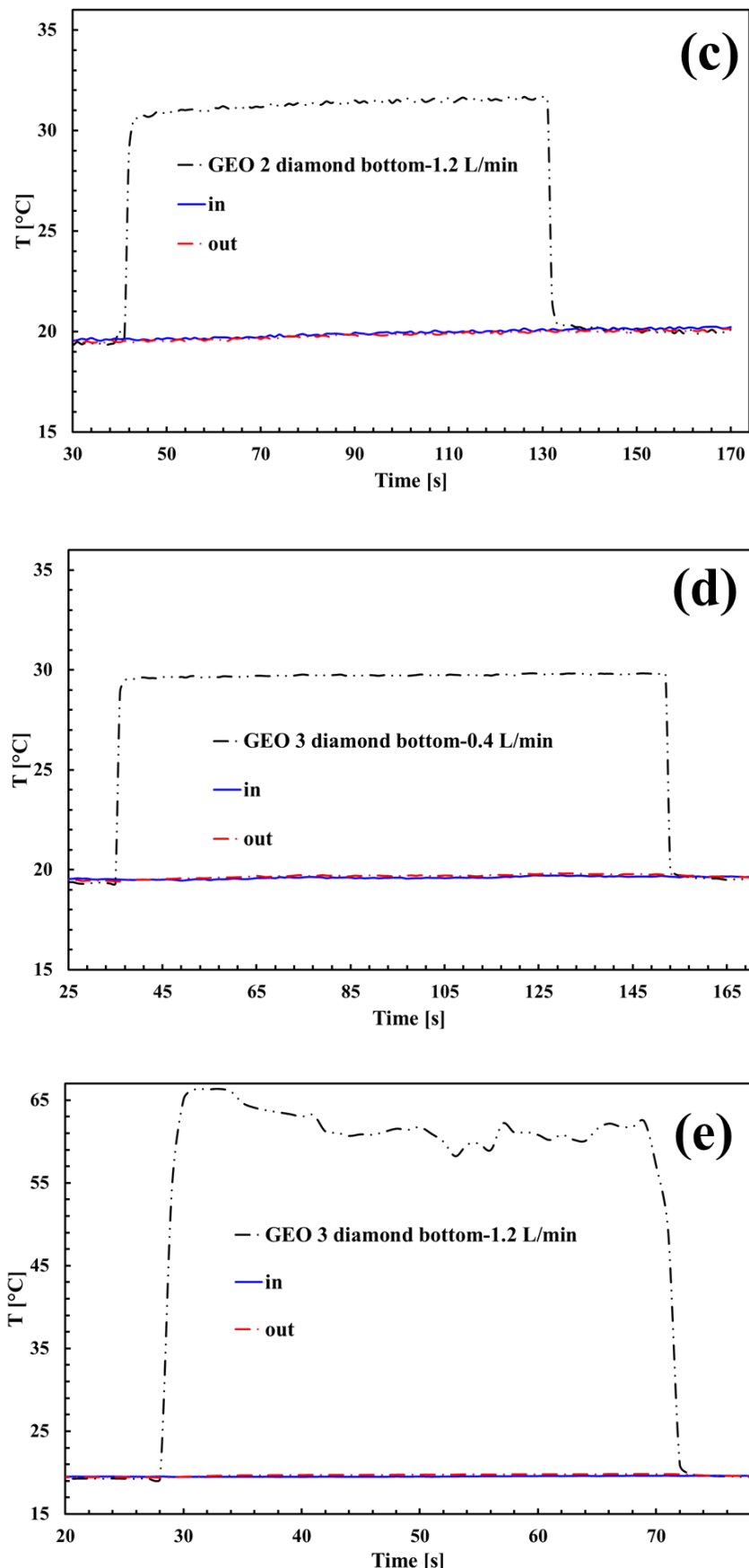


Figure 5. 31 Temperature measured in the experiment for GEO 1, GEO 2 and GEO 3

- ***Heat transfer coefficient and thermal resistance***

In order to quantify the thermal performance of different types of the microfluidic channel, the heat transfer coefficient and the thermal resistance were calculated and illustrated in Figure 5. 32. The heat transfer coefficient of the GEO 1 with the flow rate of 0.4 L/min was 32.718 kW/(m².°C). The heat transfer coefficient of the GEO 2 with the same flow rate was about 54.212 kW/(m².°C) which was 1.7 times higher than its counterpart. And with 3 times increase of the flow rate, the heat transfer coefficient showed a slight increase of 5.439 kW/(m².°C). The heat transfer coefficient for the GEO 3 was 2.0 times higher the GEO 1 with the flow rate of 0.4 L/min. With the flow rate increase to 1.2 L/min, an 11.518 kW/(m².°C) heat transfer coefficient was observed.

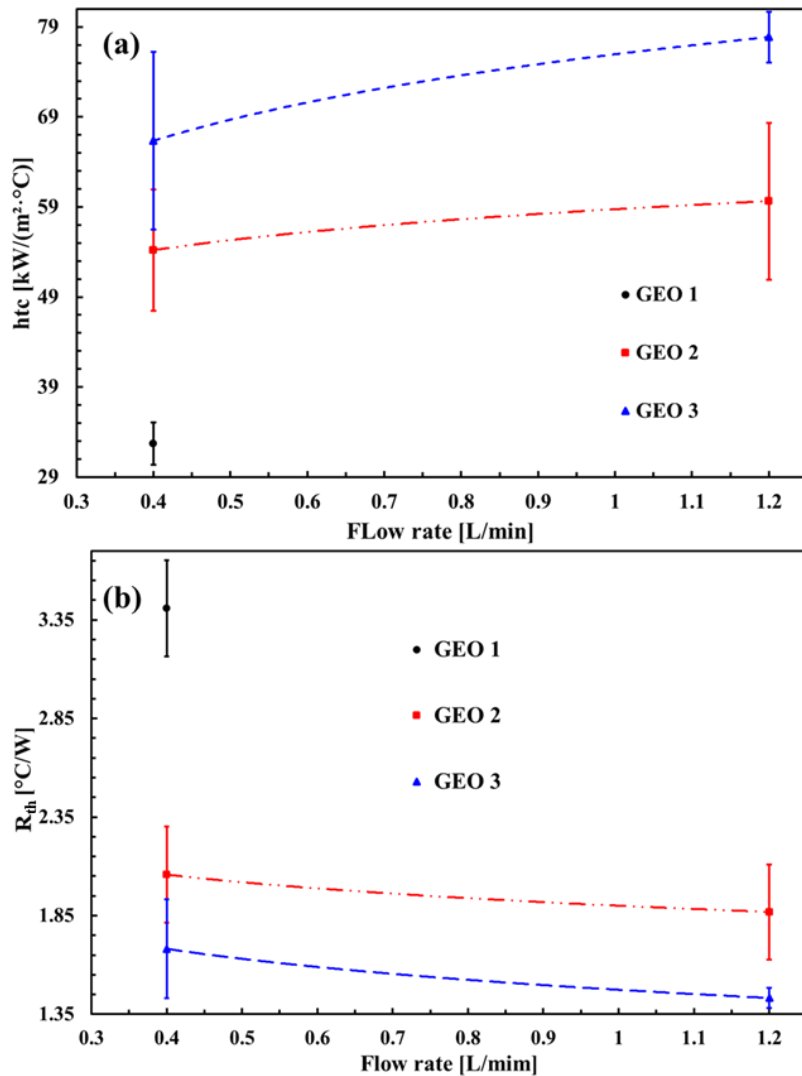


Figure 5. 32 (a) Heat transfer coefficient and (b) the thermal resistance of the copper-foam channel with the flow rate

The thermal resistance showed similar trends. With the flow rate of 0.4 L/min, the thermal resistance in the microfluidic channel for GEO 1 was $3.41\text{ }^{\circ}\text{C/W}$. This value showed $1.35\text{ }^{\circ}\text{C/W}$ decrease for GEO 2 and further $0.38\text{ }^{\circ}\text{C/W}$ was observed for GEO 3. With the flow rate of 1.2 L/min, the thermal resistance in the microfluidic channel for GEO 2 was $1.87\text{ }^{\circ}\text{C/W}$. It was $0.19\text{ }^{\circ}\text{C/W}$ lower than the same geometry with the flow rate of 0.4 L/min. The lowest thermal resistance of $1.43\text{ }^{\circ}\text{C/W}$ was observed for GEO 3 with the flow rate of 1.2 L/min.

- ***Summary for copper-foam based microfluidic channel***

From the copper-foam based microfluidic channel experiments detailed above, the following main observations are obtained

- The feasibility of a thermal package of the microchips with copper-foam-based microfluidic channels has been illustrated. The 3D printing technology was successfully used for the fabrication of miniaturised and optimized geometry of the microfluidic channels.
- Three generations of the designs were performed. The GEO 1 had a heat transfer coefficient of $32.714\text{ kW/(m}^2\cdot{}^{\circ}\text{C)}$ with a flow rate of 0.4 L/min. This value was doubled with the GEO 3. When the flow rate was increased to 1.2 L/min with GEO3, the heat transfer coefficient was $77.874\text{ kW/(m}^2\cdot{}^{\circ}\text{C)}$. As will be shown later, this value is still a lot smaller than the micro-jet impingement channel with a flow rate of 0.25 L/min which has a maximum heat transfer coefficient of $158.5\text{ kW/(m}^2\cdot{}^{\circ}\text{C)}$.
- The GEO 1 had a thermal resistance of $3.41\text{ }^{\circ}\text{C/W}$ with a flow rate of 0.4 L/min. This value decreased to $1.68\text{ }^{\circ}\text{C/W}$ with the optimized geometry of GEO 3. With the flow rate increased to 1.2 L/min with the GEO 3, the thermal resistance further decreased to $1.43\text{ }^{\circ}\text{C/W}$.
- The experiments also showed that the die was burnt out with an applied power of 28.888W . Many reasons could be responsible for this, including low thermal conductivity of the die-attach material, the high SiC layer ($400\text{ }\mu\text{m}$) and insufficient heat transfer coefficient of the microfluidic channel.

5.2.2. Performance of micro-jet channel with deionised water based fluids

This sub-section presents the experimental and modelling results of micro-jet impingement channels with both the DI water and nanofluids including 0.5 wt. % BN/DI water nanofluid, EG+DW (6:4) and the 2.0 wt. % rGO/EG+DW.

- *Characterisation of Micro-jet channel*

The micro-jet impingement channels were introduced in the previous chapter. The designed size for the micro-jet nozzles was 600 μm . As is illustrated in Figure 5. 33, the size of the fabricated nozzle changed slightly within a range of 550 μm -650 μm .

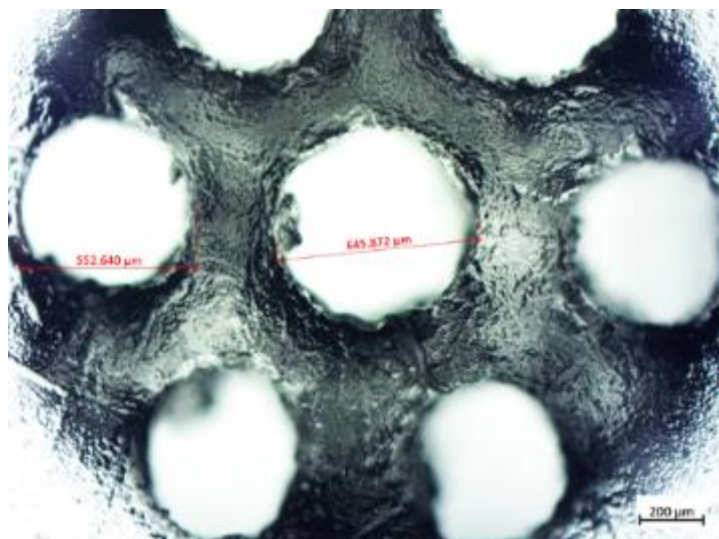


Figure 5. 33 Size of the jetting array

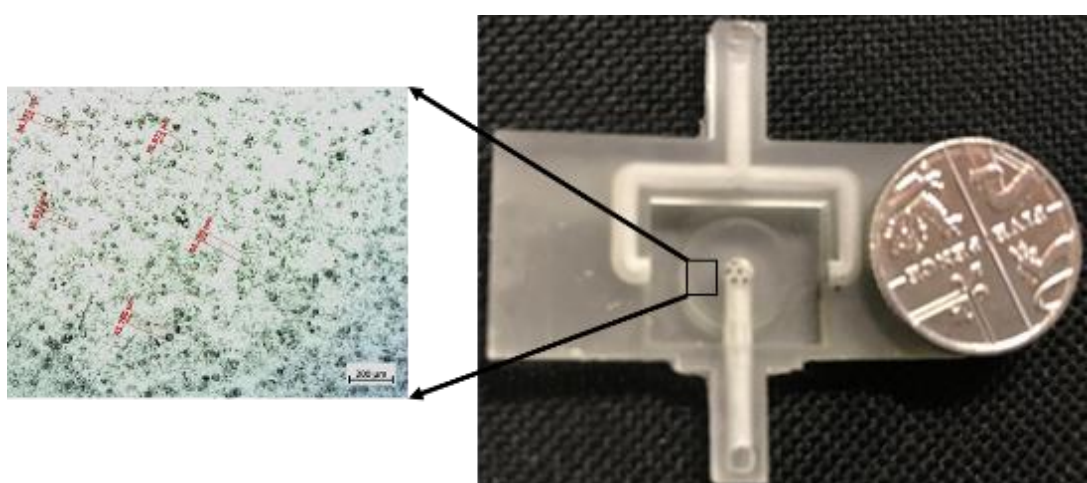


Figure 5. 34 The surface of micro-jet impingement under a microscope.

The reasons for the difference between the designed and fabricated channels include the following:

- The debris of photo-polymeric resin with high viscosity attached to the inner wall cannot be thoroughly cleaned and it solidification with the UV light curing,
- The UV curing with high temperature slightly deforms the orifices.

The morphology of the surface of the micro-jet impingement channel under the microscope is shown in Figure 5. 34. It can be observed that the surface of the micro-jet channel was not quite smooth. There are lots of holes with a diameter of around 45 μm . This might affect the pressure drop for the whole channel.

- ***Experiment and validation of simulation with deionised water***

The IR camera was used to illustrate the temperature distribution on the microchip and diamond surface as is illustrated in Figure 5. 35. There were three measuring points inserted in the IR image as P1, P2 and P5. It can be observed that with power applied on the microchip, all the given the measured area heated up. It can be also seen from the image that the temperature on the diamond surface seemed to be homogeneous. The golden wire and the PCB pads seemed to have a high temperature that indicated that not all the heat powered by power supplier was applied on the microchips. There was energy loss in the circuit.

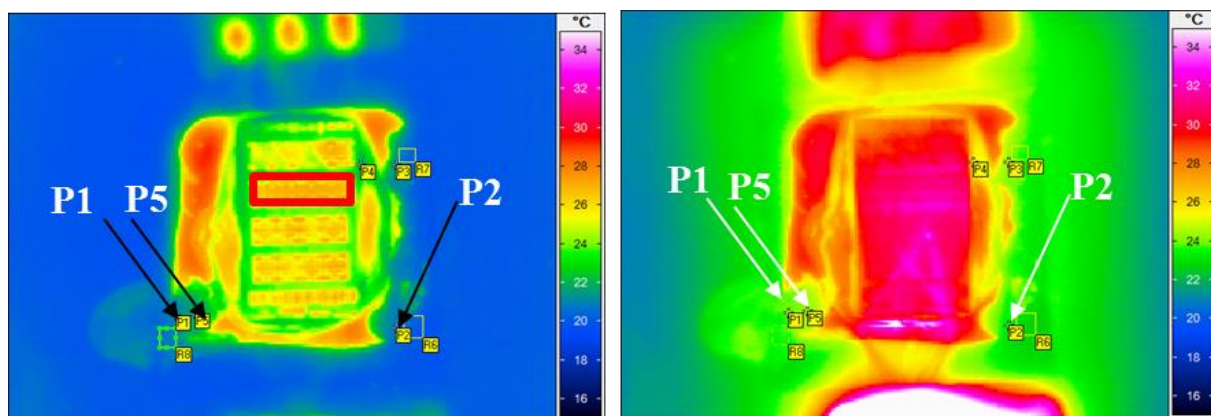


Figure 5. 35 IR image of microchip and diamond surface at a flow rate of 0.2L/min (left) without power applied; (right)with the power of 6.118 W

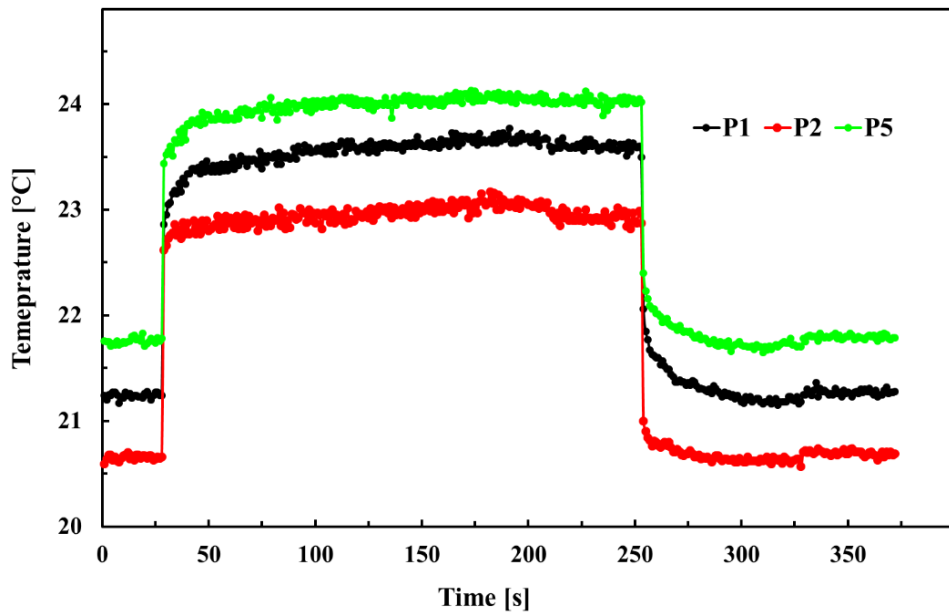


Figure 5. 36 Temperature on diamond surface 0.2L/min

As is illustrated in Figure 5. 36, with power applied on the die, the whole device reached a steady state in a very short time. With the power off, due to the highly efficient heat dissipation, the temperature immediately decreased to the cooling temperature. For the data analysis, the temperature difference in the same location on the diamond surface with and without power applied was used to compare with the simulation results.

Table 5. 2 Thermophysical properties of water with temperature

T °C	k W/(m · K)	η Pa · s	Pr
20	0.599	1.004E-03	7.02
25	0.609	9.028E-04	6.22
35	0.627	7.274E-04	4.87
45	0.642	6.014E-04	3.93
55	0.654	5.097E-04	3.27
65	0.664	4.380E-04	2.77
75	0.671	3.806E-04	2.38

As is illustrated in Table 5. 2, the properties of DI water related to the heat transfer and pressure drop was not temperature independence. The thermal conductivity increases with the increase of temperature while the viscosity shows the opposite trend with temperature. The given data in the table were used in the simulation for DI water.

As is indicated in Figure 5. 37, the temperature difference between inlet and outlet showed a linear decrease with increase in the flow rate. It suggested that the heat dissipated by the heat transfer fluid did not significantly change within measured flow rates. The dissipated heat by water can be obtained by the following equation:

$$Q_{dis} = \rho C_p v \nabla T \quad (5-11)$$

Where ρ is the density, C_p is the specific heat capacity, v is the velocity of the fluid and ∇T is the temperature difference between inlet and outlet.

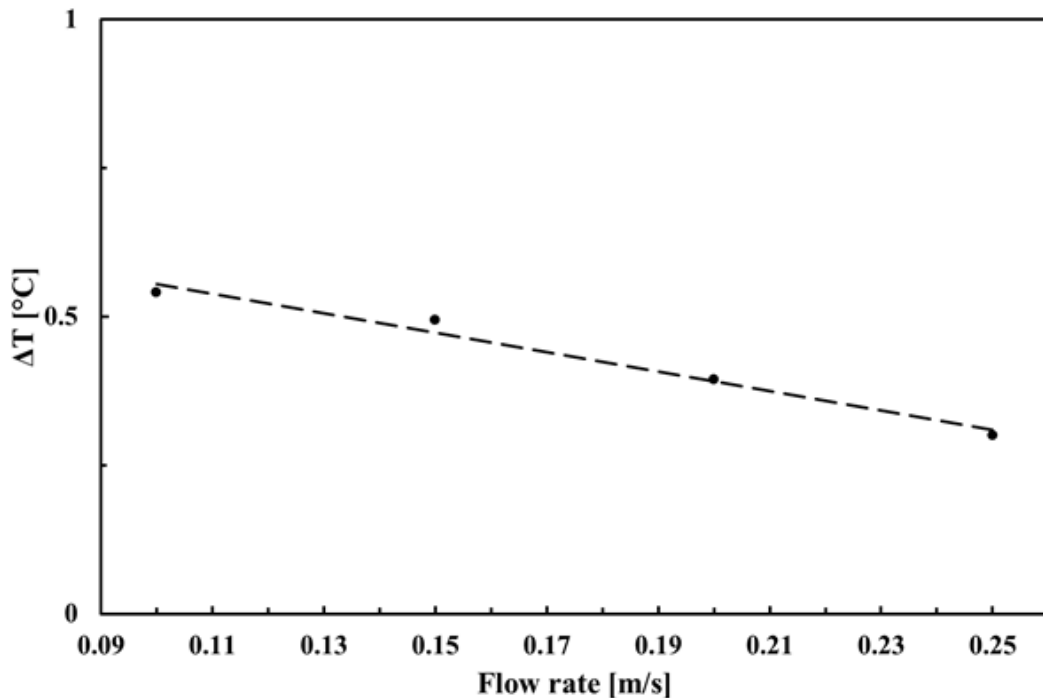


Figure 5. 37 Temperature difference between inlet and outlet

Table 5. 3 showed the power generated by the DC power supplier and the heat dissipated by HTF. During the experiment, the voltage applied on the microelectronic was set to be 3.500 V with the slight fluctuating current for different flow rates. The average total output power was about 6.1 W. However,

CHAPTER 5 RESULTS AND DISCUSSIONS

the average heat dissipated by the HTF was about 5.3 W. The value with 0.10 L/min seemed to be slight than the average value. This might due to the low flow rate. Thus, 5.3 W was used as heat dissipated from the microchips in the simulation.

Table 5. 3 Power generated by power supplier and dissipated by water

flow rate	Voltage	Current	Power	Heat dissipated by HTF
L/min	V	A	W	W
0.10	3.500	1.754	6.139	3.766
0.15	3.500	1.745	6.108	5.163
0.20	3.500	1.745	6.108	5.500
0.25	3.500	1.748	6.118	5.237

The numerical simulation was used to validate the performance of the micro-jet impingement channel. As was illustrated in Figure 5. 38, the top view with the die and the diamond surface showed its temperature distribution. To compare with the experiment results, a point position with coordination of 8.5 mm and 7.5 mm was used to monitor the temperature increase in this location. This location was the same as the location of P1 in the experiment. It can also be seen that the temperature gradient across the diamond surface seemed to be small. This simulation result was validated with the experiment results, as is shown in Figure 5. 39. The temperature increase among the P1, P2 and P5 had a small difference in every measured flow rate. As the htc increased with the flow rate increase, the temperature increase for P1, P2 and P5 decreased. The results also showed that the simulation results agreed well with the experiment results in every measured flow rate.

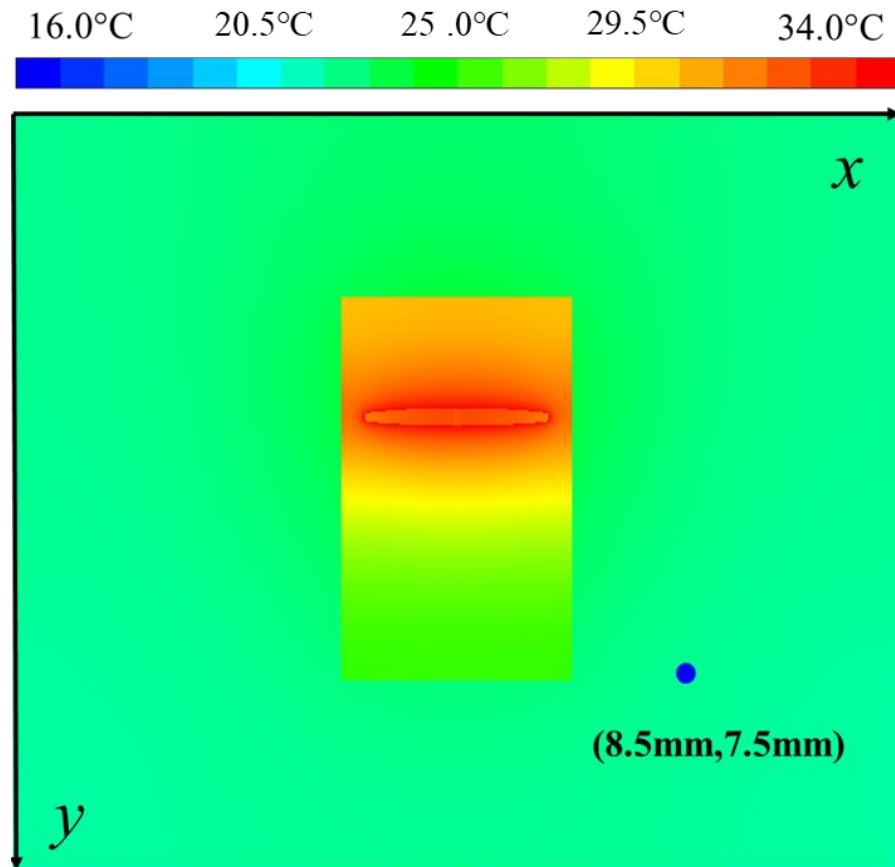


Figure 5.38 Temperature distribution and location for the point in simulation with a flow rate of 0.2 L/min

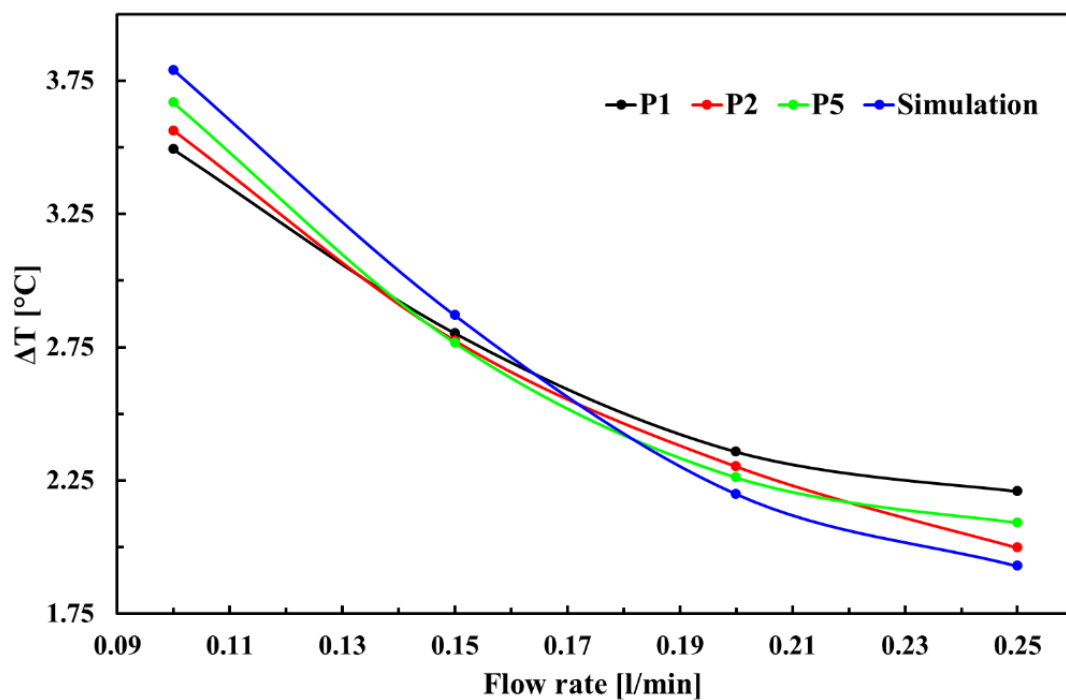


Figure 5.39 Temperature difference with simulation and experiment

- ***Experiment and validation of simulation with Boron Nitride nanofluids***

As is characterised in section 5.1, for the stable nanofluid, the 0.5 wt.% BN/DI water nanofluids showed the highest thermal conductivity meanwhile there was no noticeable increase in the viscosity for the nanofluid. Thus, in the simulation, 0.5 wt.% BN nanofluids were used with its thermophysical properties illustrated in Table 5. 4. The density and specific thermal capability were calculated via equations in Chapter 2. The measured value of the thermal conductivity of nanofluids and base fluids was applied in the simulations. Due to the insignificant increase in viscosity, the viscosity of 0.5 wt.% BN.DI water nanofluids in the simulation were the same as DI water.

Table 5. 4 Thermophysical properties of 0.5 wt.% BN/DI water nanofluids with temperature

T °C	k W/(m . K)	η Pa·s	Pr
20	0.605	1.004E-03	7.02
25	0.643	9.028E-04	6.22
35	0.660	7.274E-04	4.87
45	0.679	6.014E-04	3.93
55	0.701	5.097E-04	3.27
65	0.733	4.380E-04	2.77
75	0.797	3.806E-04	2.38

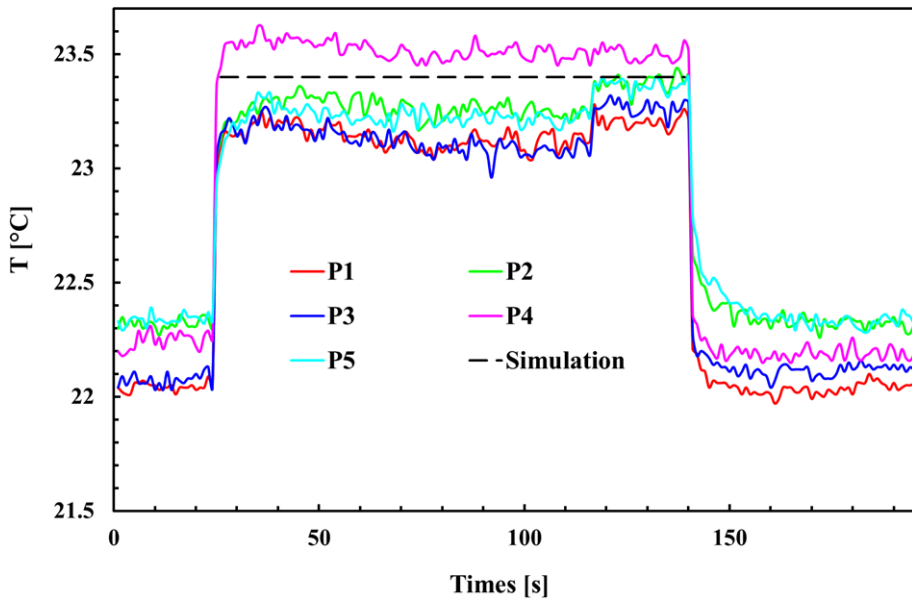


Figure 5.40 Temperature at 2.000 V 1.012A with 0.53 m/s in experiment and simulation for BN/DI water nanofluids

In the experiment, the IR camera was used to measure the temperatures on the surface of the diamond heat spreader. As is illustrated in Figure 5.40, 5 points (P1, P2, P3, P4 and P5) for the measurement were inserted in different locations. During the test, without any power applied on the die, the temperatures on the diamond were uniform with only ± 0.15 °C difference for the 5 selected points. With the electrical energy applied on the microchip, the temperature on the diamond surface instantly soared up to a new plateau. It can be seen that there is no significant difference in the measuring area with power applied. Thus, in the simulation, the same location in Figure 5.38 was used for the numerical validation. The simulation result for the diamond heat spreader was 23.4 °C, which was close to measured values in all the 5 points. Once the power on the die was removed, the temperature on diamond heat spreader seemed to simultaneously decrease to the initial temperature.

- ***Performance of deionised water - flow rate***

The numerical simulation was used to obtain the heat transfer coefficient distribution with different flow rate on the diamond surface as is illustrated in Figure 5.41. The results showed that the high heat transfer coefficient area was the proximity to micro-jet orifices. It can also be seen that with the inlet velocity increase, the maximum heat transfer coefficient almost doubled from 84.1 kW/(m²·K) to 158.5 kW/(m²·K) with flow rate increase from 0.10 L/min to 0.25 L/min. A similar amount of heat transfer

coefficient can be found in some research [209]. Remco et al [238] with micro-jetting can obtain a htc of $730 \text{ kW}/(\text{m}^2 \cdot \text{K})$ near the jetting area in the experiment. The area with high htc gradually increased with the increase of velocity. The average htc on the diamond surface was displayed in Figure 5. 42. The average heat transfer coefficient was much smaller than the maximum htc in the same flow rate that indicated the highly inhomogeneous distribution of heat transfer coefficient on the diamond heat spreader surface as was illustrated in the htc distribution on the diamond surface. It can also be obtained that the average heat transfer coefficient seemed to show a power function growth trend with flow rate.

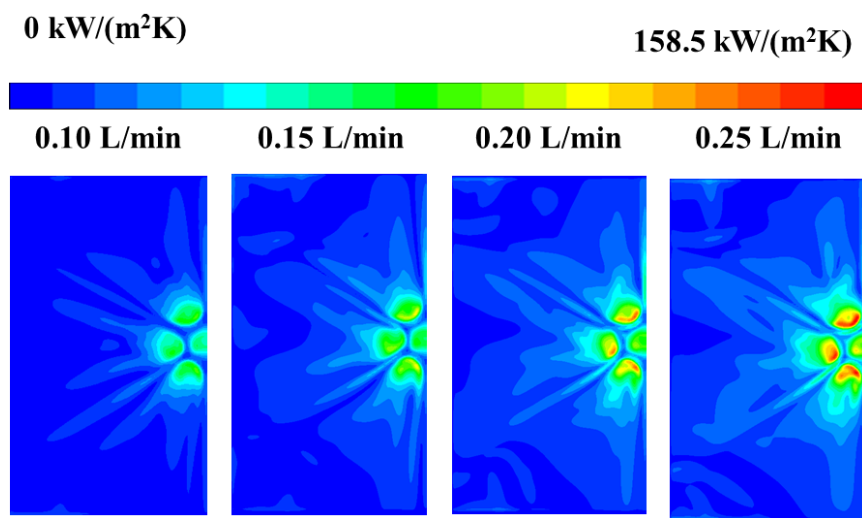


Figure 5. 41 Distribution of the heat transfer coefficient with the different flow rates

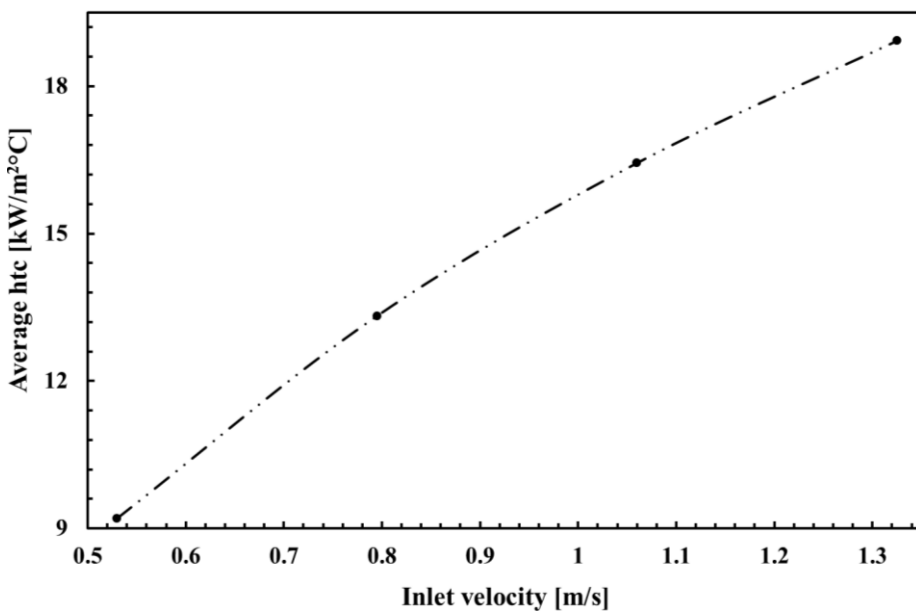


Figure 5. 42 Average htc heat transfer coefficient with inlet velocity

- *Performance of deionised water - inlet temperature*

One of the main concern for the given heat transfer coefficient is its inlet temperature. It affects the temperature on the diamond surface thus influenced the temperature on the microchip. The distribution of the heat transfer coefficient with different inlet temperature as illustrated in Figure 5. 43. With the inlet temperature decreased from 50 °C to 20 °C, the shapes for the high htc area barely changed. However, the maximum heat transfer coefficient slightly linear decreased by 17% as was illustrated in Figure 5. 44. The average htc showed similarity with the maximum htc with about 21% decrease with the same temperature decrease.

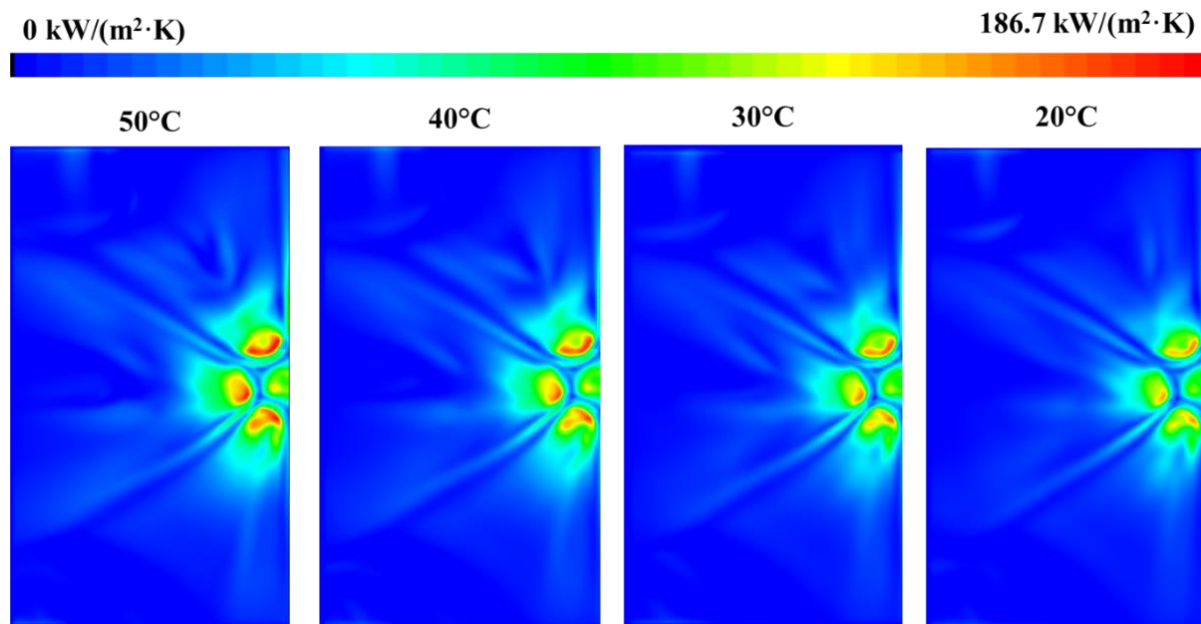


Figure 5. 43 Distribution of the htc with inlet temperature at a heat flux of 5W/mm²

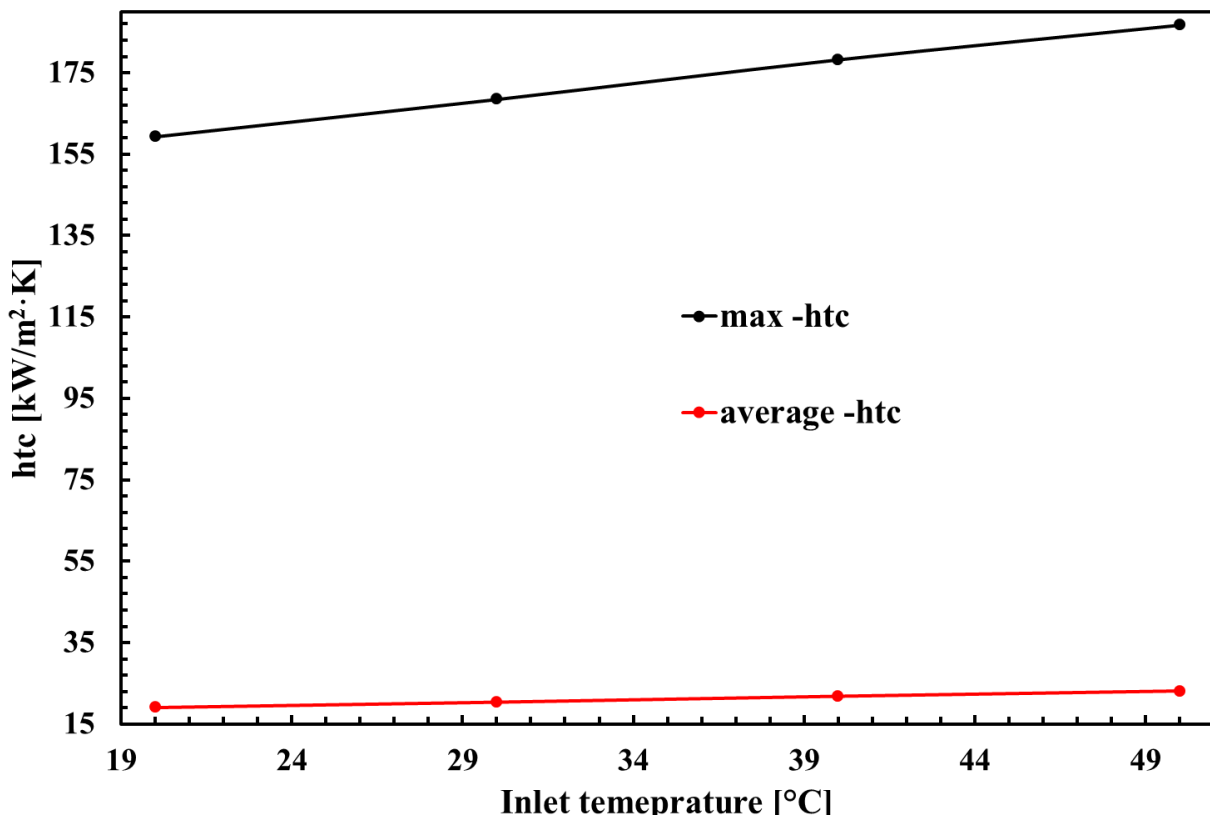


Figure 5. 44 Average and maximum heat transfer coefficient with inlet temperature at a heat flux of 5W/mm^2

Table 5. 5 illustrated the maximum, minimum and average temperature on the diamond heat spreader surface with 5 W/mm^2 . The results showed that the average temperature was much closer to the minimum temperature on the diamond surface than its counterpart was. This echoed to htc distribution and difference between the maximum htc and average htc. It can also be seen from the figure that with a $30\text{ }^\circ\text{C}$ temperature increase from $20\text{ }^\circ\text{C}$ to $50\text{ }^\circ\text{C}$, almost a linear increase with approximately $30\text{ }^\circ\text{C}$ increase in all the case.

Table 5. 5 Temperature on the diamond with inlet temperature at a heat flux of 5 W/mm^2

inlet °C	max on diamond °C	min on diamond °C	average on diamond °C
50.00	50.91	50.34	50.49
40.00	40.95	40.37	40.52
30.00	31.00	30.41	30.56
20.00	21.06	20.45	20.61

- ***Performance of deionised water - heat flux***

Another important factor affecting the temperature distribution in the test rig is the heat flux applied one the microchips. As is illustrated in Figure 5. 45, with heat flux increase from 0 W/mm² to 60 W/mm², the maximum temperature on the diamond surface, the minimum temperature on the diamond surface and the average temperature on the diamond almost linearly increased by 13.51 °C, 6.12 °C and 8.12 °C, respectively. The linear increase seemed to suggest that there was no significant change in the htc distribution. As is shown in Figure 5. 46, the htc distribution on the diamond surface had little change with the heat flux increased from 10 W/mm² to 60 W/mm².

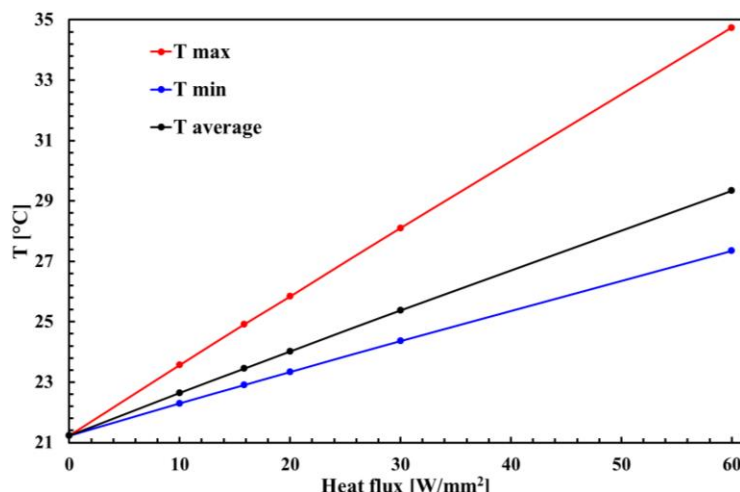


Figure 5. 45 Temperature on the diamond with heat flux

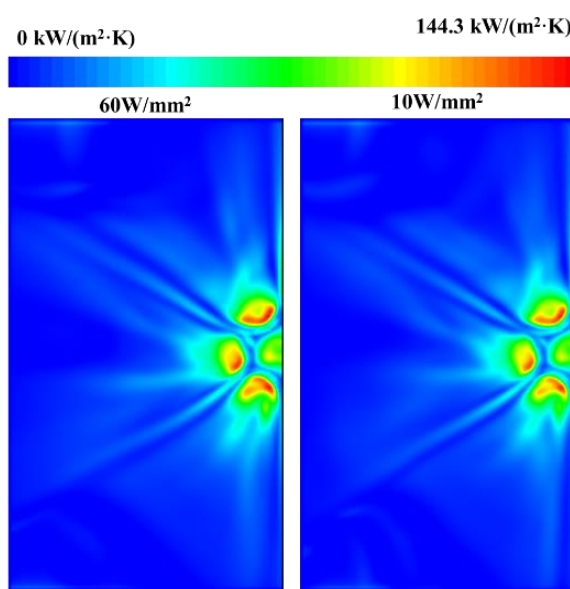


Figure 5. 46 Distribution of the htc with heat flux

- *Comparison of the base fluid and nanofluid*

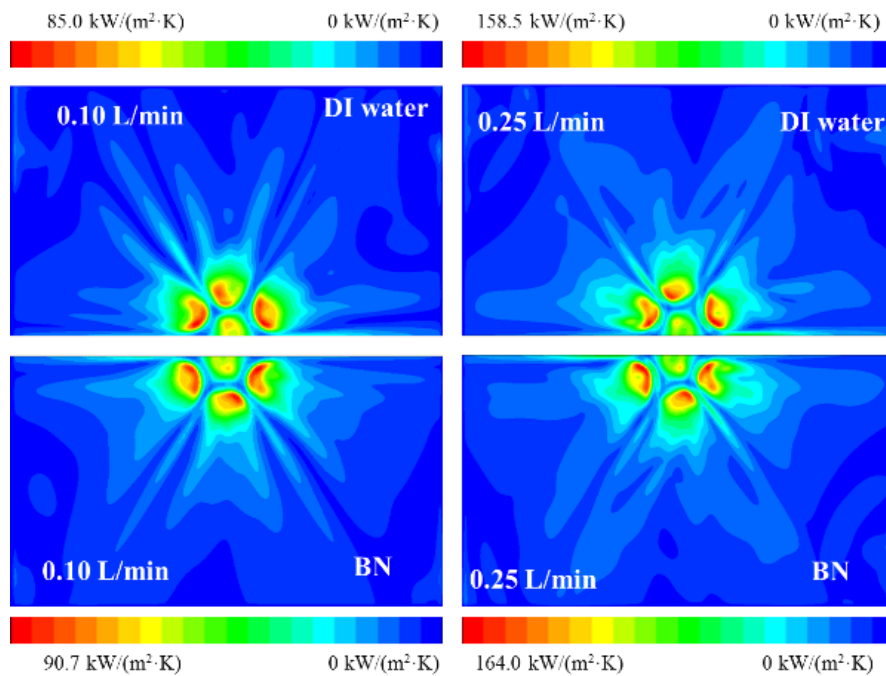


Figure 5.47 Heat transfer coefficient distribution on the surface of the diamond heat spreader

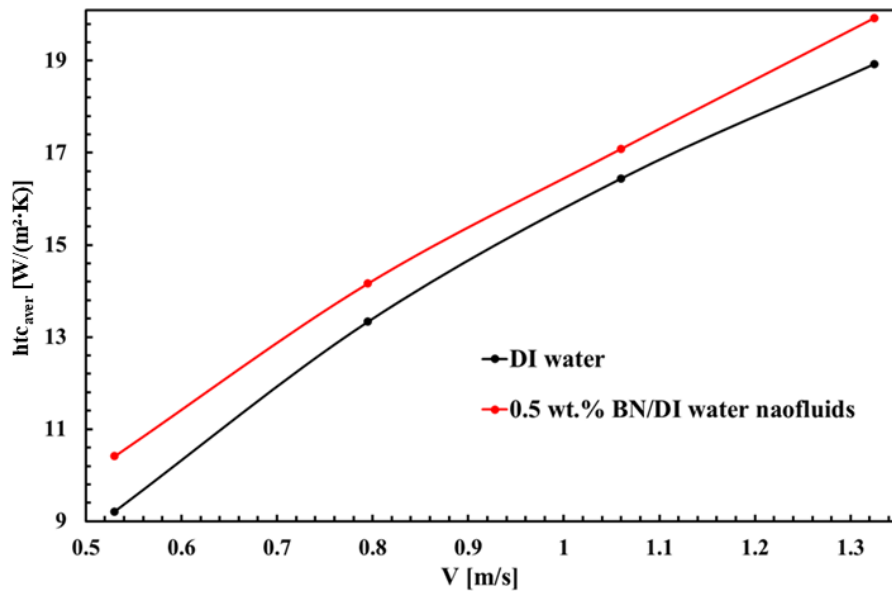


Figure 5.48 Average heat transfer coefficient of DI water and 0.5 wt.% BN/DI water nanofluids with velocity

In order to evaluate the thermal performance of the 0.5 wt. % BN/DI water nanofluid, the heat transfer coefficient on the surface of the diamond heat spreader was analysed and compared with its counterpart. As is shown in Figure 5.47, with the flow rate increase from 0.10 L/min to 0.25 L/min, the maximum heat flux coefficient for the BN nanofluid escalated from 90.7 kW/(m²·K) to 164.0 kW/(m²·K), which

were 6.7 % and 3.4% higher than the DI water in the same condition, respectively. The average heat transfer coefficient with velocity, as is illustrated in Figure 5. 48, showed similar trends for both DI water and 0.5 wt.% BN/DI water nanofluids. The BN nanofluids had nearly 5% higher heat transfer coefficient than the base fluid.

- ***Dimensionless analysis***

For the given micro-jet impingement channel, a dimensionless analysis of fluid parameter relevant to the heat transfer suggested that the Nusselt number had a functional dependence as shown in the following equation;

$$\overline{Nu} = C Re^m Pr^n \quad (5-12)$$

The least-square method has been used with Reynolds number, Nusselt number and Prandtl number obtained from the simulation. In those simulations, the water ($Pr \approx 4.5$) in the turbulence flow was used to fit the correlation given by;

$$\overline{Nu} = 0.015 Re^{0.847} Pr^{0.562} \quad (5-13)$$

The dependence of Reynolds number is a typical value which was previously shown for the micro-jetting array. The exponential value is 0.847 close to 0.78 used in some papers [239]. The reason is that entire heater area lay within the “impingement zone” for all of the jetting arrays. Meanwhile, the Prandtl number dependence is also similar in previous studies. The exponential value is 0.562 close to 0.44 used in the correlation of some paper [240].

- ***Summary of micro-jet channel with deionised water based nanofluid***

The following is a summary of observations with DI water and BN/DI water nanofluids:

- The 0.5 wt.% BN nanofluid had better performance than the base fluid. The results showed the BN nanofluid had about a 5% enhancement for the heat transfer coefficient than the DI water.
- The increase in the flow rate increased the heat transfer coefficient for both DI water and its counterpart.

CHAPTER 5 RESULTS AND DISCUSSIONS

- Inlet temperature can slightly change the maximum heat transfer coefficient of the micro-jet array channel. However, the average heat transfer coefficient did not show a significant change.
- The heat flux in the given range did not significantly change the distribution of heat transfer coefficient. Thus, a linear trend for the maximum temperature in the die can be obtained with the increase of heat flux.

5.2.3. Performance of micro-jet channel with ethylene glycol+distilled water-based fluids

The microchips may be used at ambient temperature as low as -50 °C. The EG+DW based rGO nanofluids were studied and the results are presented in this sub-section.

- *Experiments and validation of simulation with ethylene glycol+distilled water-based fluid*

The viscosity and thermal conductivity of the EG+DW base fluid and 2.0 wt. % rGO/EG+DW nanofluid were listed in Table 5. 6. With the temperature increased from 228.15K (-45 °C) to 298.15K (25 °C), the viscosity of both base fluid and nanofluid showed a dramatic decrease. Meanwhile, the thermal conductivity of the base fluid and nanofluid slightly increased with the same temperature rise. The range of Prandtl number for both base fluid and nanofluid fiercely decreased with the same temperature change. It should be pointed out that the thermal conductivity of nanofluid was 17 % higher than its counterpart at the same temperature meanwhile The nanofluid had a higher viscosity than base fluid. With the temperature increasing to the room temperature, the difference of the viscosities declined to a barely noticeable value. However, both base fluid and nanofluid had approximately 10 times larger viscosity than water at the room temperature. During the experiments and simulations, the Reynolds number varied from 0.3 to 46 because of the large viscosities of fluids. It suggested nanofluid were in laminar flow.

Table 5. 6 Properties of EG+DW and 2.0 wt.% rGO nanofluid

T K	μ -base fluid Pa·s	k-base fluid W/(m·K)	Pr-base fluids	μ -2.0% nanofluid Pa·s	k-2.0% nanofluid W/(m·K)	Pr - 2.0% nanofluid
228.15	0.543	0.30	5138.8	0.676	0.352	5471.8
248.15	0.095	0.32	855.4	0.116	0.375	899.4
268.15	0.031	0.34	276.5	0.038	0.395	290.0

CHAPTER 5 RESULTS AND DISCUSSIONS

298.15	0.012	0.359	107.5	0.016	0.420	122.6
--------	-------	-------	-------	-------	-------	-------

For the base fluid and nanofluid, the IR camera was used to measure the temperature distribution as well as temperature change on the microchip and the diamond surface as is illustrated in Figure 5. 49 for EG+DW base fluid. There were two measuring points inserted in the IR image as P1 and P2. It can be seen that with power applied on the microchip, all the given the measured area was heated up. The same method of the data analysis with the DI water as the heat transfer fluid was used for the EG+DW base fluid and 2 wt. % rGO/EG+DW nanofluid. The results were given in Figure 5. 50. The temperature on different points, P2, P3 and P4 were extracted and compared with experiment.

The simulation model for EG+DW base fluid and 2 wt. % rGO/EG+DW nanofluid were the same as the water. In the simulation, the properties of the base fluid and nanofluid were imported into the CFD software to simulate the performance of the given HTFs in the micro-jet impinging channel. In the simulation, the same point was used to validate the simulation with experiment. The simulation results were validated with the experiment results, as is shown in Figure 5. 51. The temperature differences between the P1 and P2 was small in the measured flow rate. The results also showed that with the power applied on the microchip, the temperature on diamond heat spreader immediately increased and the same quick respond occurred when the power decreased. The temperature on the diamond surface for simulation was roughly around 30.54 °C, very close to the measuring value. Thus, the simulation results agreed well with the experiment results in the given condition. The same results can also be observed for 2.0 wt. % rGO/EG+DW nanofluids in Figure 5. 52.

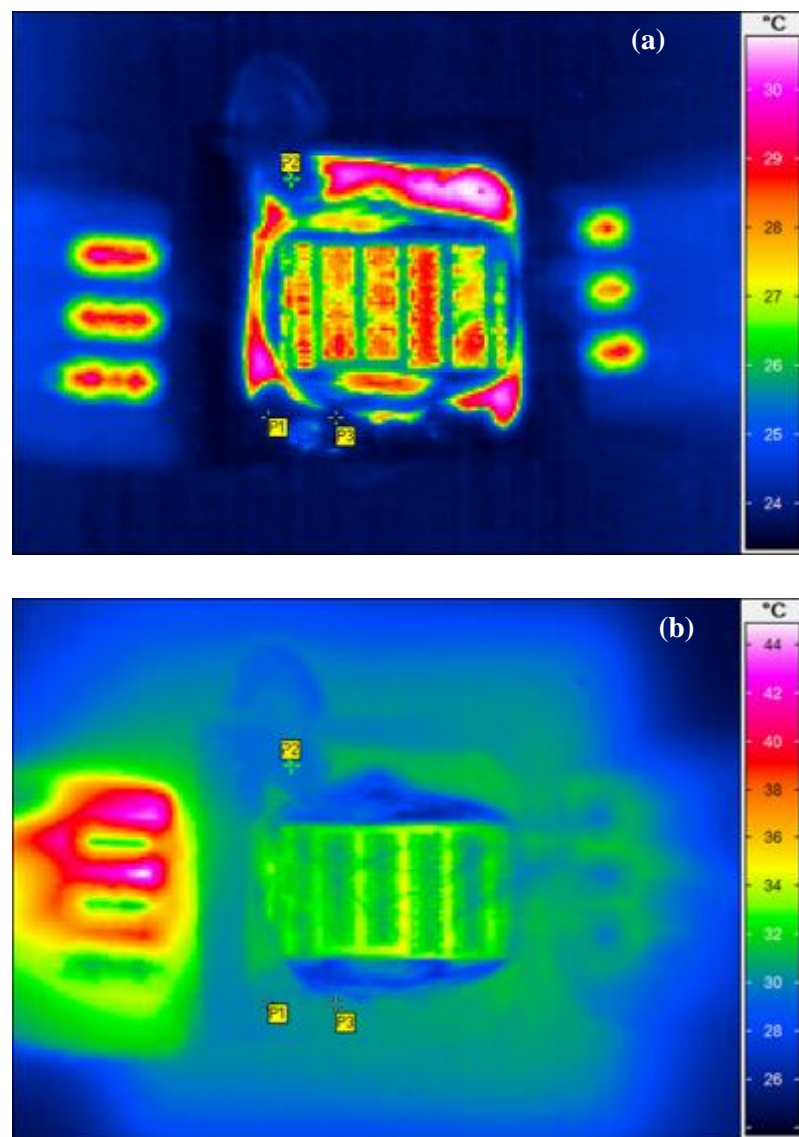
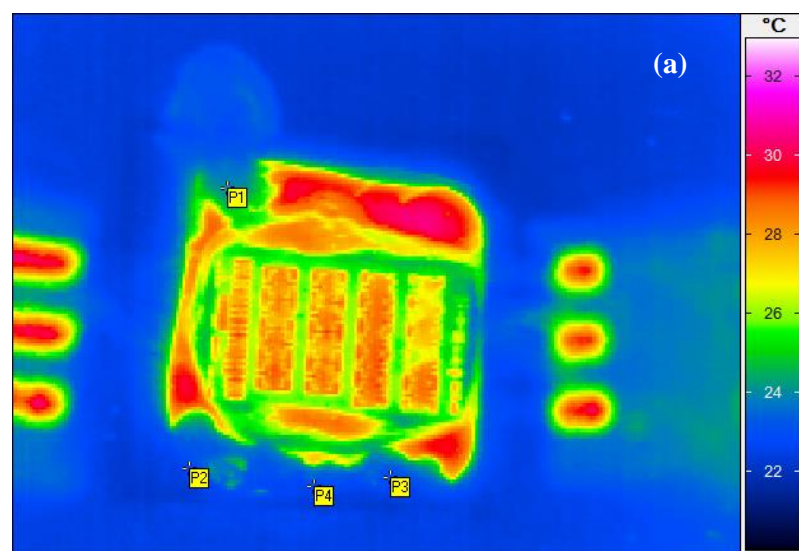


Figure 5. 49 IR images for EG+DW fluid with 2.500 V 1.270 A (a) without power and (b) with power



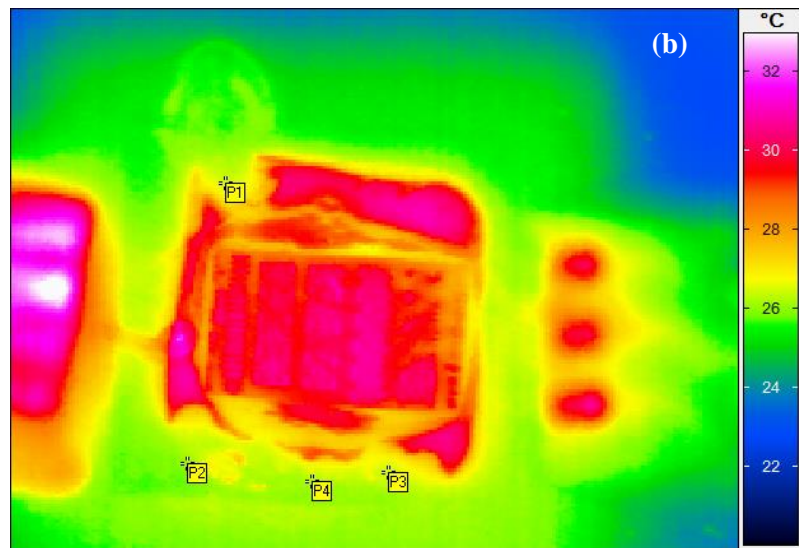


Figure 5. 50 IR images for 2.0 wt.% rGO nanofluids at 2.000 V 1.000 A (a) without power and (b) with power

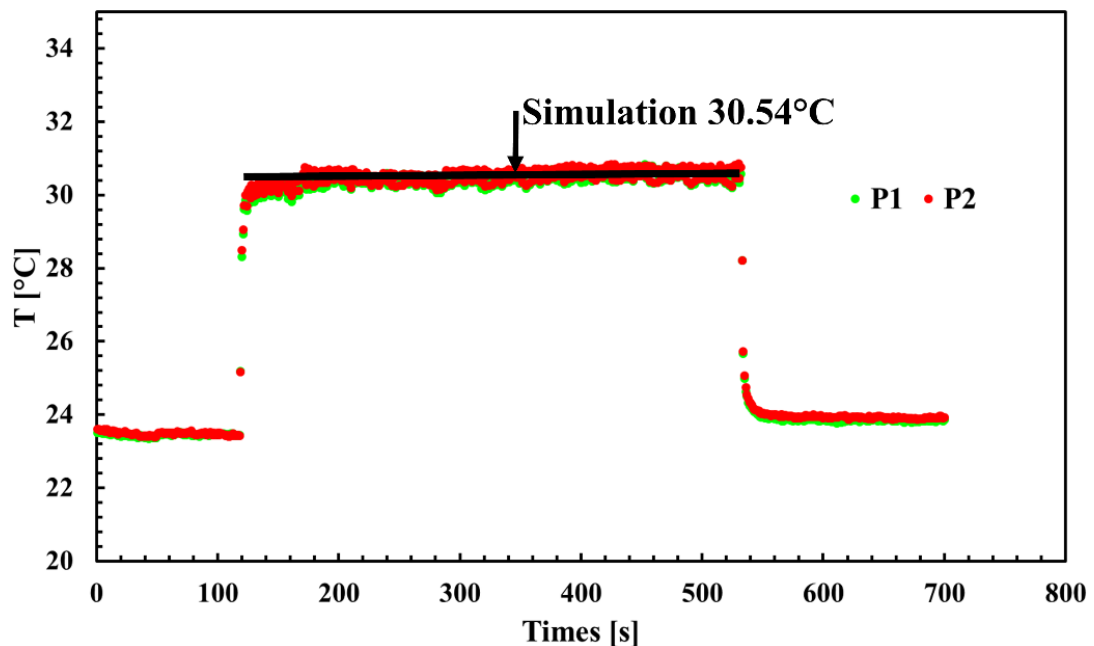


Figure 5. 51 Experiment and simulation of temperature on the diamond surface with $V_{in} = 0.246 \text{ m/s}$ for EG+DW base fluid

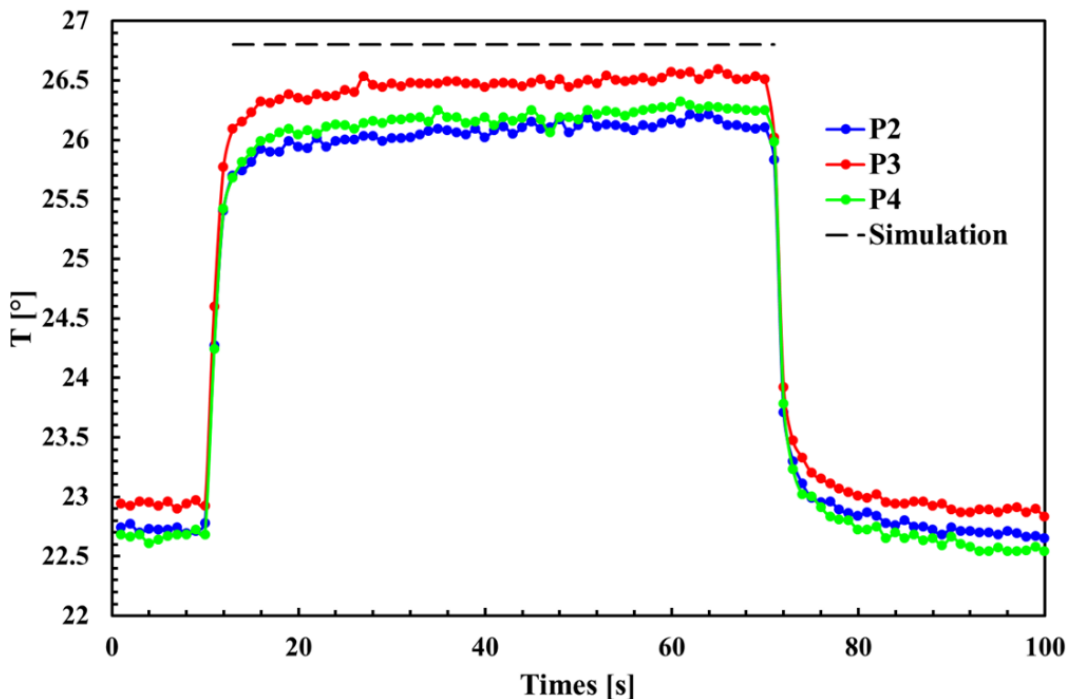


Figure 5.52 Experiment and simulation of temperature on the diamond surface with $V_{in} = 0.246$ m/s for 2.0 wt.% rGO nanofluid

It should be pointed out that the experiment was conducted in the room temperature. However, the main application for the EG+DW based fluids was acted as a coolant for temperature as low as -50 °C. Thus, the simulation mainly focuses on sub-zero temperature.

- ***Comparison of the base fluid and nanofluid***

Two main parameters, the pressure drop in the micro-jet impingement channel ΔP and the htc on the diamond heat spreader, were used to evaluate the performance of the base fluid and nanofluid as are illustrated Figure 5.53 and Figure 5.54. For the average htc on the diamond heat spreader surface, the nanofluids had a noticeably higher value than its counterpart. The reason for this was mainly due to the 17% enhancement in the thermal conductivity. The results also seemed to suggest that there was no obvious change for average htc with inlet temperature climbed from -45 °C to 20 °C. The reason for this might be a limited change in their thermal conductivity. For pressure drop across the inlet and outlet, the nanofluid also had an apparent higher value than the base fluid at the same temperature. The reason for this was mainly due to the increase in the viscosity by adding nanoparticles. The results also showed

that with inlet temperature increased from -45 °C to 20 °C, the ΔP sharply decreased. The reason for this might be the dramatical change in the viscosity.

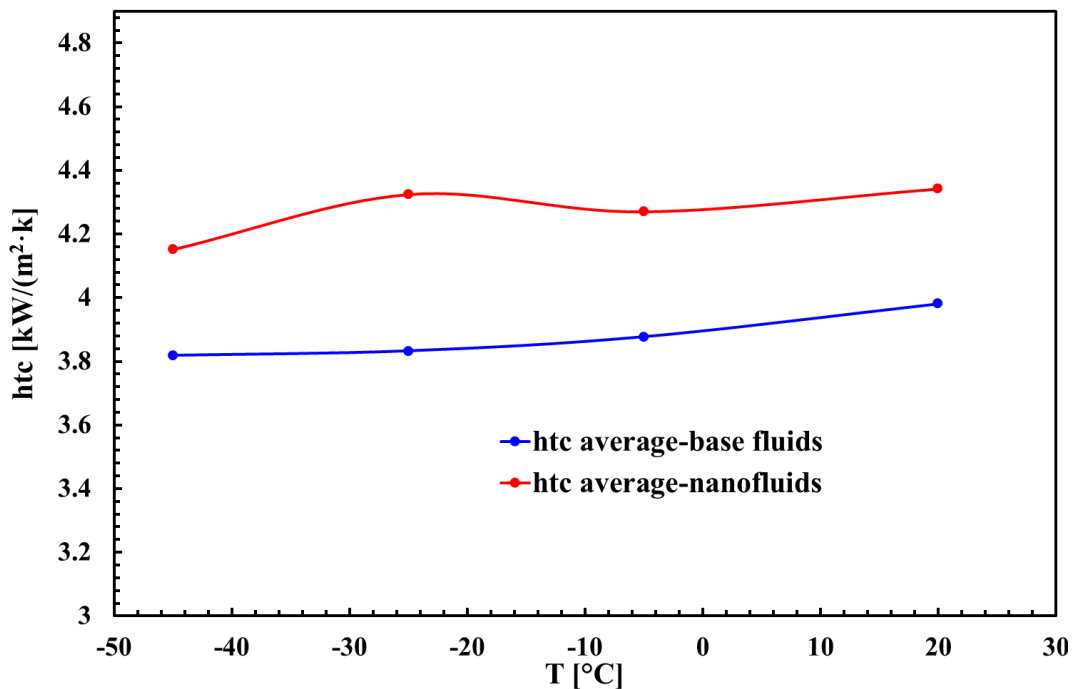
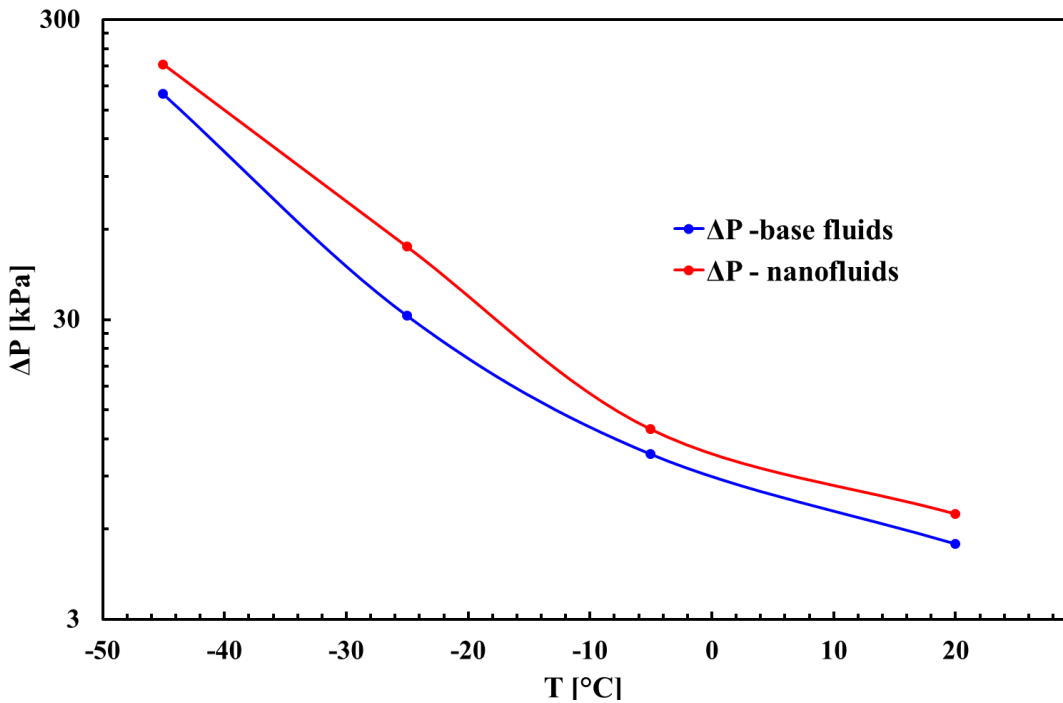
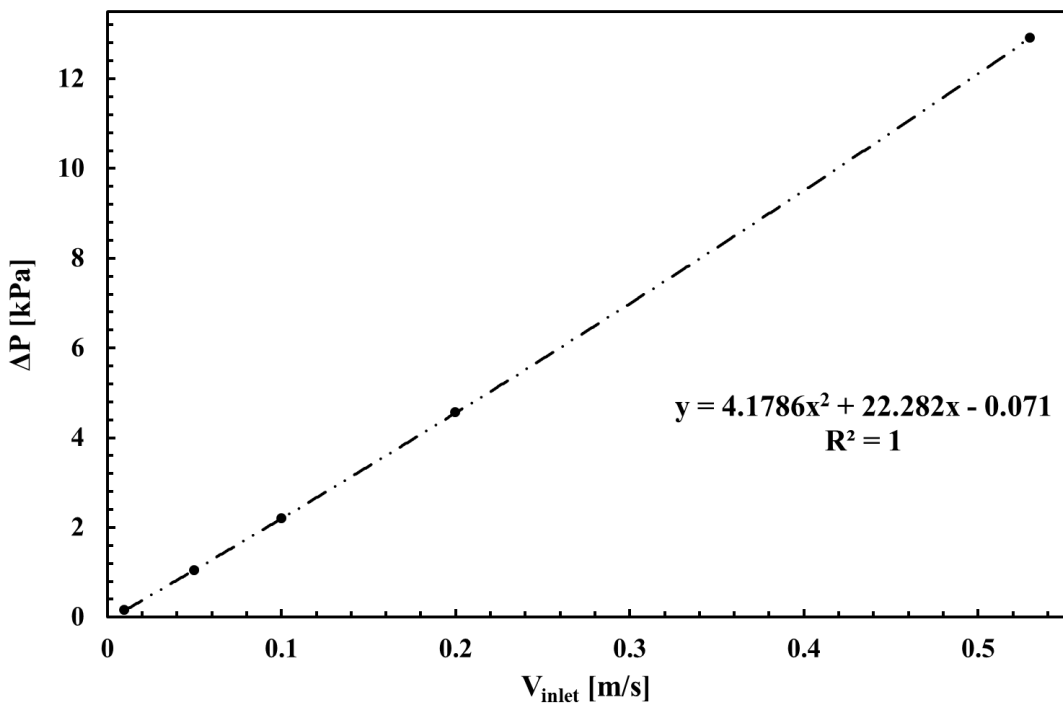


Figure 5. 53 Average htc of the base fluid and nanofluid with different inlet temperature at $v=0.53 \text{ m/s}$

Comparing the performance of base fluid and nanofluid at the same inlet temperature cannot obtain an affirmatory conclusion that the nanofluid has better performance than the base fluid as both ΔP and htc for nanofluid showed considerably increase.

Figure 5. 54 ΔP of the base fluid and nanofluid with different inlet temperature at $v=0.53$ m/sFigure 5. 55 ΔP of nanofluid with different inlet velocity at the temperature of -5 °C

In order to compare the base fluid and nanofluid, the nanofluid with different inlet velocity had been simulated to obtain the htc and ΔP at an inlet temperature of -5 °C. As is illustrated in Figure 5. 55, the pressure drop increased with the increase of the inlet velocity. The classical trend for velocity with the

CHAPTER 5 RESULTS AND DISCUSSIONS

pressure drop is quadratic. However, the fitting curve did not show a strong quadratic trend for base fluid. The reason for this might be a dramatic change in viscosity. The correlation is expressed as:

$$\Delta P = 4.1786v_{inlet}^2 + 22.282v_{inlet} - 0.071 \quad (5-14)$$

As was illustrated in Figure 5. 56, the average htc on the surface of the diamond heat spreader showed a power function growth with the inlet velocity. The correlation is expressed as:

$$htc = 5.9756v_{inlet}^{0.4177} \quad (5-15)$$

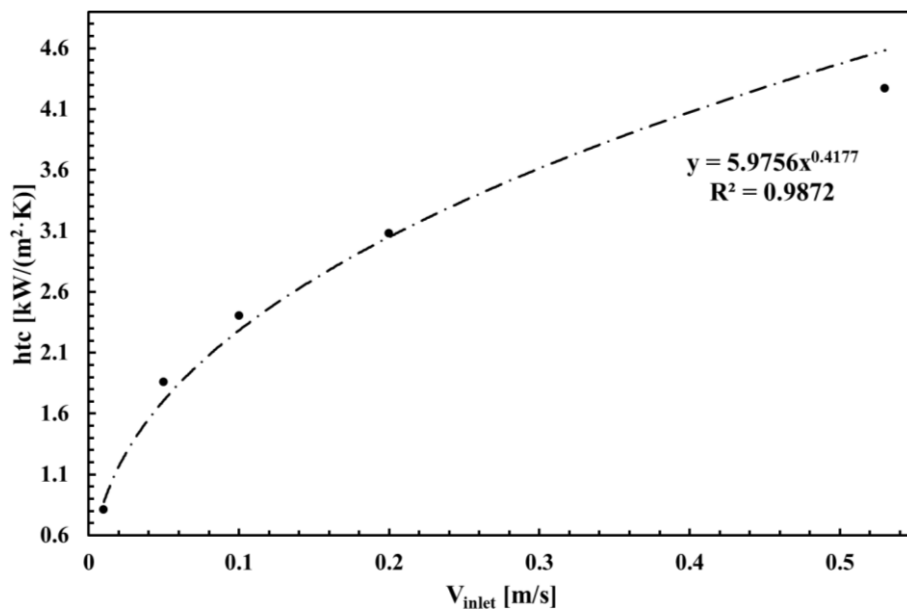


Figure 5. 56 Average htc of nanofluid with different inlet velocity at the temperature of -5 °C

Table 5. 7 Comparison of the base fluid and nanofluid

HTF	T _{inlet} °C	htc _{aver} W/(m ² ·K)	ΔP kPa
base fluid	-5	3877	10.663
nanofluid	-5	3877	8.347

Using those correlations, the htc and ΔP for nanofluid at different inlet velocity can be simultaneously acquired. As is illustrated in Table 5. 7, the average htc and ΔP of the base fluid with an inlet temperature of -5 °C and velocity of 0.53 m/s were 3877 W/(m²·K) and 10.663 kPa, respectively. In order to have the same average htc, the micro-jetting channel with rGO nanofluid required the pressure drop of 8.347

kPa, which was 2.316 kPa less than its counterpart. The result clearly showed that the performance of nanofluid was better than the base fluid. Thus, in the following study, Only rGO nanofluid was considered and simulated the nanofluids.

- ***Performance of reduced graphene oxide nanofluid - inlet temperature***

As inlet temperature affects the temperature on the diamond surface which influences the temperature on the microchip, this part is mainly focused on the impact of the inlet temperature for the thermal performance micro-jetting channel with rGO nanofluid. The average htc of two different inlet temperatures (-5 °C and -25 °C) with different inlet velocity is illustrated in Figure 5. 57. In each simulated inlet velocity, the average heat transfer coefficient for the micro-jetting channel with an inlet temperature of -25 °C had little different from the inlet temperature with a value of -5 °C. Both of them showed the same power function growth with the inlet velocity.

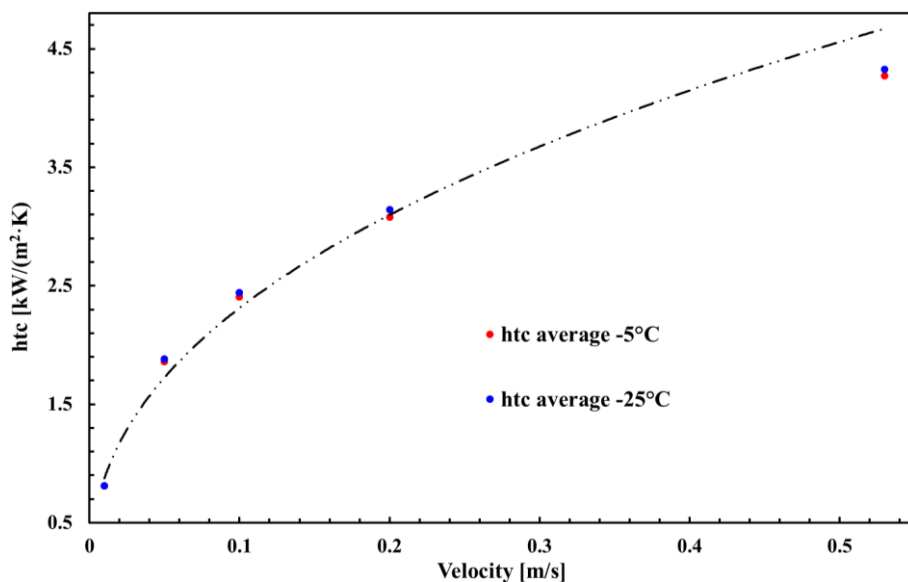


Figure 5. 57 Average htc of nanofluid with different inlet velocity and temperature

As is illustrated in Figure 5. 58, in the beginning, the maximum temperature on the diamond sharply decreased with the increase of inlet velocity. However, a much more gentle decrease had been witnessed afterwards. The reason for this might be in the power function growth of average htc with inlet velocity. As was expressed in the given correlation, the rate of change of htc with respect to inlet velocity decreased with the increase of velocity. Thus, the temperature decrease trend also slowed down. The

results also seemed to suggest that the curve for -5 °C could be obtained by adding 20 °C to the curve of -25 °C. Such a claim can be more visually obtained by comparing the temperature distribution on diamond heat spreader and microchip as is illustrated in Figure 5. 59. The image with an inlet temperature of -5 °C was almost identical to the one of -25 °C with shifting the scale bar by 20 °C. Another important factor affecting the performance of the micro-jetting channel was the pressure drop. As is shown in Figure 5. 60, the pressure drop for -25 °C was higher than the one of -5 °C. The difference between the two pressure drops sharply increased with the increase in velocity. This difference increased from 0.3 kPa to 39.5 kPa with inlet velocity increase from 0.01 m/s to 0.53 m/s.

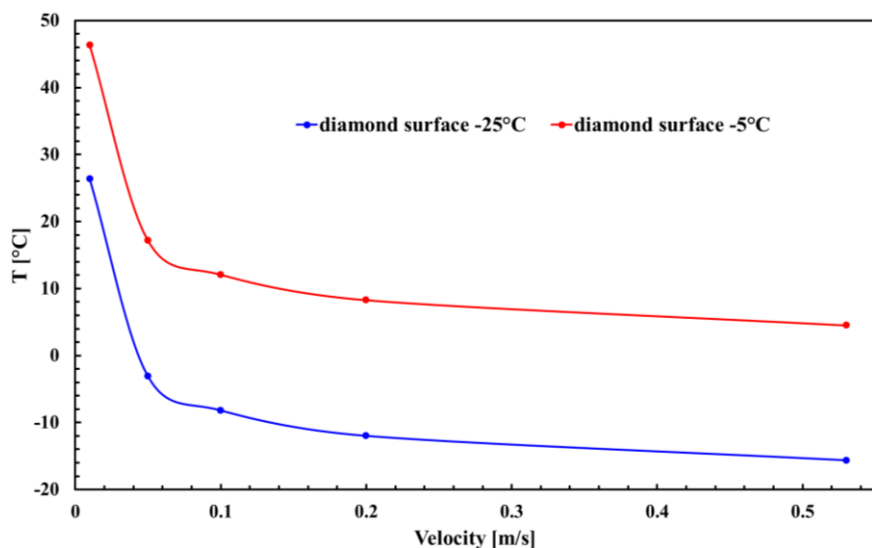


Figure 5. 58 the Tmax on the diamond surface with different inlet velocity and temperature

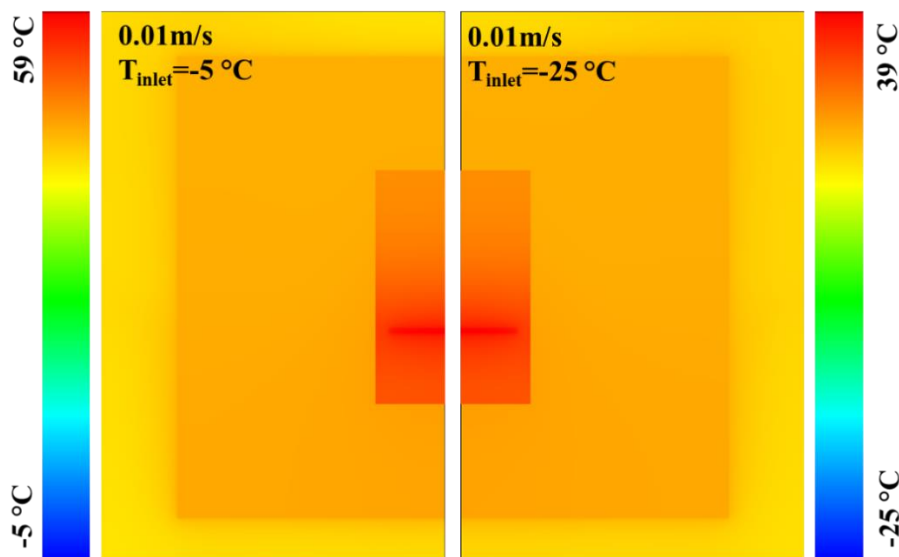
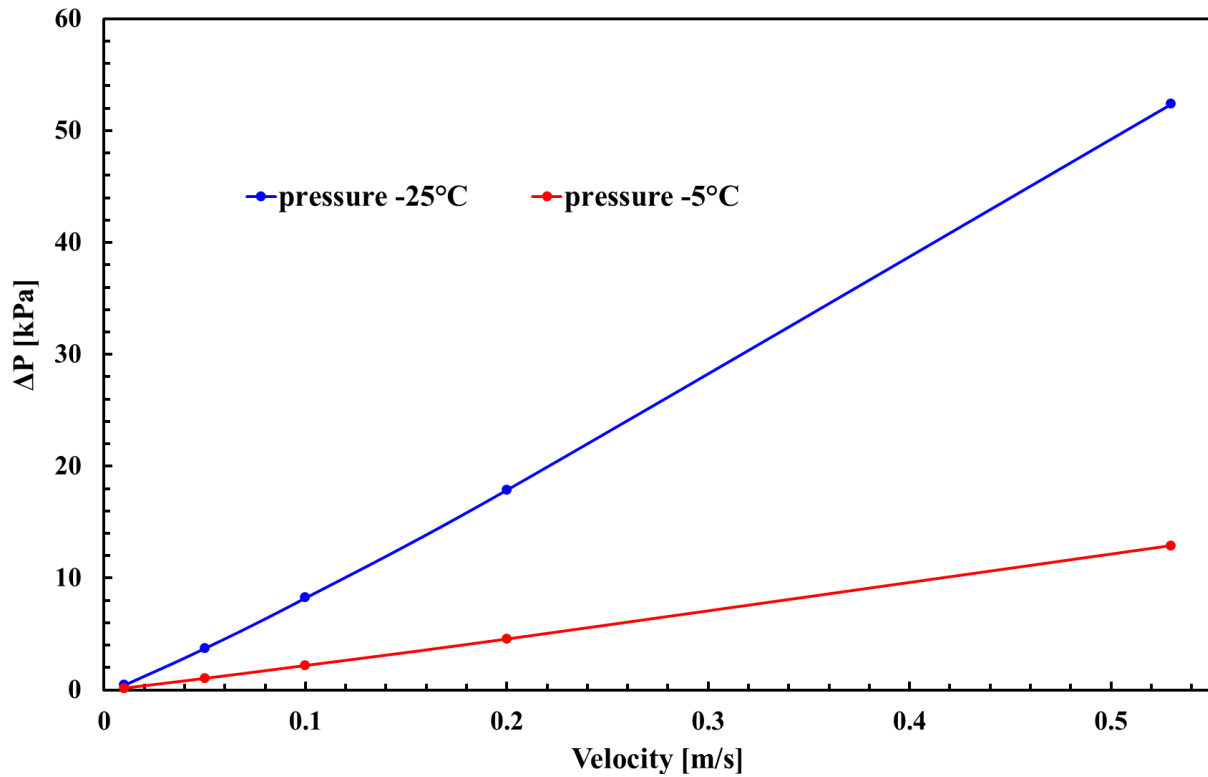


Figure 5. 59 Temperature distribution on diamond heat spreader and microchip

Figure 5. 60 ΔP of nanofluid with different inlet velocity and temperature

- *Performance of reduced graphene oxide nanofluid - heat flux*

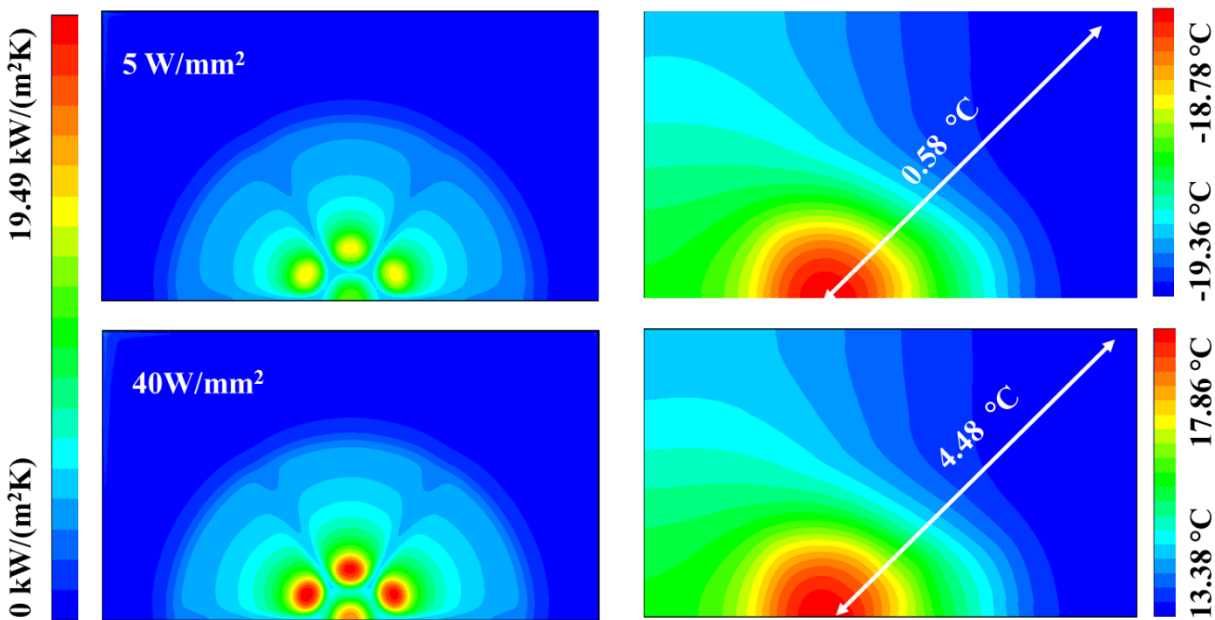


Figure 5. 61 Htc and temperature distribution on diamond heat spreader at an inlet velocity of 0.1 m/s

The heat flux applied to the microchip is another important factor affecting the temperature distribution on the test rig. As is illustrated in Figure 5. 61, with the power increase from 5 W/mm^2 to 40 W/mm^2 ,

the htc distribution clearly showed an increase in htc. This is likely due to the temperature increase in the nanofluid. The results also showed that the maximum temperature difference across the diamond heat spreader increased from 0.58 °C to 4.48 °C. The temperature on the diamond surface for heat flux increase from 0 W/mm² to 40 W/mm² with an inlet temperature of -25 °C is illustrated in Figure 5. 62. The maximum temperature on the diamond surface, the minimum temperature on the diamond surface and the average temperature on the diamond increased by 42.86 °C, 38.38 °C and 39.45 °C, respectively. The results also showed that the trend of the increase was slightly not linear when it compared to the water.

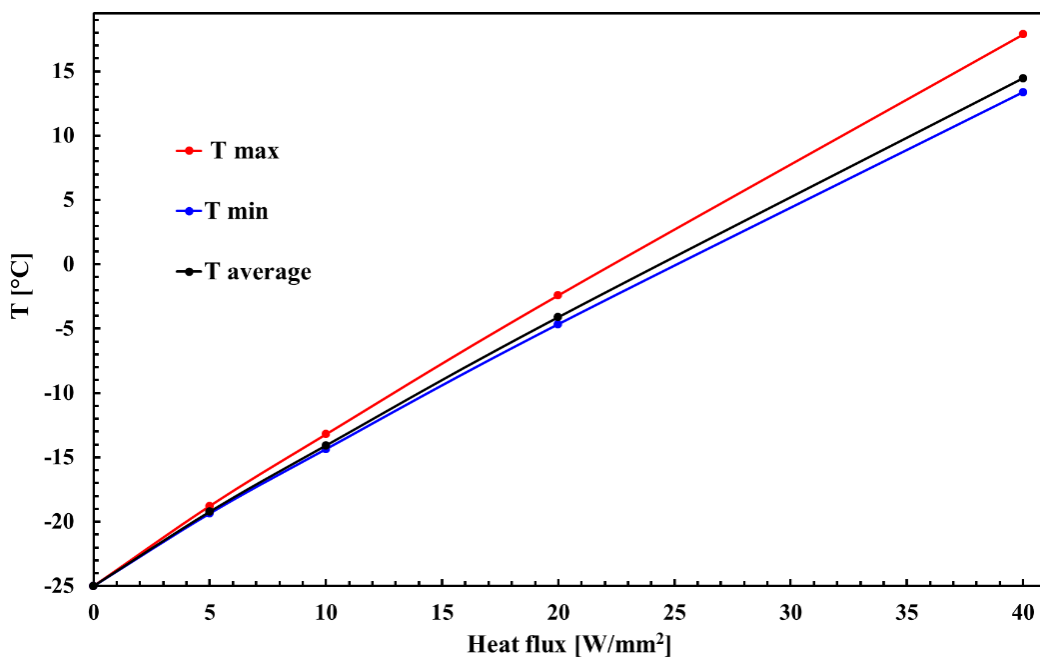
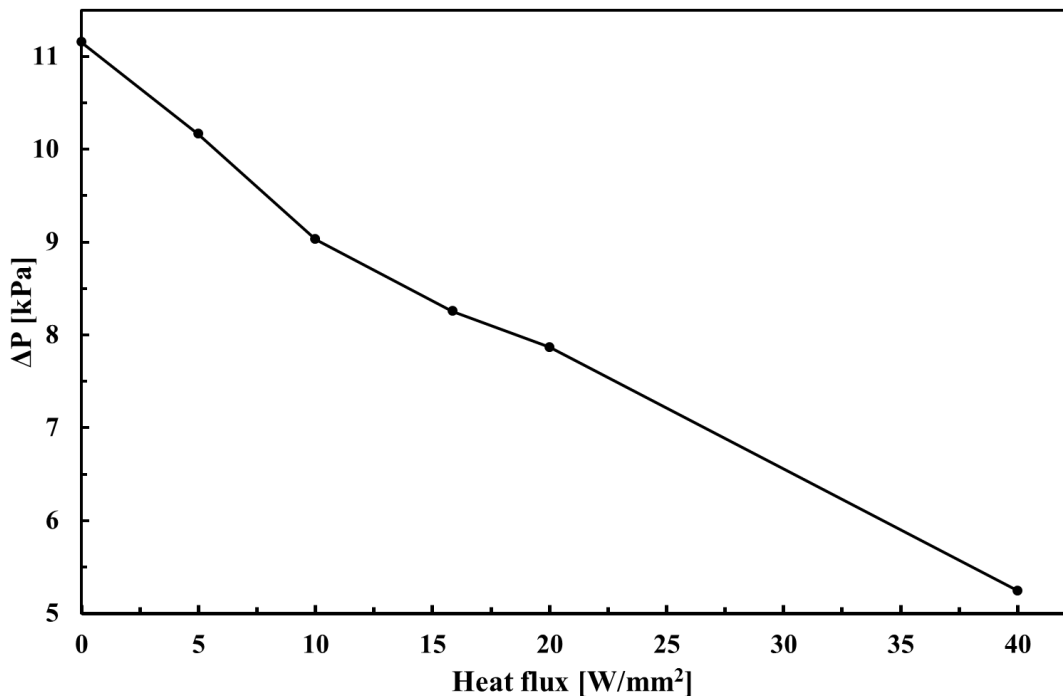


Figure 5. 62 Temperature on the diamond surface with heat flux

With the increase of the heat flux from 0 W/mm² to 40 W/mm², the pressure drop showed a linear decreasing from 11.15 kPa to 5.24 kPa as is illustrated in Figure 5. 63. This 50 % decrease was mainly due to the decrease of viscosity with the increase in temperature. In the real application of a microchip with a heat flux of 40 W/mm², if the system can provide a pressure drop of 11.15 kPa, due to the decrease of pressure drop at the same inlet velocity of 0.1 m/s, a higher htc can be obtained via increase the inlet velocity to obtain the same pressure drop. This is important as the increase of the heat flux need higher htc to maintain the temperature on the microchip. This can be obtained by an increase of inlet velocity as an acceptable pressure drop can still be maintained.

Figure 5. 63 ΔP of nanofluid with different heat flux

- ***Dimensionless analysis***

A dimensionless analysis of fluid parameter relevant to the heat transfer, for a given micro-jet impingement channel, suggests that the Nusselt number has a functional dependence as shown in the following equation:

$$\overline{Nu} = C Re^m Pr^n$$

The same least square method as is shown in the previous section has been used with the dimensionless parameter obtained from the simulation. In this study, the heat transfer performance in the laminar flow with EG+DW and 2.0 wt.% nanofluid was investigated with $0.3 \leq Re \leq 46$ and $100 \leq Pr \leq 4000$.

The EG+DW data were used to fit the correlation given by:

$$\overline{Nu} = 0.206 Re^{0.393} Pr^{0.426} \quad (5-16)$$

As is shown in 错误!未找到引用源。, the performance of the fit curve agreed quite well with the experiment by the given correlation. The index of the Reynolds number and Prandtl numbers are close

to each other. This suggests both factors play a similar influence on the thermal performance of the jetting channel.

- ***Summary of the micro-jet channel with DW ethylene glycol+distilled water based nanofluid***

The following observations were obtained on work on the rGO/EG+DW nanofluids:

- Compared with the EG+DW base fluid, the rGO nanofluid can have a lower ΔP for the same heat transfer coefficient et vice versa. This meant that 2.0 wt. % rGO/EG+DW nanofluid had better performance than the base fluid.
- The inlet temperature did not significantly change the heat transfer coefficient of the micro-jet channel. The temperature distribution had a linear shift with respect to the change of the inlet temperature.
- The heat flux affected the heat transfer coefficient of the micro-jet channel. The reason for that is likely due to the viscosity decrease with the increase of temperature in the fluids chamber.

The dimensionless analyses suggest that the index of Reynolds number be 0.393 and Prandtl number be 0.426, indicating that both factors played a similar influence on the thermal performance of the jetting channel.

5.3. Results and discussion 3 - Material selection for the thermal package

Ansys workbench was used to simulate the temperature distribution for the microchips. The simulation aimed to select suitable materials for the die-attach and heat spreader. Although GaN-on-Diamond was the final device to be investigated, the die has not yet been fabricated. As a result, commercial GaN-on-SiC transistors (TriQuint TGF2022-06 and Cree InC CGHV60040D) were used for the experimental validation. The validated model can then be used confidently for modelling GaN-on-Diamond device.

5.3.1. Assumption and geometry in simulation

Several assumptions were used in the modelling:

- The whole solid modelling domain was $\frac{1}{4}$ symmetrical in theory. To combine this model with the microfluidic channel model which was $\frac{1}{2}$ symmetrical, the simulation domain was assumed to be $\frac{1}{2}$ symmetrical;
- Convection and the radiation were negligible in the solid modelling domain;
- The bottom surface of the heat spreader was set to be $20\text{ }^{\circ}\text{C}$ with an infinite heat transfer coefficient - an ideal condition for the cooling;
- The solid materials properties were assumed to be constant and isotropic;
- There was no phase change and/or any chemical reaction in the high temperature.

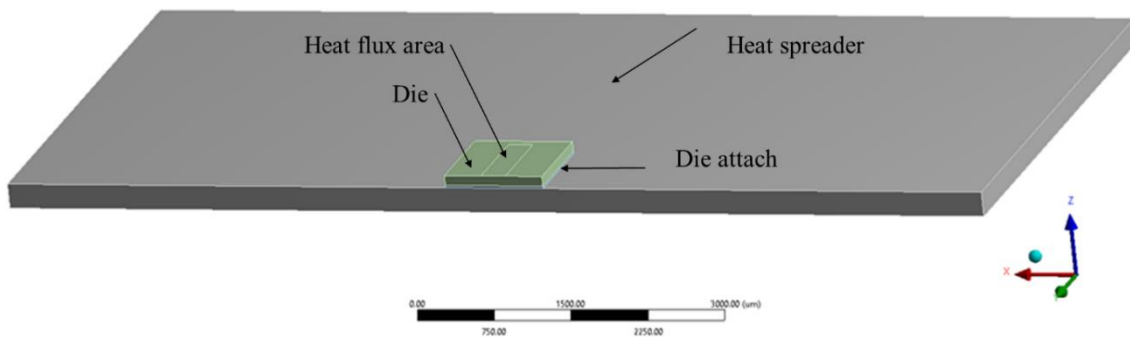


Figure 5. 64 Geometry of the die simulation

Figure 5. 64. shows the solid modelling domain, mainly the heat spreader, the die and the die-attach. Their respective models are described in the following.

1. The die in the simulation

The geometries of a GaN-on-SiC transistor and a GaN-on-Diamond transistor were simplified. The 1–1.5 µm GaN layer was not simulated in the modelling. Meanwhile, the 40 fingers of the transistor were represented by a heat flux with an area of $250 \times 1800 \mu\text{m}$ as is shown in Figure 5. 64. The power applied on the die was 50 W. The heat flux in the given area was thus 111.11 W/mm^2 . The size of the die was set to be $1000 \times 2000 \times 100 \mu\text{m}$. As is shown in Table 5. 8, the thermal resistances for the SiC and diamond dies were $2.4 \times 10^{-7} \text{ }^\circ\text{C/W}$ and $8.3 \times 10^{-8} \text{ }^\circ\text{C/W}$, respectively.

2. The die-attach in simulation

The die-attach was used as a thermal interface material (TIM) to connect the die and the heat spreader as is shown in Figure 5. 64. The size of the die-attach was $1000 \times 2000 \times 25 \mu\text{m}$ which was close to the real application on most occasions. As discussed in Chapter 2, there are several types of die-attach materials including adhesives, solders, and sintered silver etc. To investigate the effect of thermal conductivity of the TIMs on the temperature distribution, five thermal conductivities representing different TIMs were chosen, as listed in

Table 5. 9. The low thermal conductivity values of $0.14 \text{ W/(m}\cdot\text{K)}$ and $1.4 \text{ W/(m}\cdot\text{K)}$ were for the epoxy. The medium thermal conductivity of $14 \text{ W/(m}\cdot\text{K)}$ was for the silver-filled adhesive and solder; whereas the high thermal conductivity of $140 \text{ W/(m}\cdot\text{K)}$ was for the silver sintered die-attach which was claimed to have a thermal conductivity over $100 \text{ W/(m}\cdot\text{K)}$ and the ultra-high thermal conductivity of $1200 \text{ W/(m}\cdot\text{K)}$ was the same as the diamond. With an increase in the thermal conductivity from $0.14 \text{ W/(m}\cdot\text{K)}$ to $1200 \text{ W/(m}\cdot\text{K)}$, the thermal resistance decreased from $1.8 \times 10^{-4} \text{ }^\circ\text{C/W}$ to $2.1 \times 10^{-8} \text{ }^\circ\text{C/W}$.

3. The heat spreader in simulation

Traditionally, the die-attach was pasted with a metal plate such as copper, aluminium etc. before combining with a microfluidic cooling channel or other types of heat sinks. Since copper has a higher thermal conductivity than aluminium, it was used as a metal heat spreader in this layer. To increase the heat transfer in this layer, other materials were also considered in the simulation, e.g. diamond. The size of the heat spreader was $10 \times 10 \times 0.25 \text{ mm}$ as shown in Figure 5. 64. The thermal resistances of the copper heat spreader and the diamond heat spreader were $6.5 \times 10^{-7} \text{ }^\circ\text{C/W}$ and $2.1 \times 10^{-7} \text{ }^\circ\text{C/W}$, respectively.

CHAPTER 5 RESULTS AND DISCUSSIONS

Table 5. 8 Dimension of the die device

Material	Dimensions μm
Die	1000×2000×100
Die-attach	1000×2000×25
Heat spreader	10000×10000×250
Heat flux	250×1800

Table 5. 9 Material used in Ansys

Material	k W/(m·K)	R_{th} °C/W
SiC die	420	2.4E-07
Diamond die	1200	8.3E-08
Diamond heat spreader	1200	2.1E-07
Copper heat spreader	385	6.5E-07
Die-attach-1 (epoxy)	0.14	0.00018
Die-attach-2 (epoxy with Ag particle)	1.4	1.8E-05
Die-attach-3 (Au-Pb solder)	14	1.8E-06
Die-attach-4 (silver paster)	140	1.8E-07
Die-attach-5 (diamond)	1200	2.1E-08

5.3.2. Temperature difference in different layers of the microchip

- *Die layer*

Figure 5. 65 illustrates the temperature difference (ΔT) across the die layer. The x-axis of the thermal conductivity of die-attach started from 0.14 W/(m·K) which is a type of epoxy to 1200 W/(m·K) which is diamond. It can be seen that the diamond die had better performance than SiC chip; the ΔT for SiC die was >10 °C higher than that of diamond for a given heat spreader. The reason for this was mainly due to the high thermal conductivity of the diamond. For the SiC die, an increase in the thermal conductivity of the die-attach from 0.14 W/(m·K) to 1.4 W/(m·K) did not give the great increasing trend of ΔT in the die. However, with a thermal conductivity increase from 1.4 W/(m·K) to 140 W/(m·K), a clear increase was observed. The rate of the increase gradually slowed down with further thermal conductivity increase from 140 W/(m·K) to 1200 W/(m·K). The diamond die showed a similar trend. For thermal conductivity varying from 0.14 W/(m·K) to 14 W/(m·K), ΔT reduced by only 0.2 °C. With a thermal conductivity increase from 14 W/(m·K) to 140 W/(m·K), ΔT showed a clear increase. A very slow increase can be seen when the thermal conductivity increases from 140 W/(m·K) to 1200 W/(m·K).

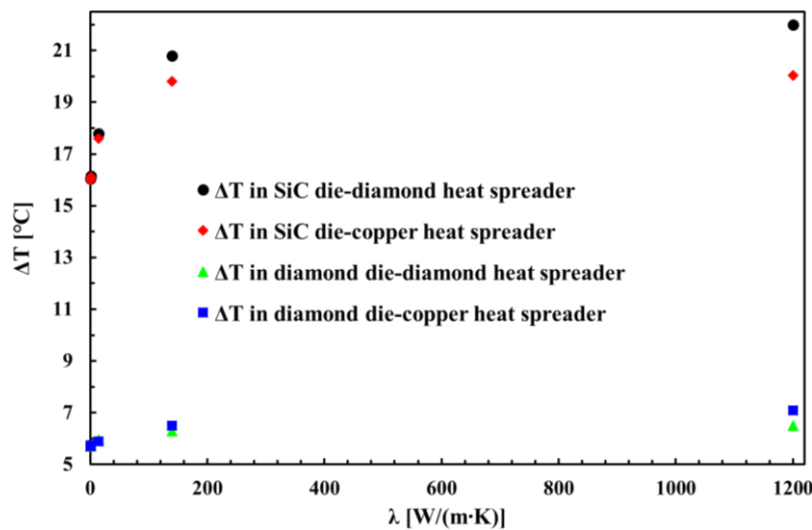


Figure 5. 65 ΔT in the die layer with different die-attach

The diamond heat spreader had a better performance than the copper heat spreader for both types of the die. The reason is due to the high thermal conductivity of the diamond heat spreader.

- ***Die -attach layer***

Figure 5. 66 illustrates the ΔT in the die-attach layer. The results showed that the die-attach greatly affected the temperature distribution for all kind of die with all kind of heat spreader. With the increase of thermal conductivity from 0.14 W/(m·K) to 140 W/(m·K), for diamond dies with diamond heat spreader, the ΔT decreased from 4487.8 °C to 9.0 °C. Then it gradually further decreased to 1.292 °C with the increase of thermal conductivity further to the 1200 W/(m·K). It can also be seen that the maximum temperature difference in the die was over 4450 °C based on the assumption of no phase change and/or chemical reaction. In reality, the die simply burnt out with this poor thermal management. Thus, the die-attach material with sintered silver seemed to have good results for the temperature decrease in the die-attach layer. Further increase of the thermal conductivity for die-attach material did not show a large decrease of ΔT in the die-attach layer. This implied that the thermal resistance of the die-attach layer with thermal conductivity larger than 140 W/(m·K) was not the main thermal resistance for the system

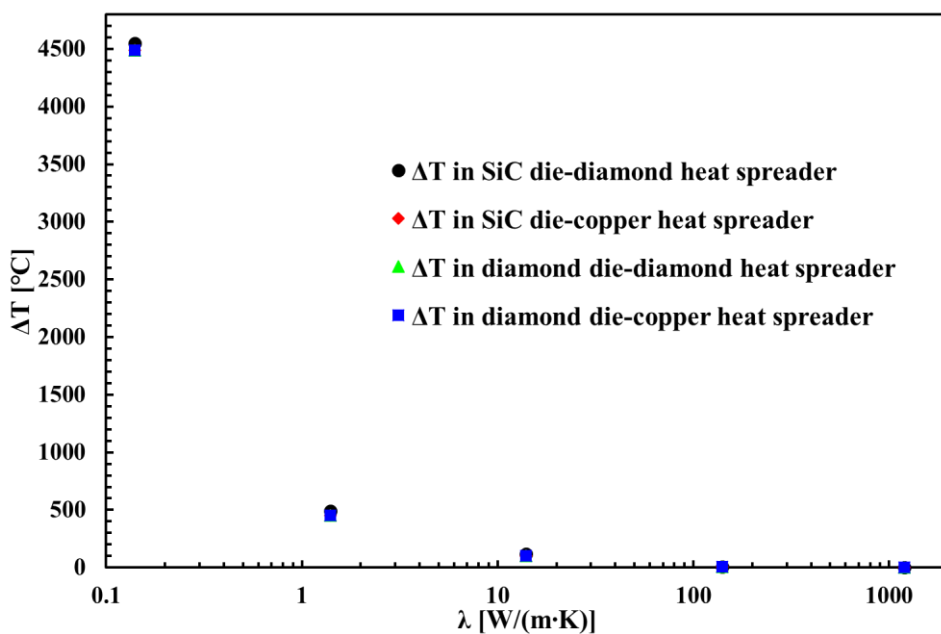


Figure 5. 66 ΔT in the die-attach layer with different die-attach

- ***Heat spreader layer***

Figure 5. 67 illustrates the ΔT in the heat spreader layer. The results showed that the diamond heat spreader had better performance than its counterpart. In each different die-attach, the ΔT in diamond heat spreader was >10 °C larger than its counterpart for the same die.

Meanwhile, it can be seen that for diamond heat spreader with die-attach's thermal conductivity increase from 0.14 W/(m·K) to 1.4 W/(m·K), the increasing trend of ΔT in the heat spreader was little. However, with thermal conductivity increase from 1.4 W/(m·K) to 140 W/(m·K), it showed an obvious increase. It can be noticed that for the thermal conductivity increase from 140 W/(m·K) to 1200 W/(m·K), there was little ΔT change for the SiC die with diamond heat spreader while the diamond die with diamond heat spreader showed just 1.6 °C decrease was obtained.

It can be easily noticed that the copper heat spreader with diamond die showed a similar trend with diamond heat spreader with diamond die. However, the copper heat spreader with SiC die showed a different trend with die-attach's thermal conductivity increase from 140 W/(m·K) to 1200 W/(m·K), the ΔT decreased about 1.1 °C.

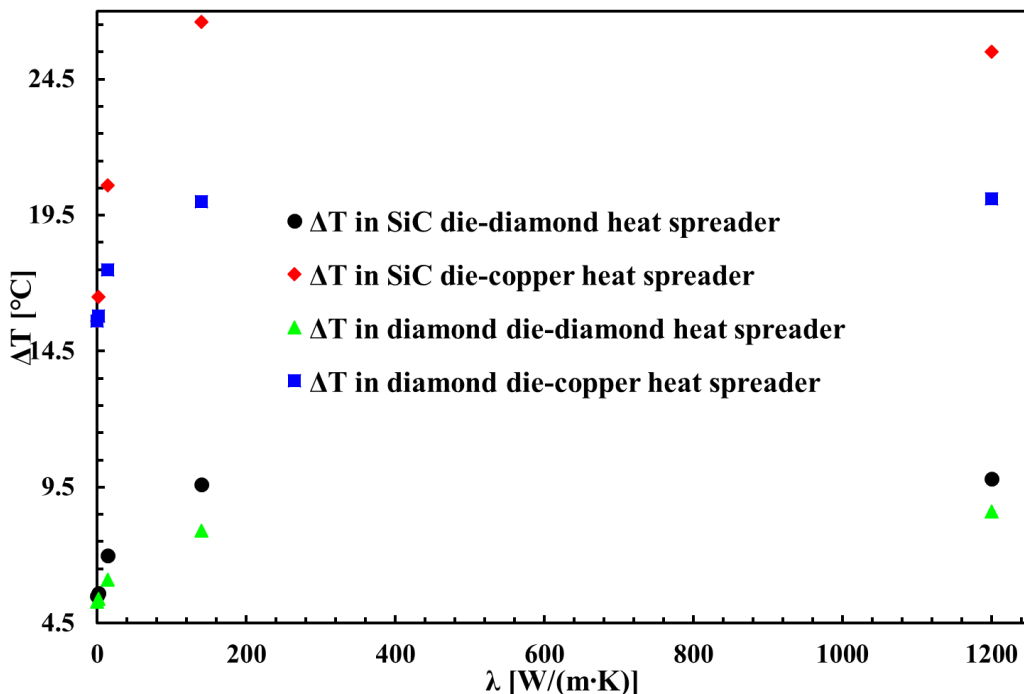


Figure 5. 67 ΔT in the heat spreader with different die-attach

CHAPTER 5 RESULTS AND DISCUSSIONS

The reason for this behaviour might be explained by the thermal resistance change in the whole devices.

According to

Table 5. 9, for the SiC die with copper heat spreader the SiC die had a thermal resistance of 2.4×10^{-7} °C/W and copper heat spreader of 6.5×10^{-7} °C/W. The die-attach with thermal conductivity of 0.14 W/(m·K), 140 W/(m·K) and 1200 W/(m·K) had the thermal resistance of 1.8×10^{-7} °C/W, 1.8×10^{-7} °C/W and 2.1×10^{-8} °C/W, respectively.

The thermal resistance flow path was drawn in Figure 5. 67. The heat was spread and conducted in all parts of the transistors. With the decrease of thermal resistance in the die-attach, more heat was conducted via Q_{die1} and $Q_{dieattach1}$ because this part had a low thermal resistance. Thus, the temperature differences increased in the die and the die-attach. This can be seen in Figure 5. 68 and Figure 5. 69. The heat flux at the bottom surface of the SiC die increased from 2.5×10^7 W/m² to 7.0×10^7 W/m² with thermal conductivity increase from 0.14 W/(m·K) to 1200 W/(m·K). The same mechanism can be used to explain the increase in temperature difference in the heat spreader.

However, with the thermal resistance further decreasing to 2.1×10^{-8} °C/W, the thermal resistance in the copper heat spreader became the largest thermal resistance among the SiC die layer, die-attach layer and copper heat spreader layer. As is shown in Figure 5. 69 and Figure 5. 70, the heat flux in $Q_{dieattach1}$ decreased, as more heat flux chose another path. The interface heat flux of die-attach and copper heat spreader decreased from 5.59×10^7 W/m² to 5.37×10^7 W/m² with the die-attach thermal conductivity increase from 140 W/(m·K) to 1200 W/(m·K). Meanwhile, the heat flux at the bottom surface of copper heat spreader decreased from 3.48×10^7 W/m² to 3.34×10^7 W/m². All this account for the decrease of the temperature differences for in copper heat spreader for GaN - on - SiC transistors.

CHAPTER 5 RESULTS AND DISCUSSIONS

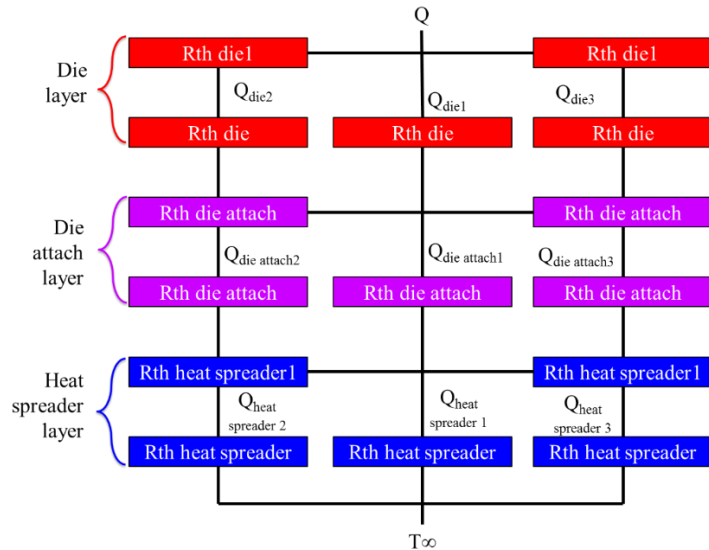


Figure 5.68 Thermal resistance schematic of the devices with heat spreader

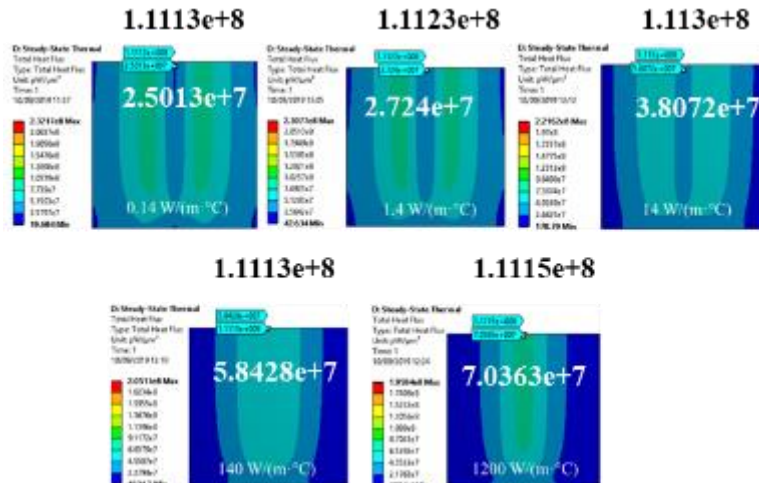


Figure 5.69 Heat flux distribution at the back of SiC die with copper heat spreader

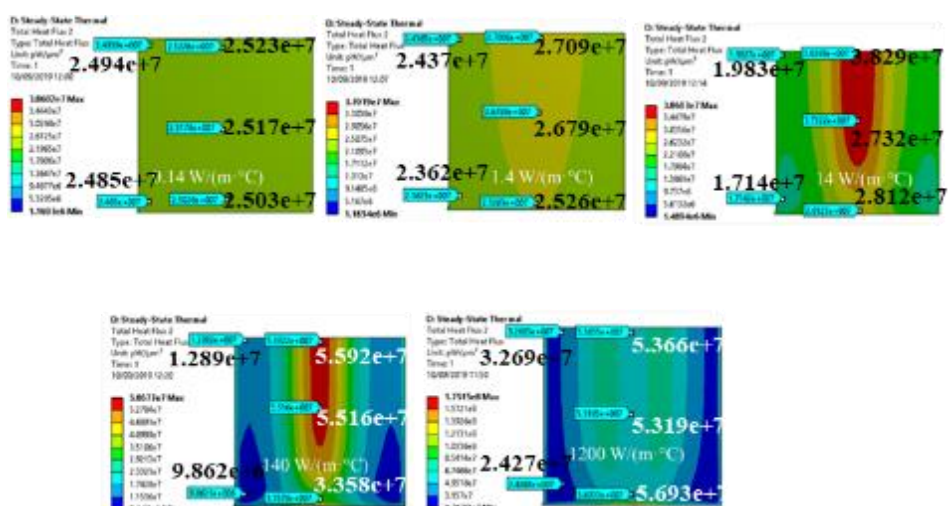


Figure 5.70 Heat flux distribution at the back of the die-attach surface with copper heat spreader

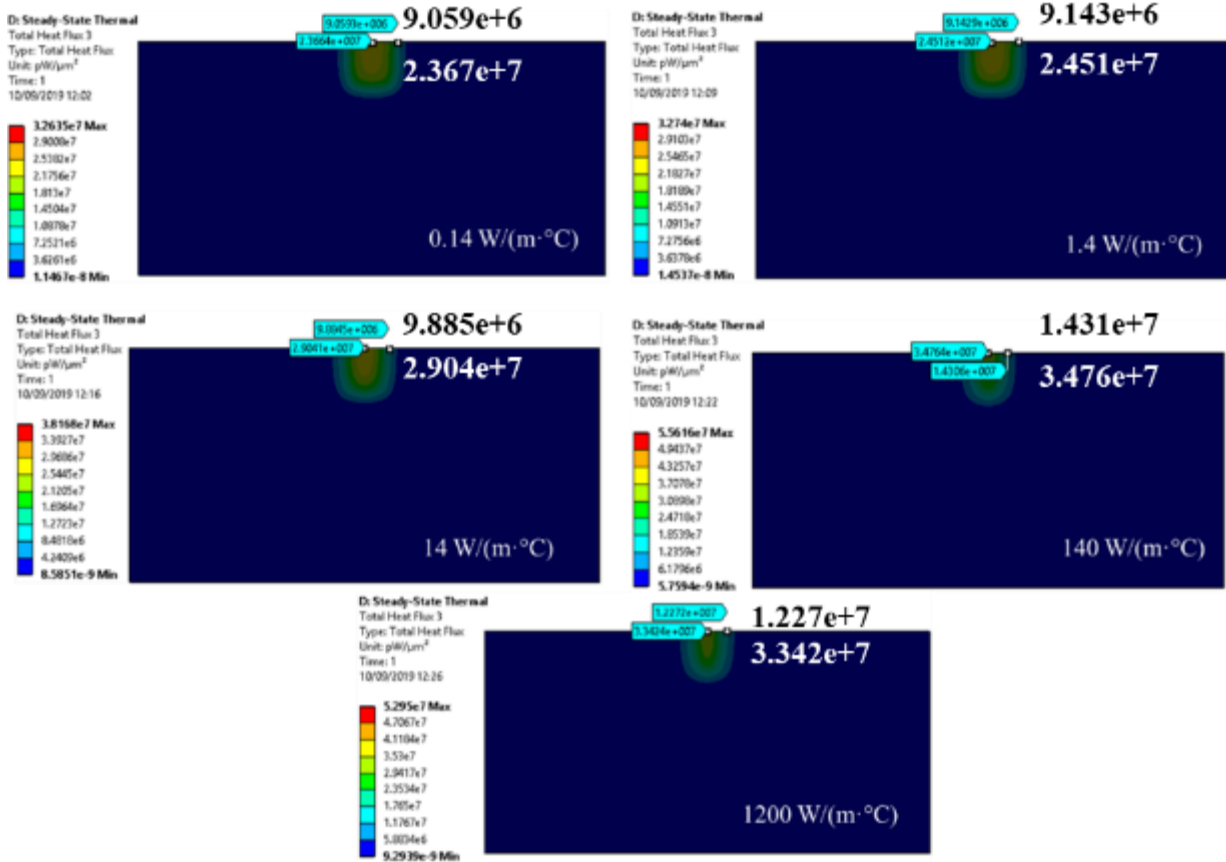


Figure 5. 71 Heat flux distribution at the back of copper heat spreader with SiC die

5.3.3. Maximum temperature on the microchip

It is important to look at the temperature on the die surface. Figure 5. 72 depicts the maximum temperature on the die with different die materials, heat spreaders and die-attach materials.

It can be observed that the most important factor influencing the die temperature is the die-attach material. For all die using epoxy as the die-attach material, which has a thermal conductivity of 0.14 W/(m·K) to 1.4 W/(m·K), the device cannot dissipate the 50 W power. It can be seen that the maximum temperature of the die can be as high as 4556 °C based on the assumption of no phase change and/or chemical reaction. In reality, the die simply burnt out due to this type of poor thermal management. The sintered silver with thermal conductivity of 140 W/(m·K) can dissipate the heat flux. The results also show that the second important factor affecting the maximum temperature in the transistor is the die material. With the die material changed from SiC to diamond, the maximum temperature in die decreases by 21.8 °C. The heat spreader also affects the maximum temperature on the die. For the

diamond die with a die-attach material with thermal conductivity of 140 W/(m·K), the maximum temperature reduces by 11.4 °C when the heat spreader material changes from copper to diamond.

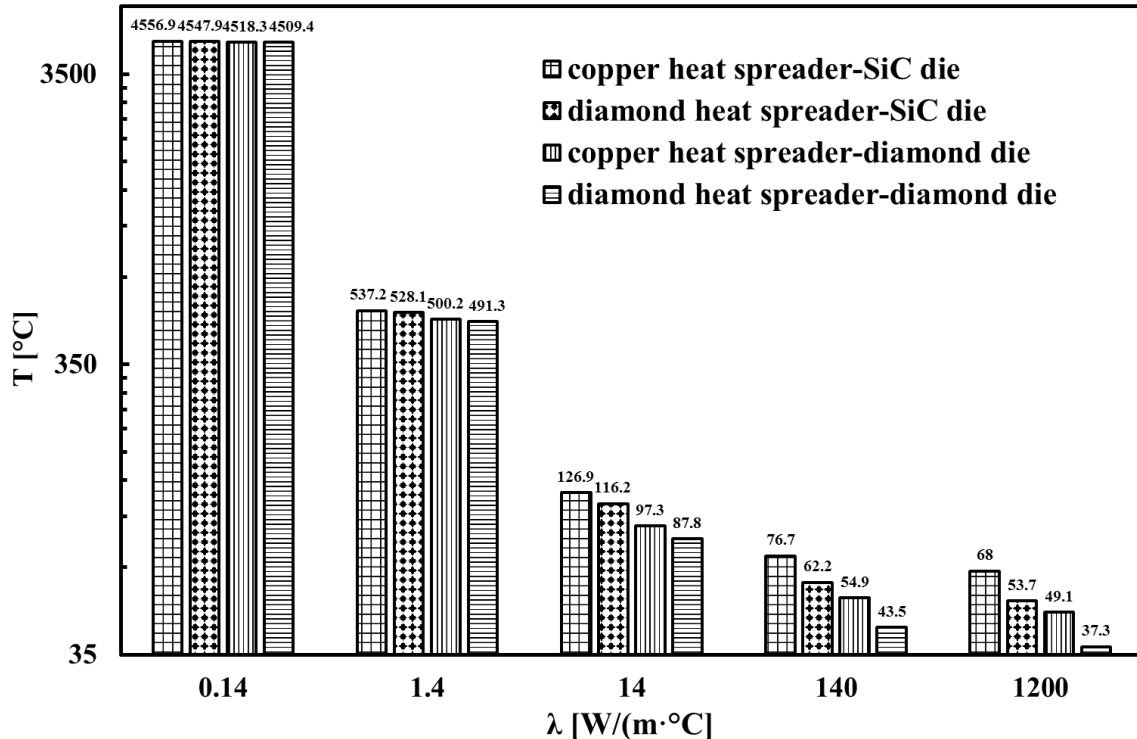


Figure 5. 72 Maximum temperature on die with different die-attach

5.3.4. Summary of material selection for the thermal package

The simulation of the die devices was done under an ideal condition to understand what sorts of materials can be used to make die-attach and heat spreader. The following observations are obtained:

- **Die-attach material** The die-attach material can significantly affect the temperature of the die. It should be noticed that the traditional die-attach materials such as epoxy with thermal conductivity of 0.14 W/(m·K) - 1.4 W/(m·K) and solder with thermal conductivity of 14 W/(m·K) cannot dissipate the required power of 50W for any types of dies. The silver sintered die-attach has a thermal conductivity of 140 W/(m·K) and can dissipate the heat flux. The results also show that although a further increase of the thermal conductivity of die-attach from 140 W/(m·K) to 1200 W/(m·K) can decrease the temperature in die-attach, it is just around 10

CHAPTER 5 RESULTS AND DISCUSSIONS

°C, the enhancement is not so apparent. The silver sintered die-attach was therefore used as the die-attach material.

- **Die material** The die-attach material is the second most important fact affecting the die temperature. Changing die material from SiC to diamond, the maximum temperature can decrease by 21.8 °C. This type of die is still in the developing stage, however, the commercial GaN-on-SiC devices were used in the experiment.
- **Heat spreader** The heat spreader affects the temperature on the die. The temperature on the copper heat spreader is 11.4 °C higher than the diamond heat spreader. The results show that the copper heat spreader could dissipate the 50 W power on the die with appropriate die-attach material. However, the diamond seems to be a better choice if the power of the die is going to further increase. Thus, the diamond heat spreader was chosen for the experiment.

5.4. Results and discussion 4 - Performance of Gallium Nitride transistors

Previous sections in this chapter have discussed the influences of different factors, including heat transfer fluids, the die-attach material, the die material, the spreader material and the micro-jet impingement channels, on the thermal management of the GaN transistors. One of the most important objectives for the PhD project is to find sets of conditions which can maintain the maximum temperature of the die below 200 °C. It is therefore important to model and experimentally measure the maximum temperature on the GaN transistor. This section presents the results of this set of studies.

5.4.1. Experiment and validation with simulation

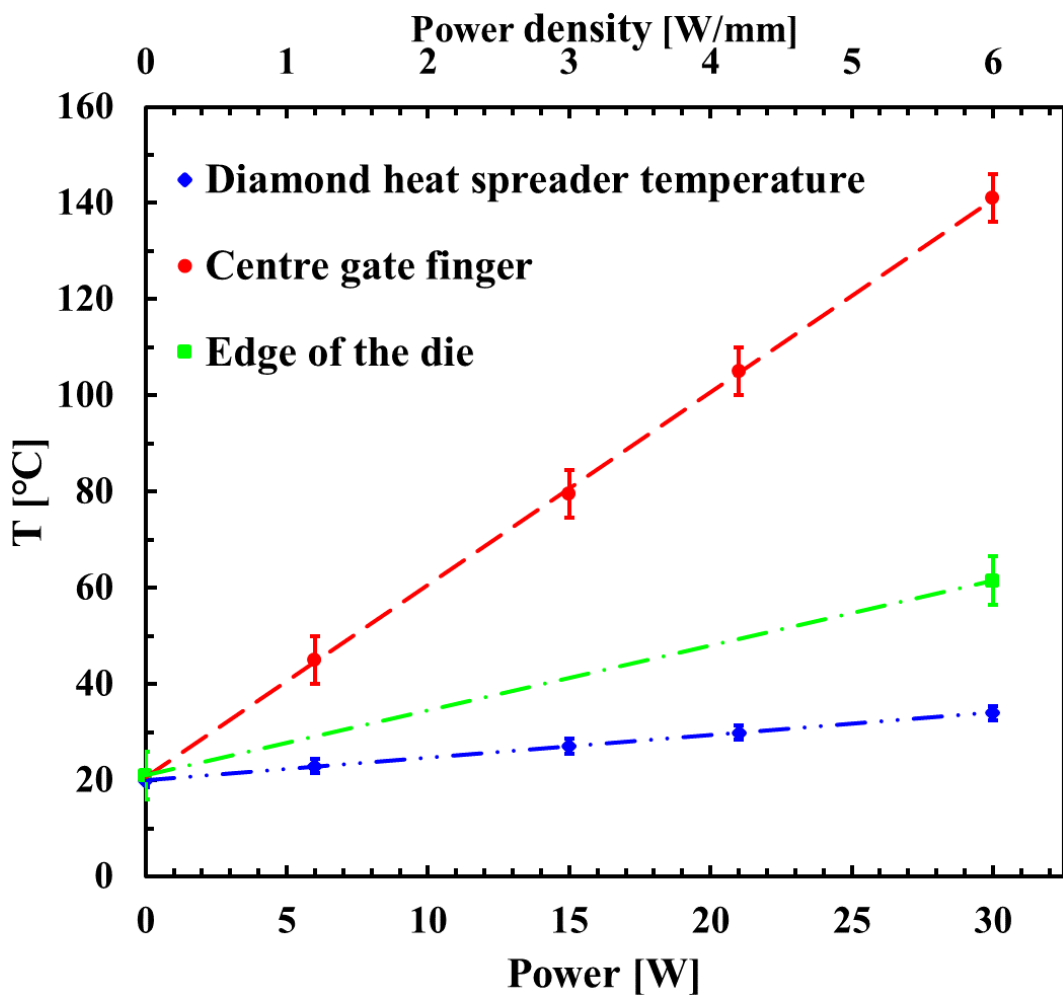


Figure 5. 73 Temperature with the power density

CHAPTER 5 RESULTS AND DISCUSSIONS

The maximum device temperature as a function of dissipated power density for the transistors via Raman thermography measurement is shown in Figure 5. 73. The measured temperature on the diamond heat spreader shows a 12.9 °C rise when the power density increases to 6 W/mm. Meanwhile, with a 30 W power applied on the devices, the maximum temperature in the fingers is around 140.57 °C, leading to a 118.57 °C temperature rise. These results also show that the peak temperature in the finger and the temperature on the diamond heat spreader increase in a linear fashion with increasing power density. This implies that the heat transfer coefficient of the fluid does not significantly change with the change in the power density.

In order to obtain the maximum temperature in the transistors, a 3D model was developed. The model was validated by the experimental results. The modelling was conducted using an ANSYS Steady-state thermal tool. As is illustrated in Figure 5. 74 (a), in the experiments, because of a spare die attaching to the diamond heat spreader, the working die was not in the centre of the diamond heat spreader. Its dimension for the offset is shown in Figure 5. 74 (b). The vertical distance to the centre was 650 µm and the horizontal offset was 1250 µm. As the location of the large heat transfer coefficient area was in the centre of the diamond heat spreader, simulations with die in the centre were also done to compare with its counterpart.

In the simulations, an output power of 30 W that was the same as the experimental condition was used for the heat flux in the GaN transistor. The bottom surface of the diamond heat spreader was applied with a convection condition. The heat transfer coefficient distribution for the convectiveal heat transfer condition which was calculated by the ANSYS fluent model for water and 2.0 wt. % of rGO nanofluids were given in the previous section. The reference temperature was set 20 °C that was the same as the measured value in the experiment.

In the simulations, the thermal conductivity of some materials was assumed to be constant as is shown in Table 5. 10. The thermal conductivity of the diamond, SiC, AlN and GaN that was dependent with the temperature as is shown in Figure 5. 75. The validation of the simulation and the experiment is shown in

CHAPTER 5 RESULTS AND DISCUSSIONS

Table 5. 11. The temperature in the 10th the finger and the edge of the die, which was measured by Raman and K type thermocouple, showed good agreement with the simulation results.

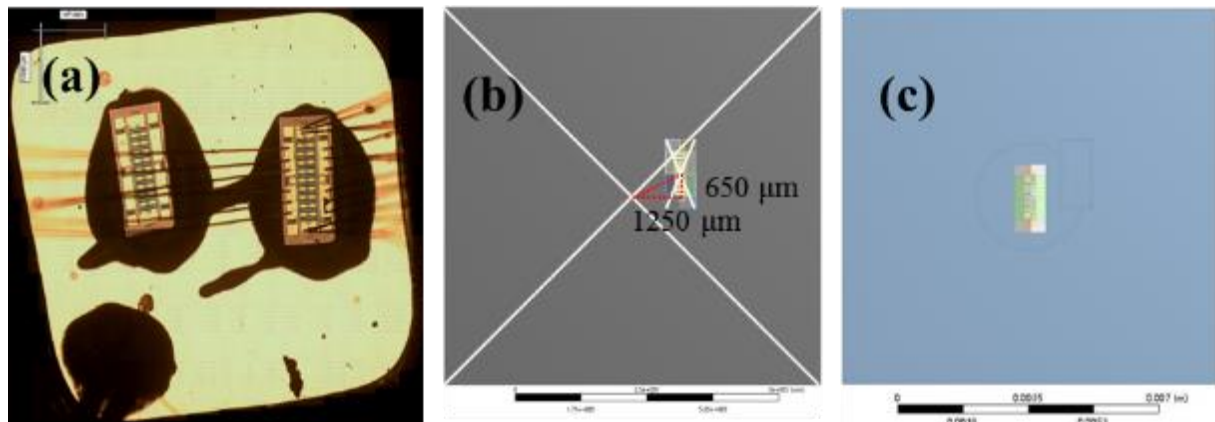


Figure 5. 74 (a) Experimental location of the die;(b) simulation with die non-centre (c) simulation with die in the centre

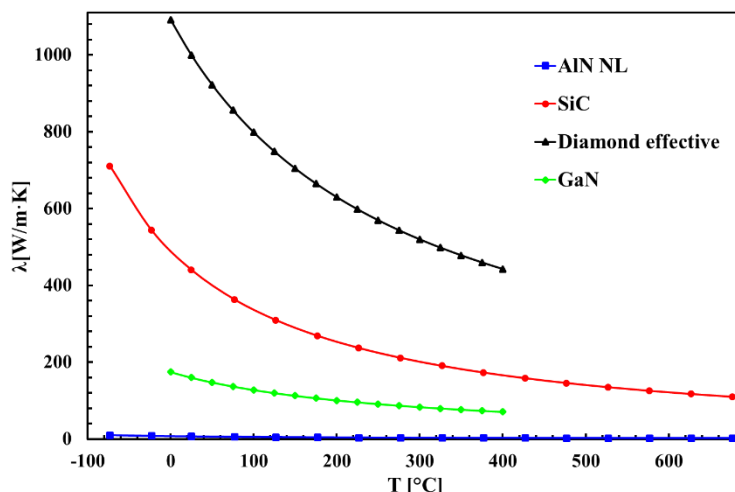


Figure 5. 75 Thermal conductivity of different materials with temperature in simulation

Table 5. 10 Thermal conductivity of different materials in the simulation

Material	k W/(m·K)
AlGaN	10
Al	210
Die attach	50
Flange TIM	3
Gold	315
SiN	3

Table 5. 11 Experimental temperature and simulation temperature

maximum T	Diamond	10 finger Raman
-----------	---------	-----------------

	°C	°C	°C
Experiment results	N	34 ± 1.5	141 ± 5
Simulation model	187.01	31.62	138.00

5.4.2. Temperature in Gallium Nitride transistors with deionised water

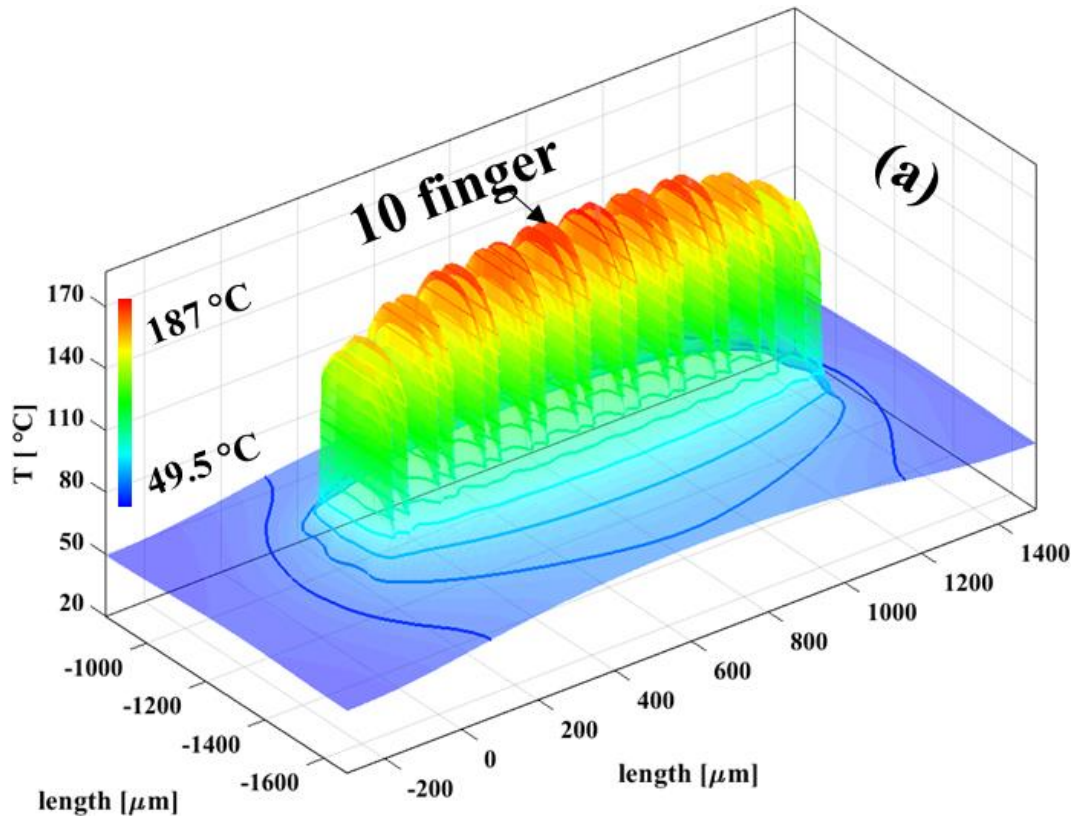
The temperature distribution and its profile were shown in Figure 5. 76. With the 30 W power applied on the die, the maximum temperature according to the Raman measurement is 141 ± 5 °C in the 10th finger. In the simulation, using the same average method, this temperature is 138 °C. The temperature difference between the simulation and the experiment was less than 5 °C.

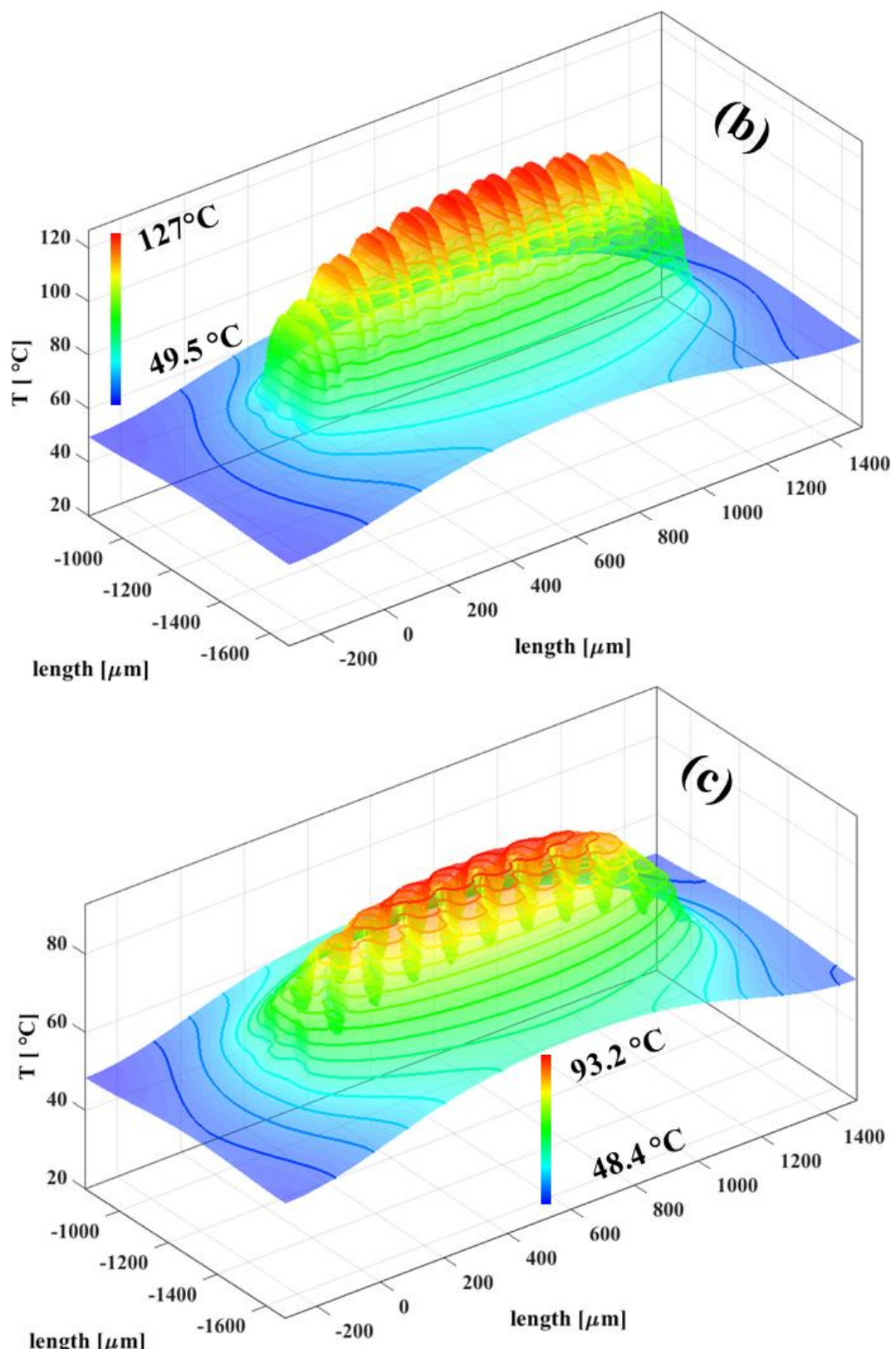
The temperature distribution for the finger layer is illustrated in Figure 5. 76 (a) and Figure 5. 76 (e). According to the simulation, the maximum temperature in the finger layer was 187.01 °C located in the centre of the die which is assigned as the gate 10. The temperature at the rim of the devices was 49.5 °C and it sharply increased to 157.31 °C (107.91 °C temperature difference) for the finger 1. However, the temperature gradually increased from finger 1 to finger 10 with the peak temperature difference of 29.60 °C. It seems to indicate that the major heat flux was concentrated in the finger area. It did not spread to the whole area in the devices. It can also be obtained that the temperature showed a quarter symmetric for the finger layer.

The temperature distribution on the top SiC layer that was about 1.5 μm away from the finger layer as illustrated in Figure 5. 76 (b) and Figure 5. 76 (e). The peak temperature distribution still was observed in this layer. The Maximum temperature in this layer was 126.57 °C that was 60.44 °C lower than the maximum peak temperature in the finger. The sharp decrease was because of the high thermal resistance in the AlGaN layer that acted as the thermal resistance. However, the peak temperature difference in this layer was 25.72 °C that was only 3.88 °C lower than its counterpart in the finger layer which might suggest the heat flux distribution did not significantly change through the GaN layer and the AlGaN layer. It should be pointed out that the temperature in this layer still showed the symmetric distribution. Both symmetric temperature distribution suggested that the asymmetric of the heat transfer coefficient did not significantly affect the heat flux distribution in the GaN layer.

The temperature distribution on the bottom SiC layer was illustrated in Figure 5. 76 (c) and Figure 5. 76 (e). The maximum temperature in the bottom of the SiC layer was 93.21 °C that is 35.36 °C lower than the maximum temperature on the top of the SiC layer. The results also showed that no obvious peak temperature could be observed in this layer. The reason for this might be that the high thermal conductivity of the SiC layer efficiently spread the heat flux. Thus, the inhomogeneous heat flux was evened. In this layer, the temperature distribution showed slightly asymmetric.

The temperature distribution in the top of diamond heat spreader was illustrated in Figure 5. 76 (d) and Figure 5. 76 (e). The maximum temperature in this layer was 49.23°C that was 43.28 °C lower than the top surface of the die-attach layer. The asymmetric temperature was observed. The peak temperature in this layer suggests that even diamond with high thermal conductivity cannot even the heterogeneous heat flux. Thus, the localised high heat transfer coefficient was suitable for thermal management of GaN transistors.





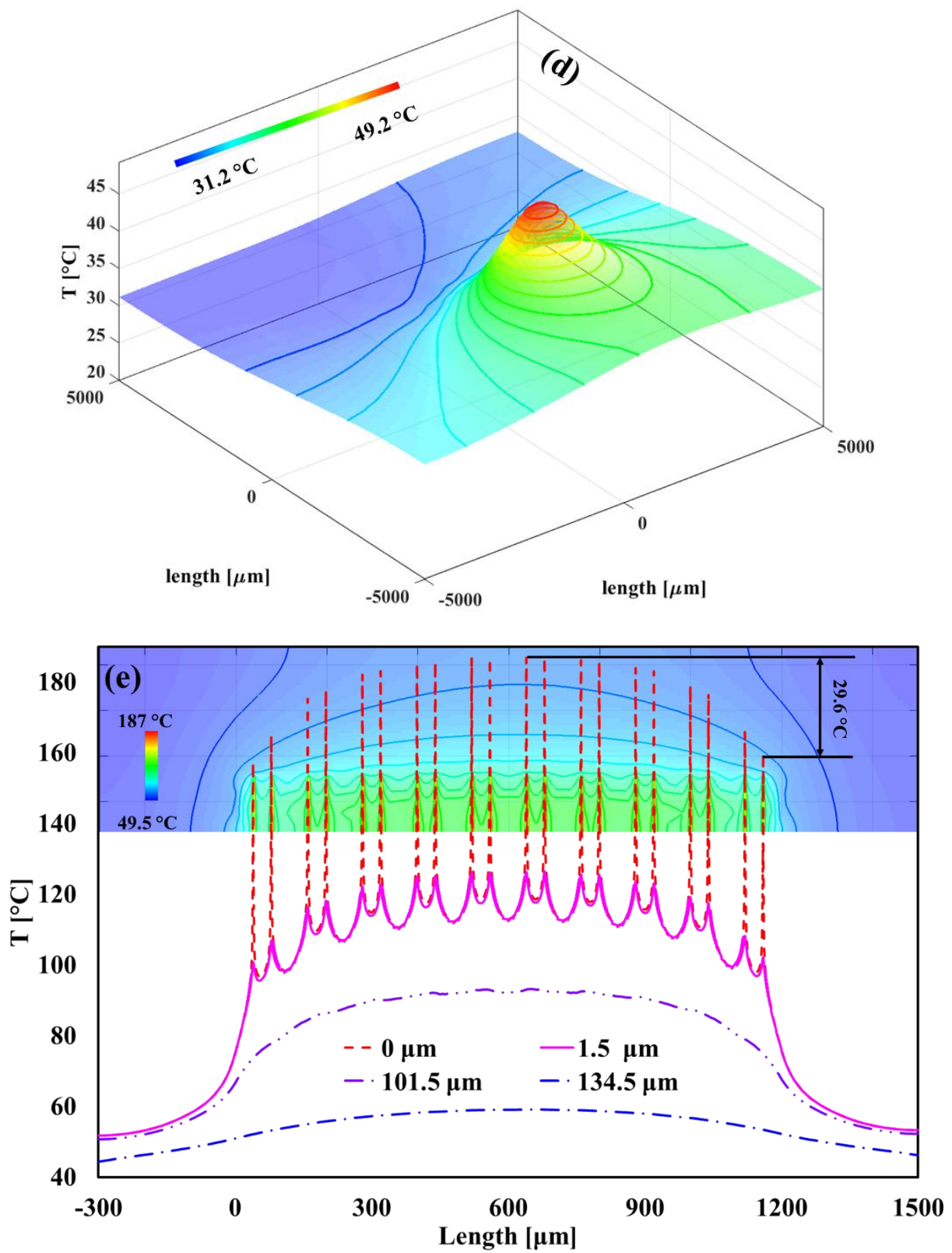
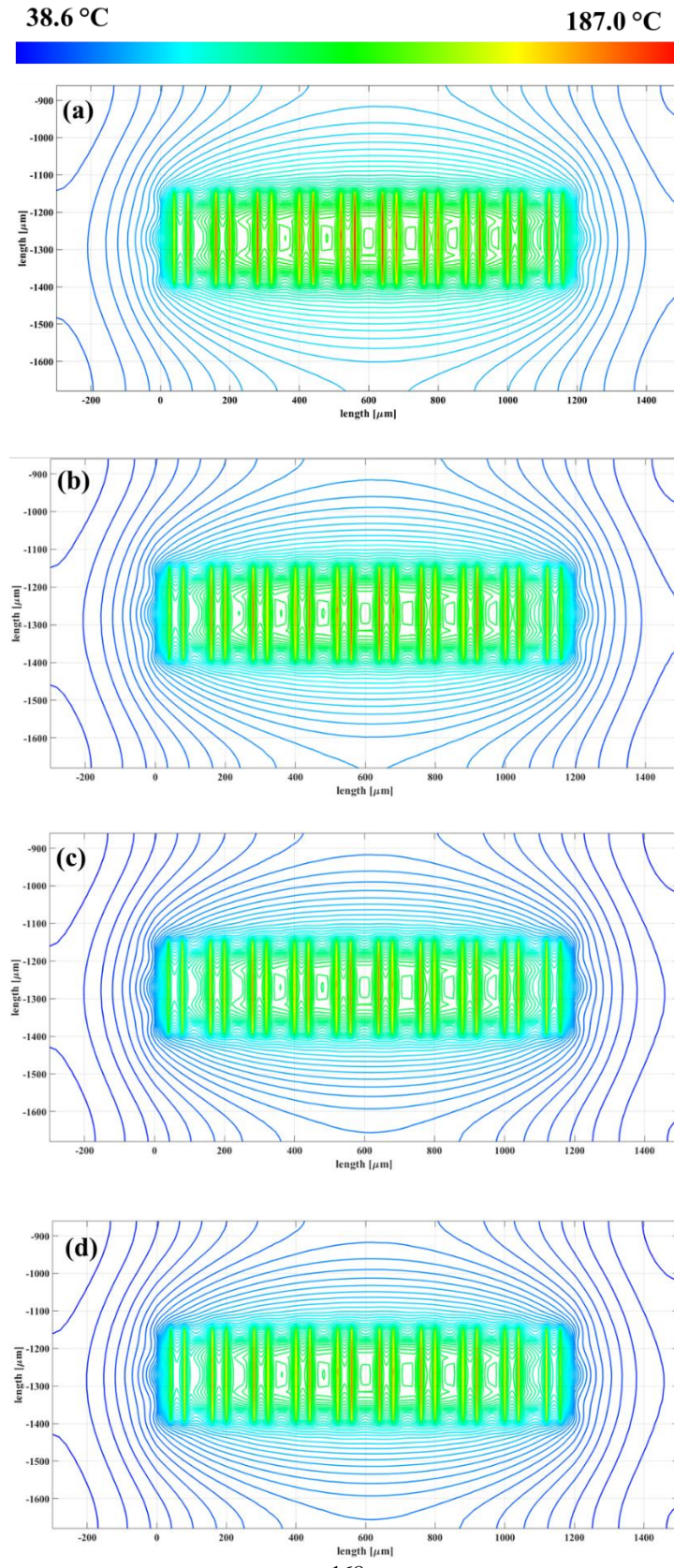


Figure 5.76 Temperature distribution (a) in fingers ($0 \mu\text{m}$); (b) bottom of the AlGaN layer ($1.5 \mu\text{m}$); (c) bottom of the SiC layer ($101.5 \mu\text{m}$), (d) bottom of the silver sintered die-attach layer and (e) cross-sectional temperature profile for the different layers with the inlet velocity of 0.53 m/s and inlet temperature of $20.0 ^{\circ}\text{C}$

5.4.3. Thermal performance of Gallium Nitride transistors

- *Inlet velocity*



CHAPTER 5 RESULTS AND DISCUSSIONS

Figure 5. 77 Temperature contour plot of the finger layer with (a) 0.53 m/s; (b) 1 m/s ;(c) 2 m/s and (d) 3m/s

With the increase of the inlet velocity, the heat transfer coefficient increased. Thus, the temperature in the whole devices decreased. Figure 5. 77 showed the temperature in the finger layer with a velocity increase from 0.53 m/s to 3 m/s. The maximum temperature in the finger was 187.01 °C, 178.82 °C, 173.17 °C and 170.87 °C for the velocity of 0.53 m/s, 1 m/s, 2 m/s and 3 m/s respectively. The temperature difference decrease of 16.14 °C was achieved from 0.53 m/s to 3 m/s. The temperature difference was 8.19 °C, 5.61 °C and 2.30 °C for the velocity change from 0.53 m/s to 1 m/s, 1 m/s to 2m/s and 2 m/s to 3 m/respectively. The decrease of the temperature difference with the same velocity difference suggested that the increase of the heat transfer coefficient in the micro-jet impingement channel part did not significantly change the maximum temperature in the die. The reason for this will be explained by the thermal resistance in the following section.

- ***Location of the die***

Due to the location of high heat transfer coefficient in the centre of the bottom surface of the diamond heat spreader, the maximum temperature of the die located in the centre of the diamond heat spreader was lower than the die off the centre as is illustrated in Figure 5. 78. The results showed that the temperature difference between different locations decreased with the increase of the inlet velocity. The temperature difference in 0.53 m/s was 4.86 °C, it decreased to 2.25 °C when the velocity increased to 3.00 m/s.

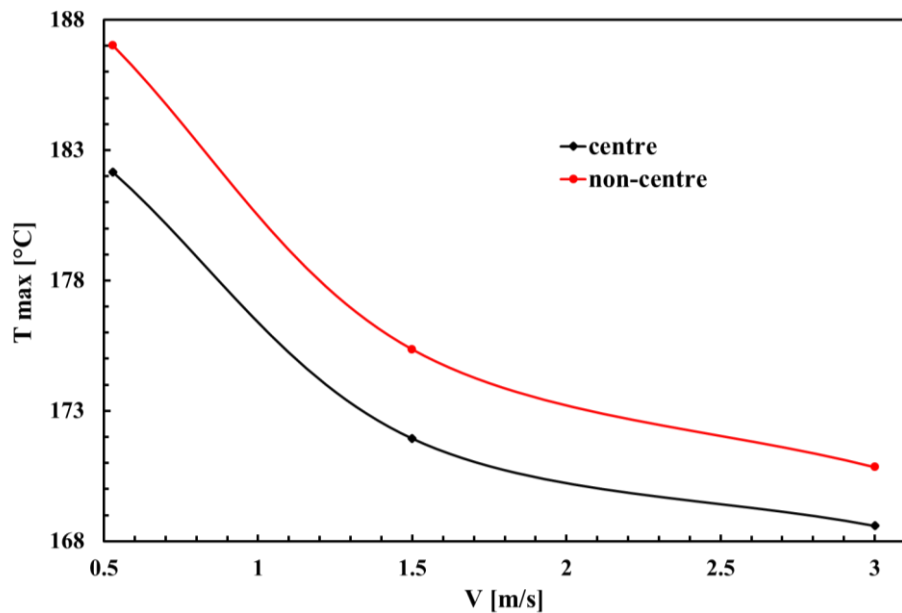


Figure 5. 78 Maximum temperature in the die with die in different locations

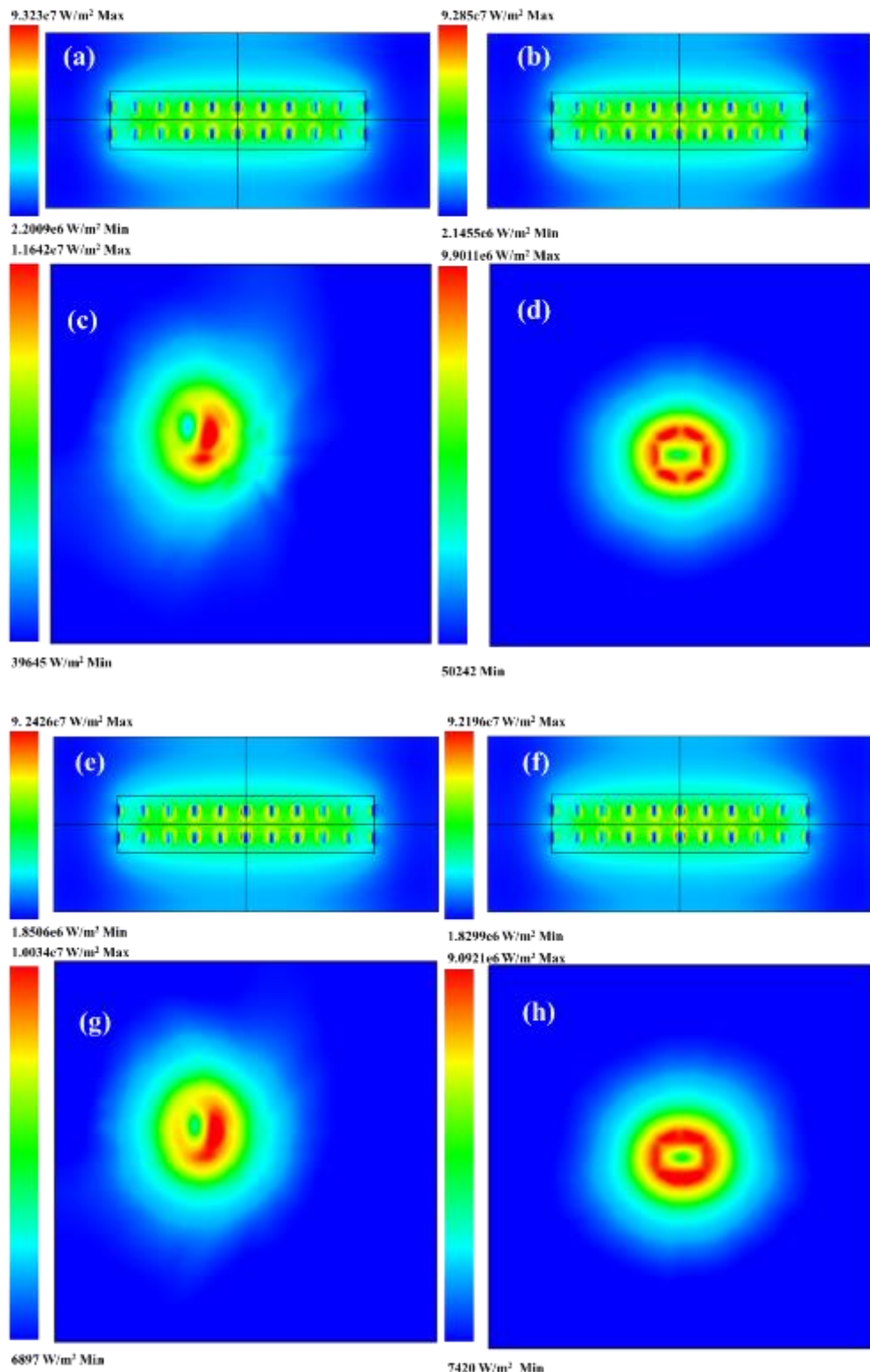


Figure 5.79 Heat flux of device with $V_{in} = 0.53$ m/s (a) bottom surface of die non-centre (b) bottom surface of die centre (c) bottom surface of diamond heat spreader non-centre (d) bottom surface of diamond heat spreader centre; with $V_{in} = 3.00$ m/s (e) bottom surface of die non-centre (f) bottom surface of die centre (g) bottom surface of diamond heat spreader non-centre (h) bottom surface of diamond heat spreader centre

The reason for the decreasing trend was mainly due to the heat flux distribution and the dependence of the thermal conductivity with the temperature in the die and the micro-jet impingement channel. With the inlet velocity of 0.53 m/s, the maximum heat flux at the bottom of the die with its position off centre and in the centre were 9.323×10^7 W/m² and 9.285×10^7 W/m² respectively, as is illustrated Figure 5. 79 (a) and Figure 5. 79 (b). While with the velocity of 3.00 m/s, the maximum heat flux at the bottom of the die with its position off centre and in the centre were 9.242×10^7 W/m² and 9.219×10^7 W/m² respectively as is illustrated Figure 5. 79 (e) and Figure 5. 79 (f). The heat flux for the former was 380,000 W/m² and the later was 230,000 W/m². Meanwhile, due to the lower temperature of the die with higher inlet velocity, the material's thermal conductivity (such as GaN and SiC) in the die was higher than the one with lower inlet velocity. Thus, the temperature difference of the die off-centre and in-centre with low inlet velocity in the die layer was higher than the one with high inlet velocity.

The similar explain can also be observed in the micro-jet impingement channel. With the velocity of 0.53 m/s, the maximum heat flux at the bottom of the die with its position off centre and in the centre were 1.1642×10^7 W/m² and 9.9011×10^6 W/m² respectively, as is illustrated Figure 5. 79 (c) and Figure 5. 79 (d). While with the velocity of 3.00 m/s, the maximum heat flux at the bottom of the die with its position off centre and in the centre were 1.0034×10^7 W/m² and 9.0921×10^6 W/m² respectively as is illustrated Figure 5. 79 (g) and Figure 5. 79 (h). The heat flux for the former is 1,740,900 W/m² and the latter is 941,900 W/m². Meanwhile, due to the lower temperature for the die with a higher heat transfer coefficient, the lower temperature can be obtained with the same heat flux. Thus, the temperature difference of the die off-centre and in-centre with low inlet velocity in the die layer was higher than the one with high inlet velocity.

- ***reduced graphene oxide nanofluid***

As was discussed in the previous chapter, with ambient temperature as low as -50 °C, the rGO/EG+DW nanofluids showed better performance than its base fluid. So in the simulation, the results from the 2.0 wt.% rGO/EG+DW nanofluids in the previous chapter were used for boundary condition in the simulation. In the simulation, the inlet temperature for 2.0 wt.% rGO/EG+DW nanofluids was set as -

45 °C to simulate the low ambient temperature. The inlet velocities for the simulations were 0.20 m/s and 0.53 m/. The locations of the die were also in-centre and off centre.

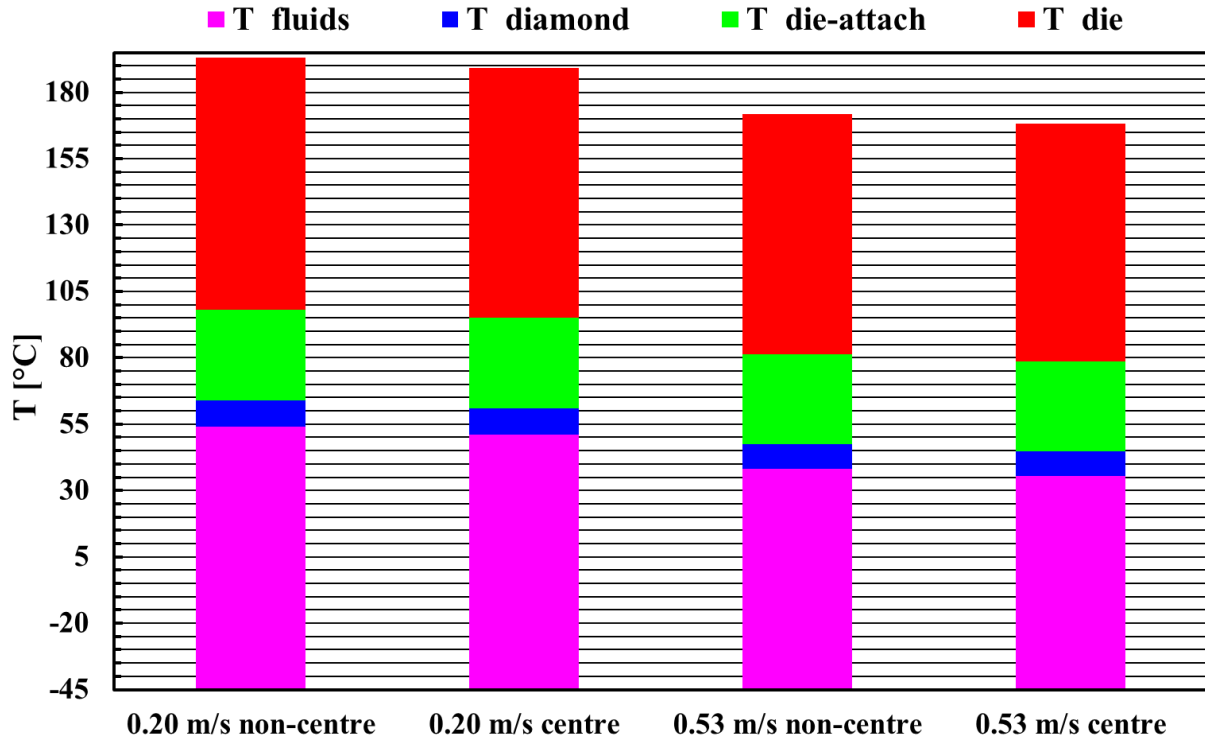


Figure 5. 80 Temperature of the packaged die with different velocity

As is shown in Figure 5. 80, the maximum temperature for the die with the velocity of 0.20 m/s was 193.00 °C and 189.25 °C for the non-centre and in-centre die, respectively. With the velocity increase to the 0.53 m/s, the maximum temperature die decreased to 171.94 °C and 168.31°C for the non-centre and in-centre die, respectively. The temperature differences for the non-centre die and in-centre die were 3.98 °C and 3.63 °C for the velocity of 0.20 m/s and 0.53 m/s respectively. The trend for the decrease in temperature difference with the velocity increase was the same as the explained one in Section 5.4.4.

The reason for the temperature difference in the same location of the die with different inlet velocity was mainly due to the temperature decrease in the micro-jet impingement channel. The maximum temperature in the micro-jet impairment channel with the velocity of 0.53 m/s that was the same as the maximum temperature in the bottom of the diamond heat spreader was 47.57 °C and 44.88 °C, which

was 16.27 °C and 16.08 °C lower than the inlet velocity of 0.20 m/s, for the non-centre and in-centre die respectively.

5.4.4. Thermal resistance of Gallium Nitride transistors

- *Deionised water*

Thermal resistance for the system analysis [241] was done to predict the thermal resistance in the device part and channel part as is shown in Figure 5. 81. The device resistance contains resistance in the transistors layer, die-attach layer and diamond heat spreader layer. The Equ.1 and Equ.2 show how to calculate the thermal resistance in the device part and channel part.

$$R_{th_device} = R_{th_die} + R_{th_{die-attach}} + R_{th_diamond} \quad (5-17)$$

$$R_{th_die} = \frac{\Delta T_{die}}{P} = \frac{T_{max_die} - T_{max_die-attach}}{P} \quad (5-18)$$

$$R_{th_die-attach} = \frac{\Delta T_{die-attach}}{P} = \frac{T_{max_die-attach} - T_{max_diamond}}{P} \quad (5-19)$$

$$R_{th_diamond} = \frac{\Delta T_{diamond}}{P} = \frac{T_{max_diamond} - T_{max_interface}}{P} \quad (5-20)$$

$$R_{th_channel} = \frac{\Delta T_{fluid}}{P} = \frac{T_{max_interface} - T_{\infty}}{P} \quad (5-21)$$

Where R_{th_device} , R_{th_die} , $R_{th_die-attach}$, $R_{th_diamond}$, and $R_{th_channel}$, is the thermal resistance in the device part, the thermal resistance in the die, the thermal resistance in the die-attach, the thermal resistance in the diamond and the thermal resistance in the micro-jet channel respectively. ΔT_{die} , $\Delta T_{die-attach}$, $\Delta T_{diamond}$ and ΔT_{fluid} , is the temperature difference in the die, die-attach, diamond heat spreader and the micro-jet channel, respectively. T_{max_die} , $T_{max_die-attach}$, $T_{max_diamond}$ and $T_{max_interface}$ is the maximum temperature in the die, the maximum temperature in the die-attach, the maximum temperature in the diamond heat spreader and the maximum temperature in the interface of the fluid and diamond heat spreader, respectively. T_{∞} is the reference temperature which is 20 °C. P is the power applied to the transistors.

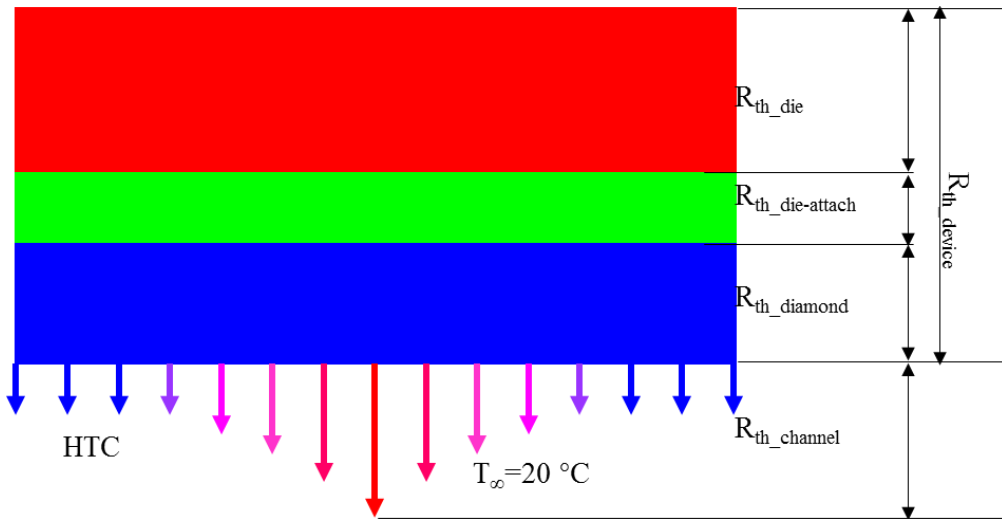


Figure 5. 81 Schematic diagram of the thermal resistance for the thermal packaging

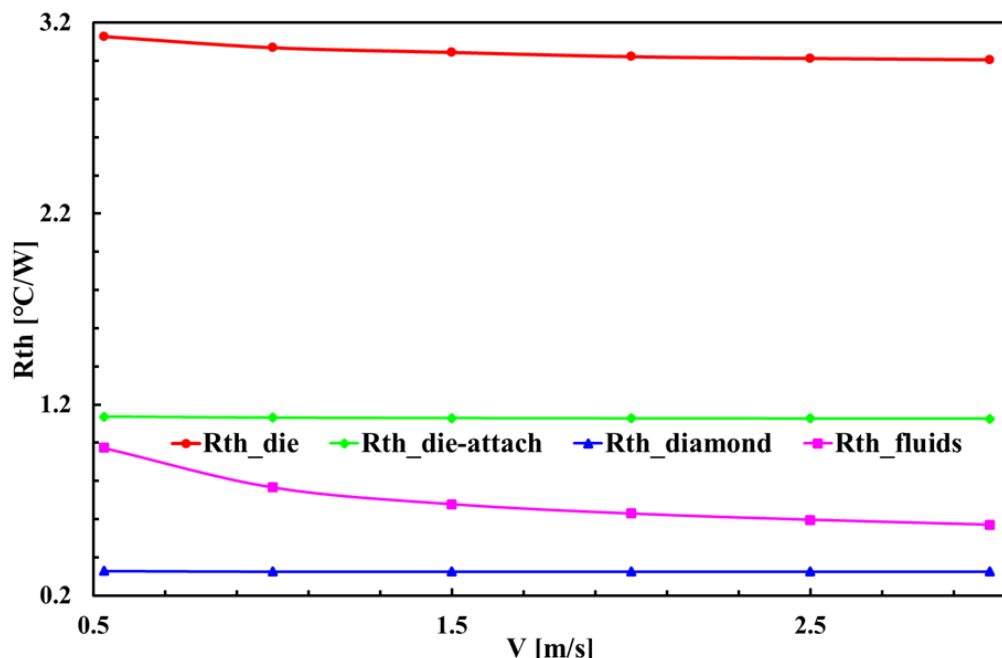


Figure 5. 82 Thermal resistance with the inlet velocity

As is shown in Figure 5. 82, Figure 5. 83 (a), (b) and (d), the thermal resistance in the die, die-attach, diamond and micro-jet channel was $3.13 \text{ } ^\circ\text{C/W}$, $1.14 \text{ } ^\circ\text{C/W}$, $0.33 \text{ } ^\circ\text{C/W}$ and $0.97 \text{ } ^\circ\text{C/W}$, respectively for the inlet velocity of 0.53 m/s . With the inlet velocity of 0.53 m/s , the thermal resistance in the diamond heat spreader accounts for the 6% of total thermal resistance. It cannot be neglected although it has a high thermal conductivity. The thermal resistance in the micro-jet channel, the die-attach and die were 3.0 times, 3.3 times, and 9.3 times, respectively, larger than the thermal resistance in the diamond heat spreader.

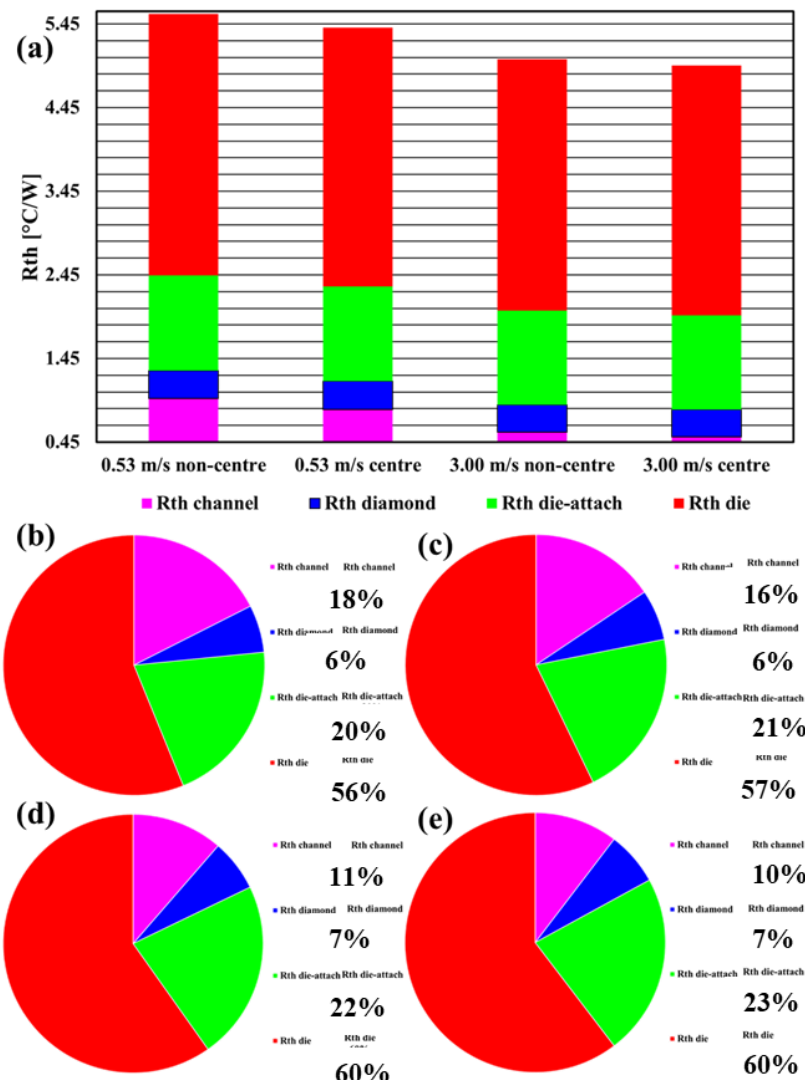


Figure 5.83 (a) Thermal resistance with different velocity and location;0.53 m/s (b) non-centre (c) in-centre;3.00 m/s (d)non-centre,(e) in-centre for deionised water

As is illustrated in Figure 5.82, the thermal resistance in the micro-jet channel gradually decreased with the increase of the inlet velocity. The thermal resistance in the die also decreased with the inlet velocity. This is due to the temperature dependence of the thermal properties of the material in the die. With the inlet velocity increased to 3.00 m/s , the thermal resistance for the die, die-attach, diamond and micro-jet channel decreased to $3.01 \text{ }^{\circ}\text{C}/\text{W}$, $1.13 \text{ }^{\circ}\text{C}/\text{W}$, $0.33 \text{ }^{\circ}\text{C}/\text{W}$ and $0.57 \text{ }^{\circ}\text{C}/\text{W}$ respectively. However, the thermal resistance in the diamond heat spreader barely changed. Besides, the thermal resistance in the micro-jet channel, the die-attach and die was 1.75 times, 3.14 times and 8.57 times, respectively larger than the diamond heat spreader. It can be observed that the thermal resistance in the micro-jet channel

was a minor factor. With a velocity of 0.53 m/s, 18 % of the total thermal resistance was in the micro-jet channel. Moreover, this value slight decreased to 11 % with the velocity increasing to 3.00 m/s.

However, over 80 % of the thermal resistance was in the device part (adding the thermal resistance in the die, the die-attach and the diamond heat spreader). Thus, to decrease the thermal resistance in the device part, such as the decrease of the thickness of the die-attach, the increase of thermal conductivity in the die-attach layer and using diamond instead of SiC as the substrate for the transistors, has significant influence in optimising the thermal performance of the system.

The trend of the decrease of thermal resistance difference for die in a different location agreed with the decreasing trend in the temperature difference for die in a different location. The total thermal resistance for the die in the centre was 5.57 °C/W and 5.03 °C/W with the inlet velocity of 0.53 m/s and 3.00 m/s, respectively which was 0.16 °C/W and 0.08 °C/W higher than the total thermal resistance for the die non-centre with the inlet velocity of 0.53 m/s and 3.00 m/s, respectively. The thermal resistance in the diamond heat spreader was slightly higher for the in-centre die than the non-centre die which suggested centring the die increased the heat flux through the diamond heat spreader.

- ***Reduced graphene oxide nanofluid***

The thermal resistance analysis of the device with the 2.0 wt. % rGO nanofluid as the heat transfer fluid showed the similarity with the water as the heat transfer fluid. However, there are some unique differences for the packaged die applied in the low temperature.

As is shown in Figure 5. 84, the thermal resistance for the devices, the die-attach and the diamond heat spreader with rGO nanofluids were similar to the ones with water. However, the thermal resistance in the micro-jet channel was one of the major thermal resistance for the whole system with rGO nanofluids. With an inlet velocity of 0.20 m/s, 40% of the total thermal resistance was in the die layer and 41% to 42% total thermal resistance was in the micro-jet channel. With the inlet velocity increase to 0.53 m/s, 38% total thermal resistance was in the micro-jet layer. This suggested the value of the thermal resistance the micro-jet channel and thermal resistance in die was similar to each other. To further decrease the thermal resistance, action needs to be taken form either the die or the micro-jet channel.

The total thermal resistance difference with in-centre die and non-centre die decreased with the increase of the inlet velocity. Meanwhile, the thermal resistance in the diamond heat spreader was slightly higher for in the centre which shows around 2 % difference. Those trends were similar to their counterpart.

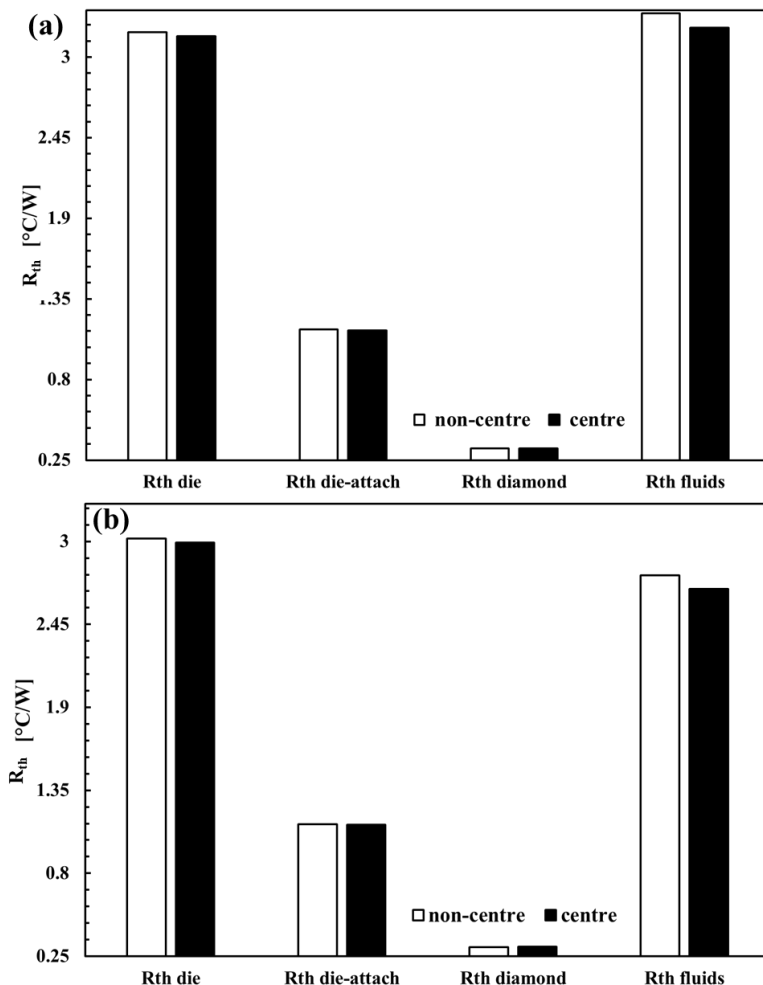


Figure 5.84 Thermal resistance of the micro-jet with inlet velocity of (a) 0.20 m/s (d) 0.53m/s for rGO nanofluids

5.4.5. Summary of thermal performance of Gallium Nitride transistors

The thermal package prototype for GaN transistors with 3D printed micro-jet impingement cooling channel is presented in this Section. The fabricating process flow is given. The Raman thermography tests show the feasibility of this approach. Meanwhile, a numerical model is built and validated with the experimental results, which can then predict the thermal performance of the fabricated thermal package that is difficult to measure experimentally.

CHAPTER 5 RESULTS AND DISCUSSIONS

According to the experiment results, with an inlet flow rate of 0.1 L/min, the measured maximum temperature in the finger of GaN transistors was 141 °C with the applied power of 30 W. The simulation result was close to the experiment results.

For the room temperature cases, (1) with the inlet temperature set as 20 °C and 30 W power applied on the die, The simulation results suggested the maximum temperature in the device was 187.01 °C with an inlet velocity of 0.53 m/s. The maximum temperature in the die decreases to the 170.87 °C with the inlet velocity increase to 3.00 m/s. (2) Due to the high thermal contact resistance between the GaN layer and the SiC layer, the sharp temperature decrease was observed in the first 1.5 μm in the SiC layer. (3) In the studied case, with the inlet velocity of 0.53 m/s, the thermal resistance in the micro-jet was 17% of total thermal resistance. This meant the micro-jet channel was not the main factor for the temperature optimization. To further decrease the maximum temperature in the die, GaN-on-SiC can be changed to the GaN-on-diamond to reduce the thermal resistance in the die. The thermal conductivity of the sliver sintered die-attach material was around 50 W/(m²·°C) which was less than half of claimed value by the manufacture. Thus, the thermal resistance was around 3.3 times higher than the thermal resistance in the diamond heat spreader. The new die-attach material with better thermal conductivity is useful to further decrease the thermal resistance in this layer.

One of the easiest ways to decrease the maximum temperature in the die is to change the location of the die on the diamond heat spreader. In-centre die and non-centre die showed an obvious difference in the temperature distribution with both DI water and rGO nanofluids as heat transfer fluids. This suggests for the thermal package, it is important to place the die in the area where the heat transfer coefficient is largest. In the simulation, a maximum of 0.16 °C/W can be obtained for total thermal resistance by locating the die in the centre of the micro-jet channel.

For the low-temperature cases, (1) with the inlet temperature set as -45 °C and 30 W power applied on the die, in order to maintain the maximum temperature in die below 200 °C, the inlet velocity should be larger than 2.0 m/s. (2) in the studied cases, the thermal resistances in the die and the channel were almost the same and they account for about 80% of the total thermal resistance. Thus to further decrease the maximum temperature in the die, the action can be taken either on the die or the micro-jet channel.

CHAPTER 5 RESULTS AND DISCUSSIONS

6. Conclusions and recommendations for future work

This PhD project aims to investigate the potential of maintaining a low temperature at the back of GaN-on-Diamond microchip. The main challenge for the objective is the high-power density on the GaN layer of the devices. To obtain the aim, the objective has divided into 3 tasks. TM with novel HTFs, microfluidic channels and thermal packaging of the devices with the microfluidic channels.

6.1. Conclusions

- *Nanofluids*

One method TM is using novel nanofluids. Nanofluids as a novel heat transfer fluids fabricated via mixing metallic, metallic oxide, ceramic, carbon-based material etc. which have high thermal conductivity into base fluids such as water, oil, glycol etc. offers, according to the literature, a possible thermal performance enhancement, as nanoparticles in the base fluids affect the fluids flow and heat transfer mechanism. However, a balance for the application of the nanofluids needs to be considered as dispersing nanoparticles into the nanofluids can positively and negatively amend the thermophysical properties of the base fluids in the investigation. In the studied cases, the increase of the effective thermal conductivity for the dispersion is a good enhancement while the increase of the apparent viscosity of the mixture increases the pressure drop in the whole flow channel. During the real application, both effects need to be considered before the selection of heat transfer fluids.

- *Material selection for the microchip*

The important part in the selection of material on the microchips also greatly affects the temperature distribution especially the microchip. The die attach combining the die and the micro jetting channel shows a high influence on this distribution in the die due to the high local heat flux. The other part is to choose the diamond as the heat spreader for the GaN transistors due to its high thermal conductivity.

CHAPTER 6 CONCLUSION AND RECOMMENDATIONS FOR FUTURE WORK

The thermal management suggests the importance of the material selection for the transistors. The thermal package of the devices needs to attach the die to the heat spreader. In the simulation results, the die-attach material plays an important part in the temperature distribution in the whole devices.

Performance of the microfluidic channel

Another method for thermal management is to choose a suitable microfluidic channel for the microchips. The micro-jetting compared with other different types of microfluidic such as microchannel; copper-foam-based channel etc. has high and localized heat transfer coefficient which is as well as the pressure drop for one-phase flow. This highly localised heat flux can match the heat flux distribution at the back of the die. Those advantages make the micro-jetting channel a good choice for single-phase liquid cooling.

- ***Thermal performance of the GaN-based microchips***

The most important aims for this project is to maintain the temperature in the fingers lower than 200 °C. Thus, the direct measurement of the temperature with Raman thermography was done. The Raman thermography was applied due to its high resolution. The experiment test suggests that with the target power density of 5 W/mm, the peak temperature in the devices was 120 °C far below 200 °C. The thermal resistance for the jetting channel was 19.76 °C mm/W. The device used in the experiment is GaN-on-SiC. For the GaN-on-Diamond, a higher power density can be obtained. To investigate the temperature distribution in the packaged GaN microchips, a model with detailed die structure with fine mesh was build to match the resolution of the micro-Raman measurement.

It could be concluded that for the thermal management of the GaN transistors, the nanofluids, material selection for the devices thermal package and micro-jet channel all play important roles once the specific GaN transistors are selected. The methodology was to decrease the thermal resistance in all 4 parts, especially the part with the largest thermal resistance.

6.2. Recommendations for future work

Based on the work of this PhD study, the following work is recommended for future research;

- *Novel heat transfer fluids with high thermal properties*

As for the novel heat transfer fluids, it is possible to select other types of nanofluids (different nanoparticle and/or fabrication methods) with higher performance as there is still no theory for the limitation of the thermal properties enhancement.

- *Materials used for the thermal package of the microchip*

As for the thermal package, to find a die attach material with higher thermal conductivity and/or direct combine the devices with the microfluidic channels can further decrease the thermal resistance in the thermal package process.

- *Microfluidic channel optimisation*

As for the micro-jet channel, the micro-jet orifices array diameter could be further decreased with micro stereolithography apparatus. The channel can be still further optimized for the low-pressure drop.

- *Thermal performance of GaN-on-Diamond microchip*

The GaN-on-diamond microchip for this project is still in the design and fabrication process. It, in theory, would have lower thermal resistance than the GaN-on-SiC microchip. To evaluate its performance, the Raman thermography for the measurement of GaN-on-Diamond devices needs to be done.

Appendix

Appendix A

SST $\kappa-\omega$ transition model

The transport equations for *SST* $\kappa - \omega$ model are displayed as:

$$\frac{\partial}{\partial \tau} (\rho k) + \nabla \cdot (\rho k \vec{v}) = \nabla \cdot (\Gamma_k \nabla k) + \widetilde{G}_k - Y_k + S_k \quad (1)$$

$$\frac{\partial}{\partial \tau} (\rho \omega) + \nabla \cdot (\rho \omega \vec{v}) = \nabla \cdot (\Gamma_\omega \nabla \omega) + G_\omega - Y_\omega + D_\omega + S_\omega \quad (2)$$

In these equations, \widetilde{G}_k represents the generation of turbulence kinetic energy due to mean velocity gradients. G_ω represents the generation of ω , Γ_k and Γ_ω represent the effective diffusivity of k and ω , respectively. Y_k and Y_ω represent the dissipation of k and ω due to turbulence. D_ω represents the cross-diffusion term, calculated as described below. S_k and S_ω are user-defined source terms.

The effective diffusivities for the SST $\kappa-\omega$ model are given by:

$$\Gamma_k = \mu + \frac{\mu_t}{\sigma_k} \quad (3)$$

$$\Gamma_\omega = \mu + \frac{\mu_t}{\sigma_\omega} \quad (4)$$

Where σ_k and σ_ω are the turbulent Prandtl numbers for k and ω , respectively.

The turbulence μ_t is calculated as:

$$\mu_t = \frac{\rho k}{\omega} \frac{1}{\max \left[\frac{1}{\alpha^*}, \frac{SF_2}{a_1 \omega} \right]} \quad (5)$$

$$\sigma_k = \frac{1}{F_1/\sigma_{k,1} + (1-F_1)/\sigma_{k,2}} \quad (6)$$

$$\sigma_\omega = \frac{1}{F_1/\sigma_{\omega,1} + (1-F_1)/\sigma_{\omega,2}} \quad (7)$$

Where S is the strain rate magnitude.

$$F_1 = \tanh(\Phi_1^4) \quad (9)$$

$$\Phi_1 = \min \left[\max \left(\frac{\sqrt{k}}{0.09\omega y}, \frac{500\mu}{\rho y^2 \omega} \right), \frac{4\rho k}{\sigma_{\omega,2} D_\omega^+ y^2} \right] \quad (10)$$

$$D_\omega^+ = \max \left[2\rho \frac{1}{\sigma_{\omega,2}} \frac{1}{\omega} \frac{\partial k}{\partial x_j} \frac{\partial \omega}{\partial x_j}, 10^{-10} \right] \quad (11)$$

$$F_2 = \tanh(\Phi_2^2) \quad (12)$$

$$\Phi_2 = \max \left(2 \frac{\sqrt{k}}{0.09\omega y}, \frac{500\mu}{\rho y^2 \omega} \right) \quad (13)$$

The turbulence production for the SST $k-\omega$ model is given by:

$$\tilde{S}_k = \min(G_k, 10\rho\beta^*\omega k) \quad (14)$$

$$G_\omega = \frac{\alpha}{v_t} G_k \quad (15)$$

$$\alpha_\infty = F_1 \alpha_{\infty,1} + (1 - F_1) \alpha_{\infty,2} \quad (16)$$

$$\alpha_{\infty,1} = \frac{\beta_{i,1}}{\beta_\infty^*} - \frac{k^2}{\sigma_{\omega,1} \sqrt{\beta_\infty^*}} \quad (17)$$

$$\alpha_{\infty,2} = \frac{\beta_{i,2}}{\beta_\infty^*} - \frac{k^2}{\sigma_{\omega,2} \sqrt{\beta_\infty^*}} \quad (18)$$

The turbulence dissipation for the SST $\kappa-\omega$ model is given by:

$$Y_k = \rho\beta^*k\omega \quad (19)$$

$$Y_\omega = \rho\beta\omega^2 \quad (20)$$

$$\beta_i = F_1 \beta_{i,1} + (1 - F_1) \beta_{i,2} \quad (21)$$

The cross-diffusion modification is defined as:

$$D_w = 2(1 - F_1)\rho\sigma_{w,2} \frac{\partial k}{\partial x_j} \frac{\partial \omega}{\partial x_j} \quad (22)$$

The transport equation for the intermittency γ is defined as:

$$\frac{\partial(\rho\gamma)}{\partial t} + \frac{\partial(\rho U_j \gamma)}{\partial x_i} = P_{\gamma 1} - E_{\gamma 1} + P_{\gamma 2} - E_{\gamma 2} + \frac{\partial}{\partial x_j} [(\mu + \frac{\mu_t}{\sigma_\gamma}) \frac{\partial \gamma}{\partial x_j}] \quad (23)$$

The transition sources are defined as follows:

$$P_{\gamma 1} = C_{a1} F_{length} \rho S [\gamma F_{onset}]^{C_{\gamma 3}} \quad (24)$$

$$E_{\gamma 1} = C_{e1} P_{\gamma 1} \gamma \quad (25)$$

Where S is the strain rate magnitude, F_{length} is an empirical correlation that controls the length of the transition region, and C_{a1} and C_{e1} hold the values of 2 and 1, respectively. The destruction/relaminarization sources are defined as follows:

$$P_{\gamma 2} = C_{a2} \rho \Omega \gamma F_{turb} \quad (26)$$

$$E_{\gamma 2} = C_{e2} P_{\gamma 2} \gamma \quad (27)$$

Where Ω is the vorticity magnitude, the transition onset is controlled by the following functions:

$$Re_V = \frac{\rho \gamma^2 S}{\mu} \quad (28)$$

$$R_T = \frac{\rho k}{\mu \omega} \quad (29)$$

$$F_{onset1} = \frac{Re_V}{2.193 Re_{\theta c}} \quad (30)$$

$$F_{onset2} = \min (\max(F_{onset1}, F_{onset1}^4), 2.0) \quad (31)$$

$$F_{onset3} = \max (1 - \left(\frac{R_T}{2.5} \right)^2, 0) \quad (32)$$

$$F_{onset} = \max (F_{onset2} - F_{onset3}, 0) \quad (33)$$

$$F_{turb} = e^{-\left(\frac{R_T}{4}\right)^4} \quad (34)$$

Appendix B

Hot-wire theory

The theory for the thermal conductivity with the hot-wire method can be described as following;

$$\frac{\partial T}{\partial \tau} = \alpha_T \frac{\partial^2 T}{\partial r^2} \quad (35)$$

$$\alpha_T = \frac{k}{c_p \rho} \quad (36)$$

The analytical solution for this equation is

$$T - T_0 = -\frac{q}{4\pi k} E_i\left(-\frac{r^2}{4\alpha_T \tau}\right) \quad (37)$$

Where Ei is exponential integral,

$$E_i = \gamma + \ln x - \frac{x}{1 \times 1!} + \frac{x^2}{2 \times 2!} - \frac{x^3}{3 \times 3!} + \dots \quad (38)$$

With $\gamma=0.5772$ as Euler-Mascheroni constant

When $\tau \gg \frac{r^2}{4\alpha_T}$, the solution can have an approximation

$$T - T_0 = -\frac{q}{4\pi k} \left(\ln \frac{4\alpha_T \tau}{r^2 \gamma} \right) \quad (39)$$

The system uses an extremely small amount of the heat flux. The system calculates the actual energy input for each point of measurement of the temperature profile

$$k = \frac{q}{4\pi(T_2 - T_1)} \ln \frac{\tau_1}{\tau_2} \quad (40)$$

Appendix C

IR camera theory

The principles applied for IR camera are Planck's law, Stefan-Boltzmann law, Kirchhoff's law of thermal radiation, and Wien's displacement law. They will be explained in the following;

Planck's law of black body shows the spectral density of the radiation emitted by a black body in thermal equilibrium at a given temperature T. The equation is as flow;

$$B_v(v, T) = \frac{2\pi hc^2}{k^5} \frac{1}{e^{hc/(kk_B T)} - 1} \quad (41)$$

Where c is the speed of the light,

h is Planck constant,

k_B is the Boltzmann constant, k is the wavelength.

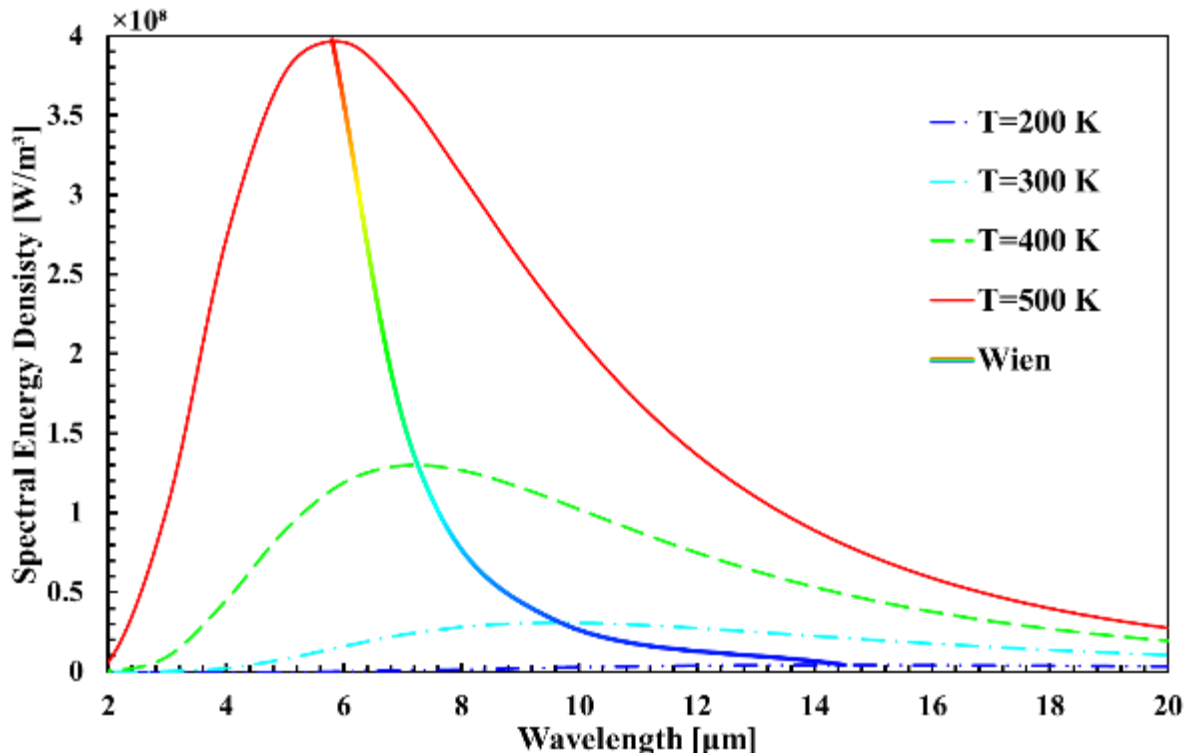


Figure 1 Blackbody Radiation Spectrum from Planck's law and Wien's displacement law

According to the Wien's displacement law, the back-body spectral density of the radiation with wavelength for different temperature peaks at a different wavelength that is inversely proportional to the temperature as is illustrated in Figure 1. The material at room temperature or slightly higher than room temperature will give off the major radiation as the infrared light. This is the main reason for the IR camera to set its spectral range from 7.5 μm to 14 μm .

The expression of the Wien's displacement law is;

$$k_{\max} = \frac{b}{T} \quad (42)$$

Where b is $2.898 \times 10^{-3} \text{ m}\cdot\text{K}$.

Stefan-Boltzmann law as is shown below provides the relationship between the power radiated from a grey body and its temperature emissivity and surface area;

$$E = A\epsilon\sigma T^4 \quad (43)$$

Where A is the surface area of the grey body, ϵ is the emissivity of the grey body, T is the temperature of the body, σ is the Stefan-Boltzmann constant, and E is the radiation power.

Kirchhoff's law of thermal radiation states that for an arbitrary body emitting and absorbing thermal radiation in thermodynamic equilibrium, the emissivity is equal to the absorptivity.

$$\alpha_k = \epsilon_k \quad (44)$$

Appendix D

Raman thermography

As is illustrated in Figure 2, scattering, absorption reflection and transmission are the common interactions for the light interacting with matter. As is pictured in Figure 3, there are two types of mechanism for the scattering. The domain mechanism for the light goes through a transparent material is the Rayleigh or elastic scattering. This type of scattering does not change the energy of the photon. Therefore, the wavelength of the light remains the same. In Rayleigh scattering, the electron cloud is polarized when a photon interacts with a molecule. Thus, it raises to virtual states. In a short-lived time,

the molecule drops back down to the ground vibrational state with a photon released from any direction which results. Since the initial state and the final state for the molecule do not change, the wavelength for the scattered light is the same as the interacted light.

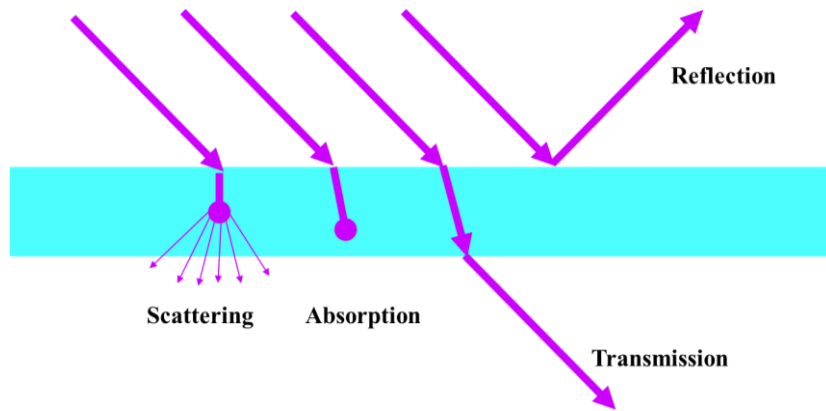


Figure 2 Schematic diagram of light interacting with matter

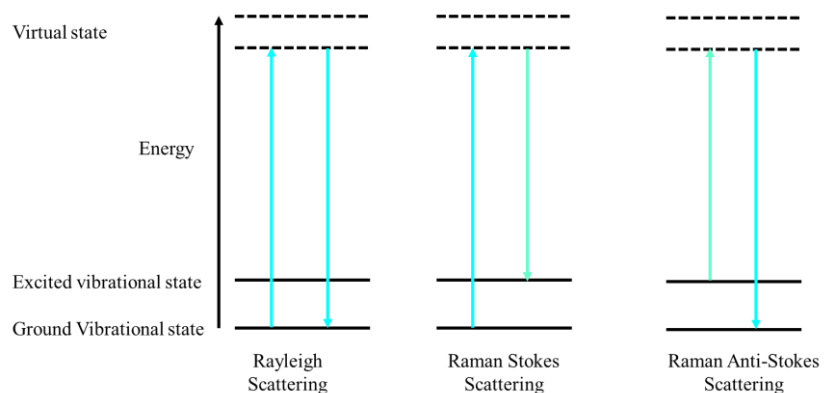


Figure 3 Schematic diagram for Rayleigh scattering, Raman Stokes scattering and Raman anti-stokes scattering

The other type of scattering is known as Raman scattering that was discovered by C.V. Raman in 1928. Since then it was applied to much important technology and Raman spectroscopy shows one of the greatest importance among them. Raman scattering is inelastic. During this type of scattering process, the photons gain or lose the energy. Therefore, the wavelength of the scattering light decreases or increases, respectively. If molecules start with the ground vibration state and end with the excited vibrational state, the wavelength of the scattering light is longer due to the energy lost in the process. This is called Raman Stokes scattering. If molecules begin from the excited vibrational state and go to the ground vibrational state during the scattering, the wavelength of the scattering light is shorter as the scattered phonon gains more energy. This is called Raman anti-Stokes scattering. Approximately one

in 10^7 scattered photons undergo the Raman Stokes scattering. The amount of the Raman anti-Stokes scattering is less than its counterpart due to the majority of the molecules is in the ground states.

The Raman spectrum

Raman shift is defined as the difference in the inverse wavelength of incident light and scattering light, as is shown;

$$\text{Wavelength} = \frac{1}{k_0} - \frac{1}{k} \quad (45)$$

Where, k_0 is the wavelength of the incident light, k is the wavelength of the scattered light.

The light dispersed in the spectrometer is captured by a CCD for most Raman spectroscopy systems. The CCD can convert the intensity of the light into the electrical signal and computer software is used to plot the Raman shift and counts as is illustrated in Figure 4. The software then applies a Voigt profile to locate the centre of the peak position. Many factors affect the precision of the Raman peak position, such as the CCD pixel size, the spectrometer optical characteristics and intensity of Raman shift.

In the plot for GaN-on-SiC, three peaks can be found with the Raman shift from 500 cm^{-1} to 850 cm^{-1} . The peak position with centroids are at 568 cm^{-1} , 736 cm^{-1} and 777 cm^{-1} for GaN E₂ (high), GaN A₁ (LO) and SiC FTO respectively.

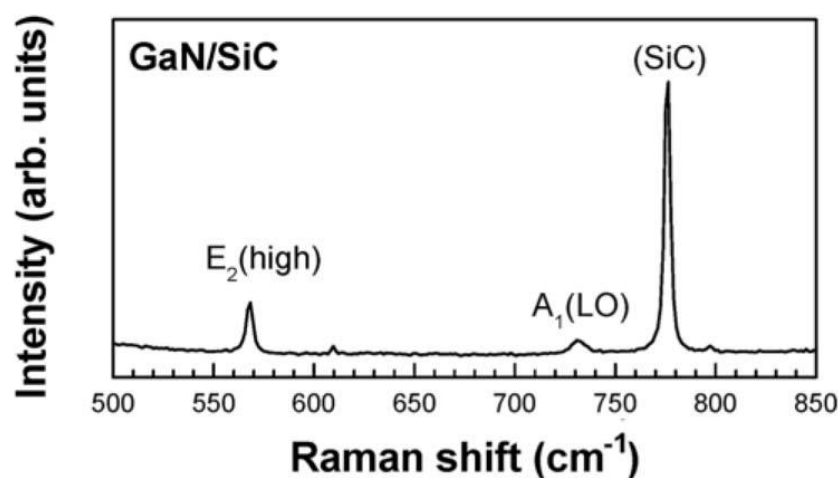


Figure 4 Raman spectrum of GaN on the SiC die

Temperature measurement

The phonon energy (Raman shift) can be used for the temperature measurement. The total change in the phonon energy ($\Delta\omega$) can be divided into two main parts: (1) the change of lattice temperature for the bulk strain material ($\Delta\omega_T$) and the change due to the mechanical strain ($\Delta\omega_\varepsilon$).

$$\Delta\omega = \Delta\omega_T + \Delta\omega_\varepsilon \quad (46)$$

The most commonly used and simplest method for Raman thermography measurement is to use an empirical formula to fit the Raman shift with the temperature:

$$\Delta\omega = \omega_0 - \frac{A}{e^{\left(\frac{B\hbar\omega}{k_B T}\right)} - 1} \quad (47)$$

Where A and B are fitting coefficient which is unique to each phonon and material, ω_0 is the phonon frequency at $T=0$ K, \hbar is the reduced Planck's constant and k_B is the Boltzmann constant.

In order to have the most accurate measured temperature, it is necessary to separate the temperature and stress influence on the phonon shift. The strain and temperature coefficient for the GaN material is given in Table 1. Compared to the E₂ mode, A₁ is less sensitive to the stress with respect to temperature. It should be pointed out that it is not necessary to use the complex analysis for all the experiments. In most cases, the sufficient accuracy of temperature with the simplified method for analyzing the A₁ mode for GaN material.

$$\Delta\omega = \omega_0 - \frac{A}{e^{\left(\frac{B\hbar\omega}{k_B T}\right)} - 1} + \Delta\omega_\varepsilon \quad (48)$$

Table 1 GaN phonon strain and temperature coefficients

Phonon mode	Deformation potentials cm ⁻¹ /GPa	T. dependence dω/dT @ 25 °C 10 ⁻² cm ⁻¹ /°C
E2 (high)	2.41	0.87
A1(LO)	1.91	2.3

In the given temperature range, a more simplified mode is to use the linear fitting curve of the Raman peak shift with the temperature.

$$\Delta\omega = A(T_\omega - T_0) + \omega_0 \quad (49)$$

Another possibility for the Raman thermography is to analyze the intensity of the Raman peaks. The temperature can be obtained via the intensity of Stokes I_S and Anti-stokes I_{AS} Raman peaks,

$$\frac{I_S}{I_{AS}} = \left(\frac{k_S}{k_{AS}}\right)^4 e^{\hbar\omega/k_B T} \quad (50)$$

Where k_S and k_{AS} are the wavelength of the Stokes and Anti-stokes scattering light, respectively. The material such as GaAs and InP with low phonon energy is easier for this analyzation than the material with high phonon energy such as GaN, SiC and diamond. As the device used in the experiment are mainly made of GaN, SiC and diamond, this method is not used.

Spatial Resolution

The Raman thermography measurement, the lateral spatial resolution and axial resolution need to be considered due to the laser-based microscopy measurement. In the measurement of temperature on GaN with 488 nm laser wavelength,

The lateral resolution is given as:

$$r_{\text{lateral}} = \frac{0.51k}{NA} \quad (51)$$

Where r_{lateral} is the lateral resolution and NA is the numerical aperture which is 0.6 in the measurement.

The axial resolution is given as:

$$r_{\text{axial}} = \frac{1}{2\alpha} \quad (52)$$

Where α is the absorption coefficient GaN.

Appendix E

Dynamic Light Scattering

Dynamic Light Scattering (DLS) can be used to indirectly measure the particle size in the solvent. The Brownian motion measured in the DLS relates to the size of particles as is shown in Figure 5. The velocity of the Brownian motion is defined as the translational diffusion coefficient.

This value in one solvent at a constant temperature is determined by the size of the particle. The smaller the particle, the quicker the Brownian motion will be, et vice versa. The size of the particle calculated via the Stokes-Einstein equation is defined as the hydrodynamic diameter.

$$d(H) = \frac{kT}{3\pi\mu D} \quad (53)$$

Where: $d(H)$ is the hydrodynamic diameter, D is the translational diffusion coefficient, k is Boltzmann's constant, T is the absolute temperature and μ is the viscosity.

Due to the size refers to the diffusion of the particles within a fluid, this diameter measured by technique refers to the diameter of a sphere that has the same translational diffusion coefficient as the particle. It should be pointed out that the concentration and types of ions in the solvent, the surface structure of the particles and the size of the particle have an influence on the translational diffusion coefficient.

The thickness of the electric double layer will change according to the ions types and their concentration. A high conductivity medium will produce a shortened double layer of ions around particles. Thus, the diffusion speed increases and the apparent hydrodynamic diameter is smaller et vice versa.

The change of the surface of particles affecting the diffusion speed will change the hydrodynamic diameter of the particle. Adding the surfactants will correspondingly change the apparent size of the particle.

The inherent problem of this technique is to describe the size of the non-spherical particles such as the graphene, the carbon nanotube, and the flake shape BN nanoparticles. The only shape that can be unambiguously described is the spherical shape.

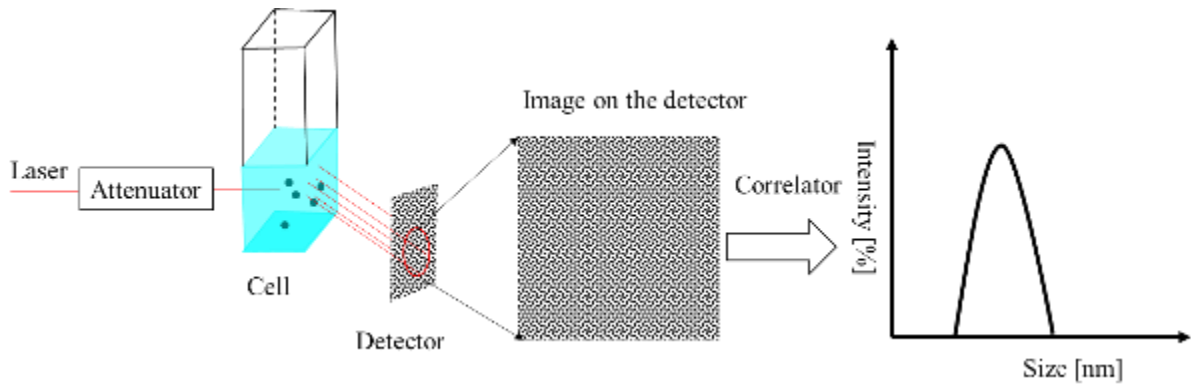


Figure 5 Schematic diagram of the DLS measurement

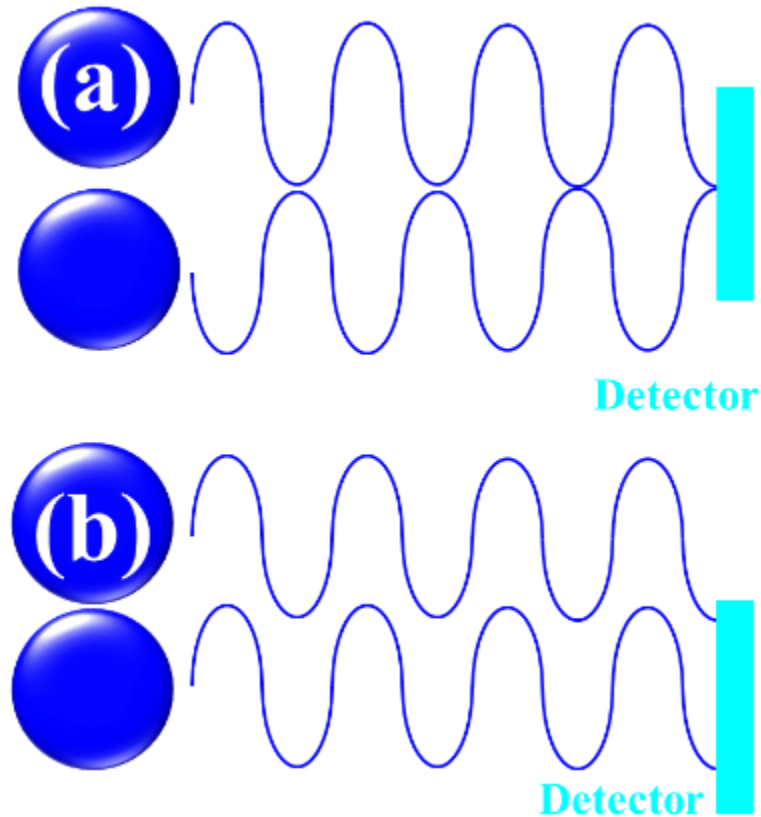


Figure 6 Phase addition of scattered light falling on the detector. (A), the opposite phase of two beams cancels each other out resulting in a decreased intensity. (B), the same phase two beams enhance each other resulting in an increased intensity

The DLS obtains the hydrodynamic size of the particles by measuring the diffusion speed that the particles have. The speed measurement is done by measuring the rate at which the intensity of the scattered light fluctuates when detected using a suitable optical arrangement. As is shown in Figure 5, the light scattered by the particles forms a speckle pattern on the detector. In some part of the detector, it shows the dark spaces as the phase additions of the scattered light are mutually destructive and cancel

each other out as is illustrated in Figure 6 (a). In some part of the detector, it shows bright blobs as the scattered light from the particles arrive with the same phase and interfere constructively as is illustrated in Figure 6 (b). Due to the Brownian motion, the image of the bright and dark positions constantly changes. The rate of these intensity fluctuations depends on the size of the particle. In general, the large particles cause the intensity to fluctuate slower than the small ones.

The size of the particles is obtained from the correlation function via some algorithms. (1) Cumulants analysis can obtain the mean size (z-average diameter) and the polydispersity index (which refers to the width of the distribution via monodisperse model and (2) Non-negative least squares can obtain the distribution of the particle sizes via multidisperse model.

In general, the intensity size distribution is plotted according to the relative intensity of the light scattered in various size class. The volume size distribution and the number size distribution have a similar definition. However, in the DLS, the volume and number size distribution is calculated by the according to the intensity size distribution.

If the intensity distribution has a single smooth peak, the peaks for the intensity, volume, and number size are the same. However, if more than one peak appeared in the intensity size distribution, the refractive index of the sample is needed to obtain a realistic volume size distribution. In general term, the three different sizes will be seen:

$$d(\text{intensity}) > d(\text{volume}) > d(\text{number}) \quad (54)$$

During the test, the non-invasive backscatter detection was used to measure the nanoparticles in the dispersion. The non-invasive refers to the indirect contact of the optics with the sample. The backscattering refers to the information of the scattering light is collected at 173° . There are many advantages of the backscatter detection (1): The backscatter reduces the multiple scattering that refers to the light from one particle is itself scattered by other particles. (2) The contaminants with large particle size such as dust particle which is larger than the sample size (several and/or hundreds of nanometre) mainly scattered in the forward direction. Thus, backscatter detection decreases this effect.

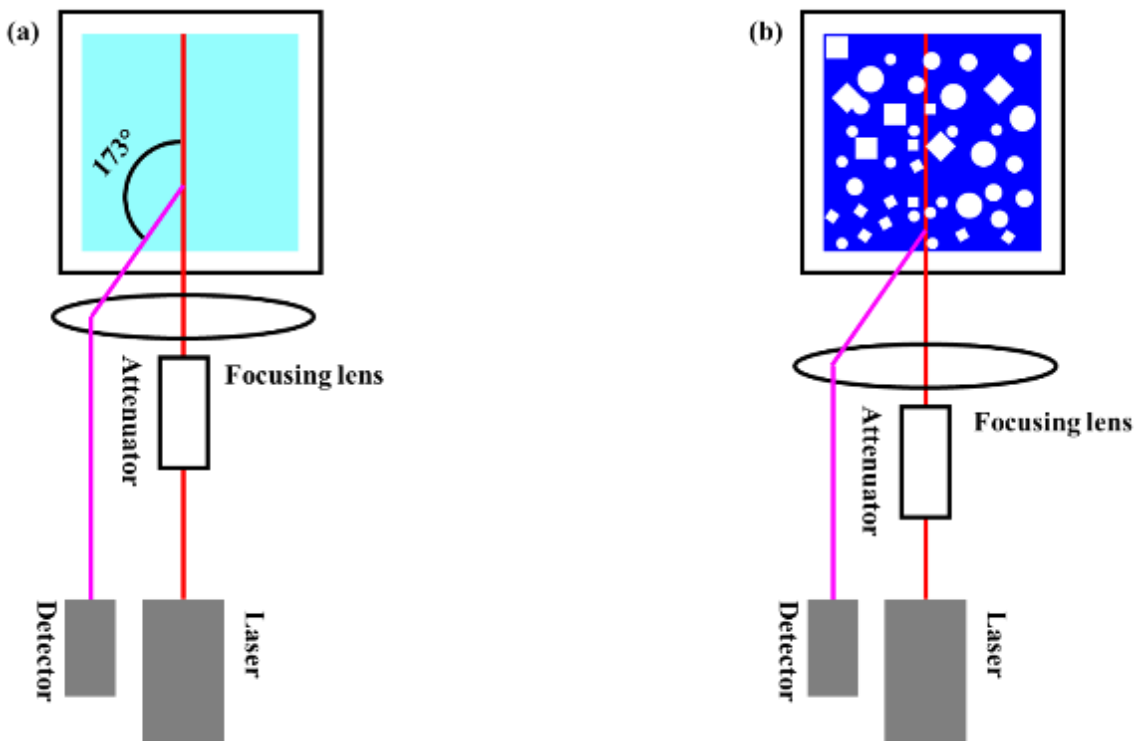


Figure 7 Schematic diagram of the measurement position with moving of the focus lens for (a) small, weakly scattering samples and for (b) concentrated, opaque samples.

For the small particles and/or low concentration as is shown in Figure 7 (a), the amount of the scattering needs to be maximised. In this case (1) the attenuator will permit more light to go through the sample. (2) the location of the lens moves the measuring point towards the centre of the cuvette to remove the effect of the flare which occurs during the light passing through the wall of cuvette into the dispersant.

For the large particles and/or high concentration as is shown in Figure 7 (b), the amount of the scattering needs to be decreased. In this case (1) the attenuator will decrease light to go through the sample. (2) The location of the lens moves the measuring point towards the wall of the cuvette to decreases the effect of multiply scattering. The appropriate attenuator position and the measurement position are determined automatically by the equipment.

Appendix F

Zeta potential

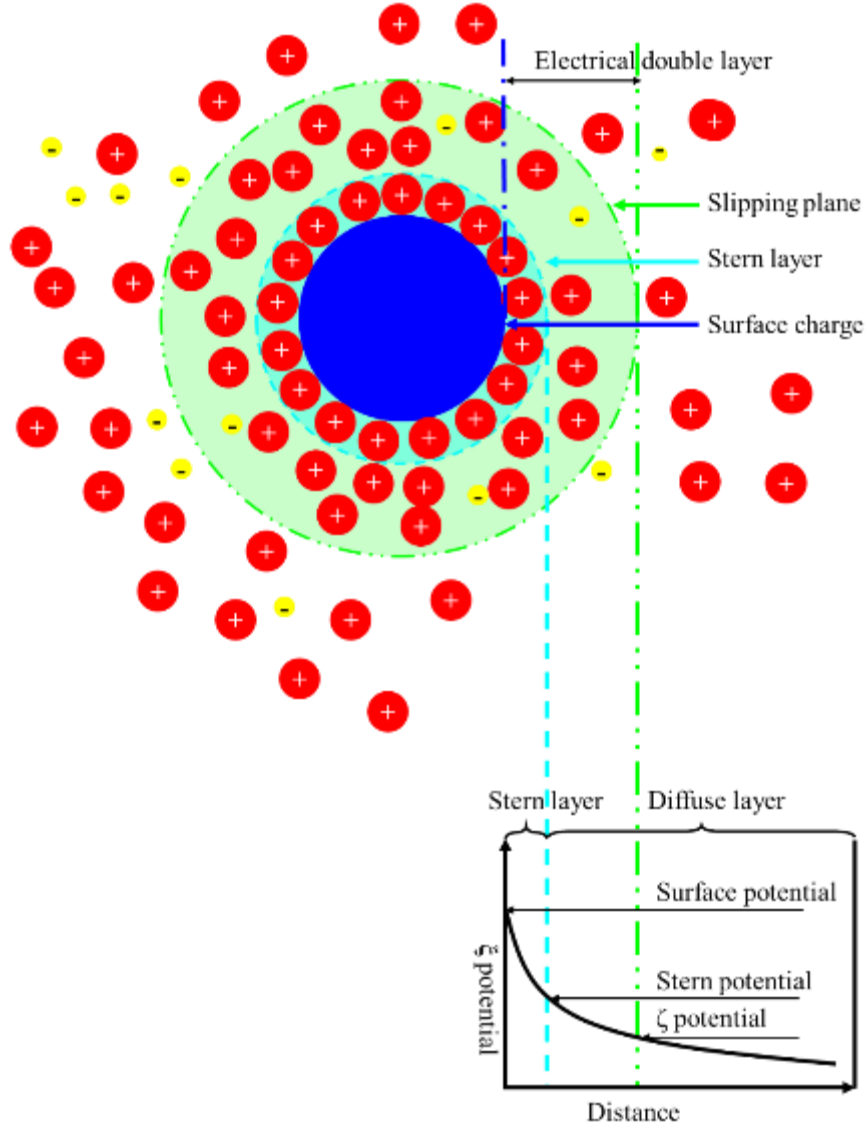


Figure 8 Schematic illustration of the ζ potential

All particle in the dispersion exhibits the zeta potential. It can be used to predict the stability of the nanofluids. It can also be used to optimise the colloid formulation. The zeta potential was long recognised as a good index of the magnitude of the interaction between colloidal particles. Its value was measured to assess the stability of the system.

Two parts exist as the particle is surrounded by the liquid layer, as is shown in Figure 8. (1) The Stern layer is the inner layer where the ions strongly bonded to the surface of the particle and (2) the diffuse

layer is the outer layer where the ions are less firmly associated. It should be mentioned that in the diffusion layer there is a boundary where the particles and ions form a stable entity. The ions with this boundary move together with the particle. The potential at this surface (surface of the hydrodynamic shear) is zeta potential.

The stability of the colloids can be represented by the magnitude of the zeta potential. If the colloidal system has a large positive or negative zeta potential, the particles in the dispersion tend to repel each other. Thus, the system shows good stability. However, if the system shows low zeta potential, the particles seem to be easily come together and agglomerated.

Electrokinetic effects

The electrokinetic effects refer to the interaction of the surface charged particles in the system with an applied electric field. Four different effects can be observed. There are electrophoresis, electroosmosis, streaming potential and sedimentation potential.

The effect used for the zeta potential measurement is the electrophoresis. The electrophoretic mobility refers to the velocity of a particle in a unit electric field. According to the Henry equation, ζ can be calculated by:

$$\zeta = \frac{3\mu U_E}{2\epsilon f(ka)} \quad (55)$$

Where ζ is zeta potential;

μ is viscosity;

ϵ is dielectric constant;

$F(ka)$ is Henry's function; and U_E is electrophoretic mobility;

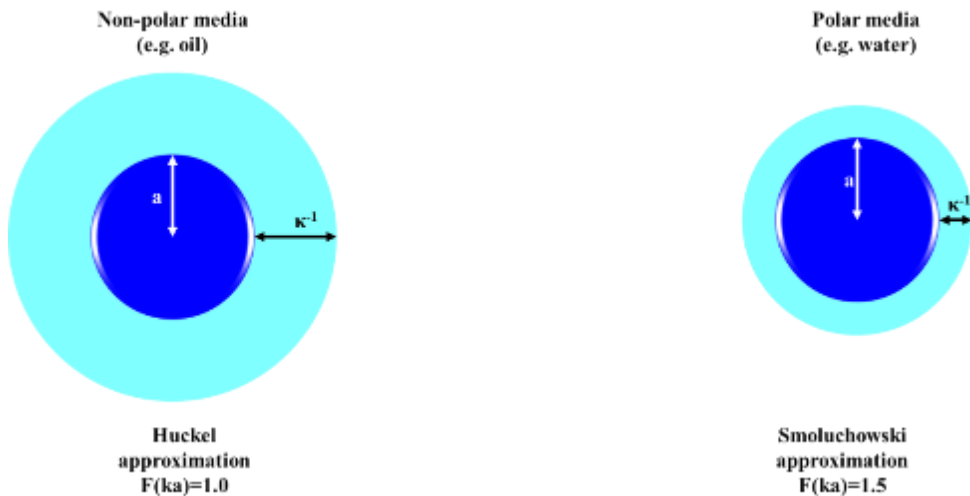


Figure 9 Schematic of the Huckel approximation and the Smoluchowski approximation

It should be pointed out that the $F(ka)$ is determined by the properties of the media. The κ^{-1} referred to the thickness of the electrical double layer. As is shown in Figure 9, For the polar media such as water-based colloids, the $F(ka)$ is 1.5 which is referred to the Smoluchowski approximation. If the particles were dispersed in the non-polar media such as oil, the approximation is the Huckel approximation in which $F(ka)$ is 1.0.

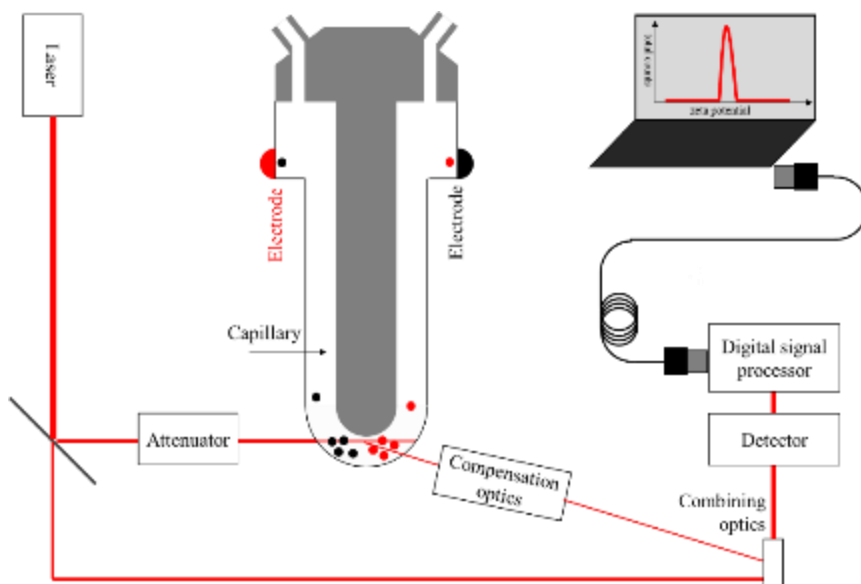


Figure 10 Optical configuration of the Zetasizer Nano series for zeta potential measurements

The equipment used in zeta potential is shown in Figure 10. The incident beam generated by the laser was split into the reference beam and measurement beam by the beam splitter. The attenuator was used

to adjust the intensity of the light to go through the cuvette. In the cuvette, an electric field is applied in order to measure the movement of the particle via the fluctuation of the beam. The frequency of the intensity of the light is proportional to the particle speed. The scattered beam with that information was collected at the 173 ° with the compensation optics to maintain optimum alignment. Then the digital signal processor is applied to produce the frequency spectrum from which the electrophoretic mobility was obtained. The calculation of the zeta potential is done Henry equation.

Reference

- [1] S. M. Sohel Murshed and C. A. Nieto de Castro, “A critical review of traditional and emerging techniques and fluids for electronics cooling,” *Renewable and Sustainable Energy Reviews*, 2017.
- [2] A. Bar-Cohen, P. Wang, and E. Rahim, “Thermal management of high heat flux nanoelectronic chips,” *Microgravity Sci. Technol.*, vol. 19, no. 3–4, pp. 48–52, 2007.
- [3] G. Agarwal, T. Kazior, T. Kenny, and D. Weinstein, “Modeling and Analysis for Thermal Management in Gallium Nitride HEMTs Using Microfluidic Cooling,” *J. Electron. Packag.*, vol. 139, no. 1, pp. 11001–11011, Nov. 2016.
- [4] Z. Lu *et al.*, “Design and modeling of membrane-based evaporative cooling devices for thermal management of high heat fluxes,” *IEEE Trans. Components, Packag. Manuf. Technol.*, vol. 6, no. 7, pp. 1058–1067, 2016.
- [5] A. R. Chabi, S. Zarrinabadi, S. M. Peyghambarzadeh, S. H. Hashemabadi, and M. Salimi, “Local convective heat transfer coefficient and friction factor of CuO/water nanofluid in a microchannel heat sink,” *Heat Mass Transf.*, vol. 53, no. 2, pp. 661–671, 2016.
- [6] L. Zheng, Y. Xie, and D. Zhang, “Numerical investigation on heat transfer performance and flow characteristics in circular tubes with dimpled twisted tapes using Al₂O₃-water nanofluid,” *Int. J. Heat Mass Transf.*, vol. 111, pp. 962–981, 2017.
- [7] B. Sun, Y. Qu, and D. Yang, “Heat transfer of Single Impinging Jet with Cu Nanofluids,” *Appl. Therm. Eng.*, vol. 102, pp. 701–707, 2016.
- [8] M. Ghanbarpour, N. Nikkam, R. Khodabandeh, and M. S. Toprak, “Improvement of heat transfer characteristics of cylindrical heat pipe by using SiC nanofluids,” *Appl. Therm. Eng.*, vol. 90, pp. 127–135, 2015.
- [9] M. Ghanbarpour, R. Khodabandeh, and K. Vafai, “An investigation of thermal performance

improvement of a cylindrical heat pipe using Al₂O₃ nanofluid,” *Heat Mass Transf.*, vol. 53, no. 3, pp. 973–983, 2016.

- [10] A. M. Bayomy and M. Z. Saghir, “Experimental study of using γ -Al₂O₃–water nanofluid flow through aluminum foam heat sink: Comparison with numerical approach,” *Int. J. Heat Mass Transf.*, vol. 107, pp. 181–203, 2017.
- [11] A. M. Bayomy and M. Z. Saghir, “Experimental Investigation of Using γ -Al₂O₃ –Water Nanofluid Flow in Aluminum Foam Heat Sink,” *ICTEA Int. Conf. Therm. Eng.*, vol. 2017, pp. 1–5, 2017.
- [12] R. Dyga and M. Płaczek, “Heat transfer through metal foam-fluid system,” *Exp. Therm. Fluid Sci.*, vol. 65, pp. 1–12, 2015.
- [13] T. J. Lu, H. a. Stone, and M. F. Ashby, “Heat transfer in open-cell metal foams,” *Acta Mater.*, vol. 46, no. 10, pp. 3619–3635, 1998.
- [14] Y. F. Wu *et al.*, “30-W/mm GaN HEMTs by Field Plate Optimization,” *IEEE Electron Device Lett.*, vol. 25, no. 3, pp. 117–119, 2004.
- [15] F. D. and B. H. 2012 52 2200-4 Lambert B, Thorpe J, Behtash R, Schauwecker B, Bourgeois F, Jung H, Bataille J, Mezenge P, Gourdon C, Ollivier C, “Reliability data’s of 0.5 μ m AlGaN/GaN on SiC technology qualification,” *Microelectron Reliab.*, vol. 52, no. 9–10, pp. 2200–2204, 2012.
- [16] M. Garven and J. P. Calame, “Simulation and optimization of gate temperatures in GaN-on-SiC monolithic microwave integrated circuits,” *IEEE Trans. Components Packag. Technol.*, vol. 32, no. 1, pp. 63–72, 2009.
- [17] J. W. Pomeroy and M. Kuball, “Optimizing GaN-on-diamond transistor geometry for maximum output power,” *Tech. Dig. - IEEE Compd. Semicond. Integr. Circuit Symp. CSIC*, pp. 31–34, 2014.
- [18] N. A. and M. H. Francis D, Faili F, Babic D, Ejekam F, “Formation and characterization of 4-

inch GaN-on-diamond substrates,” *Diam. Relat. Mater.*, vol. 19, no. 2–3, pp. 229–233, 2010.

- [19] F. Dumka, D.C., Chowdhury, U., Jimenez, J.L., Chou, T.M., Ketterson, A., Fanning, D.M., Murdock, B., Francis, D., Faili, F. and Ejeckam, “Near-junction thermal management in high power gan hemts.,” in *In Government Microcircuit Applications and Critical Technology Conf.(GOMACTech).*, 2012.
- [20] S. Mandal *et al.*, “Thick, Adherent Diamond Films on AlN with Low Thermal Barrier Resistance,” *ACS Appl. Mater. Interfaces*, vol. 11, no. 43, pp. 40826–40834, 2019.
- [21] S. Mandal *et al.*, “Low thermal resistance GaN-on-diamond transistors characterized by three-dimensional Raman thermography mapping,” *Appl. Phys. Lett.*, vol. 11, no. 43, pp. 40826–40834, 2014.
- [22] S. U. S. Choi, “Enhancing thermal conductivity of fluids with nanoparticles,” in *Proceedings of the 1995 ASME International Mechanical Engineering Congress and Exposition*, 1995, vol. 66, pp. 99–105.
- [23] M. Mehrali *et al.*, “Preparation, characterization, viscosity, and thermal conductivity of nitrogen-doped graphene aqueous nanofluids,” *J. Mater. Sci.*, vol. 49, no. 20, pp. 7156–7171, 2014.
- [24] R. Agarwal, K. Verma, N. Kumar, and R. Singh, “Sensitivity of thermal conductivity for Al₂O₃ nanofluids,” *Exp. Therm. Fluid Sci.*, vol. 80, pp. 19–26, 2017.
- [25] W. Yu, H. Xie, X. Wang, and X. Wang, “Significant thermal conductivity enhancement for nanofluids containing graphene nanosheets,” *Phys. Lett. Sect. A Gen. At. Solid State Phys.*, vol. 375, no. 10, pp. 1323–1328, 2011.
- [26] D. Madhesh and S. Kalaiselvam, “Experimental study on the heat transfer and flow properties of Ag–ethylene glycol nanofluid as a coolant,” *Heat Mass Transf.*, vol. 50, no. 11, pp. 1597–1607, 2014.
- [27] X. Li, C. Zou, L. Zhou, and A. Qi, “Experimental study on the thermo-physical properties of

diathermic oil based SiC nanofluids for high temperature applications,” *Int. J. Heat Mass Transf.*, vol. 97, pp. 631–637, 2016.

- [28] J. P. Vallejo, S. Gómez-Barreiro, D. Cabaleiro, C. Gracia-Fernández, J. Fernández-Seara, and L. Lugo, “Flow behaviour of suspensions of functionalized graphene nanoplatelets in propylene glycol–water mixtures,” *Int. Commun. Heat Mass Transf.*, vol. 91, pp. 150–157, 2018.
- [29] H. Yarmand *et al.*, “Graphene nanoplatelets-silver hybrid nanofluids for enhanced heat transfer,” *Energy Convers. Manag.*, vol. 100, pp. 419–428, 2015.
- [30] M. Mehrali *et al.*, “Heat transfer and entropy generation analysis of hybrid graphene/Fe₃O₄ ferro-nanofluid flow under the influence of a magnetic field,” *Powder Technol.*, vol. 308, pp. 149–157, 2017.
- [31] H. K. Dawood, H. A. Mohammed, N. A. C. Sidik, K. M. Munisamy, and O. A. Alawi, “Heat transfer augmentation in concentric elliptic annular by ethylene glycol based nanofluids,” *Int. Commun. Heat Mass Transf.*, vol. 82, pp. 29–39, 2017.
- [32] H. T. Zhu, Y. S. Lin, and Y. S. Yin, “A novel one-step chemical method for preparation of copper nanofluids,” *J. Colloid Interface Sci.*, vol. 277, no. 1, pp. 100–103, 2004.
- [33] R. Kamatchi and S. Venkatachalapathy, “Parametric study of pool boiling heat transfer with nanofluids for the enhancement of critical heat flux: A review,” *Int. J. Therm. Sci.*, vol. 87, pp. 228–240, 2015.
- [34] J. Taha-Tijerina *et al.*, “Electrically insulating thermal nano-oils using 2D fillers,” *ACS Nano*, vol. 6, no. 2, pp. 1214–1220, 2012.
- [35] N. K. Gupta, A. K. Tiwari, and S. K. Ghosh, “Heat transfer mechanisms in heat pipes using nanofluids – A review,” *Exp. Therm. Fluid Sci.*, vol. 90, pp. 84–100, Jan. 2018.
- [36] K. Khanafer and K. Vafai, “A review on the applications of nanofluids in solar energy field,” *Renew. Energy*, Feb. 2018.

- [37] Y. Li *et al.*, “Investigation on two abnormal phenomena about thermal conductivity enhancement of BN/EG nanofluids.,” *Nanoscale Res. Lett.*, vol. 6, no. 1, p. 443, 2011.
- [38] G. Żyła, J. Fal, J. Traciak, M. Gizowska, and K. Perkowski, “Huge thermal conductivity enhancement in boron nitride – ethylene glycol nanofluids,” *Mater. Chem. Phys.*, vol. 180, pp. 250–255, 2016.
- [39] B. Ilhan, M. Kurt, and H. Ertürk, “Experimental investigation of heat transfer enhancement and viscosity change of hBN nanofluids,” *Exp. Therm. Fluid Sci.*, vol. 77, pp. 272–283, 2016.
- [40] D. Cabaleiro *et al.*, “DESIGN AND TRANSPORT PROPERTIES OF (ETHYLENE GLYCOL + WATER) - BASED NANOFUIDS CONTAINING GRAPHENE NANOPLATELETS,” pp. 1687–1692.
- [41] A. Tang *et al.*, “CMOS (Sub)-mm-Wave System-on-Chip for exploration of deep space and outer planetary systems,” *Proc. IEEE 2014 Cust. Integr. Circuits Conf. CICC 2014*, 2014.
- [42] Y. R. Sekhar and K. V. Sharma, “Study of viscosity and specific heat capacity characteristics of water-based Al₂O₃ nanofluids at low particle concentrations,” *J. Exp. Nanosci.*, vol. 10, no. 2, pp. 86–102, 2013.
- [43] B. Jo and D. Banerjee, “Enhanced specific heat capacity of molten salt-based nanomaterials: Effects of nanoparticle dispersion and solvent material,” *Acta Mater.*, vol. 75, pp. 80–91, Aug. 2014.
- [44] L. di Zhang *et al.*, “A critical investigation of the anomalous behavior of molten salt-based nanofluids,” *Nanoscale Res. Lett.*, vol. 11, no. 1, pp. 99–105, 2016.
- [45] P. Kumar and D. Dey, “A Recent Review on Thermo-Physical Properties of Nanofluid,” pp. 3555–3560, 2016.
- [46] T. Srinivas and A. Venu Vinod, “Heat transfer intensification in a shell and helical coil heat exchanger using water-based nanofluids,” *Chem. Eng. Process. Process Intensif.*, vol. 102, pp. 1–8, 2016.

- [47] K. S. Suganthi and K. S. Rajan, “Metal oxide nanofluids: Review of formulation, thermo-physical properties, mechanisms, and heat transfer performance,” *Renew. Sustain. Energy Rev.*, vol. 76, no. February, pp. 226–255, 2017.
- [48] B. İlhan and H. Ertürk, “Experimental characterization of laminar forced convection of hBN-water nanofluid in circular pipe,” *Int. J. Heat Mass Transf.*, vol. 111, pp. 500–507, 2017.
- [49] M. Krishnam, S. Bose, and C. Das, “Boron nitride (BN) nanofluids as cooling agent in thermal management system (TMS),” *Appl. Therm. Eng.*, vol. 106, pp. 951–958, 2016.
- [50] M. Ghanbarpour, N. Nikkam, R. Khodabandeh, and M. S. Toprak, “Thermal performance of inclined screen mesh heat pipes using silver nanofluids,” *Int. Commun. Heat Mass Transf.*, vol. 67, pp. 14–20, 2015.
- [51] W. M. El-Maghly, A. A. Hanafy, A. A. Hassan, and M. A. El-Magid, “Experimental study of Cu-water nanofluid heat transfer and pressure drop in a horizontal double-tube heat exchanger,” *Exp. Therm. Fluid Sci.*, vol. 78, pp. 100–111, 2016.
- [52] S. S. Ghadikolaei, M. Yassari, H. Sadeghi, K. Hosseinzadeh, and D. D. Ganji, “Investigation on thermophysical properties of TiO_2 –Cu/H₂O hybrid nanofluid transport dependent on shape factor in MHD stagnation point flow,” *Powder Technol.*, vol. 322, pp. 428–438, 2017.
- [53] T. Tharayil, L. G. Asirvatham, M. J. Dau, and S. Wongwises, “Entropy generation analysis of a miniature loop heat pipe with graphene–water nanofluid: Thermodynamics model and experimental study,” *Int. J. Heat Mass Transf.*, vol. 106, pp. 407–421, 2017.
- [54] B. Sun, A. Yang, and D. Yang, “Experimental study on the heat transfer and flow characteristics of nanofluids in the built-in twisted belt external thread tubes,” *Int. J. Heat Mass Transf.*, vol. 107, pp. 712–722, 2017.
- [55] S. Iranmanesh, M. Mehrali, E. Sadeghinezhad, B. C. Ang, H. C. Ong, and A. Esmaeilzadeh, “Evaluation of viscosity and thermal conductivity of graphene nanoplatelets nanofluids through a combined experimental–statistical approach using respond surface methodology

method,” *Int. Commun. Heat Mass Transf.*, vol. 79, pp. 74–80, 2016.

- [56] M. P. Beck, Y. Yuan, P. Warrier, and A. S. Teja, “The effect of particle size on the thermal conductivity of alumina nanofluids,” *J. Nanoparticle Res.*, vol. 11, no. 5, pp. 1129–1136, 2009.
- [57] K. B. Anoop, T. Sundararajan, and S. K. Das, “Effect of particle size on the convective heat transfer in nanofluid in the developing region,” *Int. J. Heat Mass Transf.*, vol. 52, no. 9–10, pp. 2189–2195, 2009.
- [58] T. P. Teng, Y. H. Hung, T. C. Teng, H. E. Mo, and H. G. Hsu, “The effect of alumina/water nanofluid particle size on thermal conductivity,” *Appl. Therm. Eng.*, vol. 30, no. 14–15, pp. 2213–2218, 2010.
- [59] H. Xie, J. Wang, T. Xi, Y. Liu, F. Ai, and Q. Wu, “Thermal conductivity enhancement of suspensions containing nanosized alumina particles,” *J. Appl. Phys.*, vol. 91, no. 7, pp. 4568–4572, 2002.
- [60] M. A. Esfahani and D. Toghraie, “Experimental investigation for developing a new model for the thermal conductivity of Silica/Water-Ethylene glycol (40%–60%) nanofluid at different temperatures and solid volume fractions,” *J. Mol. Liq.*, vol. 232, pp. 105–112, 2017.
- [61] M. Hossein Karimi Darvanooghi and M. Nasr Esfahany, “Experimental investigation of the effect of nanoparticle size on thermal conductivity of in-situ prepared silica–ethanol nanofluid,” *Int. Commun. Heat Mass Transf.*, vol. 77, pp. 148–154, 2016.
- [62] O. Mahian, A. Kianifar, S. Z. Heris, and S. Wongwises, “Natural convection of silica nanofluids in square and triangular enclosures: Theoretical and experimental study,” *Int. J. Heat Mass Transf.*, vol. 99, pp. 792–804, 2016.
- [63] Z. Haddad, C. Abid, A. A. Mohamad, O. Rahli, and S. Bawazer, “Natural convection of silica–water nanofluids based on experimental measured thermophysical properties: critical analysis,” *Heat Mass Transf. und Stoffuebertragung*, vol. 52, no. 8, pp. 1649–1663, 2016.

- [64] S. Akilu, A. T. Baheta, A. A. Minea, and K. V. Sharma, “Rheology and thermal conductivity of non-porous silica (SiO_2) in viscous glycerol and ethylene glycol based nanofluids,” *Int. Commun. Heat Mass Transf.*, vol. 88, no. October, pp. 245–253, 2017.
- [65] M. H. Esfe, S. Saedodin, O. Mahian, and S. Wongwises, “Thermal conductivity of Al_2O_3 /water nanofluids: Measurement, correlation, sensitivity analysis, and comparisons with literature reports,” *J. Therm. Anal. Calorim.*, vol. 117, no. 2, pp. 675–681, 2014.
- [66] C. Jumpholkul, O. Mahian, A. Kasaean, A. S. Dalkilic, and S. Wongwises, “An experimental study to determine the maximum efficiency index in turbulent flow of SiO_2 /water nanofluids,” *Int. J. Heat Mass Transf.*, vol. 112, pp. 1113–1121, 2017.
- [67] J. Koo and C. Kleinstreuer, “Impact analysis of nanoparticle motion mechanisms on the thermal conductivity of nanofluids,” *Int. Commun. Heat Mass Transf.*, vol. 32, no. 9, pp. 1111–1118, 2005.
- [68] R. Kamatchi, “Experimental investigations on nucleate boiling heat transfer of aqua based reduced graphene oxide nanofluids,” *Heat Mass Transf.*, 2017.
- [69] M. Ghanbarpour and R. Khodabandeh, “Entropy generation analysis of cylindrical heat pipe using nanofluid,” *Thermochim. Acta*, vol. 610, pp. 37–46, 2015.
- [70] S. Mirfendereski, A. Abbassi, and M. Saffar-Avval, “Experimental and numerical investigation of nanofluid heat transfer in helically coiled tubes at constant wall heat flux,” *Adv. Powder Technol.*, vol. 26, no. 5, pp. 1483–1494, 2015.
- [71] S. Yan, F. Wang, Z. G. Shi, and R. Tian, “Heat transfer property of SiO_2 /water nanofluid flow inside solar collector vacuum tubes,” *Appl. Therm. Eng.*, vol. 118, pp. 385–391, 2017.
- [72] S. Iranmanesh, H. C. Ong, B. C. Ang, E. Sadeghinezhad, A. Esmaeilzadeh, and M. Mehrali, “Thermal performance enhancement of an evacuated tube solar collector using graphene nanoplatelets nanofluid,” *J. Clean. Prod.*, vol. 162, pp. 121–129, 2017.
- [73] R. Ranjbarzadeh, A. Karimipour, M. Afrand, A. H. M. Isfahani, and A. Shirneshan, “Empirical

analysis of heat transfer and friction factor of water/graphene oxide nanofluid flow in turbulent regime through an isothermal pipe,” *Appl. Therm. Eng.*, vol. 126, pp. 538–547, 2017.

- [74] J. C. Maxwell, *An elementary treatise on electricity*, 2nd ed. Oxford: Clarendon Press, 1881.
- [75] C. W. Nan, R. Birringer, D. R. Clarke, and H. Gleiter, “Effective thermal conductivity of particulate composites with interfacial thermal resistance,” *J. Appl. Phys.*, vol. 81, no. 10, pp. 6692–6699, 1997.
- [76] R. L. Hamilton, “Thermal conductivity of heterogeneous two-component systems,” *Ind. Eng. Chem. Fundam.*, vol. 1, no. 3, pp. 187–191, 1962.
- [77] J. Koo and C. Kleinstreuer, “Laminar nanofluid flow in microheat-sinks,” *Int. J. Heat Mass Transf.*, vol. 48, no. 13, pp. 2652–2661, 2005.
- [78] C. S. U. S., “Interfacial Layers in the Enhanced Thermal conductivity of Nanofluids: A Renovated Maxwell Model,” *J. Nanopart. Res.*, vol. 5, p. 167, 2003.
- [79] R. Prasher, P. Bhattacharya, and P. E. Phelan, “Thermal conductivity of nanoscale colloidal solutions (nanofluids),” *Phys. Rev. Lett.*, vol. 94, no. 2, pp. 3–6, 2005.
- [80] M. Kole and T. K. Dey, “Investigation of thermal conductivity, viscosity, and electrical conductivity of graphene based nanofluids,” *J. Appl. Phys.*, vol. 113, no. 8, 2013.
- [81] D. Cabaleiro, L. Colla, S. Barison, L. Lugo, L. Fedele, and S. Bobbo, “Heat Transfer Capability of (Ethylene Glycol + Water)-Based Nanofluids Containing Graphene Nanoplatelets: Design and Thermophysical Profile,” *Nanoscale Res. Lett.*, vol. 12, no. 1, 2017.
- [82] M. Hadadian, E. K. Goharshadi, and A. Youssefi, “Electrical conductivity, thermal conductivity, and rheological properties of graphene oxide-based nanofluids,” *J. Nanoparticle Res.*, vol. 16, no. 12, 2014.
- [83] M. Mehrali *et al.*, “Investigation of thermal conductivity and rheological properties of nanofluids containing graphene nanoplatelets,” *Nanoscale Res. Lett.*, vol. 9, no. 1, p. 15, 2014.

- [84] M. Kole and T. K. Dey, “Investigation of thermal conductivity , viscosity , and electrical conductivity of graphene based nanofluids Investigation of thermal conductivity , viscosity , and electrical conductivity of graphene based nanofluids,” vol. 084307, no. 2013, 2014.
- [85] W. Yu, H. Xie, X. Wang, and X. Wang, “Significant thermal conductivity enhancement for nanofluids containing graphene nanosheets,” *Phys. Lett. Sect. A Gen. At. Solid State Phys.*, vol. 375, no. 10, pp. 1323–1328, 2011.
- [86] T. T. Baby and S. Ramaprabhu, “Investigation of thermal and electrical conductivity of graphene based nanofluids,” vol. 124308, no. 2010, 2011.
- [87] A. Einstein, “Eine neue Bestimmung der Moleküldimensionen,” *Ann. Phys.*, vol. 342, pp. 289–306, 1906.
- [88] B. Abedian and M. Kachanov, “On the effective viscosity of suspensions,” *Int. J. Eng. Sci.*, vol. 48, no. 11, pp. 962–965, 2010.
- [89] H. C. Brinkman, “The viscosity of concentrated suspensions and solutions,” *J. Chem. Phys.*, vol. 20, no. 4, p. 571, 1952.
- [90] Y. Xuan and W. Roetzel, “Conceptions for heat transfer correlation of nanofluids,” *Int. J. Heat Mass Transf.*, vol. 43, no. 19, pp. 3701–3707, 2000.
- [91] B. Ilhan, M. Kurt, and H. Erturk, “Preperation and Thermal Conductivity of Water Based Hbn Nanofluids,” *Proceeding First Therm. Fluids Eng. Summer Conf.*, pp. 1–4, 2016.
- [92] C. Zhi, Y. Xu, Y. Bando, and D. Golberg, “Highly thermo-conductive fluid with boron nitride nanofillers,” *ACS Nano*, vol. 5, no. 8, pp. 6571–6577, 2011.
- [93] B. X. Du and X. L. Li, “High thermal conductivity transformer oil filled with BN n anoparticles,” *IEEE Electr. Insul. Mag.*, vol. June 30, no. 2, pp. 1–4, 2014.
- [94] Y. Gao, H. Wang, A. P. Sasmito, and A. S. Mujumdar, “Measurement and modeling of thermal conductivity of graphene nanoplatelet water and ethylene glycol base nanofluids,” *Int.*

J. Heat Mass Transf., vol. 123, pp. 97–109, 2018.

- [95] W. Yu, H. Xie, and D. Bao, “Enhanced thermal conductivities of nanofluids containing graphene oxide nanosheets,” *Nanotechnology*, vol. 21, no. 5, 2010.
- [96] Y. Wang, H. A. I. Al-Saaidi, M. Kong, and J. L. Alvarado, “Thermophysical performance of graphene based aqueous nanofluids,” *Int. J. Heat Mass Transf.*, vol. 119, pp. 408–417, 2018.
- [97] M. Mehrali *et al.*, “An ecofriendly graphene-based nanofluid for heat transfer applications,” *J. Clean. Prod.*, vol. 137, pp. 555–566, 2016.
- [98] A. Amiri *et al.*, “Performance dependence of thermosyphon on the functionalization approaches: An experimental study on thermo-physical properties of graphene nanoplatelet-based water nanofluids,” *Energy Convers. Manag.*, vol. 92, pp. 322–330, 2015.
- [99] G. J. Lee and C. K. Rhee, “Enhanced thermal conductivity of nanofluids containing graphene nanoplatelets prepared by ultrasound irradiation,” *J. Mater. Sci.*, vol. 49, no. 4, pp. 1506–1511, 2014.
- [100] N. Ahammed, L. G. Asirvatham, J. Titus, J. R. Bose, and S. Wongwises, “Measurement of thermal conductivity of graphene-water nanofluid at below and above ambient temperatures,” *Int. Commun. Heat Mass Transf.*, vol. 70, pp. 66–74, 2016.
- [101] H. Akhavan-Zanjani, M. Saffar-Avval, M. Mansourkiae, F. Sharif, and M. Ahadi, “Experimental investigation of laminar forced convective heat transfer of Graphene-water nanofluid inside a circular tube,” *Int. J. Therm. Sci.*, vol. 100, pp. 316–323, 2016.
- [102] H. Yarmand *et al.*, “Experimental investigation of thermo-physical properties, convective heat transfer and pressure drop of functionalized graphene nanoplatelets aqueous nanofluid in a square heated pipe,” *Energy Convers. Manag.*, vol. 114, pp. 38–49, 2016.
- [103] Z. Hajjar, A. morad Rashidi, and A. Ghozatloo, “Enhanced thermal conductivities of graphene oxide nanofluids,” *Int. Commun. Heat Mass Transf.*, vol. 57, pp. 128–131, 2014.

- [104] W. Yu, H. Xie, and W. Chen, “Experimental investigation on thermal conductivity of nanofluids containing graphene oxide nanosheets,” *J. Appl. Phys.*, vol. 107, no. 9, 2010.
- [105] T. T. Baby and S. Ramaprabhu, “Enhanced convective heat transfer using graphene dispersed nanofluids.,” *Nanoscale Res. Lett.*, vol. 6, no. 1, p. 289, 2011.
- [106] A. Ghozatloo, M. Shariaty-Niasar, and A. M. Rashidi, “Preparation of nanofluids from functionalized Graphene by new alkaline method and study on the thermal conductivity and stability,” *Int. Commun. Heat Mass Transf.*, vol. 42, pp. 89–94, 2013.
- [107] H. Zhang, S. Wang, Y. Lin, M. Feng, and Q. Wu, “Stability, thermal conductivity, and rheological properties of controlled reduced graphene oxide dispersed nanofluids,” *Appl. Therm. Eng.*, vol. 119, pp. 132–139, 2017.
- [108] S. S. Park and N. J. Kim, “Influence of the oxidation treatment and the average particle diameter of graphene for thermal conductivity enhancement,” *J. Ind. Eng. Chem.*, vol. 20, no. 4, pp. 1911–1915, 2014.
- [109] J. Ditri, M. K. McNulty, and S. Igoe, “S3-P10: Embedded microfluidic cooling of high heat flux electronic components,” *Lester Eastman Conf. 2014 - High Perform. Devices, LEC 2014*, pp. 1–4, 2014.
- [110] J. Kähler, N. Heuck, A. Wagner, A. Stranz, E. Peiner, and A. Waag, “Sintering of Copper Particles for Die Attach,” vol. 2, no. 10, pp. 1587–1591, 2012.
- [111] H. Zhang, S. Nagao, and K. Suganuma, “Thermostable Ag die-attach structure for high-temperature power devices,” *J. Mater. Sci. Mater. Electron.*, vol. 27, no. 2, pp. 1337–1344, 2016.
- [112] S. D. Material, T. Suzuki, T. Terasaki, Y. Kawana, and D. Ishikawa, “Effect of Manufacturing Process on Micro-Deformation Behavior of,” *IEEE Trans. Device Mater. Reliab.*, vol. 16, no. 4, pp. 588–596, 2016.
- [113] P. O. Quintero and F. P. Mccluskey, “Temperature Cycling Reliability of High-Temperature

Lead-Free Die-Attach Technologies,” *IEEE Trans. Device Mater. Reliab.*, vol. 11, no. 4, pp. 531–539, 2011.

- [114] D. Road and L. Ln, “Evaluation of Ag sintering die attach for high temperature power module applications,” *2014 15th Int. Conf. Electron. Packag. Technol.*, pp. 200–204, 2014.
- [115] A. Larsson, T. Andre, K. Høydalsvik, D. A. G. W. Breiby, and K. Aasmundtveit, “Au-Sn SLID Bonding : A Reliable HT Interconnect and Die Attach Technology,” 2013.
- [116] F. Dugal and M. Ciappa, “Microelectronics Reliability Study of thermal cycling and temperature aging on PbSnAg die attach solder joints for high power modules,” *Microelectron. Reliab.*, vol. 54, no. 9–10, pp. 1856–1861, 2014.
- [117] Z. Z. Zhang and G. Lu, “Pressure-Assisted Low-Temperature Sintering of Silver Paste as an Alternative Die-Attach Solution to Solder Reflow,” *IEEE Trans. Electron. Packag. Manuf.*, vol. 25, no. 4, pp. 279–283, 2002.
- [118] L. C. Wai *et al.*, “Study on Silver Sintered Die Attach Material with Different Metal Surfaces for High Temperature and High Pressure (300 °C / 30kpsi) Applications,” *2013 IEEE 15th Electron. Packag. Technol. Conf. (EPTC 2013)*, pp. 335–340, 2013.
- [119] D. Lu *et al.*, “Enhancement of thermal conductivity of die attach adhesives (DAAs) using nanomaterials for high brightness light-emitting diode (HBLED),” *2011 IEEE 61st Electron. Components Technol. Conf.*, pp. 667–672, 2011.
- [120] L. C. Wai, D. M. Zhi, V. S. Rao, M. Woo, and D. Rhee, “Process Characterization of Highly Conductive Silver Paste Die Attach Materials for Thin Die on QFN,” *2012 IEEE 14th Electron. Packag. Technol. Conf.*, pp. 372–378, 2012.
- [121] I. De Microelectrònica and D. B. N. De Microelectrònica, “Silver nano-particles sintering process for the die-attach of power devices for high temperature applications,” pp. 97–102, 2012.
- [122] T. Youssef *et al.*, “Microelectronics Reliability Power modules die attach : A comprehensive

evolution of the nanosilver sintering physical properties versus its porosity,” *MR*, vol. 55, no. 9–10, pp. 1997–2002, 2015.

- [123] S. Amir, A. Mansourian, Y. Noh, K. Khtatba, and S. H. Mannan, “Thermally stable high temperature die attach solution,” *JMADE*, vol. 89, pp. 1310–1314, 2016.
- [124] F. Yu *et al.*, “Reliability of Ag Sintering for Power Semiconductor Die Attach in High-Temperature Applications,” *IEEE Trans. Power Electron.*, vol. 32, no. 9, pp. 7083–7095, 2017.
- [125] T. A. O. Wang, M. Zhao, X. U. Chen, G. Lu, K. Ngo, and S. Luo, “Shrinkage and Sintering Behavior of a Low-Temperature Sinterable Nanosilver Die-Attach Paste,” vol. 41, no. 9, pp. 2543–2552, 2012.
- [126] N. Heuck *et al.*, “Analysis and Modeling of Thermomechanically Improved Silver-Sintered Die-Attach Layers Modified by Additives,” *IEEE Trans. Components, Packag. Manuf. Technol.*, vol. 1, no. 11, pp. 1846–1855, 2011.
- [127] C. Chen *et al.*, “Mechanical Deformation of Sintered Porous Ag Die Attach at High Temperature and Its Size Effect for Wide-Bandgap Power Device Design,” vol. 46, no. 3, pp. 1576–1586, 2017.
- [128] T. Krebs, S. Duch, W. Schmitt, S. Kötter, P. Prenosil, and S. Thomas, “A Breakthrough in Power Electronics Reliability – New Die Attach and Wire Bonding Materials,” pp. 1746–1752, 2013.
- [129] W. Sabbah, S. Azzopardi, C. Buttay, R. Meuret, and E. Woirgard, “Microelectronics Reliability Study of die attach technologies for high temperature power electronics : Silver sintering and gold – germanium alloy,” *Microelectron. Reliab.*, vol. 53, no. 9–11, pp. 1617–1621, 2013.
- [130] M. Kim and H. Nishikawa, “ScienceDirect Silver nanoporous sheet for solid-state die attach in power device packaging,” *Scr. Mater.*, vol. 92, pp. 43–46, 2014.

- [131] H. A. O. Zhang, S. Nagao, and K. Suganuma, “Addition of SiC Particles to Ag Die-Attach Paste to Improve High-Temperature Stability ; Grain Growth Kinetics of Sintered Porous Ag,” vol. 44, no. 10, pp. 3896–3903, 2015.
- [132] L. Braunwarth, S. Amrhein, T. Schreck, and M. Kaloudis, “Ecological comparison of soldering and sintering as die-attach technologies in power electronics,” *J. Clean. Prod.*, vol. 102, pp. 408–417, 2015.
- [133] C. Chen, C. Chen, R. Horng, D. Wuu, and J. Hong, “Thermal Management and Interfacial Properties in High-Power GaN-Based Light-Emitting Diodes Employing Diamond-Added Sn-3 wt .% Ag-0 .5 wt .% Cu Solder as a Die-Attach Material,” vol. 39, no. 12, pp. 2618–2626, 2010.
- [134] J. Kähler, N. Heuck, A. Stranz, A. Waag, and E. Peiner, “Pick-and-Place Silver Sintering Die Attach of Small-Area Chips,” vol. 2, no. 2, pp. 199–207, 2012.
- [135] H. Kim, S. Choi, S. Shin, Y. Lee, S. Choi, and S. Yi, “Thermal transient characteristics of die attach in high power LED PKG,” vol. 48, pp. 445–454, 2008.
- [136] W. Vxfk *et al.*, “WDFW 3DVWH / HDG) UHH 6ROXWLR RQ IRU ’ LH \$ WWDFK,” pp. 16–18, 2010.
- [137] G. Lu, M. Zhao, G. Lei, J. N. Calata, X. Chen, and S. Luo, “Emerging Lead-free , High-temperature Die-attach Technology Enabled by Low-temperature Sintering of Nanoscale Silver Pastes,” *2009 Int. Conf. Electron. Packag. Technol. High Density Packag.*, pp. 461–466, 2009.
- [138] F. Lacroix and J. Barbot, “SiC Die Attach for High-Temperature Applications,” vol. 43, no. 3, pp. 695–701, 2014.
- [139] P. Quintero, T. Oberc, and P. Mccluskey, “Reliability Assessment of High Temperature Lead-Free Device Attach Technologies,” *2008 58th Electron. Components Technol. Conf.*, pp. 2131–2138, 2008.

- [140] X. Cao, T. Wang, G. Lu, and K. D. T. Ngo, “Characterization of Lead-Free Solder and Sintered Nano-Silver Die-Attach Layers Using Thermal Impedance,” *2010 Int. Power Electron. Conf. - ECCE ASIA* -, pp. 546–552, 2010.
- [141] W. Lai *et al.*, “Experimental Investigation on the Effects of Narrow Junction Temperature Cycles on Die-Attach Solder Layer in an IGBT Module,” *IEEE Trans. Power Electron.*, vol. 32, no. 2, pp. 1431–1441, 2017.
- [142] K. Suganuma, S. Sakamoto, N. Kagami, D. Wakuda, K. Kim, and M. Nogi, “Microelectronics Reliability Low-temperature low-pressure die attach with hybrid silver particle paste,” *Microelectron. Reliab.*, vol. 52, no. 2, pp. 375–380, 2012.
- [143] H. A. Mustain, W. D. Brown, L. Fellow, and S. S. Ang, “Transient Liquid Phase Die Attach for High-Temperature Silicon Carbide Power Devices,” *IEEE Trans. Components Packag. Technol.*, vol. 33, no. 3, pp. 563–570, 2010.
- [144] V. Raja, M. Khairunisak, and A. Razak, “Physical and electrical attributes of sintered Ag 80 – Al 20 high temperature die attach material with different organic additives content,” pp. 720–733, 2013.
- [145] V. R. Manikam, K. A. Razak, and K. Y. Cheong, “Microelectronics Reliability Reliability of sintered Ag 80 – Al 20 die attach nanopaste for high temperature applications on SiC power devices,” *Microelectron. Reliab.*, vol. 53, no. 3, pp. 473–480, 2013.
- [146] T. Kunimune, M. Kuramoto, S. Ogawa, and T. Sugahara, “ScienceDirect Ultra thermal stability of LED die-attach achieved by pressureless Ag stress-migration bonding at low temperature,” *Acta Mater.*, vol. 89, pp. 133–140, 2015.
- [147] F. Le Henaff, S. Azzopardi, J. Y. Deletage, E. Woirgard, S. Bontemps, and J. Joguet, “Microelectronics Reliability A preliminary study on the thermal and mechanical performances of sintered nano-scale silver die-attach technology depending on the substrate metallization,” *Microelectron. Reliab.*, vol. 52, no. 9–10, pp. 2321–2325, 2012.

- [148] S. Kim, K. Kim, and S. Kim, “Interfacial Reaction and Die Attach Properties of Zn-Sn High-Temperature Solders,” vol. 38, no. 2, 2009.
- [149] L. F. Yee, C. Lo, W. Yew, and P. J. Selangor, “Die Attach Materials Impacts to Copper Wire bonding : New Challenges,” *2012 IEEE 14th Electron. Packag. Technol. Conf.*, pp. 263–268, 2012.
- [150] T. L. Solder, F. Engineering, K. Lumpur, and T. Ag, “Effect ofNi Metallization on Interfacial Reactions and Die Attach Properties of Zn-Al-Mg-Ga High,” 2010.
- [151] B. S. Lee, S. Keun, H. Jeong, and W. Yoon, “Cu – Sn and Ni – Sn transient liquid phase bonding for die-attach technology applications in high-temperature power electronics packaging,” *J. Mater. Sci. Mater. Electron.*, vol. 28, no. 11, pp. 7827–7833, 2017.
- [152] A. Haque, B. H. Lim, A. S. M. A. Haseeb, and H. H. Masjuki, “Die attach properties of Zn – Al – Mg – Ga based high-temperature lead-free solder on Cu lead-frame,” pp. 115–123, 2012.
- [153] D. C. Katsis and J. Daniel, “A Thermal , Mechanical , and Electrical Study of Voiding in the Solder Die-Attach of Power MOSFETs,” vol. 29, no. 1, pp. 127–136, 2006.
- [154] B. Yan, J. P. You, N. T. Tran, Y. He, F. G. Shi, and S. Member, “Influence of Die Attach Layer on Thermal Performance of High Power Light Emitting Diodes,” *IEEE Trans. Components Packag. Technol.*, vol. 33, no. 4, pp. 722–727, 2010.
- [155] S. Baraty Beni, A. Bahrami, and M. R. Salimpour, “Design of novel geometries for microchannel heat sinks used for cooling diode lasers,” *Int. J. Heat Mass Transf.*, vol. 112, pp. 689–698, 2017.
- [156] S. R. Reddy *et al.*, “Multi-Objective Optimization of Micro Pin-Fin Arrays for Cooling of High Heat Flux Electronics with a Hot Spot,” *Heat Transf. Eng.*, vol. 38, no. 14–15, pp. 1235–1246, 2017.
- [157] A. A. Y. Al-Waaly, M. C. Paul, and P. Dobson, “Liquid cooling of non-uniform heat flux of a chip circuit by subchannels,” *Appl. Therm. Eng.*, vol. 115, pp. 558–574, 2017.

- [158] Z. Azizi, A. Alamdari, and M. R. Malayeri, “Convective heat transfer of Cu-water nanofluid in a cylindrical microchannel heat sink,” *Energy Convers. Manag.*, vol. 101, pp. 515–524, 2015.
- [159] Z. Nikkhah *et al.*, “Forced convective heat transfer of water/functionalized multi-walled carbon nanotube nanofluids in a microchannel with oscillating heat flux and slip boundary condition,” *Int. Commun. Heat Mass Transf.*, vol. 68, pp. 69–77, 2015.
- [160] D. Issadore, K. J. Humphry, K. A. Brown, L. Sandberg, D. A. Weitz, and R. M. Westervelt, “Microwave dielectric heating of drops in microfluidic devices.,” *Lab Chip*, vol. 9, no. 12, pp. 1701–6, 2009.
- [161] J. P. Calame, R. E. Myers, S. C. Binari, F. N. Wood, and M. Garven, “Experimental investigation of microchannel coolers for the high heat flux thermal management of GaN-on-SiC semiconductor devices,” *Int. J. Heat Mass Transf.*, vol. 50, no. 23–24, pp. 4767–4779, 2007.
- [162] J. P. Calame, R. E. Myres, F. N. Wood, and S. C. Binari, “Simulations of direct-die-attached microchannel coolers for the thermal management of GaN-on-SiC microwave amplifiers,” *IEEE Trans. Components Packag. Technol.*, vol. 28, no. 4, pp. 797–809, 2005.
- [163] C. Y. Zhao, “Review on thermal transport in high porosity cellular metal foams with open cells,” *Int. J. Heat Mass Transf.*, vol. 55, no. 13–14, pp. 3618–3632, 2012.
- [164] A. M. Bayomy, M. Z. Saghir, and T. Yousefi, “Electronic cooling using water flow in aluminum metal foam heat sink: Experimental and numerical approach,” *Int. J. Therm. Sci.*, vol. 109, pp. 182–200, 2016.
- [165] H. Wang and L. Guo, “Experimental investigation on pressure drop and heat transfer in metal foam filled tubes under convective boundary condition,” *Chem. Eng. Sci.*, vol. 155, pp. 438–448, 2016.
- [166] M. Nazari, M. Ashouri, M. H. Kayhani, and A. Tamayol, “Experimental study of convective heat transfer of a nanofluid through a pipe filled with metal foam,” *Int. J. Therm. Sci.*, vol. 88,

pp. 33–39, 2015.

- [167] P. Smakulski and S. Pietrowicz, “A review of the capabilities of high heat flux removal by porous materials, microchannels and spray cooling techniques,” *Appl. Therm. Eng.*, vol. 104, pp. 636–646, 2016.
- [168] R. Kneer, W. Rohlfs, J. Jorg, S. Taraborrelli, G. Sarriegui, and R. W. De Doncker, “Direct Single Impinging Jet Cooling of a MOSFET Power Electronic Module,” *IEEE Trans. Power Electron.*, vol. 33, no. 5, pp. 4224–4237, 2017.
- [169] J. Jorg, S. Taraborrelli, E. Sabelberg, R. Kneer, R. De Doncker, and W. Rohlfs, “Hot spot removal in power electronics by means of direct liquid jet cooling,” *Proc. 16th Intersoc. Conf. Therm. Thermomechanical Phenom. Electron. Syst. ITherm 2017*, pp. 471–481, 2017.
- [170] W. Deng and A. Gomez, “Electrospray cooling for microelectronics,” *Int. J. Heat Mass Transf.*, vol. 54, no. 11–12, pp. 2270–2275, 2011.
- [171] J. F. Maddox, R. W. Knight, and S. H. Bhavnani, “Local thermal measurements of a confined array of impinging liquid jets for power electronics cooling,” *Annu. IEEE Semicond. Therm. Meas. Manag. Symp.*, vol. 2015-April, pp. 228–234, 2015.
- [172] Y. Han, B. L. Lau, G. Tang, X. Zhang, and D. M. W. Rhee, “Si-Based Hybrid Microcooler with Multiple Drainage Microtrenches for High Heat Flux Cooling,” *IEEE Trans. Components, Packag. Manuf. Technol.*, vol. 7, no. 1, pp. 50–57, 2017.
- [173] A. J. Robinson, R. Kempers, J. Colenbrander, N. Bushnell, and R. Chen, “A single phase hybrid micro heat sink using impinging micro-jet arrays and microchannels,” *Appl. Therm. Eng.*, vol. 136, no. February, pp. 408–418, 2018.
- [174] A. J. Robinson *et al.*, “A New Hybrid Heat Sink with Impinging Micro-Jet Arrays and Microchannels Fabricated using High Volume Additive Manufacturing,” 2017.
- [175] J. Y. San and J. J. Chen, “Effects of jet-to-jet spacing and jet height on heat transfer characteristics of an impinging jet array,” *Int. J. Heat Mass Transf.*, vol. 71, pp. 8–17, 2014.

- [176] X. Huang, W. Yang, T. Ming, W. Shen, and X. Yu, “Heat transfer enhancement on a microchannel heat sink with impinging jets and dimples,” *Int. J. Heat Mass Transf.*, vol. 112, pp. 113–124, 2017.
- [177] D. Li *et al.*, “3D Multiphysics Modelling of High Voltage IGBT Module Packaging,” *2015 16th Int. Conf. Electron. Packag. Technol.*, pp. 598–602, 2015.
- [178] A. Vipradas, A. Takawale, S. Tripathi, and V. Swakul, “A Parametric Study of a Typical High Power LED Package to Enhance Overall Thermal Performance,” *13th Intersoc. Conf. Therm. Thermomechanical Phenom. Electron. Syst.*, pp. 308–313, 2012.
- [179] A. Chvála, D. Donoval, and A. Šatka, “Advanced Methodology for Fast 3-D TCAD Device / Circuit Electrothermal Simulation and Analysis of Power HEMTs,” *IEEE Trans. Electron Devices*, vol. 62, no. 3, pp. 828–834, 2015.
- [180] M. H. Wong, Y. Morikawa, K. Sasaki, A. Kuramata, S. Yamakoshi, and M. Higashiwaki, “Characterization of channel temperature in Ga₂O₃ metal-oxide-semiconductor field- effect transistors by electrical measurements and thermal modeling,” vol. 193503, 2016.
- [181] N. Kudsieh, M. Khizar, and M. Y. A. Raja, “Controlling thermal uniformity among LED chips assembly packages for high-power solid state lighting,” *2013 High Capacit. Opt. Networks Emerging/Enabling Technol.*, pp. 78–83, 2013.
- [182] N. Kudsieh, M. K. Bhutta, and M. Y. A. Raja, “Optik High power LED assemblies for solid state lighting – Thermal analysis,” *Opt. - Int. J. Light Electron Opt.*, vol. 126, no. 22, pp. 3452–3456, 2015.
- [183] R. Vairavan, Z. Sauli, and V. Retnasamy, “High Power LED Heat Dissipation Analysis Using Cylindrical Al Based Slug Using Ansys,” *RSM 2013 IEEE Reg. Symp. Micro Nanoelectron.*, pp. 186–189, 2013.
- [184] A. Y. Tang, E. Schlecht, G. Chattopadhyay, R. Lin, C. Lee, and J. Gill, “Steady-State and Transient Thermal Analysis of High-Power Planar Schottky Diodes,” no. April, pp. 26–28,

2011.

- [185] Q. Cheng, “Management of High-power White LED Package,” vol. 00, pp. 3–7, 2007.
- [186] A. Chvála, J. Marek, P. Príbytný, A. Šatka, M. Donoval, and D. Donoval, “Effective 3-D Device Electrothermal Simulation Analysis of Influence of Metallization Geometry on Multifinger Power HEMTs Properties,” *IEEE Trans. Electron Devices*, vol. 64, no. 1, pp. 333–336, 2017.
- [187] and J. C. D. J. M. Rousseau, A. Soltani, “Efficient physical-thermal model for thermal effects in AlGaN / GaN high electron mobility transistors,” *This Lett. Descr. Therm. Behav. AlGaN/GaN high electron Mobil. transistors Differ. substrates thanks to a fully consistent Phys. Model. Self-heating Explain. drastic Reduct. Curr. Flow. from drain to source*, vol. 122101, no. July 2012, pp. 99–102, 2012.
- [188] T. Lu and J. Jin, “Electrical-Thermal Co-Simulation for Analysis of High-Power RF/Microwave Components,” *IEEE Trans. Electromagn. Compat.*, vol. 59, no. 1, pp. 93–102, 2017.
- [189] M. Pfost, C. Boianceanu, H. Lohmeyer, and M. Stecher, “Electrothermal Simulation of Self-Heating in DMOS Transistors up to Thermal Runaway,” *IEEE Trans. Electron Devices*, vol. 60, no. 2, pp. 699–707, 2013.
- [190] Y. Won, J. Cho, D. Agonafer, M. Asheghi, and K. E. Goodson, “Fundamental Cooling Limits for High Power Density Gallium Nitride Electronics,” *IEEE Trans. Components, Packag. Manuf. Technol.*, vol. 5, no. 6, pp. 737–744, 2015.
- [191] K. Maize, G. Pavlidis, E. Heller, L. Yates, D. Kendig, and S. Graham, “High Resolution Thermal Characterization and Simulation of Power AlGaN / GaN HEMTs Using Micro-Raman Thermography and 800 Picosecond Transient Thermoreflectance Imaging,” 2014.
- [192] Z. Lin, C. Liu, and Y. Chai, “High thermally conductive and electrically insulating 2D boron nitride nanosheet for efficient heat dissipation of high-power transistors High thermally

conductive and electrically insulating 2D boron nitride nanosheet for efficient heat dissipation,” 2016.

- [193] P. H. Aaen *et al.*, “Multiphysics Modeling of RF and Microwave High-Power Transistors,” vol. 60, no. 12, pp. 4013–4023, 2012.
- [194] D. Li *et al.*, “Multi-physics Simulation in High Power IGBT Module Design,” *2016 17th Int. Conf. Therm. Mech. Multi-Physics Simul. Exp. Microelectron. Microsystems*, pp. 1–5, 2016.
- [195] A. Ziabari *et al.*, “Power Blurring : Fast Static and Transient Thermal Analysis Method for Packaged Integrated Circuits and Power Devices,” *IEEE Trans. Very Large Scale Integr. Syst.*, vol. 22, no. 11, pp. 2366–2379, 2014.
- [196] A. Wang, “Simulation of thermal management in AlGaN / GaN HEMTs with integrated diamond heat spreaders,” 2013.
- [197] A. Prejs, S. Wood, R. Pengelly, and W. Pribble, “Thermal Analysis and its application to High Power GaN HEMT Amplifiers,” *2009 IEEE MTT-S Int. Microw. Symp. Dig.*, pp. 917–920, 2009.
- [198] L. Baczkowski *et al.*, “Thermal Characterization Using Optical Methods of AlGaN / GaN HEMTs on SiC Substrate in RF Operating Conditions,” *IEEE Trans. Electron Devices*, vol. 62, no. 12, pp. 3992–3998, 2015.
- [199] H. Wu, M. Chen, L. Gao, and M. Li, “Thermal resistance analysis by numerical method for power device packaging,” *2012 13th Int. Conf. Electron. Packag. Technol. High Density Packag.*, pp. 666–670, 2012.
- [200] Y. Han, B. L. Lau, G. Tang, and X. Zhang, “Development of a Jet-based Si Micro-cooler with Multiple Drainage Micro-Trenches,” *2015 IEEE 17th Electron. Packag. Technol. Conf.*, pp. 1–5, 2015.
- [201] P. Naphon and S. Klangchart, “Effects of outlet port positions on the jet impingement heat transfer characteristics in the mini-fin heat sink ☆,” *Int. Commun. Heat Mass Transf.*, vol.

38, no. 10, pp. 1400–1405, 2011.

- [202] A. Gorodetsky *et al.*, “International Journal of Thermal Sciences Flow and heat transfer analysis of hybrid cooling schemes : Adding micro-jets to a micro-gap,” *Int. J. Therm. Sci.*, vol. 138, no. June 2018, pp. 367–383, 2019.
- [203] Y. Han, G. Tang, B. L. Lau, and X. Zhang, “Hybrid Micro-Fluid Heat Sink for High Power Dissipation of Liquid-Cooled Data Centre,” pp. 17–20, 2017.
- [204] P. R. Parida, S. V Ekkad, and K. Ngo, “International Journal of Heat and Mass Transfer Impingement-based high performance cooling configurations for automotive power converters,” *Int. J. Heat Mass Transf.*, vol. 55, no. 4, pp. 834–847, 2012.
- [205] K. Gould, S. Q. Cai, C. Neft, and S. Member, “Liquid Jet Impingement Cooling of a Silicon Carbide Power Conversion Module for Vehicle Applications,” *IEEE Trans. Power Electron.*, vol. 30, no. 6, pp. 2975–2984, 2015.
- [206] J. Shin, T. Rozenfeld, T. Shockner, and A. K. Vutha, “Local heat transfer under an array of micro jet impingement using HFE-7000,” *Appl. Therm. Eng.*, vol. 158, no. May, p. 113716, 2019.
- [207] P. S. Penumadu and A. G. Rao, “Numerical investigations of heat transfer and pressure drop characteristics in multiple jet impingement system,” *Appl. Therm. Eng.*, vol. 110, pp. 1511–1524, 2017.
- [208] J. Barrau, M. Omri, D. Chemisana, J. Rosell, M. Ibañez, and L. Tadrist, “Numerical study of a hybrid jet impingement / micro-channel cooling scheme,” *Appl. Therm. Eng.*, vol. 33–34, pp. 237–245, 2012.
- [209] Y. Han, B. L. Lau, and X. Zhang, “Package-Level Microjet-Based Hotspot Cooling Solution for Microelectronic Devices,” *IEEE Electron Device Lett.*, vol. 36, no. 5, pp. 502–504, 2015.
- [210] K. Na-pompet and W. Boonsupthip, “Effect of a narrow channel on heat transfer enhancement of a slot-jet impingement system,” *J. Food Eng.*, vol. 103, no. 4, pp. 366–376, 2011.

- [211] Z. Yan, F. A. N. Jing-yu, and L. I. U. Johan, “Numerical investigation on thermal properties of micro-pin-fin cooler,” vol. 15, no. 10702037, pp. 272–278, 2011.
- [212] Y. Yang, S. Lin, Y. Wang, and J. Hsu, “Numerical simulation and optimization of impingement cooling for rotating and stationary pin – fin heat sinks,” *Int. J. Heat Fluid Flow*, vol. 44, pp. 383–393, 2013.
- [213] A. A. Ranjbar, A. Ramiar, and M. Rahgoshay, “Numerical simulation of forced convection of nanofluid in a confined jet,” pp. 1995–2005, 2012.
- [214] E. Farsad, S. P. Abbasi, M. S. Zabihi, and J. Sabbaghzadeh, “Numerical simulation of heat transfer in a micro channel heat sinks using nanofluids,” pp. 479–490, 2011.
- [215] J. Ortega-casanova and F. J. Granados-ortiz, “Numerical simulation of the heat transfer from a heated plate with surface variations to an impinging jet,” *Int. J. Heat Mass Transf.*, vol. 76, pp. 128–143, 2014.
- [216] A. Kumar *et al.*, “International Journal of Heat and Mass Transfer Spatial temperature resolution in single-phase micro slot jet impingement cooling,” *Int. J. Heat Mass Transf.*, vol. 118, pp. 720–733, 2018.
- [217] Z. Y. Wang, T. N. Wong, and F. Duan, “Submerged Liquid Jet Impingement Cooling,” *2011 IEEE 13th Electron. Packag. Technol. Conf.*, pp. 660–666, 2011.
- [218] R. Q. J. Dq *et al.*, “7khupdo 0dqdjphqw ri +rwvsrwv 8vlqj 8svwuhdp /dplqdu 0lfur - hw ,pslqlqj \$uud\,” pp. 83–87, 2013.
- [219] Y. Han, B. L. Lau, X. Zhang, S. Member, Y. C. Leong, and K. F. Choo, “Thermal Management of Hotspots With a Microjet-Based Hybrid Heat Sink for,” *IEEE Trans. Components, Packag. Manuf. Technol.*, vol. 4, no. 9, pp. 1441–1450, 2014.
- [220] R. Wu, T. Hong, Q. Cheng, H. Zou, Y. Fan, and X. Luo, “International Journal of Heat and Mass Transfer Thermal modeling and comparative analysis of jet impingement liquid cooling for high power electronics,” *Int. J. Heat Mass Transf.*, vol. 137, pp. 42–51, 2019.

- [221] S. Ndaø, Y. Peles, and M. K. Jensen, “Micro device design and fabrication for the experimental investigation of jet impingement on an array of micro pin fins,” 2014.
- [222] A. Husain, M. Ariz, N. Z. H. Al-rawahi, and M. Z. Ansari, “Thermal performance analysis of a hybrid micro-channel , -pillar and -jet impingement heat sink,” *Appl. Therm. Eng.*, vol. 102, pp. 989–1000, 2016.
- [223] G. K. Batchelor. and Dynamics., *An Introduction to Fluid Dynamics*. Cambridge Univ. Press, Cambridge, England, 1967.
- [224] F. Menter and T. Esch, “16th BRAZILIAN CONGRESS OF MECHANICAL ENGINEERING ELEMENTS OF INDUSTRIAL HEAT TRANSFER PREDICTIONS,” 2001.
- [225] J. Cao, Y. Ding, and C. Ma, “Aqueous Al₂O₃ nanofluids: The important factors impacting convective heat transfer,” *Heat Mass Transf. und Stoffuebertragung*, vol. 50, no. 12, pp. 1639–1648, 2014.
- [226] H. Jin, T. Andritsch, I. A. Tsekmes, R. Kochetov, P. H. F. Morshuis, and J. J. Smit, “Thermal conductivity of fullerene and TiO₂ nanofluids,” *Annu. Rep. - Conf. Electr. Insul. Dielectr. Phenomena, CEIDP*, pp. 711–714, 2013.
- [227] K. Paulovičová, J. Tóthová, M. Rajnák, M. Timko, P. Kopčanský, and V. Lisý, “Electro-rheological properties of transformer oil-based magnetic fluids,” *Acta Phys. Pol. A*, vol. 131, no. 4, pp. 1141–1143, 2017.
- [228] P. Lukacs, A. Pietrikova, and T. Rovensky, “Viscosity Measurement of Silver Based Naninks,” *Period. Polytech. Electr. Eng. Comput. Sci.*, vol. 62, no. 4, pp. 181–186, 2018.
- [229] M. Kaszuba, J. Corbett, F. M. N. Watson, and A. Jones, “High-concentration zeta potential measurements using light-scattering techniques,” *Philos. Trans. R. Soc. A Math. Phys. Eng. Sci.*, vol. 368, no. 1927, pp. 4439–4451, 2010.
- [230] M. Jaworska, E. Sikora, M. Zielina, and J. Ogonowski, “Studies on the formation of O/W

nano-emulsions, by low-energy emulsification method, suitable for cosmeceutical applications,” *Acta Biochim. Pol.*, vol. 60, no. 4, pp. 779–782, 2013.

- [231] S. E. McNeil, *Challenges for nanoparticle characterization.*, vol. 697. 2011.
- [232] R. Marsalek, “Particle Size and Zeta Potential of ZnO,” *APCBEE Procedia*, vol. 9, pp. 13–17, 2014.
- [233] F. Carle, B. Sobac, and D. Brutin, “Hydrothermal waves on ethanol droplets evaporating under terrestrial and reduced gravity levels,” *J. Fluid Mech.*, vol. 712, pp. 614–623, 2012.
- [234] D. Bartocha, T. Wróbel, J. Szajnar, W. Adamczyk, W. Jamrozik, and M. Dojka, “The influence of casting velocity on structure of Al continuous ingots,” *Arch. Metall. Mater.*, vol. 62, no. 3, pp. 1609–1613, 2017.
- [235] M. Mehrali *et al.*, “Investigation of thermal conductivity and rheological properties of nanofluids containing graphene nanoplatelets.,” *Nanoscale Res. Lett.*, vol. 9, no. 1, p. 15, 2014.
- [236] W. S. Hummers and R. E. Offeman, “Preparation of Graphitic Oxide,” *J. Am. Chem. Soc.*, vol. 80, no. 6, p. 1339, 1958.
- [237] C. W. Nan, Z. Shi, and Y. Lin, “A simple model for thermal conductivity of carbon nanotube-based composites,” *Chem. Phys. Lett.*, vol. 375, no. 5–6, pp. 666–669, 2003.
- [238] R. van Erp, R. Soleiman-zadeh, L. Nela, G. Kampitsis, and E. Matioli, “Co-designing electronics with microfluidics for more sustainable cooling,” *Nature*, vol. 585, no. 7824, pp. 211–216, 2020.
- [239] K. S. Choo and S. J. Kim, “Comparison of thermal characteristics of confined and unconfined impinging jets,” *Int. J. Heat Mass Transf.*, vol. 53, no. 15–16, pp. 3366–3371, 2010.
- [240] P. Tie, Q. Li, and Y. Xuan, “Investigation on the submerged liquid jet arrays impingement cooling,” *Appl. Therm. Eng.*, vol. 31, no. 14–15, pp. 2757–2763, 2011.
- [241] S. Zhang, E. Laboure, D. Labrousse, and S. Lefebvre, “Thermal management for GaN power

devices mounted on PCB substrates,” *2017 IEEE Int. Work. Integr. Power Packag. IWIPP 2017*, vol. 285, pp. 1–5, 2017.